1 **Global Carbon Budget 2021**

3 Pierre Friedlingstein[1,2], Matthew W. Jones[3], Michael O'Sullivan[1], Robbie M. Andrew[4],

4 Dorothee, C. E. Bakker[5], Judith Hauck[6], Corinne Le Quéré[3], Glen P. Peters[4], Wouter

5 Peters[7,8], Julia Pongratz[9,10], Stephen Sitch[11], Josep G. Canadell[12], Philippe Ciais[13], Rob B.

6 Jackson[14], Simone R. Alin[15], Peter Anthoni[16], Nicholas R. Bates[17], Meike Becker[18,19], Nicolas

7 Bellouin[20], Laurent Bopp[2], Thi Tuyet Trang Chau[13], Frédéric Chevallier[13], Louise P. Chini[21],

8 Margot Cronin[22], Kim I. Currie[23], Bertrand Decharme[24], Laique M. Djeutchouang[25,26], Xinyu

[1] College of Engineering, Mathematics and Physical Sciences, University of Exeter, Exeter EX4 4QF, UK

[2] Laboratoire de Météorologie Dynamique, Institut Pierre-Simon Laplace, CNRS-ENS-UPMC-X

[3] Tyndall Centre for Climate Change Research, School of Environmental Sciences, University of East Anglia, Norwich Research Park, Norwich NR4 7TJ, UK

[4] CICERO Center for International Climate Research, Oslo 0349, Norway

[5] School of Environmental Sciences, University of East Anglia, Norwich Research Park, Norwich NR4 7TJ, UK

[6] Alfred-Wegener-Institut, Helmholtz-Zentrum für Polar- und Meeresforschung, Am Handelshafen 12, 27570 Bremerhaven

[7] Wageningen University, Environmental Sciences Group, P.O. Box 47, 6700AA, Wageningen, The Netherlands

[8] University of Groningen, Centre for Isotope Research, Groningen, The Netherlands

[9] Ludwig-Maximilians-Universität München, Luisenstr. 37, 80333 München, Germany

[10] Max Planck Institute for Meteorology, Bundesstr. 53, 20146 Hamburg, Germany

[11] College of Life and Environmental Sciences, University of Exeter, Exeter EX4 4RJ, UK

[12] CSIRO Oceans and Atmosphere, Canberra, ACT 2101, Australia

[13] Laboratoire des Sciences du Climat et de l'Environnement, LSCE/IPSL, CEA-CNRS-UVSQ, Université Paris-Saclay, F-91198 Gif-sur-Yvette, France

[14] Department of Earth System Science, Woods Institute for the Environment, and Precourt Institute for Energy, Stanford University, Stanford, CA 94305–2210, United States of America

[15] National Oceanic & Atmospheric Administration, Pacific Marine Environmental Laboratory (NOAA/PMEL), 7600 Sand Point Way NE, Seattle, WA 98115, USA

[16] Karlsruhe Institute of Technology, Institute of Meteorology and Climate Research/Atmospheric Environmental Research, 82467 Garmisch-Partenkirchen, Germany

[17] Bermuda Institute of Ocean Sciences (BIOS), 17 Biological Lane, Ferry Reach, St. Georges, GEO1, Bermuda

[18] Geophysical Institute, University of Bergen, Bergen, Norway

[19] Bjerknes Centre for Climate Research, Bergen, Norway

[20] Department of Meteorology, University of Reading, Reading, UK

[21] Department of Geographical Sciences, University of Maryland, College Park, Maryland 20742, USA

[22] Marine Institute, Ireland

[23] NIWA, Union Place West, Dunedin, New Zealand

[24] CNRM, Université de Toulouse, Météo-France, CNRS, Toulouse, France

[25] Department of Oceanography, University of Cape Town, Cape Town, 7701, South Africa

[26] SOCCO, Council for Scientific and Industrial Research, Cape Town, 7700, South Africa

Dou[27], Wiley Evans[28], Richard A. Feely[15], Liang Feng[29], Thomas Gasser[30], Dennis Gilfillan[31], Thanos Gkritzalis[32], Giacomo Grassi[33], Luke Gregor[34], Nicolas Gruber[34], Özgür Gürses[6], Ian Harris[35], Richard A. Houghton[36], George C. Hurtt[21], Yosuke Iida[37], Tatiana Ilyina[10], Ingrid T. Luijkx[7], Atul Jain[38], Steve D. Jones[18,19], Etsushi Kato[39], Daniel Kennedy[40], Kees Klein Goldewijk[41], Jürgen Knauer[12,42], Jan Ivar Korsbakken[4], Arne Körtzinger[43], Peter Landschützer[10], Siv K. Lauvset[19,44], Nathalie Lefèvre[45], Sebastian Lienert[46], Junjie Liu[47],

Dou[27], Wiley Evans[28], Richard A. Feely[15], Liang Feng[29], Thomas Gasser[30], Dennis Gilfillan[31], Thanos Gkritzalis[32], Giacomo Grassi[33], Luke Gregor[34], Nicolas Gruber[34], Özgür Gürses[6], Ian Harris[35], Richard A. Houghton[36], George C. Hurtt[21], Yosuke Iida[37], Tatiana Ilyina[10], Ingrid T. Luijkx[7], Atul Jain[38], Steve D. Jones[18,19], Etsushi Kato[39], Daniel Kennedy[40], Kees Klein Goldewijk[41], Jürgen Knauer[12,42], Jan Ivar Korsbakken[4], Arne Körtzinger[43], Peter Landschützer[10], Siv K. Lauvset[19,44], Nathalie Lefèvre[45], Sebastian Lienert[46], Junjie Liu[47],

[27] Department of Earth System Science, Tsinghua University, Beijing, China

[28] Hakai Institute, Heriot Bay, BC, Canada

[29] National Centre for Earth Observation, University of Edinburgh, UK

[30] International Institute for Applied Systems Analysis (IIASA), Schlossplatz 1 A-2361 Laxenburg, Austria

[31] North Carolina School for Science and Mathematics, Durham, North Carolina, USA

[32] Flanders Marine Institute (VLIZ), InnovOceanSite, Wandelaarkaai 7, 8400 Ostend, Belgium

[33] European Commission, Joint Research Centre, 21027 Ispra (VA), Italy

[34] Environmental Physics Group, ETH Zürich, Institute of Biogeochemistry and Pollutant Dynamics and Center for Climate Systems Modeling (C2SM), 8092 Zurich, Switzerland

[35] NCAS-Climate, Climatic Research Unit, School of Environmental Sciences, University of East Anglia, Norwich Research Park, Norwich, NR4 7TJ, UK

[36] Woodwell Climate Research Center, Falmouth, MA 02540, USA

[37] Atmosphere and Ocean Department, Japan Meteorological Agency, Minato-Ku, Tokyo 105-8431, Japan

[38] Department of Atmospheric Sciences, University of Illinois, Urbana, IL 61821, USA

[39] Institute of Applied Energy (IAE), Minato-ku, Tokyo 105-0003, Japan

[40] National Center for Atmospheric Research, Climate and Global Dynamics, Terrestrial Sciences Section, Boulder, CO 80305, USA

[41] Utrecht University, Faculty of Geosciences, Department IMEW, Copernicus Institute of Sustainable Development, Heidelberglaan 2, P.O. Box 80115, 3508 TC, Utrecht, the Netherlands

[42] Hawkesbury Institute for the Environment, Western Sydney University, Penrith, New South Wales, Australia

[43] GEOMAR Helmholtz Centre for Ocean Research Kiel, Düsternbrooker Weg 20, 24105 Kiel, Germany

[44] NORCE Norwegian Research Centre, Jahnebakken 5, 5007 Bergen, Norway

[45] LOCEAN/IPSL laboratory, Sorbonne Université, CNRS/IRD/MNHN, Paris, France

[46] Climate and Environmental Physics, Physics Institute and Oeschger Centre for Climate Change Research, University of Bern, Bern, Switzerland

[47] NASA JPL

Gregg Marland[48,49], Patrick C. McGuire[50], Joe R. Melton[51], David R. Munro[52,53], Julia E.M.S Nabel[10,54] Shin-Ichiro Nakaoka[55], Yosuke Niwa[55,56], Tsuneo Ono[57], Denis Pierrot[58], Benjamin Poulter[59], Gregor Rehder[60], Laure Resplandy[61], Eddy Robertson[62], Christian Rödenbeck[54], Thais M Rosan[11], Jörg Schwinger[44,19], Clemens Schwingshackl[9], Roland Séférian[24], Adrienne J. Sutton[15], Colm Sweeney[53], Toste Tanhua[43], Pieter P Tans[63], Hanqin Tian[64], Bronte Tilbrook[65,66], Francesco Tubiello[67], Guido R. van der Werf[68], Nicolas Vuichard[13], Chisato Wada[55] Rik Wanninkhof[58], Andrew J. Watson[11], David Willis[3], Andrew J. Wiltshire[62], Wenping Yuan[69], Chao Yue[13], Xu Yue[70], Sönke Zaehle[54], Jiye Zeng[55]

---

[48] Research Institute for Environment, Energy, and Economics, Appalachian State University, Boone, North Carolina, USA

[49] Department of Geological and Environmental Sciences, Appalachian State University, Boone, North Carolina, USA

[50] Department of Meteorology, Department of Geography & Environmental Science, National Centre for Atmospheric Science, University of Reading, Reading, UK

[51] Climate Research Division, Environment and Climate Change Canada, Victoria, BC, Canada

[52] Cooperative Institute for Research in Environmental Sciences, University of Colorado, Boulder, CO, 80305, USA

[53] National Oceanic & Atmospheric Administration/Global Monitoring Laboratory (NOAA/GML), Boulder, CO, 80305, USA

[54] Max Planck Institute for Biogeochemistry, Jena, Germany

[55] Earth System Division, National Institute for Environmental Studies, 16-2 Onogawa, Tsukuba, Ibaraki, 305-8506 Japan

[56] Meteorological Research Institute, 1-1 Nagamine, Tsukuba, Ibaraki, 305-0052 Japan

[57] Japan Fisheries Research and Education Agency, 2-12-4 Fukuura, Kanazawa-Ku, Yokohama 236-8648, Japan

[58] National Oceanic & Atmospheric Administration/Atlantic Oceanographic & Meteorological Laboratory (NOAA/AOML), Miami, FL 33149, USA

[59] NASA Goddard Space Flight Center, Biospheric Sciences Laboratory, Greenbelt, Maryland 20771, USA

[60] Leibniz Institute for Baltic Sea Research Warnemuende (IOW), Seestrasse 15; 18119 Rostock, Germany

[61] Princeton University, Department of Geosciences and Princeton Environmental Institute, Princeton, NJ, USA

[62] Met Office Hadley Centre, FitzRoy Road, Exeter EX1 3PB, UK

[63] National Oceanic and Atmospheric Administration, Earth System Research Laboratory (NOAA ESRL),Boulder, CO 80305, USA

[64] School of Forestry and Wildlife Sciences, Auburn University, 602 Ducan Drive, Auburn, AL 36849, USA

[65] CSIRO Oceans and Atmosphere, PO Box 1538, Hobart Tasmania 7001, Australia

[66] Australian Antarctic Partnership Program, University of Tasmania, Hobart, Australia

[67] Statistics Division, Food and Agriculture Organization of the United Nations, Via Terme di Caracalla, Rome 00153, Italy

[68] Faculty of Earth and Life Sciences, VU University, Amsterdam, The Netherlands

[69] School of Atmospheric Sciences, Sun Yat-sen University, Zhuhai, Guangdong 510245, China

[70] School of Environmental Science and Engineering, Nanjing University of Information Science and Technology (NUIST)

25
26
27
28
29
30
31
32
33
34
35
36
37
38
39
40
41
42
43
44
45
46 **Correspondence**: Pierre Friedlingstein (p.friedlingstein@exeter.ac.uk)
47
48
49 **Abstract**
50
51 Accurate assessment of anthropogenic carbon dioxide (CO_2) emissions and their
52 redistribution among the atmosphere, ocean, and terrestrial biosphere in a changing
53 climate is critical to better understand the global carbon cycle, support the development of
54 climate policies, and project future climate change. Here we describe and synthesise data
55 sets and methodology to quantify the five major components of the global carbon budget
56 and their uncertainties. Fossil CO_2 emissions (E_{FOS}) are based on energy statistics and
57 cement production data, while emissions from land-use change (E_{LUC}), mainly deforestation,
58 are based on land-use and land-use change data and bookkeeping models. Atmospheric CO_2
59 concentration is measured directly, and its growth rate (G_{ATM}) is computed from the annual
60 changes in concentration. The ocean CO_2 sink (S_{OCEAN}) is estimated with global ocean
61 biogeochemistry models and observation-based data-products. The terrestrial CO_2 sink
62 (S_{LAND}) is estimated with dynamic global vegetation models. The resulting carbon budget
63 imbalance (B_{IM}), the difference between the estimated total emissions and the estimated
64 changes in the atmosphere, ocean, and terrestrial biosphere, is a measure of imperfect data

65 and understanding of the contemporary carbon cycle. All uncertainties are reported as ±1σ.

66 For the first time, an approach is shown to reconcile the difference in our E_{LUC} estimate with

67 the one from national greenhouse gases inventories, supporting the assessment of

68 collective countries' climate progress.

69 For the year 2020, E_{FOS} declined by 5.4% relative to 2019, with fossil emissions at 9.5 ± 0.5

70 GtC yr^{-1} (9.3 ± 0.5 GtC yr^{-1} when the cement carbonation sink is included), E_{LUC} was 0.9 ± 0.7

71 GtC yr^{-1}, for a total anthropogenic CO_2 emission of 10.2 ± 0.8 GtC yr^{-1} (37.4 ± 2.9 GtCO$_2$).

72 Also, for 2020, G_{ATM} was 5.0 ± 0.2 GtC yr^{-1} (2.4 ± 0.1 ppm yr^{-1}), S_{OCEAN} was 3.0 ± 0.4 GtC yr^{-1}

73 and S_{LAND} was 2.9 ± 1 GtC yr^{-1}, with a B_{IM} of -0.8 GtC yr^{-1}. The global atmospheric CO_2

74 concentration averaged over 2020 reached 412.45 ± 0.1 ppm. Preliminary data for 2021,

75 suggest a rebound in E_{FOS} relative to 2020 of +4.8% (4.2% to 5.4%) globally.

76 Overall, the mean and trend in the components of the global carbon budget are consistently

77 estimated over the period 1959-2020, but discrepancies of up to 1 GtC yr^{-1} persist for the

78 representation of annual to semi-decadal variability in CO_2 fluxes. Comparison of estimates

79 from multiple approaches and observations shows: (1) a persistent large uncertainty in the

80 estimate of land-use changes emissions, (2) a low agreement between the different

81 methods on the magnitude of the land CO_2 flux in the northern extra-tropics, and (3) a

82 discrepancy between the different methods on the strength of the ocean sink over the last

83 decade. This living data update documents changes in the methods and data sets used in

84 this new global carbon budget and the progress in understanding of the global carbon cycle

85 compared with previous publications of this data set (Friedlingstein et al., 2020;

86 Friedlingstein et al., 2019; Le Quéré et al., 2018b, 2018a, 2016, 2015b, 2015a, 2014, 2013).

87 The data presented in this work are available at https://doi.org/10.18160/gcp-2021

88 (Friedlingstein et al., 2021).

89   **Executive Summary**

90   **Global fossil CO_2 emissions (excluding cement carbonation) in 2021 are returning towards**

91   **their 2019 levels after decreasing [5.4%] in 2020.** The 2020 decrease was 0.52 GtC yr^{-1} (1.9

92   GtCO$_2$ yr^{-1}), bringing 2020 emissions to 9.5 ± 0.5 GtC yr^{-1} (34.8 ± 1.8 GtCO$_2$ yr^{-1}), comparable

93   to the emissions level of 2012. Preliminary estimates based on data available in March 2022

94   suggest fossil CO_2 emissions rebounded 4.8% in 2021 (4.2% to 5.4%), bringing emissions at

95   9.9 GtC yr^{-1} (36.4 GtCO$_2$ yr^{-1}), back to about the same level as in 2019 (10.0 ± 0.5 GtC yr^{-1},

96   36.7 ± 1.8 GtCO$_2$ yr^{-1}). Emissions from coal and gas in 2021 are expected to have rebounded

97   above 2019 levels, while emissions from oil were still below their 2019 level. Emissions are

98   expected to have been 5.7% higher in 2021 than in 2019 in China, reaching 3.0 GtC (11.1

99   GtCO$_2$) and also higher in India with a 3.2% increase in 2021 relative to 2019, reaching 0.74

100   GtC (2.7 GtCO$_2$). In contrast, projected 2021 emissions in the United States (1.4 GtC, 5.0

101   GtCO$_2$), European Union (0.8 GtC, 2.8 GtCO$_2$), and the rest of the world (4.0 GtC, 14.8 GtCO$_2$,

102   in aggregate) remained respectively 4.5%, 5.3%, and 4.0% below their 2019 levels. These

103   changes in 2021 emissions reflect the stringency of the COVID-19 confinement levels in

104   2020 and the pre-covid background trends in emissions in these countries.

105   **Fossil CO_2 emissions significantly decreased in 23 countries during the decade 2010-2019.**

106   Altogether, these 23 countries contribute to about 2.5 GtC yr^{-1} fossil fuel CO_2 emissions over

107   the last decade, only about one quarter of world CO_2 fossil emissions.

108   **Global CO_2 emissions from land-use, land-use change, and forestry (LUC) converge based**

109   **on revised data of land-use change and show a small decrease over the past two decades.**

110   Near constant gross emissions estimated at 3.8 ± 0.6 GtC yr^{-1} in the 2011-2020 decade are

111   only partly offset by growing carbon removals on managed land of 2.7 ± 0.4 GtC yr^{-1},

112   resulting in the net emissions in managed land of 1.1 ± 0.7 GtC yr^{-1} (4.1 ± 2.6 GtCO2 yr^{-1}).

113   These net emissions decreased by 0.2 GtC in 2020 compared to 2019 levels, with large

114   uncertainty. Preliminary estimates for emissions in 2021 suggest a 0.1 GtC decrease for

115   2021, giving net emissions of 0.8 GtC yr^{-1} (2.9 GtCO2 yr^{-1}). The small decrease in net LUC

116   emissions amidst large uncertainty prohibits robust conclusions concerning trend changes of

117   total anthropogenic emissions. For the first time, we link the global carbon budget models'

118   estimates to the official country reporting of national greenhouse gases inventories. While

119   the global carbon budget distinguishes anthropogenic from natural drivers of land carbon

120   fluxes, country reporting is area-based and attributes part of the natural terrestrial sink on

121   managed land to the land-use sector. Accounting for this redistribution, the two approaches

122   are shown to be consistent with each other.

123   **The remaining carbon budget for a 50% likelihood to limit global warming to 1.5°C, 1.7°C**

124   **and 2°C has respectively reduced to 120 GtC (420 GtCO$_2$), 210 GtC (770 GtCO$_2$) and 350 GtC**

125   **(1270 GtCO$_2$) from the beginning of 2022, equivalent to 11, 20 and 32 years, assuming**

126   **2021 emissions levels.** Total anthropogenic emissions were 10.4 GtC yr^{-1} (38.0 GtCO$_2$ yr-1) in

127   2020, with a preliminary estimate of 10.7 GtC yr^{-1} (39.3 GtCO2 yr^{-1}) for 2021. The remaining

128   carbon budget to keep global temperatures below these climate targets has shrunk by 21

129   GtC (77 GtCO$_2$) since the release of the IPCC AR6 Working Group 1 assessment. Reaching

130   zero CO$_2$ emissions by 2050 entails cutting total anthropogenic CO$_2$ emissions by about 0.4

131   GtC (1.4 GtCO$_2$) each year on average, comparable to the decrease during 2020, highlighting

132   the scale of the action needed.

133   **The concentration of CO$_2$ in the atmosphere is set to reach 414.7 ppm in 2021, 50% above**

134   **pre-industrial levels.** The atmospheric CO$_2$ growth was 5.1 ± 0.02 GtC yr^{-1} during the decade

135   2011-2020 (47% of total CO$_2$ emissions) with a preliminary 2021 growth rate estimate of

136   around 5 GtC yr^{-1}.

137   **The ocean CO$_2$ sink resumed a more rapid growth in the past decade after low or no**

138   **growth during the 1991-2002 period.** However, the growth of the ocean CO$_2$ sink in the

139   past decade has an uncertainty of a factor of three, with estimates based on data products

140   and estimates based on models showing an ocean sink increase of 0.9 GtC yr^{-1} and 0.3 GtC

141   yr^{-1} since 2010, respectively. The discrepancy in the trend originates from all latitudes but is

142   largest in the Southern Ocean. The ocean CO$_2$ sink was 2.8 ± 0.4 GtC yr^{-1} during the decade

143   2011-2020 (26% of total CO$_2$ emissions), with a preliminary 2021 estimate of around 2.9 GtC

144   yr^{-1}.

145   **The land CO$_2$ sink continued to increase during the 2011-2020 period primarily in response**

146   **to increased atmospheric CO$_2$, albeit with large interannual variability.** The land CO$_2$ sink

147   was 3.1 ± 0.6 GtC yr^{-1} during the 2011-2020 decade (29% of total CO$_2$ emissions), 0.5 GtC yr^{-1}

148   larger than during the previous decade (2000-2009), with a preliminary 2021 estimate of

149 around 3.3 GtC yr^{-1}. Year to year variability in the land sink is about 1 GtC yr^{-1}, making small

150 annual changes in anthropogenic emissions hard to detect in global atmospheric CO_2

151 concentration.

1   Introduction

The concentration of carbon dioxide (CO_2) in the atmosphere has increased from approximately 277 parts per million (ppm) in 1750 (Joos and Spahni, 2008), the beginning of the Industrial Era, to 412.4 ± 0.1 ppm in 2020 (Dlugokencky and Tans, 2022); Fig. 1). The atmospheric CO_2 increase above pre-industrial levels was, initially, primarily caused by the release of carbon to the atmosphere from deforestation and other land-use change activities (Canadell et al., 2021). While emissions from fossil fuels started before the Industrial Era, they became the dominant source of anthropogenic emissions to the atmosphere from around 1950 and their relative share has continued to increase until present. Anthropogenic emissions occur on top of an active natural carbon cycle that circulates carbon between the reservoirs of the atmosphere, ocean, and terrestrial biosphere on time scales from sub-daily to millennia, while exchanges with geologic reservoirs occur at longer timescales (Archer et al., 2009).

The global carbon budget (GCB) presented here refers to the mean, variations, and trends in the perturbation of CO_2 in the environment, referenced to the beginning of the Industrial Era (defined here as 1750). This paper describes the components of the global carbon cycle over the historical period with a stronger focus on the recent period (since 1958, onset of atmospheric CO_2 measurements), the last decade (2011-2020), the last year (2020) and the current year (2021). We quantify the input of CO_2 to the atmosphere by emissions from human activities, the growth rate of atmospheric CO_2 concentration, and the resulting changes in the storage of carbon in the land and ocean reservoirs in response to increasing atmospheric CO_2 levels, climate change and variability, and other anthropogenic and natural changes (Fig. 2). An understanding of this perturbation budget over time and the underlying variability and trends of the natural carbon cycle is necessary to understand the response of natural sinks to changes in climate, CO_2 and land-use change drivers, and to quantify emissions compatible with a given climate stabilisation target.

The components of the CO_2 budget that are reported annually in this paper include separate and independent estimates for the CO_2 emissions from (1) fossil fuel combustion and oxidation from all energy and industrial processes; also including cement production and carbonation (E_{FOS}; GtC yr^{-1}) and (2) the emissions resulting from deliberate human activities on land, including those leading to land-use change (E_{LUC}; GtC yr^{-1}); and their partitioning

183   among (3) the growth rate of atmospheric CO_2 concentration (G_{ATM}; GtC yr^{-1}), and the

184   uptake of CO_2 (the 'CO_2 sinks') in (4) the ocean (S_{OCEAN}; GtC yr^{-1}) and (5) on land (S_{LAND}; GtC

185   yr^{-1}). The CO_2 sinks as defined here conceptually include the response of the land (including

186   inland waters and estuaries) and ocean (including coasts and territorial seas) to elevated

187   CO_2 and changes in climate and other environmental conditions, although in practice not all

188   processes are fully accounted for (see Section 2.7). Global emissions and their partitioning

189   among the atmosphere, ocean and land are in reality in balance. Due to the combination of

190   imperfect spatial and/or temporal data coverage, errors in each estimate, and smaller terms

191   not included in our budget estimate (discussed in Section 2.7), the independent estimates

192   (1) to (5) above do not necessarily add up to zero. We therefore (a) additionally assess a set

193   of global atmospheric inverse model results that by design close the global carbon balance

194   (see Section 2.6), and (b) estimate a budget imbalance (B_{IM}), which is a measure of the

195   mismatch between the estimated emissions and the estimated changes in the atmosphere,

196   land and ocean, as follows:

197    $$B_{IM} = E_{FOS} + E_{LUC} - (G_{ATM} + S_{OCEAN} + S_{LAND}) \qquad (1)$$

198   G_{ATM} is usually reported in ppm yr^{-1}, which we convert to units of carbon mass per year, GtC

199   yr^{-1}, using 1 ppm = 2.124 GtC (Ballantyne et al., 2012; Table 1). All quantities are presented

200   in units of gigatonnes of carbon (GtC, 10^{15} gC), which is the same as petagrams of carbon

201   (PgC; Table 1). Units of gigatonnes of CO_2 (or billion tonnes of CO_2) used in policy are equal

202   to 3.664 multiplied by the value in units of GtC.

203   We also include a quantification of E_{FOS} by country, computed with both territorial and

204   consumption-based accounting (see Section 2), and discuss missing terms from sources

205   other than the combustion of fossil fuels (see Section 2.7).

206   The global CO_2 budget has been assessed by the Intergovernmental Panel on Climate

207   Change (IPCC) in all assessment reports (Prentice et al., 2001; Schimel et al., 1995; Watson

208   et al., 1990; Denman et al., 2007; Ciais et al., 2013; Canadell et al., 2021), and by others (e.g.

209   Ballantyne et al., 2012). The Global Carbon Project (GCP, www.globalcarbonproject.org, last

210   access: 11 March 2022) has coordinated this cooperative community effort for the annual

211   publication of global carbon budgets for the year 2005 (Raupach et al., 2007; including fossil

212   emissions only), year 2006 (Canadell et al., 2007), year 2007 (GCP, 2008), year 2008 (Le

213   Quéré et al., 2009), year 2009 (Friedlingstein et al., 2010), year 2010 (Peters et al., 2012b),

214   year 2012 (Le Quéré et al., 2013; Peters et al., 2013), year 2013 (Le Quéré et al., 2014), year

215   2014 (Le Quéré et al., 2015a; Friedlingstein et al., 2014), year 2015 (Jackson et al., 2016; Le

216   Quéré et al., 2015b), year 2016 (Le Quéré et al., 2016), year 2017 (Le Quéré et al., 2018a;

217   Peters et al., 2017), year 2018 (Le Quéré et al., 2018b; Jackson et al., 2018) year 2019

218   (Friedlingstein et al., 2019; Jackson et al., 2019; Peters et al., 2020) and more recently the

219   year 2020 (Friedlingstein et al., 2020; Le Quéré et al., 2021) . Each of these papers updated

220   previous estimates with the latest available information for the entire time series.

221   We adopt a range of ±1 standard deviation (σ) to report the uncertainties in our estimates,

222   representing a likelihood of 68% that the true value will be within the provided range if the

223   errors have a Gaussian distribution, and no bias is assumed. This choice reflects the difficulty

224   of characterising the uncertainty in the CO_2 fluxes between the atmosphere and the ocean

225   and land reservoirs individually, particularly on an annual basis, as well as the difficulty of

226   updating the CO_2 emissions from land-use change. A likelihood of 68% provides an

227   indication of our current capability to quantify each term and its uncertainty given the

228   available information. The uncertainties reported here combine statistical analysis of the

229   underlying data, assessments of uncertainties in the generation of the data sets, and expert

230   judgement of the likelihood of results lying outside this range. The limitations of current

231   information are discussed in the paper and have been examined in detail elsewhere

232   (Ballantyne et al., 2015; Zscheischler et al., 2017). We also use a qualitative assessment of

233   confidence level to characterise the annual estimates from each term based on the type,

234   amount, quality, and consistency of the evidence as defined by the IPCC (Stocker et al.,

235   2013).

236   This paper provides a detailed description of the data sets and methodology used to

237   compute the global carbon budget estimates for the industrial period, from 1750 to 2020,

238   and in more detail for the period since 1959. It also provides decadal averages starting in

239   1960 including the most recent decade (2011-2020), results for the year 2020, and a

240   projection for the year 2021. Finally, it provides cumulative emissions from fossil fuels and

241   land-use change since the year 1750, the pre-industrial period; and since the year 1850, the

242   reference year for historical simulations in IPCC AR6 (Eyring et al., 2016). This paper is

243   updated every year using the format of 'living data' to keep a record of budget versions and

244   the changes in new data, revision of data, and changes in methodology that lead to changes

245 in estimates of the carbon budget. Additional materials associated with the release of each

246 new version will be posted at the Global Carbon Project (GCP) website

247 (http://www.globalcarbonproject.org/carbonbudget, last access: 11 March 2022), with fossil

248 fuel emissions also available through the Global Carbon Atlas

249 (http://www.globalcarbonatlas.org, last access: 11 March 2022). With this approach, we aim

250 to provide the highest transparency and traceability in the reporting of CO_2, the key driver

251 of climate change.

252 **2   Methods**

253 Multiple organisations and research groups around the world generated the original

254 measurements and data used to complete the global carbon budget. The effort presented

255 here is thus mainly one of synthesis, where results from individual groups are collated,

256 analysed, and evaluated for consistency. We facilitate access to original data with the

257 understanding that primary data sets will be referenced in future work (see Table 2 for how

258 to cite the data sets). Descriptions of the measurements, models, and methodologies follow

259 below, and detailed descriptions of each component are provided elsewhere.

260 This is the 16th version of the global carbon budget and the tenth revised version in the

261 format of a living data update in Earth System Science Data. It builds on the latest published

262 global carbon budget of Friedlingstein et al. (2020). The main changes are: the inclusion of

263 (1) data to year 2020 and a projection for the global carbon budget for year 2021; (2) a Kaya

264 analysis to identify the driving factors behind the recent trends in fossil fuel emissions

265 (changes in population, GDP per person, energy use per GDP, and CO_2 emissions per unit

266 energy), (3) an estimate of the ocean sink from models and data-products combined, (4) an

267 assessment of the relative contributions of increased atmospheric CO_2 and climate change

268 in driving the land and ocean sinks, and (5) an assessment of the current trends in

269 anthropogenic emissions and implications for the remaining carbon budget for specific

270 climate targets. The main methodological differences between recent annual carbon

271 budgets (2016-2020) are summarised in Table 3 and previous changes since 2006 are

272 provided in Table A7.

2.1 Fossil CO$_2$ emissions (E$_{FOS}$)

2.1.1 Historical period 1850-2020

The estimates of global and national fossil CO$_2$ emissions (E$_{FOS}$) include the oxidation of fossil fuels through both combustion (e.g., transport, heating) and chemical oxidation (e.g. carbon anode decomposition in aluminium refining) activities, and the decomposition of carbonates in industrial processes (e.g. the production of cement). We also include CO$_2$ uptake from the cement carbonation process. Several emissions sources are not estimated or not fully covered: coverage of emissions from lime production are not global, and decomposition of carbonates in glass and ceramic production are included only for the "Annex 1" countries of the United Nations Framework Convention on Climate Change (UNFCCC) for lack of activity data. These omissions are considered to be minor. Short-cycle carbon emissions - for example from combustion of biomass - are not included here but are accounted for in the CO$_2$ emissions from land use (see section 2.2).

Our estimates of fossil CO$_2$ emissions are derived using the standard approach of activity data and emission factors, relying on data collection by many other parties. Our goal is to produce the best estimate of this flux, and we therefore use a prioritisation framework to combine data from different sources that have used different methods, while being careful to avoid double counting and undercounting of emissions sources. The CDIAC-FF emissions dataset, derived largely from UN energy data, forms the foundation, and we extend emissions to year Y-1 using energy growth rates reported by BP. We then proceed to replace estimates using data from what we consider to be superior sources, for example Annex 1 countries' official submissions to the UNFCCC. All data points are potentially subject to revision, not just the latest year. For full details see Andrew and Peters (2021).

Other estimates of global fossil CO$_2$ emissions exist, and these are compared by Andrew (2020a). The most common reason for differences in estimates of global fossil CO$_2$ emissions is a difference in which emissions sources are included in the datasets. Datasets such as those published by BP energy company, the US Energy Information Administration, and the International Energy Agency's 'CO$_2$ emissions from fuel combustion' are all generally limited to emissions from combustion of fossil fuels. In contrast, datasets such as PRIMAP-hist, CEDS, EDGAR, and GCP's dataset aim to include all sources of fossil CO$_2$ emissions. See Andrew (2020a) for detailed comparisons and discussion.

304 Cement absorbs CO_2 from the atmosphere over its lifetime, a process known as 'cement

305 carbonation'. We estimate this CO_2 sink as the average of two studies in the literature (Cao

306 et al., 2020; Guo et al., 2021). Both studies use the same model, developed by Xi et al.

307 (2016), with different parameterisations and input data. Since carbonation is a function of

308 both current and previous cement production, we extend these estimates by one year to

309 2020 by using the growth rate derived from the smoothed cement emissions (10-year

310 smoothing) fitted to the carbonation data.

311 We use the Kaya Identity for a simple decomposition of CO_2 emissions into the key drivers

312 (Raupach et al., 2007). While there are variations (Peters et al 2017), we focus here on a

313 decomposition of CO_2 emissions into population, GDP per person, energy use per GDP, and

314 CO_2 emissions per energy. Multiplying these individual components together returns the

315 CO_2 emissions. Using the decomposition, it is possible to attribute the change in CO_2

316 emissions to the change in each of the drivers. This method gives a first order understanding

317 of what causes CO_2 emissions to change each year.

318 **2.1.2   2021 projection**

319 We provide a projection of global CO_2 emissions in 2021 by combining separate projections

320 for China, USA, EU, India, and for all other countries combined. The methods are different

321 for each of these. For China we combine monthly fossil fuel production data from the

322 National Bureau of Statistics, import/export data from the Customs Administration, and

323 monthly coal consumption estimates from SX Coal (2021), giving us partial data for the

324 growth rates to date of natural gas, petroleum, and cement, and of the consumption itself

325 for raw coal. We then use a regression model to project full-year emissions based on

326 historical observations. For the USA our projection is taken directly from the Energy

327 Information Administration's (EIA) Short-Term Energy Outlook (EIA, 2022), combined with

328 the year-to-date growth rate of cement production. For the EU we use monthly energy data

329 from Eurostat to derive estimates of monthly CO_2 emissions through July, with coal

330 emissions extended first through September using a statistical relationship with reported

331 electricity generation from coal and other factors, then through December assuming normal

332 seasonal patterns. EU emissions from natural gas - a strongly seasonal cycle - are extended

333 through December using bias-adjusted Holt-Winters exponential smoothing (Chatfield,

334 1978). EU emissions from oil are derived using the EIA's projection of oil consumption for

335   Europe. EU cement emissions are based on available year-to-date data from two of the

336   largest producers, Germany and Poland. India's projected emissions are derived from

337   estimates through August (September for coal) using the methods of Andrew (2020b) and

338   extrapolated assuming normal seasonal patterns. Emissions for the rest of the world are

339   derived using projected growth in economic production from the IMF (2022) combined with

340   extrapolated changes in emissions intensity of economic production. More details on the

341   E_{FOS} methodology and its 2021 projection can be found in Appendix C.1.

342   **2.2   CO$_2$ emissions from land-use, land-use change and forestry (E_{LUC})**

343   The net CO$_2$ flux from land-use, land-use change and forestry (E_{LUC}, called land-use change

344   emissions in the rest of the text) includes CO$_2$ fluxes from deforestation, afforestation,

345   logging and forest degradation (including harvest activity), shifting cultivation (cycle of

346   cutting forest for agriculture, then abandoning), and regrowth of forests following wood

347   harvest or abandonment of agriculture. Emissions from peat burning and drainage are

348   added from external datasets.

349   Three bookkeeping approaches (updated estimates each of BLUE (Hansis et al., 2015),

350   OSCAR (Gasser et al., 2020), and H&N2017 (Houghton and Nassikas, 2017)) were used to

351   quantify gross sources and sinks and the resulting net E_{LUC}. Uncertainty estimates were

352   derived from the Dynamic Global vegetation Models (DGVMs) ensemble for the time period

353   prior to 1960, using for the recent decades an uncertainty range of ±0.7 GtC yr-1, which is a

354   semi-quantitative measure for annual and decadal emissions and reflects our best value

355   judgement that there is at least 68% chance (±1σ) that the true land-use change emission

356   lies within the given range, for the range of processes considered here. This uncertainty

357   range had been increased from 0.5 GtC yr-1 after new bookkeeping models were included

358   that indicated a larger spread than assumed before (Le Quéré et al., 2018). Projections for

359   2021 are based on fire activity from tropical deforestation and degradation as well as

360   emissions from peat fires and drainage.

361

362   Our E_{LUC} estimates follow the definition of global carbon cycle models of CO$_2$ fluxes related

363   to land-use and land management and differ from IPCC definitions adopted in National GHG

364   Inventories (NGHGI) for reporting under the UNFCCC, which additionally generally include,

365   through adoption of the IPCC so-called managed land proxy approach, the terrestrial fluxes

366 occurring on land defined by countries as managed. This partly includes fluxes due to

367 environmental change (e.g. atmospheric CO_2 increase), which are part of S_{LAND} in our

368 definition. This causes the global emission estimates to be smaller for NGHGI than for the

369 global carbon budget definition (Grassi et al., 2018). The same is the case for the Food

370 Agriculture Organization (FAO) estimates of carbon fluxes on forest land, which include,

371 compared to S_{LAND}, both anthropogenic and natural sources on managed land (Tubiello et

372 al., 2021). Using the approach outlined in Grassi et al. (2021), here we map as additional

373 information the two definitions to each other, to provide a comparison of the

374 anthropogenic carbon budget to the official country reporting to the climate convention.

375 More details on the E_{LUC} methodology can be found in Appendix C.2.

376 **2.3   Growth rate in atmospheric CO_2 concentration (G_{ATM})**

377 **2.3.1   Historical period**

378 The rate of growth of the atmospheric CO_2 concentration is provided for years 1959-2020 by

379 the US National Oceanic and Atmospheric Administration Earth System Research Laboratory

380 (NOAA/ESRL; Dlugokencky and Tans, 2022), which is updated from Ballantyne et al. (2012)

381 and includes recent revisions to the calibration scale of atmospheric CO_2 measurements

382 (Hall et al., 2021). For the 1959-1979 period, the global growth rate is based on

383 measurements of atmospheric CO_2 concentration averaged from the Mauna Loa and South

384 Pole stations, as observed by the CO_2 Program at Scripps Institution of Oceanography

385 (Keeling et al., 1976). For the 1980-2020 time period, the global growth rate is based on the

386 average of multiple stations selected from the marine boundary layer sites with well-mixed

387 background air (Ballantyne et al., 2012), after fitting each station with a smoothed curve as

388 a function of time, and averaging by latitude band (Masarie and Tans, 1995). The annual

389 growth rate is estimated by Dlugokencky and Tans (2022) from atmospheric CO_2

390 concentration by taking the average of the most recent December-January months

391 corrected for the average seasonal cycle and subtracting this same average one year earlier.

392 The growth rate in units of ppm yr^{-1} is converted to units of GtC yr^{-1} by multiplying by a

393 factor of 2.124 GtC per ppm, assuming instantaneous mixing of CO_2 throughout the

394 atmosphere (Ballantyne et al., 2012).

395 Starting in 2020, NOAA/ESRL now provides estimates of atmospheric CO_2 concentrations

396 with respect to a new calibration scale, referred to as WMO-CO2-X2019, in line with the

397 recommendation of the World Meteorological Organization (WMO) Global Atmosphere

398 Watch (GAW) community (Hall et al., 2021). The WMO-CO2-X2019 scale improves upon the

399 earlier WMO-CO2-X2007 scale by including a broader set of standards, which contain CO_2 in

400 a wider range of concentrations that span the range 250-800 ppm (versus 250–520 ppm for

401 WMO-CO2-X2007). In addition, NOAA/ESRL made two minor corrections to the analytical

402 procedure used to quantify CO_2 concentrations, fixing an error in the second virial

403 coefficient of CO_2 and accounting for loss of a small amount of CO_2 to materials in the

404 manometer during the measurement process. The difference in concentrations measured

405 using WMO-CO2-X2019 versus WMO-CO2-X2007 is ~+0.18 ppm at 400 ppm and the

406 observational record of atmospheric CO_2 concentrations have been revised accordingly. The

407 revisions have been applied retrospectively in all cases where the calibrations were

408 performed by NOAA/ESRL, thus affecting measurements made by members of the WMO-

409 GAW programme and other regionally coordinated programmes (e.g., Integrated Carbon

410 Observing System, ICOS). Changes to the CO_2 concentrations measured across these

411 networks propagate to the global mean CO_2 concentrations. Comparing the estimates of

412 G_{ATM} made by Dlugokencky and Tans (2020), used in the Global Carbon Budget 2020

413 (Friedlingstein et al., 2020), with updated estimates from Dlugokencky and Tans (2022),

414 used here, we find that G_{ATM} reduced on average by -0.06 GtC yr^{-1} during 2010-2019 and by -

415 0.01 GtC yr^{-1} during 1959-2019 due to the new calibration. These changes are well within

416 the uncertainty ranges reported below. Hence the change in analytical procedures made by

417 NOAA/ESRL has a negligible impact on the atmospheric growth rate G_{ATM}.

418 The uncertainty around the atmospheric growth rate is due to four main factors. First, the

419 long-term reproducibility of reference gas standards (around 0.03 ppm for 1σ from the

420 1980s; Dlugokencky and Tans, 2022). Second, small unexplained systematic analytical errors

421 that may have a duration of several months to two years come and go. They have been

422 simulated by randomising both the duration and the magnitude (determined from the

423 existing evidence) in a Monte Carlo procedure. Third, the network composition of the

424 marine boundary layer with some sites coming or going, gaps in the time series at each site,

425 etc (Dlugokencky and Tans, 2022). The latter uncertainty was estimated by NOAA/ESRL with

426   a Monte Carlo method by constructing 100 "alternative" networks (Masarie and Tans, 1995;

427   NOAA/ESRL, 2019). The second and third uncertainties, summed in quadrature, add up to

428   0.085 ppm on average (Dlugokencky and Tans, 2022). Fourth, the uncertainty associated

429   with using the average CO_2 concentration from a surface network to approximate the true

430   atmospheric average CO_2 concentration (mass-weighted, in 3 dimensions) as needed to

431   assess the total atmospheric CO_2 burden. In reality, CO_2 variations measured at the stations

432   will not exactly track changes in total atmospheric burden, with offsets in magnitude and

433   phasing due to vertical and horizontal mixing. This effect must be very small on decadal and

434   longer time scales, when the atmosphere can be considered well mixed. Preliminary

435   estimates suggest this effect would increase the annual uncertainty, but a full analysis is not

436   yet available. We therefore maintain an uncertainty around the annual growth rate based

437   on the multiple stations data set ranges between 0.11 and 0.72 GtC yr^{-1}, with a mean of 0.61

438   GtC yr^{-1} for 1959-1979 and 0.17 GtC yr^{-1} for 1980-2020, when a larger set of stations were

439   available as provided by Dlugokencky and Tans (2022) but recognise further exploration of

440   this uncertainty is required. At this time, we estimate the uncertainty of the decadal

441   averaged growth rate after 1980 at 0.02 GtC yr^{-1} based on the calibration and the annual

442   growth rate uncertainty but stretched over a 10-year interval. For years prior to 1980, we

443   estimate the decadal averaged uncertainty to be 0.07 GtC yr^{-1} based on a factor

444   proportional to the annual uncertainty prior and after 1980 (0.02 * [0.61/0.17] GtC yr^{-1}).

445   We assign a high confidence to the annual estimates of G_{ATM} because they are based on

446   direct measurements from multiple and consistent instruments and stations distributed

447   around the world (Ballantyne et al., 2012; Hall et al., 2021).

448   To estimate the total carbon accumulated in the atmosphere since 1750 or 1850, we use an

449   atmospheric CO_2 concentration of 277 ± 3 ppm or 286 ± 3 ppm, respectively, based on a

450   cubic spline fit to ice core data (Joos and Spahni, 2008). For the construction of the

451   cumulative budget shown in Figure 3, we use the fitted estimates of CO_2 concentration from

452   Joos and Spahni (2008) to estimate the annual atmospheric growth rate using the

453   conversion factors shown in Table 1. The uncertainty of ±3 ppm (converted to ±1σ) is taken

454   directly from the IPCC's AR5 assessment (Ciais et al., 2013). Typical uncertainties in the

455   growth rate in atmospheric CO_2 concentration from ice core data are equivalent to ±0.1-

456 0.15 GtC yr^{-1} as evaluated from the Law Dome data (Etheridge et al., 1996) for individual 20-
457 year intervals over the period from 1850 to 1960 (Bruno and Joos, 1997).

458 **2.3.2   2021 projection**

459 We provide an assessment of G_{ATM} for 2021 based on the monthly calculated global
460 atmospheric CO_2 concentration (GLO) through August (Dlugokencky and Tans, 2022), and
461 bias-adjusted Holt–Winters exponential smoothing with additive seasonality (Chatfield,
462 1978) to project to January 2022. Additional analysis suggests that the first half of the year
463 (the boreal winter-spring-summer transition) shows more interannual variability than the
464 second half of the year (the boreal summer-autumn-winter transition), so that the exact
465 projection method applied to the second half of the year has a relatively smaller impact on
466 the projection of the full year. Uncertainty is estimated from past variability using the
467 standard deviation of the last 5 years' monthly growth rates.

468 **2.4   Ocean CO_2 sink**

469 The reported estimate of the global ocean anthropogenic CO_2 sink S_{OCEAN} is derived as the
470 average of two estimates. The first estimate is derived as the mean over an ensemble of
471 eight global ocean biogeochemistry models (GOBMs, Table 4 and Table A2). The second
472 estimate is obtained as the mean over an ensemble of seven observation-based data-
473 products (Table 4 and Table A3). An eighth product (Watson et al., 2020) is shown, but is not
474 included in the ensemble average as it differs from the other products by adjusting the flux
475 to a cool, salty ocean surface skin (see Appendix C.3.1 for a discussion of the Watson
476 product). The GOBMs simulate both the natural and anthropogenic CO_2 cycles in the ocean.
477 They constrain the anthropogenic air-sea CO_2 flux (the dominant component of S_{OCEAN}) by
478 the transport of carbon into the ocean interior, which is also the controlling factor of
479 present-day ocean carbon uptake in the real world. They cover the full globe and all seasons
480 and were recently evaluated against surface ocean carbon observations, suggesting they are
481 suitable to estimate the annual ocean carbon sink (Hauck et al., 2020). The data-products
482 are tightly linked to observations of fCO_2 (fugacity of CO_2, which equals pCO_2 corrected for
483 the non-ideal behaviour of the gas; Pfeil et al., 2013), which carry imprints of temporal and
484 spatial variability, but are also sensitive to uncertainties in gas-exchange parameterizations
485 and data-sparsity. Their asset is the assessment of interannual and spatial variability (Hauck

486   et al., 2020). We further use two diagnostic ocean models to estimate S_{OCEAN} over the

487   industrial era (1781-1958).

488   The global fCO_2-based flux estimates were adjusted to remove the pre-industrial ocean

489   source of CO_2 to the atmosphere of 0.61 GtC yr^{-1} from river input to the ocean (the average

490   of 0.45 ± 0.18 GtC yr^{-1} by Jacobson et al. (2007) and 0.78 ± 0.41 GtC yr^{-1} by Resplandy et al.,

491   2018), to satisfy our definition of S_{OCEAN} (Hauck et al., 2020). The river flux adjustment was

492   distributed over the latitudinal bands using the regional distribution of Aumont et al. (2001;

493   North: 0.16 GtC yr^{-1}, Tropics: 0.15 GtC yr^{-1}, South: 0.30 GtC yr^{-1}), acknowledging that the

494   boundaries of Aumont et al (2001; namely 20°S and 20°N) are not consistent with the

495   boundaries otherwise used in the GCB (30°S and 30°N). A recent modelling study (Lacroix et

496   al., 2020) suggests that more of the riverine outgassing is located in the tropics than in the

497   Southern Ocean; and hence this regional distribution is associated with a major uncertainty.

498   Anthropogenic perturbations of river carbon and nutrient transport to the ocean are not

499   considered (see section 2.7).

500   We derive S_{OCEAN} from GOBMs by using a simulation (sim A) with historical forcing of climate

501   and atmospheric CO_2, accounting for model biases and drift from a control simulation (sim

502   B) with constant atmospheric CO_2 and normal year climate forcing. A third simulation (sim

503   C) with historical atmospheric CO_2 increase and normal year climate forcing is used to

504   attribute the ocean sink to CO_2 (sim C minus sim B) and climate (sim A minus sim C) effects.

505   Data-products are adjusted to represent the full ocean area by a simple scaling approach

506   when coverage is below 98%. GOBMs and data-products fall within the observational

507   constraints over the 1990s (2.2 ± 0.7 GtC yr^{-1}, Ciais et al., 2013) after applying adjustments .

508   We assign an uncertainty of ± 0.4 GtC yr^{-1} to the ocean sink based on a combination of

509   random (ensemble standard deviation) and systematic uncertainties (GOBMs bias in

510   anthropogenic carbon accumulation, previously reported uncertainties in fCO_2-based data-

511   products; see section C.3.3). We assess a medium confidence level to the annual ocean CO_2

512   sink and its uncertainty because it is based on multiple lines of evidence, it is consistent with

513   ocean interior carbon estimates (Gruber et al., 2019, see section 3.5.5) and the results are

514   consistent in that the interannual variability in the GOBMs and data-based estimates are all

515   generally small compared to the variability in the growth rate of atmospheric CO_2

516   concentration. We refrain from assigning a high confidence because of the systematic

517 deviation between the GOBM and data-product trends since around 2002. More details on

518 the S_{OCEAN} methodology can be found in Appendix C.3.

519 The ocean CO_2 sink forecast for the year 2021 is based on the annual historical and

520 estimated 2021 atmospheric CO_2 concentration (Dlugokencky and Tans 2021), historical and

521 estimated 2021 annual global fossil fuel emissions from this year's carbon budget, and the

522 spring (March, April, May) Oceanic Niño Index (ONI) index (NCEP, 2022). Using a non-linear

523 regression approach, i.e., a feed-forward neural network, atmospheric CO_2, the ONI index

524 and the fossil fuel emissions are used as training data to best match the annual ocean CO_2

525 sink (i.e. combined S_{OCEAN} estimate from GOBMs and data products) from 1959 through

526 2020 from this year's carbon budget. Using this relationship, the 2021 S_{OCEAN} can then be

527 estimated from the projected 2021 input data using the non-linear relationship established

528 during the network training. To avoid overfitting, the neural network was trained with a

529 variable number of hidden neurons (varying between 2-5) and 20% of the randomly

530 selected training data were withheld for independent internal testing. Based on the best

531 output performance (tested using the 20% withheld input data), the best performing

532 number of neurons was selected. In a second step, we trained the network 10 times using

533 the best number of neurons identified in step 1 and different sets of randomly selected

534 training data. The mean of the 10 trainings is considered our best forecast, whereas the

535 standard deviation of the 10 ensembles provides a first order estimate of the forecast

536 uncertainty. This uncertainty is then combined with the S_{OCEAN} uncertainty (0.4 GtC yr^{-1}) to

537 estimate the overall uncertainty of the 2021 prediction.

538 **2.5 Terrestrial CO_2 sink**

539 The terrestrial land sink (S_{LAND}) is thought to be due to the combined effects of fertilisation

540 by rising atmospheric CO_2 and N inputs on plant growth, as well as the effects of climate

541 change such as the lengthening of the growing season in northern temperate and boreal

542 areas. S_{LAND} does not include land sinks directly resulting from land-use and land-use change

543 (e.g., regrowth of vegetation) as these are part of the land-use flux (E_{LUC}), although system

544 boundaries make it difficult to attribute exactly CO_2 fluxes on land between S_{LAND} and E_{LUC}

545 (Erb et al., 2013).

546 S_{LAND} is estimated from the multi-model mean of 17 DGVMs (Table A1). As described in

547 Appendix C.4, DGVMs simulations include all climate variability and CO_2 effects over land,

548   with 12 DGVMs also including the effect of N inputs. The DGVMs estimate of S_{LAND} does not

549   include the export of carbon to aquatic systems or its historical perturbation, which is

550   discussed in Appendix D3. See Appendix C.4 for DGVMs evaluation and uncertainty

551   assessment for S_{LAND}, using the International Land Model Benchmarking system (ILAMB;

552   Collier et al., 2018). More details on the S_{LAND} methodology can be found in Appendix C.4.

553   Like the ocean forecast, the land CO_2 sink (S_{LAND}) forecast is based on the annual historical

554   and estimated 2021 atmospheric CO_2 concentration (Dlugokencky and Tans 2021), historical

555   and estimated 2021 annual global fossil fuel emissions from this year's carbon budget, and

556   the summer (June, July, August) ONI index (NCEP, 2021). All training data are again used to

557   best match S_{LAND} from 1959 through 2020 from this year's carbon budget using a feed-

558   forward neural network. To avoid overfitting, the neural network was trained with a variable

559   number of hidden neurons (varying between 2-15), larger than for S_{OCEAN} prediction due to

560   the stronger land carbon interannual variability. As done for S_{OCEAN}, a pre-training selects the

561   optimal number of hidden neurons based on 20% withheld input data, and in a second step,

562   an ensemble of 10 forecasts is produced to provide the mean forecast plus uncertainty. This

563   uncertainty is then combined with the S_{LAND} uncertainty for 2020 (1.0 GtC yr^{-1}) to estimate

564   the overall uncertainty of the 2021 prediction.

565   **2.6   The atmospheric perspective**

566   The world-wide network of in-situ atmospheric measurements and satellite derived

567   atmospheric CO_2 column (xCO_2) observations put a strong constraint on changes in the

568   atmospheric abundance of CO_2. This is true globally (hence our large confidence in G_{ATM}),

569   but also regionally in regions with sufficient observational density found mostly in the extra-

570   tropics. This allows atmospheric inversion methods to constrain the magnitude and location

571   of the combined total surface CO_2 fluxes from all sources, including fossil and land-use

572   change emissions and land and ocean CO_2 fluxes. The inversions assume E_{FOS} to be well

573   known, and they solve for the spatial and temporal distribution of land and ocean fluxes

574   from the residual gradients of CO_2 between stations that are not explained by fossil fuel

575   emissions. By design, such systems thus close the carbon balance ($B_{IM} = 0$) and thus provide

576   an additional perspective on the independent estimates of the ocean and land fluxes.

577   This year's release includes six inversion systems that are described in Table A4. Each system

578   is rooted in Bayesian inversion principles but uses slightly different methodologies. These

579 differences concern the selection of atmospheric CO_2 data and the choice of a-priori fluxes

580 to refine with these datas. They also differ in spatial and temporal resolution, assumed

581 correlation structures, and mathematical approach of the models (see references in Table

582 A4 for details). Importantly, the systems use a variety of transport models, which was

583 demonstrated to be a driving factor behind differences in atmospheric inversion-based flux

584 estimates, and specifically their distribution across latitudinal bands (Gaubert et al., 2019;

585 Schuh et al., 2019). Multiple inversion systems (UoE, CTE, and CAMS) were previously tested

586 with satellite xCO_2 retrievals from GOSAT or OCO-2 measurements, but their results at the

587 larger scales (as discussed in this work) did not deviate substantially from their in-situ

588 counterparts and are therefore not separately included. One inversion this year (CMS-Flux)

589 used ACOS-GOSAT v9 retrievals between July 2009 and Dec 2014 and OCO-2 b10 retrievals

590 between Jan 2015 to Dec 2015, in addition to the in-situ observational CO_2 mole fraction

591 records.

592 The original products delivered by the inverse modellers were modified to facilitate the

593 comparison to the other elements of the budget, specifically on 3 accounts: (1) global total

594 fossil fuel emissions, (2) riverine CO_2 transport, and (3) cement carbonation CO_2 uptake.

595 Details are given below. We note that with these adjustments the inverse results no longer

596 represent the net atmosphere-surface exchange over land/ocean areas as sensed by

597 atmospheric observations. Instead for land, they become the net uptake of CO_2 by

598 vegetation and soils that is not exported by fluvial systems, similar to the DGVMs estimates.

599 For oceans, they become the net uptake of anthropogenic CO_2, similar to the GOBMs

600 estimates.

601 The inversion systems prescribe global fossil fuel emissions based on the GCP's Gridded

602 Fossil Emissions Dataset version 2021.2 (GCP-GridFEDv2021.2; Jones et al., 2021b), which is

603 an update to 2019 of the first version of GCP-GridFED presented by Jones et al. (2021a).

604 GCP-GridFEDv2021.2 scales gridded estimates of CO_2 emissions from EDGARv4.3.2

605 (Janssens-Maenhout et al., 2019) within national territories to match national emissions

606 estimates provided by the GCB for the years 1959-2020, which were compiled following the

607 methodology described in Section 2.1 with all datasets available on August 14th 2021 (R.

608 Andrew, *pers. comm.*). Small differences between the systems due to for instance regridding

609 to the transport model resolution are corrected for in the latitudinal partitioning we

610 present, to ensure agreement with the estimate of E_{FOS} in this budget. We also note that the

611 ocean fluxes used as prior by 5 out of 6 inversions are part of the suite of the ocean process

612 model or fCO2 data products listed in Section 2.4. Although these fluxes are further adjusted

613 by the atmospheric inversions, it makes the inversion estimates of the ocean fluxes not

614 completely independent of S_{OCEAN} assessed here.

615 To facilitate comparisons to the independent S_{OCEAN} and S_{LAND}, we used the same corrections

616 for transport and outgassing of carbon transported from land to ocean, as done for the

617 observation-based estimates of S_{OCEAN} (see Appendix C.3). Furthermore, the inversions did

618 not include a cement carbonation sink (see section 2.1) and therefore this GCB component

619 is implicitly part of their total land sink estimate. In the numbers presented in this budget,

620 each year's global carbonation sink from cement was subtracted from each year's estimated

621 land sink in each inversion, distributed proportional to fossil fuel emissions per region

622 (North-Tropics-South).

623 The atmospheric inversions are evaluated using vertical profiles of atmospheric CO_2

624 concentrations (Fig. B4). More than 30 aircraft programs over the globe, either regular

625 programs or repeated surveys over at least 9 months, have been used to assess model

626 performance (with space-time observational coverage sparse in the SH and tropics, and

627 denser in NH mid-latitudes; Table A6). The six models are compared to the independent

628 aircraft CO_2 measurements between 2 and 7 km above sea level between 2001 and 2020.

629 Results are shown in Fig. B4 and discussed in Section 3.7.

630 With a relatively small ensemble (N=6) of systems that moreover share some a-priori fluxes

631 used with one another, or with the process-based models, it is difficult to justify using their

632 mean and standard deviation as a metric for uncertainty across the ensemble. We therefore

633 report their full range (min-max) without their mean. More details on the atmospheric

634 inversions methodology can be found in Appendix C.5.

635 **2.7 Processes not included in the global carbon budget**

636 The contribution of anthropogenic CO and CH_4 to the global carbon budget is not fully

637 accounted for in Eq. (1) and is described in Appendix D1. The contributions of other

638 carbonates to CO_2 emissions is described in Appendix D2. The contribution of anthropogenic

639 changes in river fluxes is conceptually included in Eq. (1) in S_{OCEAN} and in S_{LAND}, but it is not

640   represented in the process models used to quantify these fluxes. This effect is discussed in

641   Appendix D3. Similarly, the loss of additional sink capacity from reduced forest cover is

642   missing in the combination of approaches used here to estimate both land fluxes (E_{LUC} and

643   S_{LAND}) and its potential effect is discussed and quantified in Appendix D4.

644

645   3   Results

646   For each component of the global carbon budget, we present results for three different time

647   periods: the full historical period, from 1850 to 2020, the six decades in which we have

648   atmospheric concentration records from Mauna Loa (1960-2020), a specific focus on last

649   year (2020), and the projection for the current year (2021). Subsequently, we assess the

650   combined constraints from the budget components (often referred to as a bottom-up

651   budget) against the top-down constraints from inverse modelling of atmospheric

652   observations. We do this for the global balance of the last decade, as well as for a regional

653   breakdown of land and ocean sinks by broad latitude bands.

654   3.1   Fossil CO_2 Emissions

655   3.1.1   Historical period 1850-2020

656   Cumulative fossil CO_2 emissions for 1850-2020 were 455 ± 25 GtC, including the cement

657   carbonation sink (Fig. 3, Table 8) .

658   In this period, 46% of fossil CO_2 emissions came from coal, 35% from oil, 14% from natural

659   gas, 3% from decomposition of carbonates, and 1% from flaring.

660   In 1850, the UK stood for 62% of global fossil CO_2 emissions. In 1891 the combined

661   cumulative emissions of the current members of the European Union reached and

662   subsequently surpassed the level of the UK. Since 1917 US cumulative emissions have been

663   the largest. Over the entire period 1850-2020, US cumulative emissions amounted to

664   110GtC (25% of world total) , the EU's to 80 GtC (18%), and China's to 60 GtC (14%).

665   There are three additional global datasets that include all sources of fossil CO_2 emissions:

666   CDIAC-FF (Gilfillan and Marland, 2021), CEDS version v_2021_04_21 (Hoesly et al., 2018);

667   O'Rourke et al., 2021) and PRIMAP-hist version 2.3.1 (Gütschow et al., 2016, 2021), although

668   these datasets are not independent. CDIAC-FF has the lowest cumulative emissions over

669   1750-2018 at 437 GtC, GCP has 443 GtC, CEDS 445 GtC, PRIMAP-hist TP 453 GtC, and

670   PRIMAP-hist CR 455 GtC. CDIAC-FF excludes emissions from lime production, while neither

671   CDIAC-FF nor GCP explicitly include emissions from international bunker fuels prior to 1950.

672   CEDS has higher emissions from international shipping in recent years, while PRIMAP-hist

673   has higher fugitive emissions than the other datasets. However, in general these four

674   datasets are in relative agreement as to total historical global emissions of fossil CO_2.

675   **3.1.2   Recent period 1960-2020**

676   Global fossil CO_2 emissions, E_{FOS} (including the cement carbonation sink), have increased

677   every decade from an average of 3.0 ± 0.2 GtC yr^{-1} for the decade of the 1960s to an average

678   of 9.5 ± 0.5 GtC yr^{-1} during 2011-2020 (Table 6, Fig. 2 and Fig. 5). The growth rate in these

679   emissions decreased between the 1960s and the 1990s, from 4.3% yr^{-1} in the 1960s (1960-

680   1969), 3.2% yr^{-1} in the 1970s (1970-1979), 1.6% yr^{-1} in the 1980s (1980-1989), to 0.9% yr^{-1} in

681   the 1990s (1990-1999). After this period, the growth rate began increasing again in the

682   2000s at an average growth rate of 3.0% yr^{-1}, decreasing to 0.6% yr^{-1} for the last decade

683   (2011-2020). China's emissions increased by +1.0% yr^{-1} on average over the last 10 years

684   dominating the global trend, followed by India's emissions increase by +3.9% yr^{-1}, while

685   emissions decreased in EU27 by −1.9% yr^{-1}, and in the USA by −1.1% yr^{-1}. Fig.6 illustrates the

686   spatial distribution of fossil fuel emissions for the 2011-2020 period.

687   E_{FOS} includes the uptake of CO_2 by cement via carbonation which has increased with

688   increasing stocks of cement products, from an average of 20 MtC yr^{-1} (0.02 GtC yr^{-1}) in the

689   1960s to an average of 200 MtC yr^{-1} (0.2 GtC yr^{-1}) during 2011-2020 (Fig. 5).

690   **3.1.3   Final year 2020**

691   Global fossil CO_2 emissions were 5.4% lower in 2020 than in 2019, because of the COVID-19

692   pandemic, with a decline of 0.5 GtC to reach 9.5 ± 0.5 GtC (9.3 ± 0.5 GtC when including the

693   cement carbonation sink) in 2020 (Fig. 5), distributed among coal (40%), oil (32%), natural

694   gas (21%), cement (5%) and others (2%). Compared to the previous year, 2020 emissions

695   from coal, oil and gas declined by 4.4%, 9.7% and 2.3% respectively, while emissions from

696   cement increased by 0.8%. All growth rates presented are adjusted for the leap year, unless

697   stated otherwise.

698   In 2020, the largest absolute contributions to global fossil CO_2 emissions were from China

699   (31%), the USA (14%), the EU27 (7%), and India (7%). These four regions account for 59% of

700   global CO_2 emissions, while the rest of the world contributed 41%, including international

701   aviation and marine bunker fuels (2.9% of the total). Growth rates for these countries from

702   2019 to 2020 were +1.4% (China), -10.6% (USA), −10.9% (EU27), and -7.3% (India), with -

703   7.0% for the rest of the world. The per-capita fossil CO_2 emissions in 2020 were 1.2 tC

704   person^{-1} yr^{-1} for the globe, and were 3.9 (USA), 2.0 (China), 1.6 (EU27) and 0.5 (India) tC

705   person^{-1} yr^{-1} for the four highest emitting countries (Fig. 5).

706   The COVID-19 induced decline in emissions of -5.4% in 2020 is close to the projected decline

707   of -6.7%, which was the median of four approaches, published in Friedlingstein et al. (2020).

708   Of the four approaches, the 'GCP' method was closest at -5.8%. That method was based on

709   national emissions projections for China, the USA, the EU27, and India using reported

710   monthly activity data when available and projections of gross domestic product corrected

711   for trends in fossil fuel intensity (I_{FOS}) for the rest of the world. Of the regions, the projection

712   for the EU27 was least accurate, and the reasons for this are discussed by Andrew (2021).

713   **3.1.4   Year 2021 Projection**

714   Globally, we estimate that global fossil CO_2 emissions will rebound 4.8% in 2021 (4.2% to

715   5.4%) to 9.9 GtC (36.4 GtCO$_2$), returning near their 2019 emission levels of 10.0 GtC (36.7

716   GtCO$_2$). Global increase in 2021 emissions per fuel types are +6.3% (range 5.5% to 7.0%) for

717   coal, +4.0% (range 2.6% to 5.4%) for oil, +3.8% (range 2.8% to 4.8%) for natural gas, and

718   +3.2% (range 1.7% to 4.6%) for cement.

719   For China, projected fossil emissions in 2021 are expected to increase by 4.3% (range 3.0%

720   to 5.4%) compared with 2020 emissions, bringing 2021 emissions for China around 3.0 GtC

721   yr^{-1} (11.1 GtCO$_2$ yr^{-1}). Chinese emissions appear to have risen in both 2020 and 2021 despite

722   the economic disruptions of COVID-19. Increases in fuel specific projections for China are

723   +4.1% for coal, +4.4% for oil, +12.8% natural gas, and a decrease of 0.1% for cement.

724   For the USA, the Energy Information Administration (EIA) emissions projection for 2021

725   combined with cement clinker data from USGS gives an increase of 6.8% (range 6.6% to

726   7.0%) compared to 2020, bringing USA 2021 emissions around 1.4 GtC yr^{-1} (5.0 GtCO$_2$ yr^{-1}).

727   This is based on separate projections for coal +17.1%, oil +9.0%, natural gas -0.8%, and

728   cement +0.3%.

729 For the European Union, our projection for 2021 is for an increase of 6.3% (range 4.3% to

730 8.3%) over 2020, with 2021 emissions around 0.8 GtC yr^{-1} (2.8 GtCO$_2$ yr^{-1}). This is based on

731 separate projections for coal of +14.6%, oil +3.7%, natural gas +4.6%, and cement 0.3%.

732 For India, our projection for 2021 is an increase of 11.2% (range of 10.7% to 11.7%) over

733 2020, with 2021 emissions around 0.7 GtC yr^{-1} (2.7 GtCO$_2$ yr^{-1}). This is based on separate

734 projections for coal of +13.9%, oil +3.4%, natural gas +4.8%, and cement +21.6%.

735 For the rest of the world, the expected growth rate for 2021 is 3.2% (range 2.0% to 4.3%).

736 This is computed using the GDP projection for the world (excluding China, the USA, the EU,

737 and India) of 4.4% made by the IMF (2022) and a decrease in I$_{FOS}$ of -1.7%yr^{-1}, which is the

738 average over 2011-2020. The uncertainty range is based on the standard deviation of the

739 interannual variability in I$_{FOS}$ during 2011–2020 of 0.6%yr^{-1} and our estimates of uncertainty

740 in the IMF's GDP forecast of 0.6%. The methodology allows independent projections for

741 coal, oil, natural gas, cement, and other components, which add to the total emissions in

742 the rest of the world. The fuel specific projected 2021 growth rates for the rest of the world

743 are: +3.2% (range 0.7% to 5.8%) for coal, +2.3% (-0.3% to +4.9%) for oil, +4.1% (2.6% to

744 5.7%) for natural gas, +4.8% (+2.7% to +6.9%) for cement.

745 Independently, the IEA has published two forecasts of global fossil energy CO$_2$ emissions

746 (i.e., a subset of fossil CO$_2$ emissions), first in April (4.8%; IEA, 2021a) and so revised in

747 October at 4% (IEA, 2021b). In March 2022 they also published a new, preliminary estimate

748 of 6% growth (IEA, 2021a). Carbon Monitor produces estimates of global emissions with low

749 temporal lag, and their estimates suggest that emissions were 5.1% higher than in 2020

750 (Carbon Monitor, 2022).

751 **3.2   Emissions from Land Use Changes**

752 **3.2.1   Historical period 1850-2020**

753 Cumulative CO$_2$ emissions from land-use changes (E$_{LUC}$) for 1850-2020 were 200 ± 65 GtC

754 (Table 8; Fig. 3; Fig. 13). The cumulative emissions from E$_{LUC}$ are particularly uncertain, with

755 large spread among individual estimates of 140 GtC (updated H&N2017), 270 GtC (BLUE),

756 and 195 GtC (OSCAR) for the three bookkeeping models and a similar wide estimate of 190 ±

757 60 GtC for the DGVMs (all cumulative numbers are rounded to the nearest 5GtC). These

758 estimates are broadly consistent with indirect constraints from vegetation biomass

759   observations, giving a cumulative source of 155 ± 50 GtC over the 1901-2012 period (Li et

760   al., 2017). However, given the large spread, a best estimate is difficult to ascertain.

3.2.2   Recent period 1960-2020

762   In contrast to growing fossil emissions, CO_2 emissions from land-use, land-use change and

763   forestry have remained relatively constant, at around 1.3 ± 0.7 GtC yr^{-1} over the 1970-1999

764   period, and even show a slight decrease over the last 20 years, reaching 1.1 ± 0.7 GtC yr^{-1} for

765   the 2011-2020 period (Table 6), but with large spread across estimates (Table 5, Fig. 7).

766   Emissions are relatively constant in the DGVMs ensemble of models since the 1970s, with

767   similar mean values until the 1990s as the bookkeeping mean and large model spread (Table

768   5, Fig. 7). The DGVMs average grows larger than the bookkeeping average in the recent

769   decades and shows no sign of decreasing emissions, which is, however, expected as DGVM-

770   based estimates include the loss of additional sink capacity, which grows with time, while

771   the bookkeeping estimates do not (Appendix D4).

772   E_{LUC} is a net term of various gross fluxes, which comprise emissions and removals. Gross

773   emissions are on average 2-4 times larger than the net E_{LUC} emissions, and remained largely

774   constant over the last 60 years, with a moderate increase from an average of 3.4 ± 0.9 GtC

775   yr^{-1} for the decade of the 1960s to an average of 3.8 ± 0.6 GtC yr^{-1} during 2011-2020 (Fig.7,

776   Table 5), showing the relevance of land management such as harvesting or rotational

777   agriculture. Increases in gross removals, from 1.9 ± 0.4 GtC yr^{-1} for the 1960s to 2.7 ± 0.4 GtC

778   yr^{-1} for 2011-2020, were larger than the increase in gross emissions. Since the processes

779   behind gross removals, foremost forest regrowth and soil recovery, are all slow, while gross

780   emissions include a large instantaneous component, short-term changes in land-use

781   dynamics, such as a temporary decrease in deforestation, influences gross emissions

782   dynamics more than gross removals dynamics. It is these relative changes to each other that

783   explain the decrease in net E_{LUC} emissions over the last two decades and the last few years.

784   Gross fluxes differ more across the three bookkeeping estimates than net fluxes, which is

785   expected due to different process representation; in particular, treatment of shifting

786   cultivation, which increases both gross emissions and removals, differs across models.

787   There is a decrease in net CO_2 emissions from land-use change over the last decade (Fig. 7,

788   Table 6), in contrast to earlier estimates of no clear trend across E_{LUC} estimates

789 (Friedlingstein et al., 2020, Hong et al., 2021). The trend in the last decade is now about -4%

790 per year, compared to the +1.8% per year reported by Friedlingstein et al. (2020). This

791 decrease is principally attributable to changes in E_{LUC} estimates from BLUE and OSCAR,

792 which relate to changes in the underlying land-use forcing, LUH2 (Chini et al. 2021, Hurtt et

793 al. 2020) based on HYDE3.3 (Klein Goldewijk et al., 2017a, b): HYDE3.3 now incorporates

794 updated estimates of agricultural areas by the FAO and uses multi-annual land cover maps

795 from satellite remote sensing (ESA CCI Land Cover) to constrain contemporary land cover

796 patterns (see Appendix C.2.2 for details) . These changes lead to lower global E_{LUC} estimates

797 in the last two decades compared to earlier versions of the global carbon budget due most

798 notably to lower emissions from cropland expansion, particularly in the tropical regions.

799 Rosan et al. (2021) showed that for Brazil, the new HYDE3.3 version is closer to

800 independent, regional estimates of land-use and land cover change (MapBiomas, 2021) with

801 respect to spatial patterns, but it shows less land-use and land cover changes than these

802 independent estimates, while HYDE3.2-based estimates had shown higher changes and

803 lower emissions. The update in land-use forcing leads to a decrease in estimated emissions

804 in Brazil across several models after the documented deforestation peak of 2003-2004 that

805 preceded policies and monitoring systems decreasing deforestation rates (Rosan et al.,

806 2021). However, estimated emissions based on the new land-use forcing do not reflect the

807 rise in Brazilian deforestation in the recent few years (Silva Junior, 2021), and associated

808 increasing emissions from deforestation would have been missed here. The update in FAO

809 agricultural areas in Brazil also implied that substantial interannual variability reported to

810 earlier FAO assessment and captured by the HYDE3.2 version since 2000 was removed. Due

811 to the asymmetry of (fast) decay (like clearing by fire) and (slower) regrowth, such reduced

812 variability is expected to decrease annual emissions. Also, the approach by Houghton and

813 Nassikas (2017) smooths land use area changes before calculating carbon fluxes by a 5-year

814 running mean, hence the three emission estimates are in better agreement than in previous

815 GCB estimates. However, differences still exist, which highlight the need for accurate

816 knowledge of land-use transitions and their spatial and temporal variability. A further caveat

817 is that global land-use change data for model input does not capture forest degradation,

818 which often occurs on small scale or without forest cover changes easily detectable from

819 remote sensing and poses a growing threat to forest area and carbon stocks that may

820 surpass deforestation effects (e.g., Matricardi et al., 2020, Qin et al., 2021).

821   Overall, therefore, we assign low confidence to the change towards a decreasing trend of

822   land-use emissions over the last two decades as seen compared to the estimate of the

823   global carbon budget 2020 (Friedlingstein et al., 2020). Our approach aims at using the most

824   up to date data and methods, such as accounting for revisions of living databases of

825   country-level agricultural statistics from FAO or including satellite remote-sensing

826   information for spatial allocation. While we start from a well-documented methodology to

827   provide gridded land-use data (Chini et al., 2021), not all changes in individual components

828   are always documented, complicating the explanation of changes from one GCB to the next.

829   The rising number of pan-tropical or global estimates of carbon stock changes based on

830   satellite remote sensing of carbon densities and forest cover changes (Fan et al. 2019; Qin

831   et al., 2021; Xu et al., 2021; Feng et al., 2022) may seem a promising path for independent

832   evaluation of the land-use emissions term. However, comparison of satellite-derived fluxes

833   to global model estimates is hampered for several reasons discussed by Pongratz et al.

834   (2021). Most importantly, satellite-based estimates usually do not distinguish between

835   anthropogenic drivers and natural forest cover losses (e.g., from drought or natural

836   wildfires), which have also increased over time in some regions, including the tropics;

837   ancillary information would be needed to attribute the observed signal of vegetation or

838   carbon stock change to different drivers. Further, satellite-based estimates often only

839   provide sub-component fluxes of E_{LUC}, excluding soil or product pool changes. Since forest

840   cover loss is better detectable from space than regrowth, satellite-based products often

841   limit their estimates to emissions from forest loss, neglecting carbon uptake from regrowth

842   of forests, as may occur following wood harvesting, abandonment, or natural disturbances;

843   such products thus provide a subset of the gross emissions term (Fig. 7b) and cannot be

844   compared to net emissions. Lastly, satellite-based fluxes typically quantify committed

845   instead of actual emissions, i.e., legacy CO_2 fluxes from potentially slow processes such as

846   slash, soil carbon or product decay, or forest regrowth are not captured at the time they

847   actually occur, but are attributed to the time of the land-use change event (Pongratz et al.,

848   2021). Using data on drivers of forest cover loss to isolate fluxes from agricultural

849   expansion, and looking into gross emissions instead of the net land-use change flux, Feng et

850   al. (2022) suggest a stronger increase in global gross emissions (though generally a smaller

851   flux) than the bookkeeping models do (see gross fluxes in Fig. 7b). This is in line with Rosan

852   et al. (2021) suggesting that the trend of net emissions in Brazil may be underestimated by

853   the updated land-use data (though patterns have improved). Further studies are needed to

854   robustly estimate the trend of global net land-use emissions. Progress is also needed on

855   accurate quantifications of land use dynamics, including less well observable management

856   types such as shifting cultivation and wood harvesting, and their distinction from natural

857   disturbances (Pongratz et al, 2021).

858   Highest land-use emissions occur in the tropical regions of all three continents, including the

859   Arc of Deforestation in the Amazon basin (Fig. 6b). This is related to massive expansion of

860   cropland, particularly in the last few decades in Latin America, Southeast Asia, and sub-

861   Saharan Africa Emissions (Hong et al., 2021), to a substantial part for export (Pendrill et al.,

862   2019). Emission intensity is high in many tropical countries, particularly of Southeast Asia,

863   due to high rates of land conversion in regions of carbon-dense and often still pristine,

864   undegraded natural forests (Hong et al., 2021). Emissions are further increased by peat fires

865   in equatorial Asia (GFED4s, van der Werf et al., 2017). Uptake due to land-use change

866   occurs, particularly in Europe, partly related to expanding forest area as a consequence of

867   the forest transition in the 19th and 20th century and subsequent regrowth of forest (Fig. 6b)

868   (Mather 2001; McGrath et al., 2015).

869   While the mentioned patterns are supported by independent literature and robust, we

870   acknowledge that model spread is substantially larger on regional than global level, as has

871   been shown for bookkeeping models (Bastos et al., 2021) as well as DGVMs (Obermeier et

872   al., 2021). A detailed analysis of country-level or regional uncertainties globally is beyond

873   the scope of this study. Assessments for individual regions will be performed as part of

874   REgional Carbon Cycle Assessment and Processes (RECCAP2; Ciais et al., 2020) or already

875   exist for selected regions (e.g., for Europe Petrescu et al., 2020, for Brazil Rosan et al., 2021).

876   National GHG inventory data (NGHGI) under the LULUCF sector or data submitted by

877   countries to FAOSTAT differ from the global models' definition of E_{LUC} we adopt here in that

878   in the NGHGI reporting, the natural fluxes (S_{LAND}) are counted towards E_{LUC} when they occur

879   on managed land (Grassi et al., 2018). In order to compare our results to the NGHGI

880   approach, we perform a re-mapping of our E_{LUC} estimate by including the S_{LAND} over

881   managed forest from the DGVMs simulations (following Grassi et al., 2021) to the

882   bookkeeping E_{LUC} estimate (see Appendix C.2.3). For the 2011-2020 period, we estimate

883   that 1.5 GtC yr^{-1} of S_{LAND} occurred on managed forests and is then reallocated to E_{LUC} here, as

884   done in the NGHGI method. Doing so, our mean estimate of E_{LUC} is reduced from a source of

885   1.1 GtC to a sink of -0.4 GtC, very similar to the NGHGI estimate of -0.6 GtC (Table A.8).

886   Though estimates between GHGI, FAOSTAT, individual process-based models and the

887   mapped budget estimates still differ in value and need further analysis, the approach taken

888   here provides a possibility to relate the global models' and NGHGI approach to each other

889   routinely and thus link the anthropogenic carbon budget estimates of land CO_2 fluxes

890   directly to the Global Stocktake, as part of UNFCCC Paris Agreement.

891   **3.2.3   Final year 2020**

892   The global CO_2 emissions from land-use change are estimated as 0.9 ± 0.7 GtC in 2020, 0.2

893   GtC lower than 2019, which had featured particularly large peat and tropical

894   deforestation/degradation fires. The surge in deforestation fires in the Amazon, causing

895   about 30% higher emissions from deforestation and degradation fires in 2019 over the

896   previous decade, continued into 2020 (GFED4.1s, van der Werf et al., 2017). However, the

897   unusually dry conditions for a non-El Niño year that occurred in Indonesia in 2019 and led to

898   fire emissions from peat burning, deforestation and degradation in equatorial Asia to be

899   about twice as large as the average over the previous decade (GFED4.1s, van der Werf et al.,

900   2017) ceased in 2020. However, confidence in the annual change remains low. While the

901   mentioned fires are clearly attributable to land-use activity, foremost deforestation and

902   peat burning, and may have been reinforced by dry weather conditions, as was the case in

903   Indonesia in 2019, wildfires also occur naturally. In particular, the extreme fire events in

904   recent years in Australia, Siberia or California were unrelated to land-use change and are

905   thus not attributed to E_{LUC}, but to the natural land sink and are discussed in Section 3.6.2.

906   Land-use change and related emissions may have been affected by the COVID-19 pandemic

907   (e.g. Poulter et al., 2021). Although emissions from tropical deforestation and degradation

908   fires have been decreasing from 2019 to 2020 on the global scale, they increased in Latin

909   America (GFED4s; van der Werf et al., 2017). During the period of the pandemic,

910   environmental protection policies and their implementation may have been weakened in

911   Brazil (Vale et al., 2021). In other countries, too, monitoring capacities and legal

912   enforcement of measures to reduce tropical deforestation have been reduced due to

913   budget restrictions of environmental agencies or impairments to ground-based monitoring

914   that prevents land grabs and tenure conflicts (Brancalion et al., 2020, Amador-Jiménez et

915   al., 2020). Effects of the pandemic on trends in fire activity or forest cover changes are hard

916   to separate from those of general political developments and environmental changes and

917   the long-term consequences of disruptions in agricultural and forestry economic activities

918   (e.g., Gruère and Brooks, 2020; Golar et al., 2020; Beckman and Countryman, 2021) remain

919   to be seen.

920   **3.2.4   Year 2021 Projection**

921   With wet conditions in Indonesia and a below-average fire season in South America our

922   preliminary estimate of E_{LUC} for 2021 is substantially lower than the 2011-2020 average. By

923   the end of September 2021 emissions from tropical deforestation and degradation fires

924   were estimated to be 222 TgC, down from 347 TgC in 2019 and 288 in 2020 (315 TgC 1997-

925   2020 average). Peat fire emissions in Equatorial Asia were estimated to be 1 TgC, down from

926   117 TgC in 2019 and 2 TgC in 2020 (74 TgC 1997-2020 average) (GFED4.1s, van der Werf et

927   al., 2017). Based on the fire emissions until the end of September, we expect E_{LUC} emissions

928   of around 0.8 GtC in 2021. Note that although our extrapolation is based on tropical

929   deforestation and degradation fires, degradation attributable to selective logging, edge-

930   effects or fragmentation will not be captured.

931   **3.3   Total anthropogenic emissions**

932   Cumulative anthropogenic CO_2 emissions for 1850-2020 totalled 660 ± 65 GtC (2420 ± 240

933    $GtCO_2$), of which almost 70% (455 GtC) occurred since 1960 and more than 30% (205 GtC)

934   since 2000 (Table 6 and 8). Total anthropogenic emissions more than doubled over the last

935   60 years, from 4.6 ± 0.7 GtC yr^{-1} for the decade of the 1960s to an average of 10.6 ± 0.8 GtC

936   yr^{-1} during 2011-2020.

937   The total anthropogenic CO_2 emissions from fossil plus land-use change amounted to 10.6 ±

938   0.8 GtC (38.9 ± 2.9 $GtCO_2$) for the 2011-2020 decade, reaching 10.2 ± 0.8 GtC (37.2 ± 2.9

939    $GtCO_2$) in 2020, while for 2021, we project global total anthropogenic CO_2 emissions from

940   fossil and land use changes to be around 10.7 GtC (39.3 $GtCO_2$).

941   During the historical period 1850-2020, 30% of historical emissions were from land use

942   change and 70% from fossil emissions. However, fossil emissions have grown significantly

943   since 1960 while land use changes have not, and consequently the contributions of land use

944 change to total anthropogenic emissions were smaller during recent periods (17% during

945 the period 1960-2020 and 10% during 2011-2020).

3.4 Atmospheric CO$_2$

3.4.1 Historical period 1850-2020

948 Atmospheric CO$_2$ concentration was approximately 277 parts per million (ppm) in 1750

949 (Joos and Spahni, 2008), reaching 300ppm in the 1910s, 350ppm in the late 1980s, and

950 reaching 412.44 ± 0.1 ppm in 2020 (Dlugokencky and Tans, 2022); Fig. 1). The mass of

951 carbon in the atmosphere increased by 48% from 590 GtC in 1750 to 876 GtC in 2020.

952 Current CO$_2$ concentrations in the atmosphere are unprecedented in the last 2 million years

953 and the current rate of atmospheric CO$_2$ increase is at least 10 times faster than at any other

954 time during the last 800,000 years (Canadell et al., 2021).

3.4.2 Recent period 1960-2020

956 The growth rate in atmospheric CO$_2$ level increased from 1.7 ± 0.07 GtC yr^{-1} in the 1960s to

957 5.1 ± 0.02 GtC yr^{-1} during 2011-2020 with important decadal variations (Table 6, Fig. 3 and

958 Fig 4).

959 During the last decade (2011-2020), the growth rate in atmospheric CO$_2$ concentration

960 continued to increase, albeit with large interannual variability (Fig. 4).

961 The airborne fraction (AF), defined as the ratio of atmospheric CO$_2$ growth rate to total

962 anthropogenic emissions:

963 $$AF = G_{ATM} / (E_{FOS} + E_{LUC}) \qquad\qquad (2)$$

964 provides a diagnostic of the relative strength of the land and ocean carbon sinks in removing

965 part of the anthropogenic CO$_2$ perturbation. The evolution of AF over the last 60 years

966 shows no significant trend, remaining nearly at around 45%, albeit showing a large

967 interannual variability driven by the year-to-year variability in G_{ATM} (Fig. 8). The observed

968 stability of the airborne fraction over the 1960-2020 period indicates that the ocean and

969 land CO$_2$ sinks have been removing on average about 55% of the anthropogenic emissions

970 (see sections 3.5 and 3.6).

3.4.3 Final year 2020

The growth rate in atmospheric CO_2 concentration was 5.0 ± 0.2 GtC (2.37 ± 0.08 ppm) in 2020 (Fig. 4; Dlugokencky and Tans, 2022), very close to the 2011-2020 average. The 2020 decrease in E_{FOS} and E_{LUC} of about 0.7 GtC propagated to an atmospheric CO_2 growth rate reduction of 0.38 GtC (0.18 ppm), given the significant interannual variability of the land carbon sink.

3.4.4 Year 2021 Projection

The 2021 growth in atmospheric CO_2 concentration (G_{ATM}) is projected to be about 5.3 GtC (2.49 ppm) based on GLO observations until the end of December 2021, bringing the atmospheric CO_2 concentration to an expected level of 414.67 ppm averaged over the year, 50% over the pre-industrial level.

3.5 Ocean Sink

3.5.1 Historical period 1850-2020

Cumulated since 1850, the ocean sink adds up to 170 ± 35 GtC, with two thirds of this amount being taken up by the global ocean since 1960. Over the historical period, the ocean sink increased in pace with the anthropogenic emissions exponential increase (Fig. 3b). Since 1850, the ocean has removed 26% of total anthropogenic emissions.

3.5.2 Recent period 1960-2020

The ocean CO_2 sink increased from 1.1 ± 0.4 GtC yr^{-1} in the 1960s to 2.8 ± 0.4 GtC yr^{-1} during 2011-2020 (Table 6), with interannual variations of the order of a few tenths of GtC yr^{-1} (Fig. 9). The ocean-borne fraction ($S_{OCEAN}/(E_{FOS}+E_{LUC})$) has been remarkably constant around 25% on average (Fig. 8). Variations around this mean illustrate decadal variability of the ocean carbon sink. So far, there is no indication of a decrease in the ocean-borne fraction from 1960 to 2020. The increase of the ocean sink is primarily driven by the increased atmospheric CO_2 concentration, with the strongest CO_2 induced signal in the North Atlantic and the Southern Ocean (Fig. 10a). The effect of climate change is much weaker, reducing the ocean sink globally by 0.12 ± 0.07 GtC yr^{-1} or 5% (2011-2020, range -0.8 to -7.4%), and does not show clear spatial patterns across the GOBMs ensemble (Fig. 10b). This is the

999   combined effect of change and variability in all atmospheric forcing fields, previously

1000   attributed to wind and temperature changes in one model (LeQuéré et al., 2010).

1001   The global net air-sea CO_2 flux is a residual of large natural and anthropogenic CO_2 fluxes

1002   into and out of the ocean with distinct regional and seasonal variations (Fig. 6 and B1).

1003   Natural fluxes dominate on regional scales, but largely cancel out when integrated globally

1004   (Gruber et al., 2009). Mid-latitudes in all basins and the high-latitude North Atlantic

1005   dominate the ocean CO_2 uptake where low temperatures and high wind speeds facilitate

1006 CO_2 uptake at the surface (Takahashi et al., 2009). In these regions, formation of mode,

1007   intermediate and deep-water masses transport anthropogenic carbon into the ocean

1008   interior, thus allowing for continued CO_2 uptake at the surface. Outgassing of natural CO_2

1009   occurs mostly in the tropics, especially in the equatorial upwelling region, and to a lesser

1010   extent in the North Pacific and polar Southern Ocean, mirroring a well-established

1011   understanding of regional patterns of air-sea CO_2 exchange (e.g., Takahashi et al., 2009,

1012   Gruber et al., 2009). These patterns are also noticeable in the Surface Ocean CO_2 Atlas

1013   (SOCAT) dataset, where an ocean fCO_2 value above the atmospheric level indicates

1014   outgassing (Fig. B1). This map further illustrates the data-sparsity in the Indian Ocean and

1015   the southern hemisphere in general.

1016   Interannual variability of the ocean carbon sink is driven by climate variability with a first-

1017   order effect from a stronger ocean sink during large El Niño events (e.g., 1997-1998) (Fig. 9;

1018   Rödenbeck et al., 2014, Hauck et al., 2020). The GOBMs show the same patterns of decadal

1019   variability as the mean of the fCO_2-based data products, with a stagnation of the ocean sink

1020   in the 1990s and a strengthening since the early 2000s (Fig. 9, Le Quéré et al., 2007;

1021   Landschützer et al., 2015, 2016; DeVries et al., 2017; Hauck et al., 2020; McKinley et al.,

1022   2020). Different explanations have been proposed for this decadal variability, ranging from

1023   the ocean's response to changes in atmospheric wind and pressure systems (e.g., Le Quéré

1024   et al., 2007, Keppler and Landschützer, 2019), including variations in upper ocean

1025   overturning circulation (DeVries et al., 2017) to the eruption of Mount Pinatubo and its

1026   effects on sea surface temperature and slowed atmospheric CO_2 growth rate in the 1990s

1027   (McKinley et al., 2020). The main origin of the decadal variability is a matter of debate with a

1028   number of studies initially pointing to the Southern Ocean (see review in Canadell et al.,

1029   2021), but also contributions from the North Atlantic and North Pacific (Landschützer et al.,

1030   2016, DeVries et al., 2019), or a global signal (McKinley et al., 2020) were proposed.

1031   Although all individual GOBMs and data-products fall within the observational constraint,

1032   the ensemble means of GOBMs, and data-products adjusted for the riverine flux diverge

1033   over time with a mean offset increasing from 0.24 GtC yr^{-1} in the 1990s to 0.66 GtC yr^{-1} in

1034   the decade 2011-2020 and reaching 1.1 GtC yr^{-1} in 2020. The S_{OCEAN} trend diverges with a

1035   factor two difference since 2002 (GOBMs: 0.3 ± 0.1 GtC yr^{-1} per decade, data-products: 0.7 ±

1036   0.2 GtC yr^{-1} per decade, best estimate: 0.5 GtC yr^{-1} per decade) and with a factor of three

1037   since 2010 (GOBMs: 0.3 ± 0.1 GtC yr^{-1} per decade, data-products: 0.9 ± 0.3 GtC yr^{-1} per

1038   decade , best estimate: 0.6 GtC yr^{-1} per decade). The GOBMs estimate is lower than in the

1039   previous global carbon budget (Friedlingstein et al., 2020), because one high-sink model was

1040   not available. The effect of two models (CNRM, MOM6-COBALT) revising their estimates

1041   downwards was largely balanced by two models revising their estimate upwards (FESOM-

1042   REcoM, PlankTOM).

1043   The discrepancy between the two types of estimates stems mostly from a larger Southern

1044   Ocean sink in the data-products prior to 2001, and from a larger S_{OCEAN} trend in the northern

1045   and southern extra-tropics since then (Fig. 12). Possible explanations for the discrepancy in

1046   the Southern Ocean could be missing winter observations and data sparsity in general

1047   (Bushinsky et al., 2019, Gloege et al., 2021), model biases (as indicated by the large model

1048   spread in the South, Figure 12, and the larger model-data mismatch, Figure B2), or

1049   uncertainties in the regional river flux adjustment (Hauck et al., 2020, Lacroix et al., 2020).

1050   During 2010-2016, the ocean CO_2 sink appears to have intensified in line with the expected

1051   increase from atmospheric CO_2 (McKinley et al., 2020). This effect is stronger in the fCO$_2$-

1052   based data products (Fig. 9, GOBMs: +0.43 GtC yr^{-1}, data-products: +0.56 GtC yr^{-1}). The

1053   reduction of -0.09 GtC yr^{-1} (range: -0.30 to +0.12 GtC yr^{-1}) in the ocean CO_2 sink in 2017 is

1054   consistent with the return to normal conditions after the El Niño in 2015/16, which caused

1055   an enhanced sink in previous years. After 2017, the GOBMs ensemble mean suggests the

1056   ocean sink levelling off at about 2.5 GtC yr^{-1}, whereas the data-products' estimate increases

1057   by 0.3 GtC yr^{-1} over the same period.

3.5.3 Final year 2020

The estimated ocean CO_2 sink was 3.0 ± 0.4 GtC in 2020. This is the average of GOBMs and data-products, and is a small increase of 0.02 GtC compared to 2019, in line with the competing effects from an expected sink strengthening from atmospheric CO_2 growth and expected sink weakening from La Niña conditions. There is, however, a substantial difference between GOBMs and fCO_2-based data-products in their mean 2020 S_{OCEAN} estimate (GOBMs: 2.5 GtC, data-products: 3.5 GtC). While the GOBMs simulate a stagnation of the sink from 2019 to 2020 (-0.02 ±0.11 GtCGtC), the data-products suggest an increase by 0.06 GtC, although not significant at the 1σ level (±0.13 GtC). Four models and four data products show an increase of S_{OCEAN} (GOBMs up to +0.18 GtC, data-product up to +0.21 GtC), while four models and three data products show no change or a decrease of S_{OCEAN} (GOBMs down to -0.12 GtC, data-products down to -0.13 GtC; Fig. 9). The data-products have a larger uncertainty at the tails of the reconstructed time series (e.g., Watson et al., 2020). Specifically, the data-products' estimate of the last year is regularly adjusted in the following release owing to the tail effect and an incrementally increasing data availability with 1-5 years lag (Figure 9 bottom).

3.5.4 Year 2021 Projection

Using a feed-forward neural network method (see section 2.4) we project an ocean sink of 2.9 GtC for 2021. This is a reduction of the sink by 0.1 GtC relative to the 2020 value which we attribute to La Niña conditions in January to May 2021 and projections of a re-emergence of La Niña later in the year.

3.5.5 Model Evaluation

The evaluation of the ocean estimates (Fig. B2) shows an RMSE from annually detrended data of 1.3 to 2.8 µatm for the seven fCO_2-based data products over the globe, relative to the fCO_2 observations from the SOCAT v2021 dataset for the period 1990-2020. The GOBMs RMSEs are larger and range from 3.3 to 5.9 µatm. The RMSEs are generally larger at high latitudes compared to the tropics, for both the data products and the GOBMs. The data products have RMSEs of 1.3 to 3.6 µatm in the tropics, 1.3 to 2.7 µatm in the north, and 2.2 to 6.1 µatm in the south. Note that the data products are based on the SOCAT v2021 database, hence the latter are not independent dataset for the evaluation of the data

products. The GOBMs RMSEs are more spread across regions, ranging from 2.7 to 4.3 µatm in the tropics, 2.9 to 6.9 µatm in the North, and 6.4 to 9.8 µatm in the South. The higher RMSEs occur in regions with stronger climate variability, such as the northern and southern high latitudes (poleward of the subtropical gyres). The upper-range of the model RMSEs have decreased somewhat relative to Friedlingstein et al. (2020), owing to one model with upper-end RMSE not being represented this year, and the reduction of RMSE in one model (MPIOM-HAMOCC6), presumably related to the inclusion of riverine carbon fluxes.

The additional simulation C allows to separate the steady-state anthropogenic carbon component (sim C - sim B) and to compare the model flux and DIC inventory change directly to the interior ocean estimate of Gruber et al (2019) without further assumptions. The GOBMs ensemble average of steady-state anthropogenic carbon inventory change 1994-2007 amounts to 2.1 GtC yr^{-1}, and is significantly lower than the 2.6 ± 0.3 GtC yr^{-1} estimated by Gruber et al (2019). Only the three models with the highest sink estimate fall within the range reported by Gruber et al. (2019). This suggests that most of the models underestimates anthropogenic carbon uptake by the ocean likely due to biases in ocean carbon transport and mixing from the surface mixed layer to the ocean interior.

The reported S_{OCEAN} estimate from GOBMs and data-products is 2.1 ± 0.4 GtC yr^{-1} over the period 1994 to 2007, which is in agreement with the ocean interior estimate of 2.2 ± 0.4 GtC yr^{-1} when accounting for the climate effect on the natural CO_2 flux of −0.4 ± 0.24 GtC yr^{-1} (Gruber et al., 2019) to match the definition of S_{OCEAN} used here (Hauck et al., 2020). This comparison depends critically on the estimate of the climate effect on the natural CO_2 flux, which is smaller from the GOBMs (section 3.5.2) than in Gruber et al. (2019).

3.6 Land Sink

3.6.1 Historical period 1850-2020

Cumulated since 1850, the terrestrial CO_2 sink amounts to 195 ± 45 GtC, 30% of total anthropogenic emissions. Over the historical period, the sink increased in pace with the anthropogenic emissions exponential increase (Fig. 3b).

3.6.2 Recent period 1960-2020

The terrestrial CO_2 sink increased from 1.2 ± 0.5 GtC yr^{-1} in the 1960s to 3.1 ± 0.6 GtC yr^{-1} during 2010-2019, with important interannual variations of up to 2 GtC yr^{-1} generally

1118   showing a decreased land sink during El Niño events (Fig. 7), responsible for the

1119   corresponding enhanced growth rate in atmospheric CO_2 concentration. The larger land CO_2

1120   sink during 2010-2019 compared to the 1960s is reproduced by all the DGVMs in response

1121   to the combined atmospheric CO_2 increase and the changes in climate, and consistent with

1122   constraints from the other budget terms (Table 5).

1123   Over the period 1960 to present the increase in the global terrestrial CO_2 sink is largely

1124   attributed to the CO_2 fertilisation effect in the models (Prentice et al., 2001, Piao et al.,

1125   2009), directly stimulating plant photosynthesis and increased plant water use in water

1126   limited systems, with a small negative contribution of climate change (Fig. 10). There is a

1127   range of evidence to support a positive terrestrial carbon sink in response to increasing

1128   atmospheric CO_2, albeit with uncertain magnitude (Walker et al., 2021). As expected from

1129   theory the greatest CO_2 effect is simulated in the tropical forest regions, associated with

1130   warm temperatures and long growing seasons (Hickler et al., 2008) (Fig. 10a). However,

1131   evidence from tropical intact forest plots indicate an overall decline in the land sink across

1132   Amazonia (1985-2011), attributed to enhanced mortality offsetting productivity gains

1133   (Brienen et al., 2005, Hubau et al., 2020). During 2011-2020 the land sink is positive in all

1134   regions (Fig. 6) with the exception of central and eastern Brazil, Southwest USA and

1135   northern Mexico, Southeast Europe and Central Asia, South Africa, and eastern Australia,

1136   where the negative effects of climate variability and change (i.e. reduced rainfall)

1137   counterbalance CO_2 effects. This is clearly visible on Figure 10 where the effects of CO_2 (Fig.

1138   10a) and climate (Fig. 10b) as simulated by the DGVMs are isolated. The negative effect of

1139   climate is the strongest in most of South America, Central America, Southwest US and

1140   Central Europe (Fig. 10b). Globally, climate change reduces the land sink by 0.45 ± 0.39 GtC

1141 yr^{-1} or 15% (2011-2020).

1142   In the past years several regions experienced record-setting fire events. While global burned

1143   area has declined over the past decades mostly due to declining fire activity in savannas

1144   (Andela et al., 2017), forest fire emissions are rising and have the potential to counter the

1145   negative fire trend in savannas (Zheng et al., 2021). Noteworthy events include the 2019-

1146   2020 Black Summer event in Australia (emissions of roughly 0.2 GtC; van der Velde et al.,

1147   2021) and Siberia in 2021 where emissions approached 0.4 GtC or three times the 1997-

1148   2020 average according to GFED4s. While other regions, including Western US and

1149 Mediterranean Europe, also experienced intense fire seasons in 2021 their emissions are

1150 substantially lower.

1151 Despite these regional negative effects of climate change on S_{LAND}, the efficiency of land to

1152 remove anthropogenic CO_2 emissions has remained broadly constant over the last six

1153 decades, with a land-borne fraction ($S_{LAND}/(E_{FOS}+E_{LUC})$ of ~30% (Fig 8).

3.6.3 Final year 2020

1155 The terrestrial CO_2 sink from the DGVMs ensemble was 2.9 ± 1.0 GtC in 2020, slightly below

1156 the decadal average of 3.1 GtC yr^{-1} (Fig. 4, Table 6). We note that the DGVMs estimate for

1157 2020 is significantly larger than the 2.1 ± 0.9 GtC yr^{-1} estimate from the residual sink from

1158 the global budget ($E_{FOS}+E_{LUC}-G_{ATM}-S_{OCEAN}$) (Table 5).

3.6.4 Year 2021 Projection

1160 Using a feed-forward neural network method (see section 2.5) we project a land sink of 3.3

1161 GtC for 2021. This is an increase of the land sink by 0.3 GtC relative to the 2020 value which

1162 we attribute to La Niña conditions in 2021.

3.6.5 Model Evaluation

1164 The evaluation of the DGVMs (Fig. B3) shows generally high skill scores across models for

1165 runoff, and to a lesser extent for vegetation biomass, GPP, and ecosystem respiration (Fig.

1166 B3, left panel). Skill score was lowest for leaf area index and net ecosystem exchange, with a

1167 widest disparity among models for soil carbon. Further analysis of the results will be

1168 provided separately, focusing on the strengths and weaknesses in the DGVMs ensemble and

1169 its validity for use in the global carbon budget.

3.7 Partitioning the carbon sinks

3.7.1 Global sinks and spread of estimates

1172 In the period 2011-2020, the bottom-up view of total global carbon sinks provided by the

1173 GCB ($S_{OCEAN} + S_{LAND} - E_{LUC}$) agrees closely with the top-down budget delivered by the

1174 atmospheric inversions. Figure 11 shows both total sink estimates of the last decade split by

1175 land and ocean, which match the difference between G_{ATM} and E_{FOS} to within 0.06–0.17 GtC

1176 yr^{-1} for inverse models, and to 0.3 GtC yr^{-1} for the GCB mean. The latter represents the B_{IM}

1177 discussed in Section 3.8, which by design is minimal for the inverse models.

1178 The distributions based on the individual models and data products reveal substantial

1179 spread but converge near the decadal means quoted in Tables 5 and 6. Sink estimates for

1180 S_{OCEAN} and from inverse models are mostly non-Gaussian, while the ensemble of DGVMs

1181 appears more normally distributed justifying the use of a multi-model mean and standard

1182 deviation for their errors in the budget. Noteworthy is that the tails of the distributions

1183 provided by the land and ocean bottom-up estimates would not agree with the global

1184 constraint provided by the fossil fuel emissions and the observed atmospheric CO_2 growth

1185 rate ($E_{FOS} - G_{ATM}$). This illustrates the power of the atmospheric joint constraint from G_{ATM}

1186 and the global CO_2 observation network it derives from.

1187 ### 3.7.2 Total atmosphere-to-land fluxes

1188 The total atmosphere-to-land fluxes ($S_{LAND} - E_{LUC}$), calculated here as the difference between

1189 S_{LAND} from the DGVMs and E_{LUC} from the bookkeeping models, amounts to a 1.9 ± 0.9 GtC yr^{-1}

1190 ^{1} sink during 2011-2020 (Table 5). Estimates of total atmosphere-to-land fluxes ($S_{LAND} - E_{LUC}$)

1191 from the DGVMs alone (1.6 ± 0.6 GtC yr^{-1}) are consistent with this estimate and also with

1192 the global carbon budget constraint ($E_{FOS} - G_{ATM} - S_{OCEAN}$, 1.7 ± 0.8 GtC yr^{-1} Table 5).

1193 Consistent with the bookkeeping models estimates, the DGVM-based E_{LUC} is substantially

1194 lower than in Friedlingstein et al., (2020) due to the improved land cover forcing (see

1195 section 3.2.2), increasing their total atmosphere-to-land fluxes and hence the consistency

1196 with the budget constraint. For the last decade (2011-2020), the inversions estimate the net

1197 atmosphere-to-land uptake to lie within a range of 1.3 to 2.0 GtC yr^{-1}, consistent with the

1198 GCB and DGVMs estimates of $S_{LAND} - E_{LUC}$ (Figure 11, Figure 12 top row).

1199 ### 3.7.3 Total atmosphere-to-ocean fluxes

1200 For the 2011-2020 period, the GOBMs (2.5 ± 0.6 GtC yr^{-1}) produce a lower estimate for the

1201 ocean sink than the fCO_2-based data products (3.1 ± 0.5 GtC yr^{-1}), which shows up in Figure

1202 11 as a separate peak in the distribution from the GOBMs (triangle symbols pointing right)

1203 and from the fCO_2-based products (triangle symbols pointing left). Atmospheric inversions

1204 (2.6 to 3.1 GtC yr^{-1}) also suggest higher ocean uptake in the recent decade (Figure 11, Figure

1205 12 top row). In interpreting these differences, we caution that the riverine transport of

1206 carbon taken up on land and outgassing from the ocean is a substantial (0.6 GtC yr^{-1}) and

1207   uncertain term that separates the various methods. A recent estimate of decadal ocean

1208   uptake from observed O_2/N_2 ratios (Tohjima et al., 2019) also points towards a larger ocean

1209   sink, albeit with large uncertainty (2012-2016: 3.1 ± 1.5 GtC yr^{-1}).

1210   **3.7.4   Regional breakdown and interannual variability**

1211   Figure 12 also shows the latitudinal partitioning of the total atmosphere-to-surface fluxes

1212   excluding fossil CO_2 emissions (S_{OCEAN} + S_{LAND} – E_{LUC}) according to the multi-model average

1213   estimates from GOBMs and ocean fCO_2-based products (S_{OCEAN}) and DGVMs (S_{LAND} – E_{LUC}),

1214   and from atmospheric inversions (S_{OCEAN} and S_{LAND} – E_{LUC}).

1215   **3.7.4.1   North**

1216   Despite being one of the most densely observed and studied regions of our globe, annual

1217   mean carbon sink estimates in the northern extra-tropics (north of 30°N) continue to differ

1218   by about 0.5 GtC yr^{-1}. The atmospheric inversions suggest an atmosphere-to-surface sink

1219   (S_{OCEAN}+ S_{LAND} – E_{LUC}) for 2011-2020 of 2.0 to 3.4 GtC yr^{-1}, which is higher than the process

1220   models' estimate of 2.1 ± 0.5 GtC yr^{-1} (Fig. 12). The GOBMs (1.1 ± 0.2 GtC yr^{-1}), fCO_2-based

1221   data products (1.3 ± 0.1 GtC yr^{-1}), and inversion models (0.9 to 1.5 GtC yr^{-1}) produce

1222   consistent estimates of the ocean sink. Thus, the difference mainly arises from the total land

1223   flux (S_{LAND} – E_{LUC}) estimate, which is 1.0 ± 0.4 GtC yr^{-1} in the DGVMs compared to 0.7 to 2.4

1224   GtC yr^{-1} in the atmospheric inversions (Figure 12, second row).

1225   Discrepancies in the northern land fluxes conforms with persistent issues surrounding the

1226   quantification of the drivers of the global net land CO_2 flux (Arneth et al., 2017; Huntzinger

1227   et al., 2017) and the distribution of atmosphere-to-land fluxes between the tropics and high

1228   northern latitudes (Baccini et al., 2017; Schimel et al., 2015; Stephens et al., 2007; Ciais et al.

1229   2019; Gaubert et al,. 2019).

1230   In the northern extratropics, the process models, inversions, and fCO_2-based data products

1231   consistently suggest that most of the variability stems from the land (Fig. 12). Inversions

1232   generally estimate similar interannual variations (IAV) over land to DGVMs (0.28 – 0.47 vs

1233   0.20 – 0.73 GtC yr^{-1}, averaged over 1990-2020), and they have higher IAV in ocean fluxes

1234   (0.03 – 0.19 GtC yr^{-1}) relative to GOBMs (0.03 – 0.05 GtC yr^{-1}, Fig. B2), and fCO_2-based data

1235   products (0.03 – 0.09 GtC yr^{-1}).

3.7.4.2 Tropics

In the tropics (30°S-30°N), both the atmospheric inversions and process models estimate a total carbon balance (S_{OCEAN}+S_{LAND}-E_{LUC}) that is close to neutral over the past decade. The GOBMs (0.0 ± 0.3 GtC yr^{-1}), fCO$_2$-based data products (0.03 ± 0.2 GtC yr^{-1}), and inversion models (-0.2 to 0.2 GtC yr^{-1}) all indicate an approximately neutral tropical ocean flux (see Fig. B1 for spatial patterns). DGVMs indicate a net land sink (S_{LAND}-E_{LUC}) of 0.6 ± 0.3 GtC yr^{-1}, whereas the inversion models indicate a net land flux between -0.7 and 0.9 GtC yr^{-1}, though with high uncertainty (Figure 12, third row).

The tropical lands are the origin of most of the atmospheric CO$_2$ interannual variability (Ahlström et al., 2015), consistently among the process models and inversions (Fig. 12). The interannual variability in the tropics is similar among the ocean data products (0.07 – 0.15 GtC yr^{-1}) and the models (0.07 – 0.15 GtC yr^{-1}, Fig. B2), which is the highest ocean sink variability of all regions. The DGVMs and inversions indicate that atmosphere-to-land CO$_2$ fluxes are more variable than atmosphere-to-ocean CO$_2$ fluxes in the tropics, with interannual variability of 0.4 to 1.2 and 0.6 to 1.1 GtC yr^{-1} respectively.

3.7.4.3 South

In the southern extra-tropics (south of 30°S), the atmospheric inversions suggest a total atmosphere-to-surface sink (S_{OCEAN}+S_{LAND}-E_{LUC}) for 2011-2020 of 1.6 to 1.9 GtC yr^{-1}, slightly higher than the process models' estimate of 1.4 ± 0.3 GtC yr^{-1} (Fig. 12). An approximately neutral total land flux (S_{LAND}-E_{LUC}) for the southern extra-tropics is estimated by both the DGVMs (0.02 ± 0.05 GtC yr^{-1}) and the inversion models (sink of -0.1 to 0.2 GtC yr^{-1}). This means nearly all carbon uptake is due to oceanic sinks south of 30°S. The southern ocean flux in the fCO$_2$-based data products (1.7 ± 0.1 GtC yr^{-1}) and inversion estimates (1.4 to 1.8 GtCyr-1) is higher than in the GOBMs (1.4 ± 0.3 GtC yr^{-1}) (Figure 12, bottom row). This might be explained by the data-products potentially underestimating the winter CO$_2$ outgassing south of the Polar Front (Bushinsky et al., 2019), by model biases, or by the uncertainty in the regional distribution of the river flux adjustment (Aumont et al., 2001, Lacroix et al., 2020) applied to fCO$_2$-based data products and inverse models to isolate the anthropogenic S_{OCEAN} flux. CO$_2$ fluxes from this region are more sparsely sampled by all methods, especially in wintertime (Fig. B1).

The interannual variability in the southern extra-tropics is low because of the dominance of ocean area with low variability compared to land areas. The split between land (S_{LAND}-E_{LUC}) and ocean (S_{OCEAN}) shows a substantial contribution to variability in the south coming from the land, with no consistency between the DGVMs and the inversions or among inversions. This is expected due to the difficulty of separating exactly the land and oceanic fluxes when viewed from atmospheric observations alone. The S_{OCEAN} interannual variability was found to be higher in the fCO_2-based data products (0.09 to 0.14 GtC yr^{-1}) compared to GOBMs (0.04 to 0.06 GtC yr^{-1}) in 1990-2020 (Fig. B2). Model subsampling experiments recently illustrated that observation-based products may overestimate decadal variability in the Southern Ocean carbon sink by 30% due to data sparsity, based on one data product with the highest decadal variability (Gloege et al., 2021).

3.7.4.4 Tropical vs northern land uptake

A continuing conundrum is the partitioning of the global atmosphere-land flux between the northern hemisphere land and the tropical land (Stephens et al., 2017; Pan et al., 2011; Gaubert et al., 2019). It is of importance because each region has its own history of land-use change, climate drivers, and impact of increasing atmospheric CO_2 and nitrogen deposition. Quantifying the magnitude of each sink is a prerequisite to understanding how each individual driver impacts the tropical and mid/high-latitude carbon balance.

We define the North-South (N-S) difference as net atmosphere-land flux north of 30N minus the net atmosphere-land flux south of 30°N. For the inversions, the N-S difference ranges from -0.1 GtC yr^{-1} to 2.9 GtC yr^{-1} across this year's inversion ensemble with an equal preference across models for either a small Northern land sink and a tropical land sink (small N-S difference), a medium Northern land sink and a neutral tropical land flux (medium N-S difference), or a large Northern land sink and a tropical land source (large N-S difference).

In the ensemble of DGVMs the N-S difference is 0.5 ± 0.5 GtC yr^{-1}, a much narrower range than the one from inversions. Only three DGVMs have a N-S difference larger than 1.0 GtC yr^{-1}. The larger agreement across DGVMs than across inversions is to be expected as there is no correlation between Northern and Tropical land sinks in the DGVMs as opposed to the inversions where the sum of the two regions being well-constrained leads to an anti-

1296   correlation between these two regions. The much smaller spread in the N-S difference

1297   between the DGVMs could help to scrutinise the inverse models further. For example, a

1298   large northern land sink and a tropical land source in an inversion would suggest a large

1299   sensitivity to CO_2 fertilisation (the dominant factor driving the land sinks) for Northern

1300   ecosystems, which would be not mirrored by tropical ecosystems. Such a combination could

1301   be hard to reconcile with the process understanding gained from the DGVMs ensembles and

1302   independent measurements (e.g. Free Air CO2 Enrichment experiments). Such

1303   investigations will be further pursued in the upcoming assessment from REgional Carbon

1304   Cycle Assessment and Processes (RECCAP2; Ciais et al., 2020).

1305   ### 3.8   Closing the Global Carbon Cycle

1306   ### 3.8.1   Partitioning of Cumulative Emissions and Sink Fluxes

1307   The global carbon budget over the historical period (1850-2020) is shown in Fig. 3.

1308   Emissions during the period 1850-2020 amounted to 660 ± 65 GtC and were partitioned

1309   among the atmosphere (270 ± 5 GtC; 41%), ocean (170 ± 35 GtC; 26%), and the land (195 ±

1310   45 GtC; 30%). The cumulative land sink is almost equal to the cumulative land-use emissions

1311   (200 ± 65 GtC), making the global land nearly neutral over the whole 1850-2020 period.

1312   The use of nearly independent estimates for the individual terms shows a cumulative

1313   budget imbalance of 25 GtC (4%) during 1850-2020 (Fig. 3, Table 8), which, if correct,

1314   suggests that emissions are slightly too high by the same proportion (4%) or that the

1315   combined land and ocean sinks are slightly underestimated (by about 7%). The bulk of the

1316   imbalance could originate from the estimation of large E_{LUC} between the mid 1920s and the

1317   mid 1960s which is unmatched by a growth in atmospheric CO_2 concentration as recorded in

1318   ice cores (Fig. 3). However, the known loss of additional sink capacity of 30-40 GtC (over the

1319   1850-2020 period) due to reduced forest cover has not been accounted for in our method

1320   and would further exacerbate the budget imbalance (Section 2.7.4).

1321   For the more recent 1960-2020 period where direct atmospheric CO_2 measurements are

1322   available, 375 ± 20 GtC (82%) of the total emissions (E_{FOS} + E_{LUC}) were caused by fossil CO_2

1323   emissions, and 80 ± 45 GtC (18%) by land-use change (Table 8). The total emissions were

1324   partitioned among the atmosphere (205 ± 5 GtC; 47%), ocean (115 ± 25 GtC; 25%), and the

1325   land (135 ± 25 GtC; 30%), with a near zero unattributed budget imbalance. All components

1326 except land-use change emissions have significantly grown since 1960, with important

1327 interannual variability in the growth rate in atmospheric CO_2 concentration and in the land

1328 CO_2 sink (Fig. 4), and some decadal variability in all terms (Table 6). Differences with

1329 previous budget releases are documented in Fig. B5.

1330 The global carbon budget averaged over the last decade (2011-2020) is shown in Fig. 2, Fig.

1331 13 (right panel) and Table 6. For this time period, 90% of the total emissions (E_{FOS} + E_{LUC})

1332 were from fossil CO_2 emissions (E_{FOS}), and 10% from land-use change (E_{LUC}). The total

1333 emissions were partitioned among the atmosphere (47%), ocean (26%) and land (29%), with

1334 a near-zero unattributed budget imbalance (~3%). For single years, the budget imbalance

1335 can be larger (Figure 4). For 2020, the combination of our sources and sinks estimates leads

1336 to a B_{IM} of -0.8 GtC, suggesting an underestimation of the anthropogenic sources

1337 (potentially E_{LUC}), and/or an overestimation of the combined land and ocean sinks

1338 **3.8.2 Carbon Budget Imbalance**

1339 The carbon budget imbalance (B_{IM}; Eq. 1, Fig.4) quantifies the mismatch between the

1340 estimated total emissions and the estimated changes in the atmosphere, land, and ocean

1341 reservoirs. The mean budget imbalance from 1960 to 2020 is very small (average of 0.03 GtC

1342 $yr^{-1)}$ and shows no trend over the full time series. The process models (GOBMs and DGVMs)

1343 and data-products have been selected to match observational constraints in the 1990s, but

1344 no further constraints have been applied to their representation of trend and variability.

1345 Therefore, the near-zero mean and trend in the budget imbalance is seen as evidence of a

1346 coherent community understanding of the emissions and their partitioning on those time

1347 scales (Fig. 4). However, the budget imbalance shows substantial variability of the order of

1348 ±1 GtC yr^{-1}, particularly over semi-decadal time scales, although most of the variability is

1349 within the uncertainty of the estimates. The positive carbon imbalance during the 1960s,

1350 and early 1990s, indicates that either the emissions were overestimated, or the sinks were

1351 underestimated during these periods. The reverse is true for the 1970s, 1980s, and for the

1352 2011-2020 period (Fig. 4, Table 6).

1353 We cannot attribute the cause of the variability in the budget imbalance with our analysis,

1354 we only note that the budget imbalance is unlikely to be explained by errors or biases in the

1355 emissions alone because of its large semi-decadal variability component, a variability that is

1356 untypical of emissions and has not changed in the past 60 years despite a near tripling in

1357   emissions (Fig. 4). Errors in S_{LAND} and S_{OCEAN} are more likely to be the main cause for the

1358   budget imbalance. For example, underestimation of the S_{LAND} by DGVMs has been reported

1359   following the eruption of Mount Pinatubo in 1991 possibly due to missing responses to

1360   changes in diffuse radiation (Mercado et al., 2009). Although in GCB2021 we have for the

1361   first time accounted for aerosol effects on solar radiation quantity and quality (diffuse vs

1362   direct), most DGVMs only used the former as input (i.e., total solar radiation). Thus, the

1363   ensemble mean may not capture the full effects of volcanic eruptions, i.e. associated with

1364   high light scattering sulphate aerosols, on the land carbon sink (O'Sullivan et al., 2021).

1365   DGVMs are suspected to overestimate the land sink in response to the wet decade of the

1366   1970s (Sitch et al., 2008). Quasi-decadal variability in the ocean sink has also been reported,

1367   with all methods agreeing on a smaller than expected ocean CO_2 sink in the 1990s and a

1368   larger than expected sink in the 2000s (Fig. 9; Landschützer et al., 2016, DeVries et al., 2019,

1369   Hauck et al., 2020, McKinley et al., 2020). Errors in sink estimates could also be driven by

1370   errors in the climatic forcing data, particularly precipitation for S_{LAND} and wind for S_{OCEAN}.

1371   The budget imbalance (B_{IM}) was negative (-0.3 GtC yr^{-1}) on average over 2011-2020,

1372   although the B_{IM} uncertainty is large (1.1 GtC yr^{-1} over the decade). Also, the B_{IM} shows

1373   substantial departure from zero on yearly time scales (Fig. 4), highlighting unresolved

1374   variability of the carbon cycle, likely in the land sink (S_{LAND}), given its large year to year

1375   variability (Fig. 4e and 7).

1376   Both the budget imbalance (B_{IM}, Table 6) and the residual land sink from the global budget

1377   ($E_{FOS}+E_{LUC}-G_{ATM}-S_{OCEAN}$, Table 5) include an error term due to the inconsistencies that arises

1378   from using E_{LUC} from bookkeeping models, and S_{LAND} from DGVMs, most notably the loss of

1379   additional sink capacity (see section 2.7). Other differences include a better accounting of

1380   land use changes practices and processes in bookkeeping models than in DGVMs, or the

1381   bookkeeping models error of having present-day observed carbon densities fixed in the

1382   past. That the budget imbalance shows no clear trend towards larger values over time is an

1383   indication that these inconsistencies probably play a minor role compared to other errors in

1384 S_{LAND} or S_{OCEAN}.

1385   Although the budget imbalance is near zero for the recent decades, it could be due to

1386   compensation of errors. We cannot exclude an overestimation of CO_2 emissions, particularly

1387   from land-use change, given their large uncertainty, as has been suggested elsewhere (Piao

1388 et al., 2018), combined with an underestimate of the sinks. A larger S_{LAND} would reconcile

1389 model results with inversion estimates for fluxes in the total land during the past decade

1390 (Fig. 12; Table 5). Likewise, a larger S_{OCEAN} is also possible given the higher estimates from

1391 the data-products (see section 3.1.2, Fig. 9 and Fig. 12) and the recently suggested upward

1392 correction of the ocean carbon sink (Watson et al., 2020, Fig. 9). If S_{OCEAN} were to be based

1393 on data-products alone, with all data-products including the Watson et al. (2020)

1394 adjustment, this would result in a 2011-2020 S_{OCEAN} of nearly 4 GtC yr^{-1}, outside of the range

1395 supported by the atmospheric inversions, with a negative B_{IM} of more than 1 GtC yr^{-1}

1396 indicating that a closure of the budget could only be achieved with either anthropogenic

1397 emissions being larger and/or the net land sink being substantially smaller than estimated

1398 here. More integrated use of observations in the Global Carbon Budget, either on their own

1399 or for further constraining model results, should help resolve some of the budget imbalance

1400 (Peters et al., 2017).

4   Tracking progress towards mitigation targets

1402 Fossil CO_2 emissions growth peaked at +3% per year during the 2000s, driven by the rapid

1403 growth in Chinese emissions. In the last decade, however, the growth rate for the preceding

1404 10 years has slowly declined, reaching a low +0.4% per year from 2012-2021 (including the

1405 2020 global decline and the expected 2021 emissions rebound). While this slowdown in

1406 global fossil CO_2 emissions growth is welcome, it is far from what is needed to be consistent

1407 with the temperature goals of the Paris Agreement.

1408 Since the 1990s, the average growth rate of fossil CO_2 emissions has continuously declined

1409 across the group of developed countries of the Organisation for Economic Co-operation and

1410 Development (OECD), with emissions peaking in around 2005 and now declining at around

1411 1% yr^{-1} (Le Quéré et al., 2021). In the decade 2010-2019, territorial fossil CO_2 emissions

1412 decreased significantly (at the 95% confidence level) in 23 countries whose economies grew

1413 significantly (also at the 95% confidence level): Barbados, Belgium, Croatia, Czech Republic,

1414 Denmark, Finland, France, Germany, Israel, Japan, Luxembourg, North Macedonia, Malta,

1415 Mexico, Netherlands, Slovakia, Slovenia, Solomon Islands, Sweden, Switzerland, Tuvalu,

1416 United Kingdom and the USA (updated from Le Quéré et al., 2019). Altogether, these 23

1417 countries contribute to 2.5 GtC yr^{-1} over the last decade, about one quarter of world CO_2

1418 fossil emissions. Consumption-based emissions are also falling significantly in 15 of these

1419   countries (Belgium, Croatia, Czech Republic, Denmark, Finland, France, Germany, Israel,

1420   Japan, Mexico, Netherlands, Slovenia, Sweden, United Kingdom, and the USA). Figure 14

1421   shows that the emission declines in the USA and the EU27 are primarily driven by increased

1422   decarbonisation (CO_2 emissions per unit energy) in the last decade compared to the

1423   previous, with smaller contributions in the EU27 from slightly weaker economic growth and

1424   slightly larger declines in energy per GDP. These countries have stable or declining energy

1425   use and so decarbonisation policies replace existing fossil fuel infrastructure (Le Quéré et al.

1426   2019).

1427   In contrast, fossil CO_2 emissions continue to grow in non-OECD countries, although the

1428   growth rate has slowed from over 5% yr^{-1} during the 2000s to around 2% yr^{-1} in the last

1429   decade. A large part of this slowdown in non-OECD countries is due to China, which has

1430   seen emissions growth declining from nearly 10% yr^{-1} in the 2000s to 2% yr^{-1} in the last

1431   decade. Excluding China, non-OECD emissions grew at 3% yr^{-1} in the 2000s compared to 2%

1432 yr^{-1} in the last decade. Figure 14 shows that compared to the previous decade, China has

1433   had weaker economic growth in the last decade and a larger decarbonisation rate, with

1434   more rapid declines in energy per GDP which are now back to levels during the 1990s. India

1435   and the rest of the world have strong economic growth that is not compensated by

1436   decarbonisation or declines in energy per GDP, implying fossil CO_2 emissions continue to

1437   grow. Despite the high deployment of renewables in some countries (e.g., India), fossil

1438   energy sources continue to grow to meet growing energy demand (Le Quéré et al. 2019).

1439   Globally, fossil CO_2 emissions growth is slowing, and this is primarily due to the emergence

1440   of climate policy and emission declines in OECD countries (Eskander and Fankhauser 2020).

1441   At the aggregated global level, decarbonisation shows a strong and growing signal in the last

1442   decade, with smaller contributions from lower economic growth and declines in energy per

1443   GDP. Despite the slowing growth in global fossil CO_2 emissions, emissions are still growing,

1444   far from the reductions needed to meet the ambitious climate goals of the UNFCCC Paris

1445   agreement.

1446   We update the remaining carbon budget assessed by the IPCC AR6 (Canadell et al., 2021),

1447   accounting for the 2020 and estimated 2021 emissions from fossil fuel combustion (E_{FOS})

1448   and land use changes (E_{LUC}). From January 2022, the remaining carbon (50% likelihood) for

1449   limiting global warming to 1.5°C, 1.7°C and 2°C is estimated to amount to 120, 210, and 350

1450   GtC (420, 770, 1270 GtCO$_2$). These numbers include an uncertainty based on model spread

1451   (as in IPCC AR6), which is reflected through the percent likelihood of exceeding the given

1452   temperature threshold. These remaining amounts correspond respectively to about 11, 20

1453   and 32 years from the beginning of 2022, at the 2021 level of total CO$_2$ emissions. Reaching

1454   net zero CO$_2$ emissions by 2050 entails cutting total anthropogenic CO$_2$ emissions by about

1455   0.4 GtC (1.4 GtCO$_2$) each year on average, comparable to the decrease during 2020.

1456   **5   Discussion**

1457   Each year when the global carbon budget is published, each flux component is updated for

1458   all previous years to consider corrections that are the result of further scrutiny and

1459   verification of the underlying data in the primary input data sets. Annual estimates may be

1460   updated with improvements in data quality and timeliness (e.g., to eliminate the need for

1461   extrapolation of forcing data such as land-use). Of all terms in the global budget, only the

1462   fossil CO$_2$ emissions and the growth rate in atmospheric CO$_2$ concentration are based

1463   primarily on empirical inputs supporting annual estimates in this carbon budget. The carbon

1464   budget imbalance, yet an imperfect measure, provides a strong indication of the limitations

1465   in observations in understanding and representing processes in models, and/or in the

1466   integration of the carbon budget components.

1467   The persistent unexplained variability in the carbon budget imbalance limits our ability to

1468   verify reported emissions (Peters et al., 2017) and suggests we do not yet have a complete

1469   understanding of the underlying carbon cycle dynamics on annual to decadal timescales.

1470   Resolving most of this unexplained variability should be possible through different and

1471   complementary approaches. First, as intended with our annual updates, the imbalance as an

1472   error term is reduced by improvements of individual components of the global carbon

1473   budget that follow from improving the underlying data and statistics and by improving the

1474   models through the resolution of some of the key uncertainties detailed in Table 9. Second,

1475   additional clues to the origin and processes responsible for the variability in the budget

1476   imbalance could be obtained through a closer scrutiny of carbon variability in light of other

1477   Earth system data (e.g., heat balance, water balance), and the use of a wider range of

1478   biogeochemical observations to better understand the land-ocean partitioning of the carbon

1479   imbalance (e.g. oxygen, carbon isotopes). Finally, additional information could also be

1480   obtained through higher resolution and process knowledge at the regional level, and

1481   through the introduction of inferred fluxes such as those based on satellite CO_2 retrievals.

1482   The limit of the resolution of the carbon budget imbalance is yet unclear, but most certainly

1483   not yet reached given the possibilities for improvements that lie ahead.

1484   Estimates of global fossil CO_2 emissions from different datasets are in relatively good

1485   agreement when the different system boundaries of these datasets are considered

1486   (Andrew, 2020a). But while estimates of E_{FOS} are derived from reported activity data

1487   requiring much fewer complex transformations than some other components of the budget,

1488   uncertainties remain, and one reason for the apparently low variation between datasets is

1489   precisely the reliance on the same underlying reported energy data. The budget excludes

1490   some sources of fossil CO_2 emissions, which available evidence suggests are relatively small

1491   (<1%). We have added emissions from lime production in China and the US, but these are

1492   still absent in most other non-Annex I countries, and before 1990 in other Annex I countries.

1493   Further changes to E_{FOS} this year are documented by Andrew and Peters (2021).

1494   Estimates of E_{LUC} suffer from a range of intertwined issues, including the poor quality of

1495   historical land-cover and land-use change maps, the rudimentary representation of

1496   management processes in most models, and the confusion in methodologies and boundary

1497   conditions used across methods (e.g., Arneth et al., 2017; Pongratz et al., 2014, see also

1498   Section 2.7.4 on the loss of sink capacity; Bastos et al., 2021). Uncertainties in current and

1499   historical carbon stocks in soils and vegetation also add uncertainty in the E_{LUC} estimates.

1500   Unless a major effort to resolve these issues is made, little progress is expected in the

1501   resolution of E_{LUC}. This is particularly concerning given the growing importance of E_{LUC} for

1502   climate mitigation strategies, and the large issues in the quantification of the cumulative

1503   emissions over the historical period that arise from large uncertainties in E_{LUC}.

1504   By adding the DGVMs estimates of CO_2 fluxes due to environmental change from countries'

1505   managed forest areas (part of S_{LAND} in this budget) to the budget E_{LUC} estimate, we

1506   successfully reconciled the large gap between our E_{LUC} estimate and the land use flux from

1507   NGHGIs using the approach described in Grassi et al. (2021). This latter estimate has been

1508   used in the recent UNFCCC's Synthesis Report on Nationally Determined Contribution

1509   (UNFCCC, 2021b) to enable the total national emission estimates to be comparable with

1510   those of the IPCC. However, while Grassi et al. (2021) used only one DGVM, here 17 DGVMs

1511   are used, thus providing a more robust value to be used as potential adjustment in the

policy context, e.g., to help assessing the collective countries' progress towards the goal of the Paris Agreement and avoiding double-accounting for the sink in managed forests. In the absence of this adjustment, collective progress would hence appear better than it is (Grassi et al. 2021).

The comparison of GOBMs, data products and inversions highlights substantial discrepancy in the Southern Ocean (Fig. 12, Hauck et al., 2020). The long-standing sparse data coverage of fCO_2 observations in the Southern compared to the Northern Hemisphere (e.g., Takahashi et al., 2009) continues to exist (Bakker et al., 2016, 2021, Fig. B1) and to lead to substantially higher uncertainty in the S_{OCEAN} estimate for the Southern Hemisphere (Watson et al., 2020, Gloege et al., 2021). This discrepancy, which also hampers model improvement, points to the need for increased high-quality fCO_2 observations especially in the Southern Ocean. At the same time, model uncertainty is illustrated by the large spread of individual GOBM estimates (indicated by shading in Fig. 12) and highlights the need for model improvement. Further uncertainty stems from the regional distribution of the river flux adjustment term being based on one model study yielding the largest riverine outgassing flux south of 20°S (Aumont et al., 2001), with a recent study questioning this distribution (Lacroix et al., 2020). The diverging trends in S_{OCEAN} from different methods is a matter of concern, which is unresolved. The assessment of the net land-atmosphere exchange from DGVMs and atmospheric inversions also shows substantial discrepancy, particularly for the estimate of the total land flux over the northern extra-tropic. This discrepancy highlights the difficulty to quantify complex processes (CO_2 fertilisation, nitrogen deposition and fertilisers, climate change and variability, land management, etc.) that collectively determine the net land CO_2 flux. Resolving the differences in the Northern Hemisphere land sink will require the consideration and inclusion of larger volumes of observations.

We provide metrics for the evaluation of the ocean and land models and the atmospheric inversions (Figs. B2 to B4). These metrics expand the use of observations in the global carbon budget, helping 1) to support improvements in the ocean and land carbon models that produce the sink estimates, and 2) to constrain the representation of key underlying processes in the models and to allocate the regional partitioning of the CO_2 fluxes. However, GOBMs skills have changed little since the introduction of the ocean model evaluation. An additional simulation this year allows for direct comparison with interior ocean

1543 anthropogenic carbon estimates and suggests that the models underestimate

1544 anthropogenic carbon uptake and storage. This is an initial step towards the introduction of

1545 a broader range of observations that we hope will support continued improvements in the

1546 annual estimates of the global carbon budget.

1547 We assessed before that a sustained decrease of –1% in global emissions could be detected

1548 at the 66% likelihood level after a decade only (Peters et al., 2017). Similarly, a change in

1549 behaviour of the land and/or ocean carbon sink would take as long to detect, and much

1550 longer if it emerges more slowly. To continue reducing the carbon imbalance on annual to

1551 decadal time scales, regionalising the carbon budget, and integrating multiple variables are

1552 powerful ways to shorten the detection limit and ensure the research community can

1553 rapidly identify issues of concern in the evolution of the global carbon cycle under the

1554 current rapid and unprecedented changing environmental conditions.

1555 **6   Conclusions**

1556 The estimation of global CO_2 emissions and sinks is a major effort by the carbon cycle

1557 research community that requires a careful compilation and synthesis of measurements,

1558 statistical estimates, and model results. The delivery of an annual carbon budget serves two

1559 purposes. First, there is a large demand for up-to-date information on the state of the

1560 anthropogenic perturbation of the climate system and its underpinning causes. A broad

1561 stakeholder community relies on the data sets associated with the annual carbon budget

1562 including scientists, policy makers, businesses, journalists, and non-governmental

1563 organisations engaged in adapting to and mitigating human-driven climate change. Second,

1564 over the last decades we have seen unprecedented changes in the human and biophysical

1565 environments (e.g., changes in the growth of fossil fuel emissions, impact of COVID-19

1566 pandemic, Earth's warming, and strength of the carbon sinks), which call for frequent

1567 assessments of the state of the planet, a better quantification of the causes of changes in

1568 the contemporary global carbon cycle, and an improved capacity to anticipate its evolution

1569 in the future. Building this scientific understanding to meet the extraordinary climate

1570 mitigation challenge requires frequent, robust, transparent, and traceable data sets and

1571 methods that can be scrutinised and replicated. This paper via 'living data' helps to keep

1572 track of new budget updates.

1573 **7   Data availability**

1574 The data presented here are made available in the belief that their wide dissemination will

1575 lead to greater understanding and new scientific insights of how the carbon cycle works,

1576 how humans are altering it, and how we can mitigate the resulting human-driven climate

1577 change. Full contact details and information on how to cite the data shown here are given at

1578 the top of each page in the accompanying database and summarised in Table 2.

1579 The accompanying database includes two Excel files organised in the following

1580 spreadsheets:

1581 File Global_Carbon_Budget_2021v1.0.xlsx includes the following:

1582   1. Summary

1583   2. The global carbon budget (1959-2020);

1584   3. The historical global carbon budget (1750-2020);

1585   4. Global CO_2 emissions from fossil fuels and cement production by fuel type, and the per-
1586   capita emissions (1959-2020);

1587   5. CO_2 emissions from land-use change from the individual methods and models (1959-
1588   2020);

1589   6. Ocean CO_2 sink from the individual ocean models and fCO_2-based products (1959-
1590   2020);

1591   7. Terrestrial CO_2 sink from the DGVMs (1959-2020).

1592

1593 File National_Carbon_Emissions_2021v1.0.xlsx includes the following:

1594   1. Summary

1595   2. Territorial country CO_2 emissions from fossil CO_2 emissions (1959-2020);

1596   3. Consumption country CO_2 emissions from fossil CO_2 emissions and emissions transfer
1597   from the international trade of goods and services (1990-2019) using CDIAC/UNFCCC
1598   data as reference;

1599   4. Emissions transfers (Consumption minus territorial emissions; 1990-2019);

1600   5. Country definitions;

1601   6. Details of disaggregated countries;

1602   7. Details of aggregated countries.

1603 Both spreadsheets are published by the Integrated Carbon Observation System (ICOS)

1604 Carbon Portal and are available at https://doi.org/10.18160/gcp-2021 (Friedlingstein et al.,

1605 2021). National emissions data are also available from the Global Carbon Atlas

1606 (http://www.globalcarbonatlas.org/, last access: 11 March 2022) and from Our World in

1607 Data (https://ourworldindata.org/co2-emissions, last access: 11 March 2022).

1608

1609 **8   Author contributions**

1610 PF, MWJ, MOS, CLQ, RMA, DCEB, JH, GPP, WP, JP and SS designed the study, conducted the

1611 analysis, and wrote the paper with input from JGC, PC and RBJ. RMA, GPP and JIK produced

1612 the fossil fuel emissions and their uncertainties and analysed the emissions data. DG and

1613 GM provided fossil fuel emission data. JP, TG, CS and RAH provided the bookkeeping land-

1614 use change emissions. JH, LB, OG, NG, TI, LR, JS, RS and DW provided an update of the global

1615 ocean biogeochemical models. SRA, TTTC, LD, LG, YI, PL, CR, AJW and JZ provided an update

1616 of the ocean fCO_2 data products, with synthesis by JH. MB, NRB, KIC, MC, WE, RAF, SRA, TG,

1617 AK, NL, SKL, DRM, ClS, CoS, SN, CW, TO, DP, GR, AJS, BT, TT, CW, and RW provided ocean

1618 fCO_2 measurements for the year 2020, with synthesis by DCEB and SDJ. PA, BD, AKJ, DK, EK,

1619 JK, SL, PCM, JRM, JEMSN, BP, HT, NV, AJW, WY, XY and SZ provided an update of the

1620 Dynamic Global Vegetation Models, with synthesis by SS. WP, FC, LF, ITL, JL, YN and CR

1621 provided an updated atmospheric inversion, developed the protocol and produced the

1622 evaluation, with synthesis by WP. RMA provided predictions of the 2021 emissions and

1623 atmospheric CO_2 growth rate. PL provided the predictions of the 2021 ocean and land sinks.

1624 LPC, GCH, KKG, TMS and GRvdW provided forcing data for land-use change. GG, FT, and CY

1625 provided data for the land-use change NGHGI mapping. PPT provided key atmospheric CO_2

1626 data. MWJ produced the historical record of atmospheric CO_2 concentration and growth

1627 rate, including the atmospheric CO_2 forcing. MOS and NB produced the aerosol diffuse

1628   radiative forcing for the DGVMs. IH provided the climate forcing data for the DGVMs. ER

1629   provided the evaluation of the DGVMs. MWJ provided the emissions prior for use in the

1630   inversion models. XD provided seasonal emissions data for years 2019-2020 for the emission

1631   prior. MWJ and MOS developed a new data management pipeline which automates many

1632   aspects of the data collation, analysis, plotting and synthesis. PF, MWJ, and MOS revised all

1633   figures, tables, text and/or numbers to ensure the update was clear from the 2020 edition

1634   and in line with the globalcarbonatlas.org.

1635

1636   **Competing interests.** The authors declare that they have no conflict of interest.

1637   **9   Acknowledgements**

1638   We thank all people and institutions who provided the data used in this global carbon budget

1639   2021 and the Global Carbon Project members for their input throughout the development of

1640   this publication. We thank Nigel Hawtin for producing Figure 2 and Figure 13. We thank Omar

1641   Jamil and Freddy Wordingham for technical support. We thank Ed Dlugokencky for providing

1642   atmospheric CO_2 measurements. We thank Vivek Arora, Ian G.C. Ashton, Erik Buitenhuis,

1643   Fatemeh Cheginig, Christian Ethé, Marion Gehlen, Lonneke Goddijn-Murphy, T. Holding,

1644   Fabrice Lacroix, Enhui Liao, Pedro M.S. Monteiro, Naiquing Pan, Tristan Quaife, Shijie Shu,

1645   Jamie D. Shutler, Jade Skye, Anthony Walker, and David K. Woolf for their involvement in the

1646   development, use and analysis of the models and data-products used here. We thank Markus

1647   Ritschel, Carmen Rodriguez, Claire Lo Monaco, Nicolas Metzl, Vassilis Kitidis, Sören Gutekunst,

1648   Anne Willstrand Wranne, Tobias Steinhoff, Jessica N. Cross, Natalie M. Monacci, Alice Benoit-

1649   Cattin, Sólveig R. Ólafsdóttir, Joe Salisbury, Doug Vandemark and Christopher W. Hunt, who

1650   contributed to the provision of surface ocean CO_2 observations for the year 2020 (see Table

1651   A5). We also thank Benjamin Pfeil, Rocío Castaño-Primo, Camilla Landa and Maren Karlsen of

1652   the Ocean Thematic Centre of the EU Integrated Carbon Observation System (ICOS) Research

1653   Infrastructure, Kevin O'Brien and Eugene Burger of NOAA's Pacific Marine Environmental

1654   Laboratory and Alex Kozyr of NOAA's National Centers for Environmental Information, for

1655   their contribution to surface ocean CO_2 data and metadata management. We thank the

1656   scientists, institutions, and funding agencies responsible for the collection and quality control

1657   of the data in SOCAT as well as the International Ocean Carbon Coordination Project (IOCCP),

1658   the Surface Ocean Lower Atmosphere Study (SOLAS) and the Integrated Marine Biosphere

1659   Research (IMBeR) program for their support. We thank data providers ObsPack

1660   GLOBALVIEWplus v6.1 and NRT v6.1.1 for atmospheric CO_2 observations. We thank the

1661   individuals and institutions that provided the databases used for the models evaluations used

1662   here. We thank Fortunat Joos, Samar Khatiwala and Timothy DeVries for providing historical

1663   data. NV thanks the whole ORCHIDEE group. YN thanks CSIRO, EC, EMPA, FMI, IPEN, JMA,

1664   LSCE, NCAR, NIES, NILU, NIWA, NOAA, SIO, and TU/NIPR for providing data for NISMON-CO2.

1665   We thank Kevin Bowman (NASA JPL) for contribution to the CMS-Flux results. JL thanks the

1666   Jet Propulsion Laboratory, California Institute of Technology. This is PMEL contribution 5317.

1667   SDJ thanks the data management team at the Bjerknes Climate Data Centre. WE thanks the

1668   Tula Foundation for funding support. Australian ocean CO_2 data were sourced from Australia's

1669   Integrated Marine Observing System (IMOS); IMOS is enabled by the National Collaborative

1670   Research Infrastructure Strategy (NCRIS). MC thanks Anthony English, Clynt Gregory and

1671   Gordon Furey (P&O Maritime Services) and Tobias Steinhoff for their support. NL thanks the

1672   crew of the Cap San Lorenzo and the US IMAGO of IRD Brest for technical support. GR is

1673   grateful for the skillful technical support of M. Glockzin and B. Sadkowiak. MWJ thanks

1674   Anthony J. De-Gol for his technical and conceptual assistance with the development of GCP-

1675   GridFED. We thank Ana Bastos and Joana Melo for helpful comments on land-use emission

1676   estimates. FAOSTAT is funded by FAO member states through their contributions to the FAO

1677   Regular Programme, data contributions by national experts are greatly acknowledged. The

1678   views expressed in this paper are the authors' only and do not necessarily reflect those of

1679   FAO. Finally, we thank all funders who have supported the individual and joint contributions

1680   to this work (see Table A9), as well as the reviewers of this manuscript and previous versions,

1681   and the many researchers who have provided feedback.

10 References

Ahlström, A., Raupach, M. R., Schurgers, G., Smith, B., Arneth, A., Jung, M., Reichstein, M., Canadell, J. G., Friedlingstein, P., Jain, A. K., Kato, E., Poulter, B., Sitch, S., Stocker, B. D., Viovy, N., Wang, Y. P., Wiltshire, A., Zaehle, S., and Zeng, N.: The dominant role of semi-arid ecosystems in the trend and variability of the land CO2 sink, 348, 895–899, https://doi.org/10.1126/science.aaa1668, 2015.

Amador-Jiménez, M., Millner, N., Palmer, C., Pennington, R. T., and Sileci, L.: The Unintended Impact of Colombia's Covid-19 Lockdown on Forest Fires, Environ Resource Econ, 76, 1081–1105, https://doi.org/10.1007/s10640-020-00501-5, 2020.

Amante, C. and Eakins, B. W.: ETOPO1 Global Relief Model converted to PanMap layer format, https://doi.org/10.1594/PANGAEA.769615, 2009.

Andela, N., Morton, D. C., Giglio, L., Chen, Y., van der Werf, G. R., Kasibhatla, P. S., DeFries, R. S., Collatz, G. J., Hantson, S., Kloster, S., Bachelet, D., Forrest, M., Lasslop, G., Li, F., Mangeon, S., Melton, J. R., Yue, C., and Randerson, J. T.: A human-driven decline in global burned area, Science, 356, 1356–1362, https://doi.org/10.1126/science.aal4108, 2017.

Andres, R. J., Boden, T. A., Bréon, F.-M., Ciais, P., Davis, S., Erickson, D., Gregg, J. S., Jacobson, A., Marland, G., Miller, J., Oda, T., Olivier, J. G. J., Raupach, M. R., Rayner, P., and Treanton, K.: A synthesis of carbon dioxide emissions from fossil-fuel combustion, Biogeosciences, 9, 1845–1871, https://doi.org/10.5194/bg-9-1845-2012, 2012.

Andres, R. J., Boden, T. A., and Higdon, D.: A new evaluation of the uncertainty associated with CDIAC estimates of fossil fuel carbon dioxide emission, Tellus B: Chemical and Physical Meteorology, 66, 23616, https://doi.org/10.3402/tellusb.v66.23616, 2014.

Andrew, R. M.: A comparison of estimates of global carbon dioxide emissions from fossil carbon sources, Earth Syst. Sci. Data, 12, 1437–1465, https://doi.org/10.5194/essd-12-1437-2020, 2020a.

Andrew, R. M.: Timely estimates of India's annual and monthly fossil CO2 emissions, Earth Syst. Sci. Data, 12, 2411–2421, https://doi.org/10.5194/essd-12-2411-2020, 2020b.

Andrew, R. M.: Towards near real-time, monthly fossil CO2 emissions estimates for the

1710   European Union with current-year projections, Atmospheric Pollution Research, 101229,

1711   https://doi.org/10.1016/j.apr.2021.101229, 2021.

1712   Andrew, R. M. and Peters, G. P.: A multi-region input–output table based on the global trade

1713   analysis project database (GTAP-MRIO), Economic Systems Research, 25, 99–121,

1714   https://doi.org/10.1080/09535314.2012.761953, 2013.

1715   Andrew, R. M. and Peters, G. P.: The Global Carbon Project's fossil CO2 emissions dataset

1716   (2021v34), https://doi.org/10.5281/ZENODO.5569235, 2021.

1717   Aragão, L. E. O. C., Anderson, L. O., Fonseca, M. G., Rosan, T. M., Vedovato, L. B., Wagner, F.

1718   H., Silva, C. V. J., Silva Junior, C. H. L., Arai, E., Aguiar, A. P., Barlow, J., Berenguer, E., Deeter,

1719   M. N., Domingues, L. G., Gatti, L., Gloor, M., Malhi, Y., Marengo, J. A., Miller, J. B., Phillips, O.

1720   L., and Saatchi, S.: 21st Century drought-related fires counteract the decline of Amazon

1721   deforestation carbon emissions, Nat Commun, 9, 536, https://doi.org/10.1038/s41467-017-

1722   02771-y, 2018.

1723   Archer, D., Eby, M., Brovkin, V., Ridgwell, A., Cao, L., Mikolajewicz, U., Caldeira, K.,

1724   Matsumoto, K., Munhoven, G., Montenegro, A., and Tokos, K.: Atmospheric Lifetime of

1725   Fossil Fuel Carbon Dioxide, Annu. Rev. Earth Planet. Sci., 37, 117–134,

1726   https://doi.org/10.1146/annurev.earth.031208.100206, 2009.

1727   Arneth, A., Sitch, S., Pongratz, J., Stocker, B. D., Ciais, P., Poulter, B., Bayer, A. D., Bondeau,

1728   A., Calle, L., Chini, L. P., Gasser, T., Fader, M., Friedlingstein, P., Kato, E., Li, W., Lindeskog,

1729   M., Nabel, J. E. M. S., Pugh, T. A. M., Robertson, E., Viovy, N., Yue, C., and Zaehle, S.:

1730   Historical carbon dioxide emissions caused by land-use changes are possibly larger than

1731   assumed, Nature Geosci, 10, 79–84, https://doi.org/10.1038/ngeo2882, 2017.

1732   Arora, V. K., Boer, G. J., Christian, J. R., Curry, C. L., Denman, K. L., Zahariev, K., Flato, G. M.,

1733   Scinocca, J. F., Merryfield, W. J., and Lee, W. G.: The Effect of Terrestrial Photosynthesis

1734   Down Regulation on the Twentieth-Century Carbon Budget Simulated with the CCCma Earth

1735   System Model, 22, 6066–6088, https://doi.org/10.1175/2009JCLI3037.1, 2009.

1736   Asaadi, A., Arora, V. K., Melton, J. R., and Bartlett, P.: An improved parameterization of leaf

1737   area index (LAI) seasonality in the Canadian Land Surface Scheme (CLASS) and Canadian

1738 Terrestrial Ecosystem Model (CTEM) modelling framework, 15, 6885–6907,

1739 https://doi.org/10.5194/bg-15-6885-2018, 2018.

1740 Aumont, O., Orr, J. C., Monfray, P., Ludwig, W., Amiotte-Suchet, P., and Probst, J.-L.:

1741 Riverine-driven interhemispheric transport of carbon, Global Biogeochem. Cycles, 15, 393–

1742 405, https://doi.org/10.1029/1999GB001238, 2001.

1743 Aumont, O., Ethé, C., Tagliabue, A., Bopp, L., and Gehlen, M.: PISCES-v2: an ocean

1744 biogeochemical model for carbon and ecosystem studies, 8, 2465–2513,

1745 https://doi.org/10.5194/gmd-8-2465-2015, 2015.

1746 Avitabile, V., Herold, M., Heuvelink, G. B. M., Lewis, S. L., Phillips, O. L., Asner, G. P.,

1747 Armston, J., Ashton, P. S., Banin, L., Bayol, N., Berry, N. J., Boeckx, P., de Jong, B. H. J.,

1748 DeVries, B., Girardin, C. A. J., Kearsley, E., Lindsell, J. A., Lopez-Gonzalez, G., Lucas, R., Malhi,

1749 Y., Morel, A., Mitchard, E. T. A., Nagy, L., Qie, L., Quinones, M. J., Ryan, C. M., Ferry, S. J. W.,

1750 Sunderland, T., Laurin, G. V., Gatti, R. C., Valentini, R., Verbeeck, H., Wijaya, A., and Willcock,

1751 S.: An integrated pan-tropical biomass map using multiple reference datasets, Glob Change

1752 Biol, 22, 1406–1420, https://doi.org/10.1111/gcb.13139, 2016.

1753 Baccini, A., Walker, W., Carvalho, L., Farina, M., Sulla-Menashe, D., and Houghton, R. A.:

1754 Tropical forests are a net carbon source based on aboveground measurements of gain and

1755 loss, Science, 358, 230–234, https://doi.org/10.1126/science.aam5962, 2017.

1756 Bakker, D. C. E., Pfeil, B., Landa, C. S., Metzl, N., O'Brien, K. M., Olsen, A., Smith, K., Cosca, C.,

1757 Harasawa, S., Jones, S. D., Nakaoka, S., Nojiri, Y., Schuster, U., Steinhoff, T., Sweeney, C.,

1758 Takahashi, T., Tilbrook, B., Wada, C., Wanninkhof, R., Alin, S. R., Balestrini, C. F., Barbero, L.,

1759 Bates, N. R., Bianchi, A. A., Bonou, F., Boutin, J., Bozec, Y., Burger, E. F., Cai, W.-J., Castle, R.

1760 D., Chen, L., Chierici, M., Currie, K., Evans, W., Featherstone, C., Feely, R. A., Fransson, A.,

1761 Goyet, C., Greenwood, N., Gregor, L., Hankin, S., Hardman-Mountford, N. J., Harlay, J.,

1762 Hauck, J., Hoppema, M., Humphreys, M. P., Hunt, C. W., Huss, B., Ibánhez, J. S. P.,

1763 Johannessen, T., Keeling, R., Kitidis, V., Körtzinger, A., Kozyr, A., Krasakopoulou, E., Kuwata,

1764 A., Landschützer, P., Lauvset, S. K., Lefèvre, N., Lo Monaco, C., Manke, A., Mathis, J. T.,

1765 Merlivat, L., Millero, F. J., Monteiro, P. M. S., Munro, D. R., Murata, A., Newberger, T., Omar,

1766 A. M., Ono, T., Paterson, K., Pearce, D., Pierrot, D., Robbins, L. L., Saito, S., Salisbury, J.,

1767   Schlitzer, R., Schneider, B., Schweitzer, R., Sieger, R., Skjelvan, I., Sullivan, K. F., Sutherland,

1768   S. C., Sutton, A. J., Tadokoro, K., Telszewski, M., Tuma, M., van Heuven, S. M. A. C.,

1769   Vandemark, D., Ward, B., Watson, A. J., and Xu, S.: A multi-decade record of high-quality

1770   CO2 data in version 3 of the Surface Ocean CO2 Atlas (SOCAT), Earth Syst. Sci. Data, 8, 383–

1771   413, https://doi.org/10.5194/essd-8-383-2016, 2016.

1772   Bakker, D. C. E., Alin, S. R., Castaño-Primo, R., Cronin, M., Gkritzalis, T., Kozyr, A., Lauvset, S.

1773   K., Metzl, N., Munro, D. R., Nakaoka, S.-I., O'Brien, K. M., Olsen, A., Omar, A. M., Pfeil, B.,

1774   Pierrot, D., Rodriguez, C., Steinhoff, T., Sutton, A. J., Tilbrook, B., Wanninkhof, R., Willstrand

1775   Wranne, A., Ahmed, M., Andersson, A., Apelthun, L. B., Bates, N., Battisti, R., Beaumont, L.,

1776   Becker, M., Benoit-Cattin, A., Berghoff, C. F., Boutin, J., Burger, E. F., Burgers, T. M., Cantoni,

1777   C., Cattrijsse, A., Chierici, M., Cross, J. N., Coppola, L., Cosca, C. E., Currie, K. I., De Carlo, E.

1778   H., Else, B., Enright, M. P., Ericson, Y., Evans, W., Feely, R. A., Fiedler, B., Fransson, A., García-

1779   Ibáñez, M. I., Gehrung, M., Glockzin, M., González Dávila, M., Gutekunst, S., Hermes, R.,

1780   Humphreys, M. P., Hunt, C. W., Ibánhez, J. S. P., Jones, S. D., Kitidis, V., Körtzinger, A.,

1781   Kosugi, N., Landa, C. S., Landschützer, P., Lefèvre, N., Lo Monaco, C., Luchetta, A., Lutz, V. A.,

1782   Macovei, V. A., Manke, A. B., Merlivat, L., Millero, F. J., Monacci, N. M., Negri, R. M.,

1783   Newberger, T., Newton, J., Nickford, S. E., Nojiri, Y., Ohman, M., Ólafsdóttir, S. R., Sweeney,

1784   C., Ono, T., Palter, J. B., Papakyriakou, T., Peterson, W. T., Plueddemann, A. J., Qi, D.,

1785   Rehder, G., Ritschel, M., Rutgersson, A., Sabine, C. L., Salisbury, J. E., Santana-Casiano, J. M.,

1786   Schlitzer, R., Send, U., Skjelvan, I., Smith, K., Sparnocchia, S., Sullivan, K. F., Sutherland, S. C.,

1787   et al.: Surface Ocean CO2 Atlas Database Version 2021 (SOCATv2021) (NCEI Accession

1788   0235360), https://doi.org/10.25921/YG69-JD96, 2021.

1789   Ballantyne, A. P., Alden, C. B., Miller, J. B., Tans, P. P., and White, J. W. C.: Increase in

1790   observed net carbon dioxide uptake by land and oceans during the past 50 years, Nature,

1791   488, 70–72, https://doi.org/10.1038/nature11299, 2012.

1792   Ballantyne, A. P., Andres, R., Houghton, R., Stocker, B. D., Wanninkhof, R., Anderegg, W.,

1793   Cooper, L. A., DeGrandpre, M., Tans, P. P., Miller, J. B., Alden, C., and White, J. W. C.: Audit

1794   of the global carbon budget: estimate errors and their impact on uptake uncertainty,

1795   Biogeosciences, 12, 2565–2584, https://doi.org/10.5194/bg-12-2565-2015, 2015.

1796   Bastos, A., O'Sullivan, M., Ciais, P., Makowski, D., Sitch, S., Friedlingstein, P., Chevallier, F.,

1797 Rödenbeck, C., Pongratz, J., Luijkx, I. T., Patra, P. K., Peylin, P., Canadell, J. G., Lauerwald, R.,
1798 Li, W., Smith, N. E., Peters, W., Goll, D. S., Jain, A. K., Kato, E., Lienert, S., Lombardozzi, D. L.,
1799 Haverd, V., Nabel, J. E. M. S., Poulter, B., Tian, H., Walker, A. P., and Zaehle, S.: Sources of
1800 Uncertainty in Regional and Global Terrestrial CO_2 Exchange Estimates, Global Biogeochem.
1801 Cycles, 34, https://doi.org/10.1029/2019GB006393, 2020.

1802 Bastos, A., Hartung, K., Nützel, T. B., Nabel, J. E. M. S., Houghton, R. A., and Pongratz, J.:
1803 Comparison of uncertainties in land-use change fluxes from bookkeeping model
1804 parameterisation, 12, 745–762, https://doi.org/10.5194/esd-12-745-2021, 2021.

1805 Basu, S., Baker, D. F., Chevallier, F., Patra, P. K., Liu, J., and Miller, J. B.: The impact of
1806 transport model differences on CO2 surface flux estimates from OCO-2 retrievals of column
1807 average CO2, Atmos. Chem. Phys., 18, 7189–7215, https://doi.org/10.5194/acp-18-7189-
1808 2018, 2018.

1809 Bauer, J. E., Cai, W.-J., Raymond, P. A., Bianchi, T. S., Hopkinson, C. S., and Regnier, P. A. G.:
1810 The changing carbon cycle of the coastal ocean, Nature, 504, 61–70,
1811 https://doi.org/10.1038/nature12857, 2013.

1812 Beckman, J. and Countryman, A. M.: The Importance of Agriculture in the Economy: Impacts
1813 from COVID-19, 103, 1595–1611, https://doi.org/10.1111/ajae.12212, 2021.

1814 Bellouin, N., Rae, J., Jones, A., Johnson, C., Haywood, J., and Boucher, O.: Aerosol forcing in
1815 the Climate Model Intercomparison Project (CMIP5) simulations by HadGEM2-ES and the
1816 role of ammonium nitrate, 116, https://doi.org/10.1029/2011JD016074, 2011.

1817 Berthet, S., Séférian, R., Bricaud, C., Chevallier, M., Voldoire, A., and Ethé, C.: Evaluation of
1818 an Online Grid-Coarsening Algorithm in a Global Eddy-Admitting Ocean Biogeochemical
1819 Model, 11, 1759–1783, https://doi.org/10.1029/2019MS001644, 2019.

1820 Brancalion, P. H. S., Broadbent, E. N., de-Miguel, S., Cardil, A., Rosa, M. R., Almeida, C. T.,
1821 Almeida, D. R. A., Chakravarty, S., Zhou, M., Gamarra, J. G. P., Liang, J., Crouzeilles, R.,
1822 Hérault, B., Aragão, L. E. O. C., Silva, C. A., and Almeyda-Zambrano, A. M.: Emerging threats
1823 linking tropical deforestation and the COVID-19 pandemic, Perspectives in Ecology and
1824 Conservation, 18, 243–246, https://doi.org/10.1016/j.pecon.2020.09.006, 2020.

1825   Brienen, R. J. W., Phillips, O. L., Feldpausch, T. R., Gloor, E., Baker, T. R., Lloyd, J., Lopez-

1826   Gonzalez, G., Monteagudo-Mendoza, A., Malhi, Y., Lewis, S. L., Vásquez Martinez, R.,

1827   Alexiades, M., Álvarez Dávila, E., Alvarez-Loayza, P., Andrade, A., Aragão, L. E. O. C., Araujo-

1828   Murakami, A., Arets, E. J. M. M., Arroyo, L., Aymard C., G. A., Bánki, O. S., Baraloto, C.,

1829   Barroso, J., Bonal, D., Boot, R. G. A., Camargo, J. L. C., Castilho, C. V., Chama, V., Chao, K. J.,

1830   Chave, J., Comiskey, J. A., Cornejo Valverde, F., da Costa, L., de Oliveira, E. A., Di Fiore, A.,

1831   Erwin, T. L., Fauset, S., Forsthofer, M., Galbraith, D. R., Grahame, E. S., Groot, N., Hérault, B.,

1832   Higuchi, N., Honorio Coronado, E. N., Keeling, H., Killeen, T. J., Laurance, W. F., Laurance, S.,

1833   Licona, J., Magnussen, W. E., Marimon, B. S., Marimon-Junior, B. H., Mendoza, C., Neill, D.

1834   A., Nogueira, E. M., Núñez, P., Pallqui Camacho, N. C., Parada, A., Pardo-Molina, G., Peacock,

1835   J., Peña-Claros, M., Pickavance, G. C., Pitman, N. C. A., Poorter, L., Prieto, A., Quesada, C. A.,

1836   Ramírez, F., Ramírez-Angulo, H., Restrepo, Z., Roopsind, A., Rudas, A., Salomão, R. P.,

1837   Schwarz, M., Silva, N., Silva-Espejo, J. E., Silveira, M., Stropp, J., Talbot, J., ter Steege, H.,

1838   Teran-Aguilar, J., Terborgh, J., Thomas-Caesar, R., Toledo, M., Torello-Raventos, M., Umetsu,

1839   R. K., van der Heijden, G. M. F., van der Hout, P., Guimarães Vieira, I. C., Vieira, S. A.,

1840   Vilanova, E., Vos, V. A., and Zagt, R. J.: Long-term decline of the Amazon carbon sink, 519,

1841   344–348, https://doi.org/10.1038/nature14283, 2015.

1842   Broecker, W. S.: Ocean chemistry during glacial time, Geochimica et Cosmochimica Acta, 46,

1843   1689–1705, https://doi.org/10.1016/0016-7037(82)90110-7, 1982.

1844   Bruno, M. and Joos, F.: Terrestrial carbon storage during the past 200 years: A Monte Carlo

1845   Analysis of CO_2 data from ice core and atmospheric measurements, Global Biogeochem.

1846   Cycles, 11, 111–124, https://doi.org/10.1029/96GB03611, 1997.

1847   Buitenhuis, E. T., Hashioka, T., and Quéré, C. L.: Combined constraints on global ocean

1848   primary production using observations and models: OCEAN PRIMARY PRODUCTION, Global

1849   Biogeochem. Cycles, 27, 847–858, https://doi.org/10.1002/gbc.20074, 2013.

1850   Burton, C., Betts, R., Cardoso, M., Feldpausch, T. R., Harper, A., Jones, C. D., Kelley, D. I.,

1851   Robertson, E., and Wiltshire, A.: Representation of fire, land-use change and vegetation

1852   dynamics in the Joint UK Land Environment Simulator vn4.9 (JULES), Geosci. Model Dev., 12,

1853   179–193, https://doi.org/10.5194/gmd-12-179-2019, 2019.

1854 Bushinsky, S. M., Landschützer, P., Rödenbeck, C., Gray, A. R., Baker, D., Mazloff, M. R.,

1855 Resplandy, L., Johnson, K. S., and Sarmiento, J. L.: Reassessing Southern Ocean Air-Sea CO 2

1856 Flux Estimates With the Addition of Biogeochemical Float Observations, Global Biogeochem.

1857 Cycles, 33, 1370–1388, https://doi.org/10.1029/2019GB006176, 2019.

1858 Canadell, J. G., Le Quere, C., Raupach, M. R., Field, C. B., Buitenhuis, E. T., Ciais, P., Conway,

1859 T. J., Gillett, N. P., Houghton, R. A., and Marland, G.: Contributions to accelerating

1860 atmospheric CO2 growth from economic activity, carbon intensity, and efficiency of natural

1861 sinks, Proceedings of the National Academy of Sciences, 104, 18866–18870,

1862 https://doi.org/10.1073/pnas.0702737104, 2007.

1863 Canadell, J. G., Monteiro, P. M. S., Costa, M. H., Cotrim da Cunha, L., Cox, P. M., Eliseev, A.

1864 V., Henson, S., Ishii, M., Jaccard, S., Koven, C., Lohila, A., Patra, P. K., Piao, S., Rogelj, J.,

1865 Syampungani, S., Zaehle, S., and Zickfeld, K.: Global Carbon and other Biogeochemical Cycles

1866 and Feedbacks. In: Climate Change 2021: The Physical Science Basis. Contribution of

1867 Working Group I to the Sixth Assessment Report of the Intergovernmental Panel on Climate

1868 Change [Masson-Delmotte, V., P. Zhai, A. Pirani, S. L. Connors, C. Péan, S. Berger, N. Caud, Y.

1869 Chen, L. Goldfarb, M. I. Gomis, M. Huang, K. Leitzell, E. Lonnoy, J.B.R. Matthews, T. K.

1870 Maycock, T. Waterfield, O. Yelekçi, R. Yu and B. Zhou (eds.)]. Cambridge University Press. In

1871 Press., 2021.

1872 Cao, Z., Myers, R. J., Lupton, R. C., Duan, H., Sacchi, R., Zhou, N., Reed Miller, T., Cullen, J.

1873 M., Ge, Q., and Liu, G.: The sponge effect and carbon emission mitigation potentials of the

1874 global cement cycle, Nat Commun, 11, 3777, https://doi.org/10.1038/s41467-020-17583-w,

1875 2020.

1876 Carbon Monitor: CO$_2$ Emissions Variation, available at: https://carbonmonitor.org/, last

1877 access: 11 March 2022., 2022.

1878 Chatfield, C.: The Holt-Winters Forecasting Procedure, 27, 264–279,

1879 https://doi.org/10.2307/2347162, 1978.

1880 Chau, T. T. T., Gehlen, M., and Chevallier, F.: QUALITY INFORMATION DOCUMENT for Global

1881 Ocean Surface Carbon Product MULTIOBS_GLO_BIO_CARBON_SURFACE_REP_015_008, Le

1882 Laboratoire des Sciences du Climat et de l'Environnement, 2020.

1883   Chau, T. T. T., Gehlen, M., and Chevallier, F.: A seamless ensemble-based reconstruction of

1884   surface ocean pCO2 and air-sea CO2 fluxes over the global coastal and open oceans, 1–30,

1885   https://doi.org/10.5194/bg-2021-207, 2021.

1886   Chevallier, F.: On the parallelization of atmospheric inversions of CO2 surface fluxes within a

1887   variational framework, 6, 783–790, https://doi.org/10.5194/gmd-6-783-2013, 2013.

1888   Chevallier, F., Fisher, M., Peylin, P., Serrar, S., Bousquet, P., Bréon, F.-M., Chédin, A., and

1889   Ciais, P.: Inferring CO 2 sources and sinks from satellite observations: Method and

1890   application to TOVS data, J. Geophys. Res., 110, D24309,

1891   https://doi.org/10.1029/2005JD006390, 2005.

1892   Chevallier, F., Remaud, M., O'Dell, C. W., Baker, D., Peylin, P., and Cozic, A.: Objective

1893   evaluation of surface- and satellite-driven carbon dioxide atmospheric inversions, Atmos.

1894   Chem. Phys., 19, 14233–14251, https://doi.org/10.5194/acp-19-14233-2019, 2019.

1895   Chini, L., Hurtt, G., Sahajpal, R., Frolking, S., Klein Goldewijk, K., Sitch, S., Ganzenmüller, R.,

1896   Ma, L., Ott, L., Pongratz, J., and Poulter, B.: Land-use harmonization datasets for annual

1897   global carbon budgets, 13, 4175–4189, https://doi.org/10.5194/essd-13-4175-2021, 2021.

1898   Ciais, P., Sabine, C., Bala, G., Bopp, L., Brovkin, V., Canadell, J. G., Chhabra, A., DeFries, R.,

1899   Galloway, J., Heimann, M., Jones, C., Le Quéré, C., Myneni, R., Piao, S., Thornton, P., Willem,

1900   J., Friedlingstein, P., and Munhoven, G.: Carbon and Other Biogeochemical Cycles, in Climate

1901   Change 2013: The Physical Science Basis, Contribution of Working Group I to the Fifth

1902   Assessment Report of the Intergovernmental Panel on Climate Change, edited by:

1903   Intergovernmental Panel on Climate Change, Cambridge University Press, Cambridge, UK,

1904   465–570, 2013.

1905   Ciais, P., Tan, J., Wang, X., Roedenbeck, C., Chevallier, F., Piao, S.-L., Moriarty, R., Broquet,

1906   G., Le Quéré, C., Canadell, J. G., Peng, S., Poulter, B., Liu, Z., and Tans, P.: Five decades of

1907   northern land carbon uptake revealed by the interhemispheric CO2 gradient, Nature, 568,

1908   221–225, https://doi.org/10.1038/s41586-019-1078-6, 2019.

1909   Ciais, P., Bastos, A., Chevallier, F., Lauerwald, R., Poulter, B., Canadell, P., Hugelius, G.,

1910   Jackson, R. B., Jain, A., Jones, M., Kondo, M., Luijkx, I., Patra, P. K., Peters, W., Pongratz, J.,

1911   Petrescu, A. M. R., Piao, S., Qiu, C., Von Randow, C., Regnier, P., Saunois, M., Scholes, R.,

1912   Shvidenko, A., Tian, H., Yang, H., Wang, X., and Zheng, B.: Definitions and methods to

1913   estimate regional land carbon fluxes for the second phase of the REgional Carbon Cycle

1914   Assessment and Processes Project (RECCAP-2), 1–46, https://doi.org/10.5194/gmd-2020-

1915   259, 2020.

1916   Collier, N., Hoffman, F. M., Lawrence, D. M., Keppel-Aleks, G., Koven, C. D., Riley, W. J., Mu,

1917   M., and Randerson, J. T.: The International Land Model Benchmarking (ILAMB) System:

1918   Design, Theory, and Implementation, J. Adv. Model. Earth Syst., 10, 2731–2754,

1919   https://doi.org/10.1029/2018MS001354, 2018.

1920   Conchedda, G. and Tubiello, F. N.: Drainage of organic soils and GHG emissions: Validation

1921   with country data, Biosphere – Biogeosciences, https://doi.org/10.5194/essd-2020-202,

1922   2020.

1923   Cooper, D. J., Watson, A. J., and Ling, R. D.: Variation of pCO2 along a North Atlantic shipping

1924   route (U.K. to the Caribbean): A year of automated observations, Marine Chemistry, 60,

1925   147–164, https://doi.org/10.1016/S0304-4203(97)00082-0, 1998.

1926   Cox, A., Vermeulen, A., Manning, A., Beyersdorf, A., Zahn, A., Manning, A., Watson, A.,

1927   Karion, A., Hensen, A., Arlyn Andrews, Frumau, A., Colomb, A., Scheeren, B., Law, B., Baier,

1928   B., Munger, B., Paplawsky, B., Viner, B., Stephens, B., Daube, B., Labuschagne, C., Myhre, C.

1929   L., Hanson, C., Miller, C. E., Plass-Duelmer, C., Plass-Duelmer, C., Gerbig, C., Sloop, C. D.,

1930   Sweeney, C., Kubistin, D., Goto, D., Jaffe, D., Say, D., Van Dinther, D., Bowling, D., Lam, D. H.

1931   Y., Dickon Young, Worthy, D., Dlugokencky, E., Kozlova, E., Gloor, E., Cuevas, E., Reyes-

1932   Sanchez, E., Hintsa, E., Kort, E., Morgan, E., Obersteiner, F., Apadula, F., Francois Gheusi,

1933   Meinhardt, F., Moore, F., Vitkova, G., Chen, G., Bentz, G., Manca, G., Brailsford, G., Forster,

1934   G., Boenisch, H., Riris, H., Meijer, H., Timas, H., Matsueda, H., Huilin Chen, Levin, I., Lehner,

1935   I., Mammarella, I., Bartyzel, J., Abshire, J. B., Elkins, J. W., Levula, J., Jaroslaw Necki, Pichon,

1936   J. M., Peischl, J., Müller-Williams, J., Turnbull, J., Miller, J. B., Lee, J., Lin, J., Josep-Anton

1937   Morgui, DiGangi, J. P., Hatakka, J., Coletta, J. D., Worsey, J., Holst, J., Kominkova, K., McKain,

1938   K., Saito, K., Aikin, K., Davis, K., Thoning, K., Tørseth, K., Haszpra, L., Mitchell, L., Gatti, L. V.,

1939   Emmenegger, L., Lukasz Chmura, Merchant, L., Sha, M. K., Delmotte, M., et al.: Multi-

1940   laboratory compilation of atmospheric carbon dioxide data for the period 1957-2019;

1941   obspack_co2_1_GLOBALVIEWplus_v6.1_2021-03-01, https://doi.org/10.25925/20201204,

1942   2021.

1943   Cox, P. M., Pearson, D., Booth, B. B., Friedlingstein, P., Huntingford, C., Jones, C. D., and

1944   Luke, C. M.: Sensitivity of tropical carbon to climate change constrained by carbon dioxide

1945   variability, Nature, 494, 341–344, https://doi.org/10.1038/nature11882, 2013.

1946   Crippa, M., Janssens-Maenhout, G., Guizzardi, D., Van Dingenen, R., and Dentener, F.:

1947   Contribution and uncertainty of sectorial and regional emissions to regional and global

1948   PM2.5 health impacts, 19, 5165–5186, https://doi.org/10.5194/acp-19-5165-2019, 2019.

1949   Dai, A. and Trenberth, K. E.: Estimates of Freshwater Discharge from Continents: Latitudinal

1950   and Seasonal Variations, 3, 660–687, https://doi.org/10.1175/1525-

1951   7541(2002)003<0660:EOFDFC>2.0.CO;2, 2002.

1952   Davis, S. J. and Caldeira, K.: Consumption-based accounting of CO_2 emissions, Proceedings

1953   of the National Academy of Sciences, 107, 5687–5692,

1954   https://doi.org/10.1073/pnas.0906974107, 2010.

1955   De Kauwe, M. G., Disney, M. I., Quaife, T., Lewis, P., and Williams, M.: An assessment of the

1956   MODIS collection 5 leaf area index product for a region of mixed coniferous forest, Remote

1957   Sensing of Environment, 115, 767–780, https://doi.org/10.1016/j.rse.2010.11.004, 2011.

1958   Decharme, B., Delire, C., Minvielle, M., Colin, J., Vergnes, J.-P., Alias, A., Saint-Martin, D.,

1959   Séférian, R., Sénési, S., and Voldoire, A.: Recent Changes in the ISBA-CTRIP Land Surface

1960   System for Use in the CNRM-CM6 Climate Model and in Global Off-Line Hydrological

1961   Applications, 11, 1207–1252, https://doi.org/10.1029/2018MS001545, 2019.

1962   Delire, C., Séférian, R., Decharme, B., Alkama, R., Calvet, J.-C., Carrer, D., Gibelin, A.-L.,

1963   Joetzjer, E., Morel, X., Rocher, M., and Tzanos, D.: The Global Land Carbon Cycle Simulated

1964   With ISBA-CTRIP: Improvements Over the Last Decade, 12, e2019MS001886,

1965   https://doi.org/10.1029/2019MS001886, 2020.

1966   Denman, K. L., Brasseur, G., Chidthaisong, A., Ciais, P., Cox, P. M., Dickinson, R. E.,

1967   Hauglustaine, D., Heinze, C., Holland, E., Jacob, D., Lohmann, U., Ramachandran, S., Leite da

1968   Silva Dias, P., Wofsy, S. C., and Zhang, X.: Couplings Between Changes in the Climate System

1969   and Biogeochemistry, in: Climate Change 2007: The Physical Science Basis. Contribution of

1970   Working Group I to the Fourth Assessment Report of the Intergovernmental Panel on

1971   Climate Change, edited by: Solomon, S., Qin, D., Manning, M., Marquis, M., Averyt, K.,

1972   Tignor, M. M. B., Miller, H. L., and Chen, Z. L., Cambridge University Press, Cambridge, UK

1973   and New York, USA, 499–587, 2007.

1974   Denning, A. S., Fung, I. Y., and Randall, D.: Latitudinal gradient of atmospheric CO_2 due to

1975   seasonal exchange with land biota, Nature, 376, 240–243,

1976   https://doi.org/10.1038/376240a0, 1995.

1977   Denvil-Sommer, A., Gehlen, M., Vrac, M., and Mejia, C.: LSCE-FFNN-v1: a two-step neural

1978   network model for the reconstruction of surface ocean pCO_2 over the global ocean, 12,

1979   2091–2105, https://doi.org/10.5194/gmd-12-2091-2019, 2019.

1980   DeVries, T.: The oceanic anthropogenic CO_2 sink: Storage, air-sea fluxes, and transports

1981   over the industrial era, Global Biogeochem. Cycles, 28, 631–647,

1982   https://doi.org/10.1002/2013GB004739, 2014.

1983   DeVries, T., Holzer, M., and Primeau, F.: Recent increase in oceanic carbon uptake driven by

1984   weaker upper-ocean overturning, Nature, 542, 215–218,

1985   https://doi.org/10.1038/nature21068, 2017.

1986   DeVries, T., Quéré, C. L., Andrews, O., Berthet, S., Hauck, J., Ilyina, T., Landschützer, P.,

1987   Lenton, A., Lima, I. D., Nowicki, M., Schwinger, J., and Séférian, R.: Decadal trends in the

1988   ocean carbon sink, PNAS, 116, 11646–11651, https://doi.org/10.1073/pnas.1900371116,

1989   2019.

1990   Di Sarra, A. G., Karion, A., Arlyn Andrews, Colomb, A., Scheeren, B., Viner, B., Myhre, C. L.,

1991   Miller, C. E., Plass-Duelmer, C., Plass-Duelmer, C., Sloop, C. D., Sweeney, C., Kubistin, D.,

1992   Jaffe, D., Dlugokencky, E., Vitkova, G., Manca, G., Huilin Chen, Lehner, I., Mammarella, I.,

1993   Pichon, J. M., Müller-Williams, J., Miller, J. B., Lee, J., Hatakka, J., Holst, J., Kominkova, K.,

1994   McKain, K., Thoning, K., Tørseth, K., Emmenegger, L., Sha, M. K., Delmotte, M., Fischer, M.

1995   L., Schumacher, M., Leuenberger, M., Steinbacher, M., De Mazière, M., Lindauer, M.,

1996   Mölder, M., Heliasz, M., Marek, M. V., Ramonet, M., Lopez, M., Laurent, O., Hermanssen, O.,

1997   Trisolino, P., Cristofanelli, P., Smith, P., Bakwin, P., Bergamaschi, P., Keronen, P., Tans, P.,

1998   Piacentino, S., Biraud, S. C., Conil, S., De Wekker, S., Biermann, T., Laurila, T., Aalto, T., and

1999   Kazan, V.: Multi-laboratory compilation of atmospheric carbon dioxide data for the years

2000   2020-2021; obspack_co2_1_NRT_v6.1.1_2021-05-17, https://doi.org/10.25925/20210517,

2001   2021.

2002   Dickson, A. G., Sabine, C. L., and Christian, J. R.: Guide to best practices for ocean CO_2

2003   measurement. Sidney, British Columbia, North Pacific Marine Science Organization, 191pp.

2004   (PICES Special Publication 3; IOCCP Report 8). DOI: https://doi.org/10.25607/OBP-1342,

2005   2007.

2006   Dlugokencky, E. and Tans, P.: Trends in atmospheric carbon dioxide, National Oceanic and

2007   Atmospheric Administration, Earth System Research Laboratory (NOAA/ESRL), available at:

2008   http://www.esrl.noaa.gov/gmd/ccgg/trends/global.html, accessed: 16 November 2020.,

2009   2020.

2010   Dlugokencky, E. and Tans, P.: Trends in atmospheric carbon dioxide, National Oceanic and

2011   Atmospheric Administration, Earth System Research Laboratory (NOAA/ESRL), available at:

2012   http://www.esrl.noaa.gov/gmd/ccgg/trends/global.html, last access: 11 March 2022., 2022.

2013   Doney, S. C., Lima, I., Feely, R. A., Glover, D. M., Lindsay, K., Mahowald, N., Moore, J. K., and

2014   Wanninkhof, R.: Mechanisms governing interannual variability in upper-ocean inorganic

2015   carbon system and air–sea CO_2 fluxes: Physical climate and atmospheric dust, Deep Sea

2016   Research Part II: Topical Studies in Oceanography, 56, 640–655,

2017   https://doi.org/10.1016/j.dsr2.2008.12.006, 2009.

2018   Duce, R. A., LaRoche, J., Altieri, K., Arrigo, K. R., Baker, A. R., Capone, D. G., Cornell, S.,

2019   Dentener, F., Galloway, J., Ganeshram, R. S., Geider, R. J., Jickells, T., Kuypers, M. M.,

2020   Langlois, R., Liss, P. S., Liu, S. M., Middelburg, J. J., Moore, C. M., Nickovic, S., Oschlies, A.,

2021   Pedersen, T., Prospero, J., Schlitzer, R., Seitzinger, S., Sorensen, L. L., Uematsu, M., Ulloa, O.,

2022   Voss, M., Ward, B., and Zamora, L.: Impacts of Atmospheric Anthropogenic Nitrogen on the

2023   Open Ocean, Science, 320, 893–897, https://doi.org/10.1126/science.1150369, 2008.

2024   Dufour, C. O., Sommer, J. L., Gehlen, M., Orr, J. C., Molines, J., Simeon, J., and Barnier, B.:

2025   Eddy compensation and controls of the enhanced sea-to-air CO_2 flux during positive phases

2026   of the Southern Annular Mode, Global Biogeochem. Cycles, 27, 950–961,

2027   https://doi.org/10.1002/gbc.20090, 2013.

2028   Eakins, B. W. and Sharman, G. F.: National Geophysical Data Center: Volumes of the World's
2029   Oceans from ETOPO1, available at:
2030   https://www.ngdc.noaa.gov/mgg/global/etopo1_ocean_volumes.html, last access: 11
2031   March 2022, U.S. Department of Commerce, 2010.

2032   Eggleston, H. S., Buendia, L., Miwa, K., Ngara, T., and Tanabe, K.: Volume 4: Agriculture,
2033   forestry and land use. in: 2006 IPCC guidelines for national greenhouse gas inventories.,
2034   2006.

2035   EIA: U.S. Energy Information Administration: Short-Term Energy Outlook, available at:
2036   http://www.eia.gov/forecasts/steo/outlook, last access: 11 March 2022., 2022.

2037   Erb, K.-H., Kastner, T., Luyssaert, S., Houghton, R. A., Kuemmerle, T., Olofsson, P., and
2038   Haberl, H.: Bias in the attribution of forest carbon sinks, Nature Clim Change, 3, 854–856,
2039   https://doi.org/10.1038/nclimate2004, 2013.

2040   Erb, K.-H., Kastner, T., Plutzar, C., Bais, A. L. S., Carvalhais, N., Fetzel, T., Gingrich, S., Haberl,
2041   H., Lauk, C., Niedertscheider, M., Pongratz, J., Thurner, M., and Luyssaert, S.: Unexpectedly
2042   large impact of forest management and grazing on global vegetation biomass, Nature, 553,
2043   73–76, https://doi.org/10.1038/nature25138, 2018.

2044   Eskander, S. M. S. U. and Fankhauser, S.: Reduction in greenhouse gas emissions from
2045   national climate legislation, Nat. Clim. Chang., 10, 750–756,
2046   https://doi.org/10.1038/s41558-020-0831-z, 2020.

2047   Etheridge, D. M., Steele, L. P., Langenfelds, R. L., Francey, R. J., Barnola, J.-M., and Morgan,
2048   V. I.: Natural and anthropogenic changes in atmospheric CO_2 over the last 1000 years from
2049   air in Antarctic ice and firn, J. Geophys. Res., 101, 4115–4128,
2050   https://doi.org/10.1029/95JD03410, 1996.

2051   Eyring, V., Bony, S., Meehl, G. A., Senior, C. A., Stevens, B., Stouffer, R. J., and Taylor, K. E.:
2052   Overview of the Coupled Model Intercomparison Project Phase 6 (CMIP6) experimental
2053   design and organization, Geosci. Model Dev., 9, 1937–1958, https://doi.org/10.5194/gmd-9-
2054   1937-2016, 2016.

2055   FAO: Global Forest Resources Assessment 2020: Main report, FAO, Rome, Italy, 184 pp.,

2056   https://doi.org/10.4060/ca9825en, 2020.

2057   FAO: FAOSTAT Statistical Database, domains Climate Change, available at:

2058   http://www.fao.org/faostat/en/#data/GT, last accessed: 11 March 2022, 2021.

2059   FAOSTAT: FAOSTAT: Food and Agriculture Organization Statistics Division, available at:

2060   http://faostat.fao.org/, last access: 11 March 2022), 2021.

2061   FAO/UNEP: Food and Agriculture Organisation / United Nations Environment Programme:

2062   The state of food and agriculture 1981, available at:

2063   https://www.fao.org/3/ap661e/ap661e.pdf, last access: 11 March 2022, 1981.

2064   Fan, L., Wigneron, J.-P., Ciais, P., Chave, J., Brandt, M., Fensholt, R., Saatchi, S. S., Bastos, A.,

2065   Al-Yaari, A., Hufkens, K., Qin, Y., Xiao, X., Chen, C., Myneni, R. B., Fernandez-Moran, R.,

2066   Mialon, A., Rodriguez-Fernandez, N. J., Kerr, Y., Tian, F., and Peñuelas, J.: Satellite-observed

2067   pantropical carbon dynamics, Nat. Plants, 5, 944–951, https://doi.org/10.1038/s41477-019-

2068   0478-9, 2019.

2069   Fay, A. R. and McKinley, G. A.: Global open-ocean biomes: mean and temporal variability, 6,

2070   273–284, https://doi.org/10.5194/essd-6-273-2014, 2014.

2071   Fay, A. R., Gregor, L., Landschützer, P., McKinley, G. A., Gruber, N., Gehlen, M., Iida, Y.,

2072   Laruelle, G. G., Rödenbeck, C., and Zeng, J.: Harmonization of global surface ocean pCO2

2073   mapped products and their flux calculations; an improved estimate of the ocean carbon

2074   sink, 1–32, https://doi.org/10.5194/essd-2021-16, 2021a.

2075   Fay, A. R., Gregor, L., Landschützer, P., McKinley, G. A., Gruber, N., Gehlen, M., Iida, Y.,

2076   Laruelle, G. G., Rödenbeck, C., Roobaert, A., and Zeng, J.: SeaFlux: harmonization of air–sea

2077   CO2 fluxes from surface pCO2 data products using a standardized approach, 13, 4693–4710,

2078   https://doi.org/10.5194/essd-13-4693-2021, 2021b.

2079   Feng, L., Palmer, P. I., Bosch, H., and Dance, S.: Estimating surface CO2 fluxes from space-

2080   borne CO2 dry air mole fraction observations using an ensemble Kalman Filter, 15, 2009.

2081   Feng, L., Palmer, P. I., Parker, R. J., Deutscher, N. M., Feist, D. G., Kivi, R., Morino, I., and

2082 Sussmann, R.: Estimates of European uptake of CO2 inferred from GOSAT XCO2 retrievals:

2083 sensitivity to measurement bias inside and outside Europe, Atmos. Chem. Phys., 16, 1289–

2084 1302, https://doi.org/10.5194/acp-16-1289-2016, 2016.

2085 Feng, Y., Zeng, Z., Searchinger, T. D., Ziegler, A. D., Wu, J., Wang, D., He, X., Elsen, P. R., Ciais,

2086 P., Xu, R., Guo, Z., Peng, L., Tao, Y., Spracklen, D. V., Holden, J., Liu, X., Zheng, Y., Xu, P.,

2087 Chen, J., Jiang, X., Song, X.-P., Lakshmi, V., Wood, E. F., and Zheng, C.: Doubling of annual

2088 forest carbon loss over the tropics during the early twenty-first century, Nat. Sustain., 1–8,

2089 https://doi.org/10.1038/s41893-022-00854-3, 2022.

2090 Friedlingstein, P., Houghton, R. A., Marland, G., Hackler, J., Boden, T. A., Conway, T. J.,

2091 Canadell, J. G., Raupach, M. R., Ciais, P., and Le Quéré, C.: Update on CO2 emissions, Nature

2092 Geosci, 3, 811–812, https://doi.org/10.1038/ngeo1022, 2010.

2093 Friedlingstein, P., Andrew, R. M., Rogelj, J., Peters, G. P., Canadell, J. G., Knutti, R., Luderer,

2094 G., Raupach, M. R., Schaeffer, M., van Vuuren, D. P., and Le Quéré, C.: Persistent growth of

2095 CO2 emissions and implications for reaching climate targets, Nature Geosci, 7, 709–715,

2096 https://doi.org/10.1038/ngeo2248, 2014.

2097 Friedlingstein, P., Jones, M. W., O'Sullivan, M., Andrew, R. M., Hauck, J., Peters, G. P., Peters,

2098 W., Pongratz, J., Sitch, S., Le Quéré, C., Bakker, D. C. E., Canadell, J. G., Ciais, P., Jackson, R.

2099 B., Anthoni, P., Barbero, L., Bastos, A., Bastrikov, V., Becker, M., Bopp, L., Buitenhuis, E.,

2100 Chandra, N., Chevallier, F., Chini, L. P., Currie, K. I., Feely, R. A., Gehlen, M., Gilfillan, D.,

2101 Gkritzalis, T., Goll, D. S., Gruber, N., Gutekunst, S., Harris, I., Haverd, V., Houghton, R. A.,

2102 Hurtt, G., Ilyina, T., Jain, A. K., Joetzjer, E., Kaplan, J. O., Kato, E., Klein Goldewijk, K.,

2103 Korsbakken, J. I., Landschützer, P., Lauvset, S. K., Lefèvre, N., Lenton, A., Lienert, S.,

2104 Lombardozzi, D., Marland, G., McGuire, P. C., Melton, J. R., Metzl, N., Munro, D. R., Nabel, J.

2105 E. M. S., Nakaoka, S.-I., Neill, C., Omar, A. M., Ono, T., Peregon, A., Pierrot, D., Poulter, B.,

2106 Rehder, G., Resplandy, L., Robertson, E., Rödenbeck, C., Séférian, R., Schwinger, J., Smith, N.,

2107 Tans, P. P., Tian, H., Tilbrook, B., Tubiello, F. N., van der Werf, G. R., Wiltshire, A. J., and

2108 Zaehle, S.: Global Carbon Budget 2019, Earth Syst. Sci. Data, 11, 1783–1838,

2109 https://doi.org/10.5194/essd-11-1783-2019, 2019.

2110 Friedlingstein, P., O'Sullivan, M., Jones, M. W., Andrew, R. M., Hauck, J., Olsen, A., Peters, G.

2111 P., Peters, W., Pongratz, J., Sitch, S., Le Quéré, C., Canadell, J. G., Ciais, P., Jackson, R. B., Alin,

2112 S., Aragão, L. E. O. C., Arneth, A., Arora, V., Bates, N. R., Becker, M., Benoit-Cattin, A., Bittig,

2113 H. C., Bopp, L., Bultan, S., Chandra, N., Chevallier, F., Chini, L. P., Evans, W., Florentie, L.,

2114 Forster, P. M., Gasser, T., Gehlen, M., Gilfillan, D., Gkritzalis, T., Gregor, L., Gruber, N., Harris,

2115 I., Hartung, K., Haverd, V., Houghton, R. A., Ilyina, T., Jain, A. K., Joetzjer, E., Kadono, K., Kato,

2116 E., Kitidis, V., Korsbakken, J. I., Landschützer, P., Lefèvre, N., Lenton, A., Lienert, S., Liu, Z.,

2117 Lombardozzi, D., Marland, G., Metzl, N., Munro, D. R., Nabel, J. E. M. S., Nakaoka, S.-I., Niwa,

2118 Y., O'Brien, K., Ono, T., Palmer, P. I., Pierrot, D., Poulter, B., Resplandy, L., Robertson, E.,

2119 Rödenbeck, C., Schwinger, J., Séférian, R., Skjelvan, I., Smith, A. J. P., Sutton, A. J., Tanhua, T.,

2120 Tans, P. P., Tian, H., Tilbrook, B., van der Werf, G., Vuichard, N., Walker, A. P., Wanninkhof,

2121 R., Watson, A. J., Willis, D., Wiltshire, A. J., Yuan, W., Yue, X., and Zaehle, S.: Global Carbon

2122 Budget 2020, Earth Syst. Sci. Data, 12, 3269–3340, https://doi.org/10.5194/essd-12-3269-

2123 2020, 2020.

2124 Friedlingstein, P., Jones, M. W., O'Sullivan, M., Andrew, R. M., Bakker, D. C. E., Hauck, J., Le

2125 Quéré, C., Peters, G. P., Peters, W., Pongratz, J., Sitch, S., Canadell, J. G., Ciais, P., Jackson, R.

2126 B., Anthoni, P., Bates, N. R., Becker, M., Bopp, L., Tuyet, T., Chau, T., Chevallier, F., Chini, L.

2127 P., Cronin, M., Currie, K. I., Decharme, B., Djeutchouang, L. M., Dou, X., Evans, W., Feely, R.

2128 A., Feng, L., Gasser, T., Gilfillan, D., Gkritzalis, T., Grassi, G., Gregor, L., Gruber, N., Gürses, Ö.,

2129 Harris, I., Houghton, R. A., Hurtt, G. C., Iida, Y., Ilyina, T., Luijkx, I. T., Jain, A. K., Jones, S. D.,

2130 Kato, E., Kennedy, D., Klein Goldewijk, K., Knauer, J., Korsbakken, J. I., Körtzinger, A.,

2131 Landschützer, P., Lauvset, S. K., Lefèvre, N., Lienert, S., Liu, J., Marland, G., McGuire, P. C.,

2132 Melton, J. R., Munro, D. R., Nabel, J. E. M. S., Nakaoka, S.-I., Niwa, Y., Ono, T., Pierrot, D.,

2133 Poulter, B., Rehder, G., Resplandy, L., Robertson, E., Rödenbeck, C., Schwinger, J.,

2134 Schwingshackl, C., Séférian, R., Sutton, A. J., Tanhua, T., Tans, P., Tian, H., Tilbrook, B.,

2135 Tubiello, F., van der Werf, G. R., Vuichard, N., Wanninkhof, R., Watson, A. J., Willis, D.,

2136 Wiltshire, A. J., Wenping Yuan, Yue, C., Yue, X., Zaehle, S., and Zeng, J.: Supplemental data of

2137 the Global Carbon Budget 2021, ICOS-ERIC Carbon Portal, https://doi.org/10.18160/gcp-

2138 2021, 2021.

2139 Gasser, T. and Ciais, P.: A theoretical framework for the net land-to-atmosphere CO_2 flux

2140 and its implications in the definition of "emissions from land-use change", Earth Syst.

2141 Dynam., 4, 171–186, https://doi.org/10.5194/esd-4-171-2013, 2013.

2142 Gasser, T., Crepin, L., Quilcaille, Y., Houghton, R. A., Ciais, P., and Obersteiner, M.: Historical

2143 CO2 emissions from land use and land cover change and their uncertainty, Biogeosciences,

2144 17, 4075–4101, https://doi.org/10.5194/bg-17-4075-2020, 2020.

2145 Gaubert, B., Stephens, B. B., Basu, S., Chevallier, F., Deng, F., Kort, E. A., Patra, P. K., Peters,

2146 W., Rödenbeck, C., Saeki, T., Schimel, D., Van der Laan-Luijkx, I., Wofsy, S., and Yin, Y.: Global

2147 atmospheric CO2 inverse models converging on neutral tropical land exchange, but

2148 disagreeing on fossil fuel and atmospheric growth rate, Biogeosciences, 16, 117–134,

2149 https://doi.org/10.5194/bg-16-117-2019, 2019.

2150 Gaubert, B., Emmons, L. K., Raeder, K., Tilmes, S., Miyazaki, K., Arellano Jr., A. F., Elguindi, N.,

2151 Granier, C., Tang, W., Barré, J., Worden, H. M., Buchholz, R. R., Edwards, D. P., Franke, P.,

2152 Anderson, J. L., Saunois, M., Schroeder, J., Woo, J.-H., Simpson, I. J., Blake, D. R., Meinardi,

2153 S., Wennberg, P. O., Crounse, J., Teng, A., Kim, M., Dickerson, R. R., He, H., Ren, X., Pusede,

2154 S. E., and Diskin, G. S.: Correcting model biases of CO in East Asia: impact on oxidant

2155 distributions during KORUS-AQ, 20, 14617–14647, https://doi.org/10.5194/acp-20-14617-

2156 2020, 2020.

2157 Giglio, L., Schroeder, W., and Justice, C. O.: The collection 6 MODIS active fire detection

2158 algorithm and fire products, Remote Sensing of Environment, 178, 31–41,

2159 https://doi.org/10.1016/j.rse.2016.02.054, 2016.

2160 Gilfillan, D. and Marland, G.: CDIAC-FF: global and national CO2 emissions from fossil fuel

2161 combustion and cement manufacture: 1751–2017, 13, 1667–1680,

2162 https://doi.org/10.5194/essd-13-1667-2021, 2021.

2163 Gloege, L., McKinley, G. A., Landschützer, P., Fay, A. R., Frölicher, T. L., Fyfe, J. C., Ilyina, T.,

2164 Jones, S., Lovenduski, N. S., Rodgers, K. B., Schlunegger, S., and Takano, Y.: Quantifying

2165 Errors in Observationally Based Estimates of Ocean Carbon Sink Variability, 35,

2166 e2020GB006788, https://doi.org/10.1029/2020GB006788, 2021.

2167 Goddijn-Murphy, L. M., Woolf, D. K., Land, P. E., Shutler, J. D., and Donlon, C.: The OceanFlux

2168 Greenhouse Gases methodology for deriving a sea surface climatology of CO2 fugacity in

2169 support of air–sea gas flux studies, 11, 519–541, https://doi.org/10.5194/os-11-519-2015,

2170 2015.

2171   Golar, G., Malik, A., Muis, H., Herman, A., Nurudin, N., and Lukman, L.: The social-economic

2172   impact of COVID-19 pandemic: implications for potential forest degradation, Heliyon, 6,

2173   e05354, https://doi.org/10.1016/j.heliyon.2020.e05354, 2020.

2174   Grassi, G., House, J., Kurz, W. A., Cescatti, A., Houghton, R. A., Peters, G. P., Sanz, M. J.,

2175   Viñas, R. A., Alkama, R., Arneth, A., Bondeau, A., Dentener, F., Fader, M., Federici, S.,

2176   Friedlingstein, P., Jain, A. K., Kato, E., Koven, C. D., Lee, D., Nabel, J. E. M. S., Nassikas, A. A.,

2177   Perugini, L., Rossi, S., Sitch, S., Viovy, N., Wiltshire, A., and Zaehle, S.: Reconciling global-

2178   model estimates and country reporting of anthropogenic forest CO_2 sinks, Nature Clim

2179   Change, 8, 914–920, https://doi.org/10.1038/s41558-018-0283-x, 2018.

2180   Grassi, G., Stehfest, E., Rogelj, J., van Vuuren, D., Cescatti, A., House, J., Nabuurs, G.-J., Rossi,

2181   S., Alkama, R., Viñas, R. A., Calvin, K., Ceccherini, G., Federici, S., Fujimori, S., Gusti, M.,

2182   Hasegawa, T., Havlik, P., Humpenöder, F., Korosuo, A., Perugini, L., Tubiello, F. N., and Popp,

2183   A.: Critical adjustment of land mitigation pathways for assessing countries' climate progress,

2184   Nat. Clim. Chang., 11, 425–434, https://doi.org/10.1038/s41558-021-01033-6, 2021.

2185   Gregg, J. S., Andres, R. J., and Marland, G.: China: Emissions pattern of the world leader in

2186   CO 2 emissions from fossil fuel consumption and cement production, Geophys. Res. Lett.,

2187   35, L08806, https://doi.org/10.1029/2007GL032887, 2008.

2188   Gregor, L. and Gruber, N.: OceanSODA-ETHZ: a global gridded data set of the surface ocean

2189   carbonate system for seasonal to decadal studies of ocean acidification, 13, 777–808,

2190   https://doi.org/10.5194/essd-13-777-2021, 2021.

2191   Gregor, L., Lebehot, A. D., Kok, S., and Scheel Monteiro, P. M.: A comparative assessment of

2192   the uncertainties of global surface ocean CO_2 estimates using a machine-learning ensemble

2193   (CSIR-ML6 version 2019a) – have we hit the wall?, 12, 5113–5136,

2194   https://doi.org/10.5194/gmd-12-5113-2019, 2019.

2195   Gruber, N., Gloor, M., Mikaloff Fletcher, S. E., Doney, S. C., Dutkiewicz, S., Follows, M. J.,

2196   Gerber, M., Jacobson, A. R., Joos, F., Lindsay, K., Menemenlis, D., Mouchet, A., Müller, S. A.,

2197   Sarmiento, J. L., and Takahashi, T.: Oceanic sources, sinks, and transport of atmospheric

2198 CO_2, 23, https://doi.org/10.1029/2008GB003349, 2009.

Gruber, N., Clement, D., Carter, B. R., Feely, R. A., van Heuven, S., Hoppema, M., Ishii, M., Key, R. M., Kozyr, A., Lauvset, S. K., Lo Monaco, C., Mathis, J. T., Murata, A., Olsen, A., Perez, F. F., Sabine, C. L., Tanhua, T., and Wanninkhof, R.: The oceanic sink for anthropogenic CO2 from 1994 to 2007, 363, 1193–1199, https://doi.org/10.1126/science.aau5153, 2019.

Gruère, G. and Brooks, J.: Viewpoint: Characterising early agricultural and food policy responses to the outbreak of COVID-19, Food Policy, 100, 102017, https://doi.org/10.1016/j.foodpol.2020.102017, 2021.

Guan, D., Liu, Z., Geng, Y., Lindner, S., and Hubacek, K.: The gigatonne gap in China's carbon dioxide inventories, Nature Clim Change, 2, 672–675, https://doi.org/10.1038/nclimate1560, 2012.

Guo, R., Wang, J., Bing, L., Tong, D., Ciais, P., Davis, S. J., Andrew, R. M., Xi, F., and Liu, Z.: Global CO2 uptake by cement from 1930 to 2019, 13, 1791–1805, https://doi.org/10.5194/essd-13-1791-2021, 2021.

Gütschow, J., Jeffery, M. L., Gieseke, R., Gebel, R., Stevens, D., Krapp, M., and Rocha, M.: The PRIMAP-hist national historical emissions time series, 8, 571–603, https://doi.org/10.5194/essd-8-571-2016, 2016.

Gütschow, J., Günther, A., and Pflüger, M.: The PRIMAP-hist national historical emissions time series (1750-2019) v2.3.1, https://doi.org/10.5281/zenodo.5494497, 2021.

Hall, B. D., Crotwell, A. M., Kitzis, D. R., Mefford, T., Miller, B. R., Schibig, M. F., and Tans, P. P.: Revision of the World Meteorological Organization Global Atmosphere Watch (WMO/GAW) CO2 calibration scale, 14, 3015–3032, https://doi.org/10.5194/amt-14-3015-2021, 2021.

Hansen, M. C., Potapov, P. V., Moore, R., Hancher, M., Turubanova, S. A., Tyukavina, A., Thau, D., Stehman, S. V., Goetz, S. J., Loveland, T. R., Kommareddy, A., Egorov, A., Chini, L., Justice, C. O., and Townshend, J. R. G.: High-Resolution Global Maps of 21st-Century Forest Cover Change, Science, 342, 850–853, https://doi.org/10.1126/science.1244693, 2013.

Hansis, E., Davis, S. J., and Pongratz, J.: Relevance of methodological choices for accounting of land use change carbon fluxes, Global Biogeochem. Cycles, 29, 1230–1246,

2227   https://doi.org/10.1002/2014GB004997, 2015.

2228   Harris, I., Jones, P. D., Osborn, T. J., and Lister, D. H.: Updated high-resolution grids of

2229   monthly climatic observations - the CRU TS3.10 Dataset, Int. J. Climatol., 34, 623–642,

2230   https://doi.org/10.1002/joc.3711, 2014.

2231   Harris, I., Osborn, T. J., Jones, P., and Lister, D.: Version 4 of the CRU TS monthly high-

2232   resolution gridded multivariate climate dataset, Sci Data, 7, 109,

2233   https://doi.org/10.1038/s41597-020-0453-3, 2020.

2234   Hauck, J., Zeising, M., Le Quéré, C., Gruber, N., Bakker, D. C. E., Bopp, L., Chau, T. T. T.,

2235   Gürses, Ö., Ilyina, T., Landschützer, P., Lenton, A., Resplandy, L., Rödenbeck, C., Schwinger,

2236   J., and Séférian, R.: Consistency and Challenges in the Ocean Carbon Sink Estimate for the

2237   Global Carbon Budget, Front. Mar. Sci., 7, 571720,

2238   https://doi.org/10.3389/fmars.2020.571720, 2020.

2239   Haverd, V., Smith, B., Nieradzik, L., Briggs, P. R., Woodgate, W., Trudinger, C. M., Canadell, J.

2240   G., and Cuntz, M.: A new version of the CABLE land surface model (Subversion revision

2241   r4601) incorporating land use and land cover change, woody vegetation demography, and a

2242   novel optimisation-based approach to plant coordination of photosynthesis, Geosci. Model

2243   Dev., 11, 2995–3026, https://doi.org/10.5194/gmd-11-2995-2018, 2018.

2244   Heinimann, A., Mertz, O., Frolking, S., Christensen, A. E., Hurni, K., Sedano, F., Chini, L. P.,

2245   Sahajpal, R., Hansen, M., and Hurtt, G.: A global view of shifting cultivation: Recent, current,

2246   and future extent, PLOS ONE, 12, e0184479, https://doi.org/10.1371/journal.pone.0184479,

2247   2017.

2248   Hertwich, E. G. and Peters, G. P.: Carbon Footprint of Nations: A Global, Trade-Linked

2249   Analysis, Environ. Sci. Technol., 43, 6414–6420, https://doi.org/10.1021/es803496a, 2009.

2250   Hickler, T., Smith, B., Prentice, I. C., Mjöfors, K., Miller, P., Arneth, A., and Sykes, M. T.: CO_2

2251   fertilization in temperate FACE experiments not representative of boreal and tropical

2252   forests, 14, 1531–1542, https://doi.org/10.1111/j.1365-2486.2008.01598.x, 2008.

2253   Ho, D. T., Wanninkhof, R., Schlosser, P., Ullman, D. S., Hebert, D., and Sullivan, K. F.: Toward

2254   a universal relationship between wind speed and gas exchange: Gas transfer velocities

measured with 3He/SF6 during the Southern Ocean Gas Exchange Experiment, 116, https://doi.org/10.1029/2010JC006854, 2011.

Hoesly, R. M., Smith, S. J., Feng, L., Klimont, Z., Janssens-Maenhout, G., Pitkanen, T., Seibert, J. J., Vu, L., Andres, R. J., Bolt, R. M., Bond, T. C., Dawidowski, L., Kholod, N., Kurokawa, J., Li, M., Liu, L., Lu, Z., Moura, M. C. P., O'Rourke, P. R., and Zhang, Q.: Historical (1750–2014) anthropogenic emissions of reactive gases and aerosols from the Community Emissions Data System (CEDS), Geosci. Model Dev., 11, 369–408, https://doi.org/10.5194/gmd-11-369-2018, 2018.

Hong, C., Burney, J. A., Pongratz, J., Nabel, J. E. M. S., Mueller, N. D., Jackson, R. B., and Davis, S. J.: Global and regional drivers of land-use emissions in 1961–2017, 589, 554–561, https://doi.org/10.1038/s41586-020-03138-y, 2021.

Hooijer, A., Page, S., Canadell, J. G., Silvius, M., Kwadijk, J., Wösten, H., and Jauhiainen, J.: Current and future CO_2 emissions from drained peatlands in Southeast Asia, Biogeosciences, 7, 1505–1514, https://doi.org/10.5194/bg-7-1505-2010, 2010.

Houghton, R. A.: Why are estimates of the terrestrial carbon balance so different?, 9, 500–509, https://doi.org/10.1046/j.1365-2486.2003.00620.x, 2003.

Houghton, R. A. and Nassikas, A. A.: Global and regional fluxes of carbon from land use and land cover change 1850-2015: Carbon Emissions From Land Use, Global Biogeochem. Cycles, 31, 456–472, https://doi.org/10.1002/2016GB005546, 2017.

Houghton, R. A., House, J. I., Pongratz, J., van der Werf, G. R., DeFries, R. S., Hansen, M. C., Le Quéré, C., and Ramankutty, N.: Carbon emissions from land use and land-cover change, Biogeosciences, 9, 5125–5142, https://doi.org/10.5194/bg-9-5125-2012, 2012.

Hubau, W., Lewis, S. L., Phillips, O. L., Affum-Baffoe, K., Beeckman, H., Cuní-Sanchez, A., Daniels, A. K., Ewango, C. E. N., Fauset, S., Mukinzi, J. M., Sheil, D., Sonké, B., Sullivan, M. J. P., Sunderland, T. C. H., Taedoumg, H., Thomas, S. C., White, L. J. T., Abernethy, K. A., Adu-Bredu, S., Amani, C. A., Baker, T. R., Banin, L. F., Baya, F., Begne, S. K., Bennett, A. C., Benedet, F., Bitariho, R., Bocko, Y. E., Boeckx, P., Boundja, P., Brienen, R. J. W., Brncic, T., Chezeaux, E., Chuyong, G. B., Clark, C. J., Collins, M., Comiskey, J. A., Coomes, D. A., Dargie,

G. C., de Haulleville, T., Kamdem, M. N. D., Doucet, J.-L., Esquivel-Muelbert, A., Feldpausch, T. R., Fofanah, A., Foli, E. G., Gilpin, M., Gloor, E., Gonmadje, C., Gourlet-Fleury, S., Hall, J. S., Hamilton, A. C., Harris, D. J., Hart, T. B., Hockemba, M. B. N., Hladik, A., Ifo, S. A., Jeffery, K. J., Jucker, T., Yakusu, E. K., Kearsley, E., Kenfack, D., Koch, A., Leal, M. E., Levesley, A., Lindsell, J. A., Lisingo, J., Lopez-Gonzalez, G., Lovett, J. C., Makana, J.-R., Malhi, Y., Marshall, A. R., Martin, J., Martin, E. H., Mbayu, F. M., Medjibe, V. P., Mihindou, V., Mitchard, E. T. A., Moore, S., Munishi, P. K. T., Bengone, N. N., Ojo, L., Ondo, F. E., Peh, K. S.-H., Pickavance, G. C., Poulsen, A. D., Poulsen, J. R., Qie, L., Reitsma, J., Rovero, F., Swaine, M. D., Talbot, J., Taplin, J., Taylor, D. M., Thomas, D. W., Toirambe, B., Mukendi, J. T., Tuagben, D., Umunay, P. M., et al.: Asynchronous carbon sink saturation in African and Amazonian tropical forests, 579, 80–87, https://doi.org/10.1038/s41586-020-2035-0, 2020.

Hugelius, G., Bockheim, J. G., Camill, P., Elberling, B., Grosse, G., Harden, J. W., Johnson, K., Jorgenson, T., Koven, C. D., Kuhry, P., Michaelson, G., Mishra, U., Palmtag, J., Ping, C.-L., O'Donnell, J., Schirrmeister, L., Schuur, E. A. G., Sheng, Y., Smith, L. C., Strauss, J., and Yu, Z.: A new data set for estimating organic carbon storage to 3 m depth in soils of the northern circumpolar permafrost region, Earth Syst. Sci. Data, 5, 393–402, https://doi.org/10.5194/essd-5-393-2013, 2013.

Humphrey, V., Zscheischler, J., Ciais, P., Gudmundsson, L., Sitch, S., and Seneviratne, S. I.: Sensitivity of atmospheric CO2 growth rate to observed changes in terrestrial water storage, 560, 628–631, https://doi.org/10.1038/s41586-018-0424-4, 2018.

Humphrey, V., Berg, A., Ciais, P., Gentine, P., Jung, M., Reichstein, M., Seneviratne, S. I., and Frankenberg, C.: Soil moisture–atmosphere feedback dominates land carbon uptake variability, 592, 65–69, https://doi.org/10.1038/s41586-021-03325-5, 2021.

Huntzinger, D. N., Michalak, A. M., Schwalm, C., Ciais, P., King, A. W., Fang, Y., Schaefer, K., Wei, Y., Cook, R. B., Fisher, J. B., Hayes, D., Huang, M., Ito, A., Jain, A. K., Lei, H., Lu, C., Maignan, F., Mao, J., Parazoo, N., Peng, S., Poulter, B., Ricciuto, D., Shi, X., Tian, H., Wang, W., Zeng, N., and Zhao, F.: Uncertainty in the response of terrestrial carbon sink to environmental drivers undermines carbon-climate feedback predictions, Sci Rep, 7, 4765, https://doi.org/10.1038/s41598-017-03818-2, 2017.

2312   Hurtt, G., Chini, L., Sahajpal, R., Frolking, S., Bodirsky, B. L., Calvin, K., Doelman, J., Fisk, J.,

2313   Fujimori, S., Klein Goldewijk, K., Hasegawa, T., Havlik, P., Heinimann, A., Humpenöder, F.,

2314   Jungclaus, J., Kaplan, J., Krisztin, T., Lawrence, D., Lawrence, P., Mertz, O., Pongratz, J., Popp,

2315   A., Riahi, K., Shevliakova, E., Stehfest, E., Thornton, P., van Vuuren, D., and Zhang, X.:

2316   input4MIPs.CMIP6.CMIP.UofMD.UofMD-landState-2-1-h,

2317   https://doi.org/10.22033/ESGF/input4MIPs.1127, 2017.

2318   Hurtt, G. C., Chini, L. P., Frolking, S., Betts, R. A., Feddema, J., Fischer, G., Fisk, J. P., Hibbard,

2319   K., Houghton, R. A., Janetos, A., Jones, C. D., Kindermann, G., Kinoshita, T., Klein Goldewijk,

2320   K., Riahi, K., Shevliakova, E., Smith, S., Stehfest, E., Thomson, A., Thornton, P., van Vuuren, D.

2321   P., and Wang, Y. P.: Harmonization of land-use scenarios for the period 1500–2100: 600

2322   years of global gridded annual land-use transitions, wood harvest, and resulting secondary

2323   lands, Climatic Change, 109, 117–161, https://doi.org/10.1007/s10584-011-0153-2, 2011.

2324   Hurtt, G. C., Chini, L., Sahajpal, R., Frolking, S., Bodirsky, B. L., Calvin, K., Doelman, J. C., Fisk,

2325   J., Fujimori, S., Klein Goldewijk, K., Hasegawa, T., Havlik, P., Heinimann, A., Humpenöder, F.,

2326   Jungclaus, J., Kaplan, J. O., Kennedy, J., Krisztin, T., Lawrence, D., Lawrence, P., Ma, L., Mertz,

2327   O., Pongratz, J., Popp, A., Poulter, B., Riahi, K., Shevliakova, E., Stehfest, E., Thornton, P.,

2328   Tubiello, F. N., van Vuuren, D. P., and Zhang, X.: Harmonization of global land use change

2329   and management for the period 850–2100 (LUH2) for CMIP6, Geosci. Model Dev., 13, 5425–

2330   5464, https://doi.org/10.5194/gmd-13-5425-2020, 2020.

2331   IEA: International Energy Agency: Global Energy Review, available at:

2332   https://www.iea.org/reports/global-energy-review-2021, last access: 11 March 2022,

2333   2021a.

2334   IEA: International Energy Agency: World Energy Outlook, available at:

2335   https://www.iea.org/reports/world-energy-outlook-2021, last access: 11 March 2022,

2336   2021b.

2337   IEA/OECD: International Energy Agency/Organisation for Economic Cooperation and

2338   Development: CO2 emissions from fuel combustion, available at:

2339   https://webstore.iea.org/co2-emissions-from-fuel-combustion-2019-highlights, last access:

2340   11 March 2022, 2019.

Iida, Y., Kojima, A., Takatani, Y., Nakano, T., Sugimoto, H., Midorikawa, T., and Ishii, M.: Trends in pCO2 and sea–air CO2 flux over the global open oceans for the last two decades, J Oceanogr, 71, 637–661, https://doi.org/10.1007/s10872-015-0306-4, 2015.

Iida, Y., Takatani, Y., Kojima, A., and Ishii, M.: Global trends of ocean CO2 sink and ocean acidification: an observation-based reconstruction of surface ocean inorganic carbon variables, J Oceanogr, 77, 323–358, https://doi.org/10.1007/s10872-020-00571-5, 2021.

Ilyina, T., Six, K. D., Segschneider, J., Maier-Reimer, E., Li, H., and Núñez-Riboni, I.: Global ocean biogeochemistry model HAMOCC: Model architecture and performance as component of the MPI-Earth system model in different CMIP5 experimental realizations: The Model Hamocc within Mpi-Esm in Cmip5, J. Adv. Model. Earth Syst., 5, 287–315, https://doi.org/10.1029/2012MS000178, 2013.

IMF: International Monetary Fund: World Economic Outlook, available at: http://www.imf.org, last access: 11 March 2022, 2022.

Inness, A., Ades, M., Agustí-Panareda, A., Barré, J., Benedictow, A., Blechschmidt, A.-M., Dominguez, J. J., Engelen, R., Eskes, H., Flemming, J., Huijnen, V., Jones, L., Kipling, Z., Massart, S., Parrington, M., Peuch, V.-H., Razinger, M., Remy, S., Schulz, M., and Suttie, M.: The CAMS reanalysis of atmospheric composition, 19, 3515–3556, https://doi.org/10.5194/acp-19-3515-2019, 2019.

IPCC: Summary for Policymakers. In: Climate Change 2021: The Physical Science Basis. Contribution of Working Group I to the Sixth Assessment Report of the Intergovernmental Panel on Climate Change [Masson-Delmotte, V., P. Zhai, A. Pirani, S.L. Connors, C. Péan, S. Berger, N. Caud, Y. Chen, L. Goldfarb, M.I. Gomis, M. Huang, K. Leitzell, E. Lonnoy, J.B.R. Matthews, T.K. Maycock, T. Waterfield, O. Yelekçi, R. Yu, and B. Zhou (eds.)]. Cambridge University Press. In Press., 2021.

Ito, A. and Inatomi, M.: Use of a process-based model for assessing the methane budgets of global terrestrial ecosystems and evaluation of uncertainty, 9, 759–773, https://doi.org/10.5194/bg-9-759-2012, 2012.

Jackson, R. B., Canadell, J. G., Le Quéré, C., Andrew, R. M., Korsbakken, J. I., Peters, G. P.,

2369   and Nakicenovic, N.: Reaching peak emissions, Nature Clim Change, 6, 7–10,

2370   https://doi.org/10.1038/nclimate2892, 2016.

2371   Jackson, R. B., Le Quéré, C., Andrew, R. M., Canadell, J. G., Korsbakken, J. I., Liu, Z., Peters, G.

2372   P., and Zheng, B.: Global energy growth is outpacing decarbonization, Environ. Res. Lett., 13,

2373   120401, https://doi.org/10.1088/1748-9326/aaf303, 2018.

2374   Jackson, R. B., Friedlingstein, P., Andrew, R. M., Canadell, J. G., Le Quéré, C., and Peters, G.

2375   P.: Persistent fossil fuel growth threatens the Paris Agreement and planetary health,

2376   Environ. Res. Lett., 14, 121001, https://doi.org/10.1088/1748-9326/ab57b3, 2019.

2377   Jacobson, A. R., Mikaloff Fletcher, S. E., Gruber, N., Sarmiento, J. L., and Gloor, M.: A joint

2378   atmosphere-ocean inversion for surface fluxes of carbon dioxide: 1. Methods and global-

2379   scale fluxes: JOINT INVERSION-METHODS AND GLOBAL FLUXES, Global Biogeochem. Cycles,

2380   21, https://doi.org/10.1029/2005GB002556, 2007.

2381   Jain, A. K., Meiyappan, P., Song, Y., and House, J. I.: CO2 emissions from land-use change

2382   affected more by nitrogen cycle, than by the choice of land-cover data, 19, 2893–2906,

2383   https://doi.org/10.1111/gcb.12207, 2013.

2384   Janssens-Maenhout, G., Crippa, M., Guizzardi, D., Muntean, M., Schaaf, E., Dentener, F.,

2385   Bergamaschi, P., Pagliari, V., Olivier, J. G. J., Peters, J. A. H. W., van Aardenne, J. A., Monni,

2386   S., Doering, U., Petrescu, A. M. R., Solazzo, E., and Oreggioni, G. D.: EDGAR v4.3.2 Global

2387   Atlas of the three major greenhouse gas emissions for the period 1970–2012, Earth Syst. Sci.

2388   Data, 11, 959–1002, https://doi.org/10.5194/essd-11-959-2019, 2019.

2389   JODI: Joint Organisations Data Initiative, available at: https://www. jodidata.org, last access:

2390   11 March 2022, 2022.

2391   Jones, M. W., Andrew, R. M., Peters, G. P., Janssens-Maenhout, G., De-Gol, A. J., Ciais, P.,

2392   Patra, P. K., Chevallier, F., and Le Quéré, C.: Gridded fossil CO2 emissions and related O2

2393   combustion consistent with national inventories 1959–2018, Sci Data, 8, 2,

2394   https://doi.org/10.1038/s41597-020-00779-6, 2021a.

2395   Jones, M. W., Andrew, R. M., Peters, G. P., Janssens-Maenhout, G., De-Gol, A. J., Dou, X., Liu,

2396   Z., Ciais, P., Patra, P. K., Chevallier, F., and Le Quéré, C.: Gridded fossil CO2 emissions and

2397   related O2 combustion consistent with national inventories 1959-2020,

2398   https://doi.org/10.5281/zenodo.5565199, 2021b.

2399   Joos, F. and Spahni, R.: Rates of change in natural and anthropogenic radiative forcing over

2400   the past 20,000 years, Proceedings of the National Academy of Sciences, 105, 1425–1430,

2401   https://doi.org/10.1073/pnas.0707386105, 2008.

2402   Jung, M., Reichstein, M., Ciais, P., Seneviratne, S. I., Sheffield, J., Goulden, M. L., Bonan, G.,

2403   Cescatti, A., Chen, J., de Jeu, R., Dolman, A. J., Eugster, W., Gerten, D., Gianelle, D., Gobron,

2404   N., Heinke, J., Kimball, J., Law, B. E., Montagnani, L., Mu, Q., Mueller, B., Oleson, K., Papale,

2405   D., Richardson, A. D., Roupsard, O., Running, S., Tomelleri, E., Viovy, N., Weber, U., Williams,

2406   C., Wood, E., Zaehle, S., and Zhang, K.: Recent decline in the global land evapotranspiration

2407   trend due to limited moisture supply, Nature, 467, 951–954,

2408   https://doi.org/10.1038/nature09396, 2010.

2409   Jung, M., Reichstein, M., Schwalm, C. R., Huntingford, C., Sitch, S., Ahlström, A., Arneth, A.,

2410   Camps-Valls, G., Ciais, P., Friedlingstein, P., Gans, F., Ichii, K., Jain, A. K., Kato, E., Papale, D.,

2411   Poulter, B., Raduly, B., Rödenbeck, C., Tramontana, G., Viovy, N., Wang, Y.-P., Weber, U.,

2412   Zaehle, S., and Zeng, N.: Compensatory water effects link yearly global land CO2 sink

2413   changes to temperature, Nature, 541, 516–520, https://doi.org/10.1038/nature20780,

2414   2017.

2415   Kalnay, E., Kanamitsu, M., Kistler, R., Collins, W., Deaven, D., Gandin, L., Iredell, M., Saha, S.,

2416   White, G., Woollen, J., Zhu, Y., Chelliah, M., Ebisuzaki, W., Higgins, W., Janowiak, J., Mo, K.

2417   C., Ropelewski, C., Wang, J., Leetmaa, A., Reynolds, R., Jenne, R., and Joseph, D.: The

2418   NCEP/NCAR 40-Year Reanalysis Project, 77, 437–472, https://doi.org/10.1175/1520-

2419   0477(1996)077<0437:TNYRP>2.0.CO;2, 1996.

2420   Kato, E., Kinoshita, T., Ito, A., Kawamiya, M., and Yamagata, Y.: Evaluation of spatially

2421   explicit emission scenario of land-use change and biomass burning using a process-based

2422   biogeochemical model, 8, 104–122, https://doi.org/10.1080/1747423X.2011.628705, 2013.

2423   Keeling, C. D., Bacastow, R. B., Bainbridge, A. E., Ekdahl, C. A., Guenther, P. R., Waterman, L.

2424   S., and Chin, J. F. S.: Atmospheric carbon dioxide variations at Mauna Loa Observatory,

2425   Hawaii, 28, 538–551, https://doi.org/10.1111/j.2153-3490.1976.tb00701.x, 1976.

2426 Keeling, R. F. and Manning, A. C.: 5.15 - Studies of Recent Changes in Atmospheric O2

2427 Content, in: Treatise on Geochemistry (Second Edition), edited by: Holland, H. D. and

2428 Turekian, K. K., Elsevier, Oxford, 385–404, https://doi.org/10.1016/B978-0-08-095975-

2429 7.00420-4, 2014.

2430 Keppler, L. and Landschützer, P.: Regional Wind Variability Modulates the Southern Ocean

2431 Carbon Sink, Sci Rep, 9, 7384, https://doi.org/10.1038/s41598-019-43826-y, 2019.

2432 Khatiwala, S., Primeau, F., and Hall, T.: Reconstruction of the history of anthropogenic CO2

2433 concentrations in the ocean, Nature, 462, 346–349, https://doi.org/10.1038/nature08526,

2434 2009.

2435 Khatiwala, S., Tanhua, T., Mikaloff Fletcher, S., Gerber, M., Doney, S. C., Graven, H. D.,

2436 Gruber, N., McKinley, G. A., Murata, A., Ríos, A. F., and Sabine, C. L.: Global ocean storage of

2437 anthropogenic carbon, Biogeosciences, 10, 2169–2191, https://doi.org/10.5194/bg-10-

2438 2169-2013, 2013.

2439 Klein Goldewijk, K., Beusen, A., Doelman, J., and Stehfest, E.: Anthropogenic land use

2440 estimates for the Holocene – HYDE 3.2, Earth Syst. Sci. Data, 9, 927–953,

2441 https://doi.org/10.5194/essd-9-927-2017, 2017a.

2442 Klein Goldewijk, K., Dekker, S. C., and van Zanden, J. L.: Per-capita estimations of long-term

2443 historical land use and the consequences for global change research, Journal of Land Use

2444 Science, 1747423X.2017.1354938, https://doi.org/10.1080/1747423X.2017.1354938,

2445 2017b.

2446 Kobayashi, S., Ota, Y., Harada, Y., Ebita, A., Moriya, M., Onoda, H., Onogi, K., Kamahori, H.,

2447 Kobayashi, C., Endo, H., Miyaoka, K., and Takahashi, K.: The JRA-55 Reanalysis: General

2448 Specifications and Basic Characteristics, Journal of the Meteorological Society of Japan, 93,

2449 5–48, https://doi.org/10.2151/jmsj.2015-001, 2015.

2450 Korsbakken, J. I., Peters, G. P., and Andrew, R. M.: Uncertainties around reductions in

2451 China's coal use and CO2 emissions, Nature Clim Change, 6, 687–690,

2452 https://doi.org/10.1038/nclimate2963, 2016.

2453 Krinner, G., Viovy, N., de Noblet-Ducoudré, N., Ogée, J., Polcher, J., Friedlingstein, P., Ciais,

2454   P., Sitch, S., and Prentice, I. C.: A dynamic global vegetation model for studies of the coupled

2455   atmosphere-biosphere system: DVGM for coupled climate studies, Global Biogeochem.

2456   Cycles, 19, https://doi.org/10.1029/2003GB002199, 2005.

2457   Lacroix, F., Ilyina, T., and Hartmann, J.: Oceanic CO2 outgassing and biological production

2458   hotspots induced by pre-industrial river loads of nutrients and carbon in a global modeling

2459   approach, Biogeosciences, 17, 55–88, https://doi.org/10.5194/bg-17-55-2020, 2020.

2460   Lacroix, F., Ilyina, T., Mathis, M., Laruelle, G. G., and Regnier, P.: Historical increases in land-

2461   derived nutrient inputs may alleviate effects of a changing physical climate on the oceanic

2462   carbon cycle, Glob Change Biol, 27, 5491–5513, https://doi.org/10.1111/gcb.15822, 2021.

2463   Landschützer, P., Gruber, N., Bakker, D. C. E., Schuster, U., Nakaoka, S., Payne, M. R., Sasse,

2464   T. P., and Zeng, J.: A neural network-based estimate of the seasonal to inter-annual

2465   variability of the Atlantic Ocean carbon sink, Biogeosciences, 10, 7793–7815,

2466   https://doi.org/10.5194/bg-10-7793-2013, 2013.

2467   Landschützer, P., Gruber, N., Bakker, D. C. E., and Schuster, U.: Recent variability of the

2468   global ocean carbon sink, Global Biogeochem. Cycles, 28, 927–949,

2469   https://doi.org/10.1002/2014GB004853, 2014.

2470   Landschützer, P., Gruber, N., Haumann, F. A., Rödenbeck, C., Bakker, D. C. E., van Heuven, S.,

2471   Hoppema, M., Metzl, N., Sweeney, C., Takahashi, T., Tilbrook, B., and Wanninkhof, R.: The

2472   reinvigoration of the Southern Ocean carbon sink, Science, 349, 1221–1224,

2473   https://doi.org/10.1126/science.aab2620, 2015.

2474   Landschützer, P., Gruber, N., and Bakker, D. C. E.: Decadal variations and trends of the global

2475   ocean carbon sink: decadal air-sea CO2 flux variability, Global Biogeochem. Cycles, 30,

2476   1396–1417, https://doi.org/10.1002/2015GB005359, 2016.

2477   Landschützer, P., Laruelle, G. G., Roobaert, A., and Regnier, P.: A uniform pCO2 climatology

2478   combining open and coastal oceans, 12, 2537–2553, https://doi.org/10.5194/essd-12-2537-

2479   2020, 2020.

2480   Lang, F., Ackermann, L., Huang, Y., Truong, S. C. H., Siems, S. T., and Manton, M. J.: A

2481   climatology of open and closed mesoscale cellular convection over the Southern Ocean

2482   derived from Himawari-8 observations, 1–27, https://doi.org/10.5194/acp-2021-681, 2021.

2483   Lasslop, G., Reichstein, M., Papale, D., Richardson, A. D., Arneth, A., Barr, A., Stoy, P., and

2484   Wohlfahrt, G.: Separation of net ecosystem exchange into assimilation and respiration using

2485   a light response curve approach: critical issues and global evaluation: Separation of NEE into

2486   GPP and RECO, 16, 187–208, https://doi.org/10.1111/j.1365-2486.2009.02041.x, 2010.

2487   Lawrence, D. M., Fisher, R. A., Koven, C. D., Oleson, K. W., Swenson, S. C., Bonan, G., Collier,

2488   N., Ghimire, B., van Kampenhout, L., Kennedy, D., Kluzek, E., Lawrence, P. J., Li, F., Li, H.,

2489   Lombardozzi, D., Riley, W. J., Sacks, W. J., Shi, M., Vertenstein, M., Wieder, W. R., Xu, C., Ali,

2490   A. A., Badger, A. M., Bisht, G., van den Broeke, M., Brunke, M. A., Burns, S. P., Buzan, J.,

2491   Clark, M., Craig, A., Dahlin, K., Drewniak, B., Fisher, J. B., Flanner, M., Fox, A. M., Gentine, P.,

2492   Hoffman, F., Keppel-Aleks, G., Knox, R., Kumar, S., Lenaerts, J., Leung, L. R., Lipscomb, W. H.,

2493   Lu, Y., Pandey, A., Pelletier, J. D., Perket, J., Randerson, J. T., Ricciuto, D. M., Sanderson, B.

2494   M., Slater, A., Subin, Z. M., Tang, J., Thomas, R. Q., Val Martin, M., and Zeng, X.: The

2495   Community Land Model Version 5: Description of New Features, Benchmarking, and Impact

2496   of Forcing Uncertainty, 11, 4245–4287, https://doi.org/10.1029/2018MS001583, 2019.

2497   Le Quéré, C., Rödenbeck, C., Buitenhuis, E. T., Conway, T. J., Langenfelds, R., Gomez, A.,

2498   Labuschagne, C., Ramonet, M., Nakazawa, T., Metzl, N., Gillett, N., and Heimann, M.:

2499   Saturation of the Southern Ocean CO2 Sink Due to Recent Climate Change, 316, 1735–1738,

2500   https://doi.org/10.1126/science.1136188, 2007.

2501   Le Quéré, C., Raupach, M. R., Canadell, J. G., Marland, G., Bopp, L., Ciais, P., Conway, T. J.,

2502   Doney, S. C., Feely, R. A., Foster, P., Friedlingstein, P., Gurney, K., Houghton, R. A., House, J.

2503   I., Huntingford, C., Levy, P. E., Lomas, M. R., Majkut, J., Metzl, N., Ometto, J. P., Peters, G. P.,

2504   Prentice, I. C., Randerson, J. T., Running, S. W., Sarmiento, J. L., Schuster, U., Sitch, S.,

2505   Takahashi, T., Viovy, N., van der Werf, G. R., and Woodward, F. I.: Trends in the sources and

2506   sinks of carbon dioxide, Nature Geosci, 2, 831–836, https://doi.org/10.1038/ngeo689, 2009.

2507   Le Quéré, C., Andres, R. J., Boden, T., Conway, T., Houghton, R. A., House, J. I., Marland, G.,

2508   Peters, G. P., van der Werf, G. R., Ahlström, A., Andrew, R. M., Bopp, L., Canadell, J. G., Ciais,

2509   P., Doney, S. C., Enright, C., Friedlingstein, P., Huntingford, C., Jain, A. K., Jourdain, C., Kato,

2510   E., Keeling, R. F., Klein Goldewijk, K., Levis, S., Levy, P., Lomas, M., Poulter, B., Raupach, M.

2511   R., Schwinger, J., Sitch, S., Stocker, B. D., Viovy, N., Zaehle, S., and Zeng, N.: The global

2512   carbon budget 1959–2011, Earth Syst. Sci. Data, 5, 165–185, https://doi.org/10.5194/essd-

2513   5-165-2013, 2013.

2514   Le Quéré, C., Peters, G. P., Andres, R. J., Andrew, R. M., Boden, T. A., Ciais, P., Friedlingstein,

2515   P., Houghton, R. A., Marland, G., Moriarty, R., Sitch, S., Tans, P., Arneth, A., Arvanitis, A.,

2516   Bakker, D. C. E., Bopp, L., Canadell, J. G., Chini, L. P., Doney, S. C., Harper, A., Harris, I.,

2517   House, J. I., Jain, A. K., Jones, S. D., Kato, E., Keeling, R. F., Klein Goldewijk, K., Körtzinger, A.,

2518   Koven, C., Lefèvre, N., Maignan, F., Omar, A., Ono, T., Park, G.-H., Pfeil, B., Poulter, B.,

2519   Raupach, M. R., Regnier, P., Rödenbeck, C., Saito, S., Schwinger, J., Segschneider, J., Stocker,

2520   B. D., Takahashi, T., Tilbrook, B., van Heuven, S., Viovy, N., Wanninkhof, R., Wiltshire, A., and

2521   Zaehle, S.: Global carbon budget 2013, Earth Syst. Sci. Data, 6, 235–263,

2522   https://doi.org/10.5194/essd-6-235-2014, 2014.

2523   Le Quéré, C., Moriarty, R., Andrew, R. M., Peters, G. P., Ciais, P., Friedlingstein, P., Jones, S.

2524   D., Sitch, S., Tans, P., Arneth, A., Boden, T. A., Bopp, L., Bozec, Y., Canadell, J. G., Chini, L. P.,

2525   Chevallier, F., Cosca, C. E., Harris, I., Hoppema, M., Houghton, R. A., House, J. I., Jain, A. K.,

2526   Johannessen, T., Kato, E., Keeling, R. F., Kitidis, V., Klein Goldewijk, K., Koven, C., Landa, C. S.,

2527   Landschützer, P., Lenton, A., Lima, I. D., Marland, G., Mathis, J. T., Metzl, N., Nojiri, Y., Olsen,

2528   A., Ono, T., Peng, S., Peters, W., Pfeil, B., Poulter, B., Raupach, M. R., Regnier, P., Rödenbeck,

2529   C., Saito, S., Salisbury, J. E., Schuster, U., Schwinger, J., Séférian, R., Segschneider, J.,

2530   Steinhoff, T., Stocker, B. D., Sutton, A. J., Takahashi, T., Tilbrook, B., van der Werf, G. R.,

2531   Viovy, N., Wang, Y.-P., Wanninkhof, R., Wiltshire, A., and Zeng, N.: Global carbon budget

2532   2014, Earth Syst. Sci. Data, 7, 47–85, https://doi.org/10.5194/essd-7-47-2015, 2015a.

2533   Le Quéré, C., Moriarty, R., Andrew, R. M., Canadell, J. G., Sitch, S., Korsbakken, J. I.,

2534   Friedlingstein, P., Peters, G. P., Andres, R. J., Boden, T. A., Houghton, R. A., House, J. I.,

2535   Keeling, R. F., Tans, P., Arneth, A., Bakker, D. C. E., Barbero, L., Bopp, L., Chang, J., Chevallier,

2536   F., Chini, L. P., Ciais, P., Fader, M., Feely, R. A., Gkritzalis, T., Harris, I., Hauck, J., Ilyina, T.,

2537   Jain, A. K., Kato, E., Kitidis, V., Klein Goldewijk, K., Koven, C., Landschützer, P., Lauvset, S. K.,

2538   Lefèvre, N., Lenton, A., Lima, I. D., Metzl, N., Millero, F., Munro, D. R., Murata, A., Nabel, J. E.

2539   M. S., Nakaoka, S., Nojiri, Y., O'Brien, K., Olsen, A., Ono, T., Pérez, F. F., Pfeil, B., Pierrot, D.,

2540   Poulter, B., Rehder, G., Rödenbeck, C., Saito, S., Schuster, U., Schwinger, J., Séférian, R.,

2541 Steinhoff, T., Stocker, B. D., Sutton, A. J., Takahashi, T., Tilbrook, B., van der Laan-Luijkx, I. T.,

2542 van der Werf, G. R., van Heuven, S., Vandemark, D., Viovy, N., Wiltshire, A., Zaehle, S., and

2543 Zeng, N.: Global Carbon Budget 2015, Earth Syst. Sci. Data, 7, 349–396,

2544 https://doi.org/10.5194/essd-7-349-2015, 2015b.

2545 Le Quéré, C., Andrew, R. M., Canadell, J. G., Sitch, S., Korsbakken, J. I., Peters, G. P.,

2546 Manning, A. C., Boden, T. A., Tans, P. P., Houghton, R. A., Keeling, R. F., Alin, S., Andrews, O.

2547 D., Anthoni, P., Barbero, L., Bopp, L., Chevallier, F., Chini, L. P., Ciais, P., Currie, K., Delire, C.,

2548 Doney, S. C., Friedlingstein, P., Gkritzalis, T., Harris, I., Hauck, J., Haverd, V., Hoppema, M.,

2549 Klein Goldewijk, K., Jain, A. K., Kato, E., Körtzinger, A., Landschützer, P., Lefèvre, N., Lenton,

2550 A., Lienert, S., Lombardozzi, D., Melton, J. R., Metzl, N., Millero, F., Monteiro, P. M. S.,

2551 Munro, D. R., Nabel, J. E. M. S., Nakaoka, S., O'Brien, K., Olsen, A., Omar, A. M., Ono, T.,

2552 Pierrot, D., Poulter, B., Rödenbeck, C., Salisbury, J., Schuster, U., Schwinger, J., Séférian, R.,

2553 Skjelvan, I., Stocker, B. D., Sutton, A. J., Takahashi, T., Tian, H., Tilbrook, B., van der Laan-

2554 Luijkx, I. T., van der Werf, G. R., Viovy, N., Walker, A. P., Wiltshire, A. J., and Zaehle, S.:

2555 Global Carbon Budget 2016, Earth Syst. Sci. Data, 8, 605–649, https://doi.org/10.5194/essd-

2556 8-605-2016, 2016.

2557 Le Quéré, C., Andrew, R. M., Friedlingstein, P., Sitch, S., Pongratz, J., Manning, A. C.,

2558 Korsbakken, J. I., Peters, G. P., Canadell, J. G., Jackson, R. B., Boden, T. A., Tans, P. P.,

2559 Andrews, O. D., Arora, V. K., Bakker, D. C. E., Barbero, L., Becker, M., Betts, R. A., Bopp, L.,

2560 Chevallier, F., Chini, L. P., Ciais, P., Cosca, C. E., Cross, J., Currie, K., Gasser, T., Harris, I.,

2561 Hauck, J., Haverd, V., Houghton, R. A., Hunt, C. W., Hurtt, G., Ilyina, T., Jain, A. K., Kato, E.,

2562 Kautz, M., Keeling, R. F., Klein Goldewijk, K., Körtzinger, A., Landschützer, P., Lefèvre, N.,

2563 Lenton, A., Lienert, S., Lima, I., Lombardozzi, D., Metzl, N., Millero, F., Monteiro, P. M. S.,

2564 Munro, D. R., Nabel, J. E. M. S., Nakaoka, S., Nojiri, Y., Padin, X. A., Peregon, A., Pfeil, B.,

2565 Pierrot, D., Poulter, B., Rehder, G., Reimer, J., Rödenbeck, C., Schwinger, J., Séférian, R.,

2566 Skjelvan, I., Stocker, B. D., Tian, H., Tilbrook, B., Tubiello, F. N., van der Laan-Luijkx, I. T., van

2567 der Werf, G. R., van Heuven, S., Viovy, N., Vuichard, N., Walker, A. P., Watson, A. J.,

2568 Wiltshire, A. J., Zaehle, S., and Zhu, D.: Global Carbon Budget 2017, Earth Syst. Sci. Data, 10,

2569 405–448, https://doi.org/10.5194/essd-10-405-2018, 2018a.

2570 Le Quéré, C., Andrew, R. M., Friedlingstein, P., Sitch, S., Hauck, J., Pongratz, J., Pickers, P. A.,

Korsbakken, J. I., Peters, G. P., Canadell, J. G., Arneth, A., Arora, V. K., Barbero, L., Bastos, A., Bopp, L., Chevallier, F., Chini, L. P., Ciais, P., Doney, S. C., Gkritzalis, T., Goll, D. S., Harris, I., Haverd, V., Hoffman, F. M., Hoppema, M., Houghton, R. A., Hurtt, G., Ilyina, T., Jain, A. K., Johannessen, T., Jones, C. D., Kato, E., Keeling, R. F., Klein Goldewijk, K., Landschützer, P., Lefèvre, N., Lienert, S., Liu, Z., Lombardozzi, D., Metzl, N., Munro, D. R., Nabel, J. E. M. S., Nakaoka, S., Neill, C., Olsen, A., Ono, T., Patra, P., Peregon, A., Peters, W., Peylin, P., Pfeil, B., Pierrot, D., Poulter, B., Rehder, G., Resplandy, L., Robertson, E., Rocher, M., Rödenbeck, C., Schuster, U., Schwinger, J., Séférian, R., Skjelvan, I., Steinhoff, T., Sutton, A., Tans, P. P., Tian, H., Tilbrook, B., Tubiello, F. N., van der Laan-Luijkx, I. T., van der Werf, G. R., Viovy, N., Walker, A. P., Wiltshire, A. J., Wright, R., Zaehle, S., and Zheng, B.: Global Carbon Budget 2018, Earth Syst. Sci. Data, 10, 2141–2194, https://doi.org/10.5194/essd-10-2141-2018, 2018b.

Le Quéré, C., Korsbakken, J. I., Wilson, C., Tosun, J., Andrew, R., Andres, R. J., Canadell, J. G., Jordan, A., Peters, G. P., and van Vuuren, D. P.: Drivers of declining CO2 emissions in 18 developed economies, Nat. Clim. Chang., 9, 213–217, https://doi.org/10.1038/s41558-019-0419-7, 2019.

Le Quéré, C., Peters, G. P., Friedlingstein, P., Andrew, R. M., Canadell, J. G., Davis, S. J., Jackson, R. B., and Jones, M. W.: Fossil CO2 emissions in the post-COVID-19 era, Nat. Clim. Chang., 11, 197–199, https://doi.org/10.1038/s41558-021-01001-0, 2021.

Li, H. and Ilyina, T.: Current and Future Decadal Trends in the Oceanic Carbon Uptake Are Dominated by Internal Variability, Geophys. Res. Lett., 45, 916–925, https://doi.org/10.1002/2017GL075370, 2018.

Li, W., Ciais, P., Peng, S., Yue, C., Wang, Y., Thurner, M., Saatchi, S. S., Arneth, A., Avitabile, V., Carvalhais, N., Harper, A. B., Kato, E., Koven, C., Liu, Y. Y., Nabel, J. E. M. S., Pan, Y., Pongratz, J., Poulter, B., Pugh, T. A. M., Santoro, M., Sitch, S., Stocker, B. D., Viovy, N., Wiltshire, A., Yousefpour, R., and Zaehle, S.: Land-use and land-cover change carbon emissions between 1901 and 2012 constrained by biomass observations, Biogeosciences, 14, 5053–5067, https://doi.org/10.5194/bg-14-5053-2017, 2017.

Liao, E., Resplandy, L., Liu, J., and Bowman, K. W.: Amplification of the Ocean Carbon Sink

2600 During El Niños: Role of Poleward Ekman Transport and Influence on Atmospheric CO2, 34,

2601 e2020GB006574, https://doi.org/10.1029/2020GB006574, 2020.

2602 Lienert, S. and Joos, F.: A Bayesian ensemble data assimilation to constrain model

2603 parameters and land-use carbon emissions, Biogeosciences, 15, 2909–2930,

2604 https://doi.org/10.5194/bg-15-2909-2018, 2018.

2605 Liu, J., Baskaran, L., Bowman, K., Schimel, D., Bloom, A. A., Parazoo, N. C., Oda, T., Carroll, D.,

2606 Menemenlis, D., Joiner, J., Commane, R., Daube, B., Gatti, L. V., McKain, K., Miller, J.,

2607 Stephens, B. B., Sweeney, C., and Wofsy, S.: Carbon Monitoring System Flux Net Biosphere

2608 Exchange 2020 (CMS-Flux NBE 2020), 13, 299–330, https://doi.org/10.5194/essd-13-299-

2609 2021, 2021.

2610 Liu, Z., Guan, D., Wei, W., Davis, S. J., Ciais, P., Bai, J., Peng, S., Zhang, Q., Hubacek, K.,

2611 Marland, G., Andres, R. J., Crawford-Brown, D., Lin, J., Zhao, H., Hong, C., Boden, T. A., Feng,

2612 K., Peters, G. P., Xi, F., Liu, J., Li, Y., Zhao, Y., Zeng, N., and He, K.: Reduced carbon emission

2613 estimates from fossil fuel combustion and cement production in China, Nature, 524, 335–

2614 338, https://doi.org/10.1038/nature14677, 2015.

2615 Liu, Z., Ciais, P., Deng, Z., Davis, S. J., Zheng, B., Wang, Y., Cui, D., Zhu, B., Dou, X., Ke, P., Sun,

2616 T., Guo, R., Zhong, H., Boucher, O., Bréon, F.-M., Lu, C., Guo, R., Xue, J., Boucher, E., Tanaka,

2617 K., and Chevallier, F.: Carbon Monitor, a near-real-time daily dataset of global CO2 emission

2618 from fossil fuel and cement production, Sci Data, 7, 392, https://doi.org/10.1038/s41597-

2619 020-00708-7, 2020a.

2620 Liu, Z., Ciais, P., Deng, Z., Lei, R., Davis, S. J., Feng, S., Zheng, B., Cui, D., Dou, X., Zhu, B., Guo,

2621 R., Ke, P., Sun, T., Lu, C., He, P., Wang, Y., Yue, X., Wang, Y., Lei, Y., Zhou, H., Cai, Z., Wu, Y.,

2622 Guo, R., Han, T., Xue, J., Boucher, O., Boucher, E., Chevallier, F., Tanaka, K., Wei, Y., Zhong,

2623 H., Kang, C., Zhang, N., Chen, B., Xi, F., Liu, M., Bréon, F.-M., Lu, Y., Zhang, Q., Guan, D.,

2624 Gong, P., Kammen, D. M., He, K., and Schellnhuber, H. J.: Near-real-time monitoring of

2625 global CO2 emissions reveals the effects of the COVID-19 pandemic, Nat Commun, 11, 5172,

2626 https://doi.org/10.1038/s41467-020-18922-7, 2020b.

2627 Ma, L., Hurtt, G. C., Chini, L. P., Sahajpal, R., Pongratz, J., Frolking, S., Stehfest, E., Klein

2628 Goldewijk, K., O'Leary, D., and Doelman, J. C.: Global rules for translating land-use change

2629 (LUH2) to land-cover change for CMIP6 using GLM2, Geosci. Model Dev., 13, 3203–3220,

2630 https://doi.org/10.5194/gmd-13-3203-2020, 2020.

2631 Maki, T., Ikegami, M., Fujita, T., Hirahara, T., Yamada, K., Mori, K., Takeuchi, A., Tsutsumi, Y.,

2632 Suda, K., and Conway, T. J.: New technique to analyse global distributions of CO_2

2633 concentrations and fluxes from non-processed observational data, 62, 797–809,

2634 https://doi.org/10.1111/j.1600-0889.2010.00488.x, 2010.

2635 MapBiomas: MapBiomas Collection 5, available at:

2636 https://plataforma.brasil.mapbiomas.org/, last access: 11 March 2022, 2021.

2637 Marland, G.: Uncertainties in Accounting for CO 2 From Fossil Fuels, 12, 136–139,

2638 https://doi.org/10.1111/j.1530-9290.2008.00014.x, 2008.

2639 Marland, G., Hamal, K., and Jonas, M.: How Uncertain Are Estimates of CO_2 Emissions?, 13,

2640 4–7, https://doi.org/10.1111/j.1530-9290.2009.00108.x, 2009.

2641 Masarie, K. A. and Tans, P. P.: Extension and integration of atmospheric carbon dioxide data

2642 into a globally consistent measurement record, J. Geophys. Res., 100, 11593,

2643 https://doi.org/10.1029/95JD00859, 1995.

2644 Mather, A.: The transition from deforestation to reforestation in Europe., 35–52, 2001.

2645 Matricardi, E. A. T., Skole, D. L., Costa, O. B., Pedlowski, M. A., Samek, J. H., and Miguel, E. P.:

2646 Long-term forest degradation surpasses deforestation in the Brazilian Amazon, 369, 1378–

2647 1382, https://doi.org/10.1126/science.abb3021, 2020.

2648 Mauritsen, T., Bader, J., Becker, T., Behrens, J., Bittner, M., Brokopf, R., Brovkin, V.,

2649 Claussen, M., Crueger, T., Esch, M., Fast, I., Fiedler, S., Fläschner, D., Gayler, V., Giorgetta,

2650 M., Goll, D. S., Haak, H., Hagemann, S., Hedemann, C., Hohenegger, C., Ilyina, T., Jahns, T.,

2651 Jimenéz-de-la-Cuesta, D., Jungclaus, J., Kleinen, T., Kloster, S., Kracher, D., Kinne, S., Kleberg,

2652 D., Lasslop, G., Kornblueh, L., Marotzke, J., Matei, D., Meraner, K., Mikolajewicz, U., Modali,

2653 K., Möbis, B., Müller, W. A., Nabel, J. E. M. S., Nam, C. C. W., Notz, D., Nyawira, S.-S.,

2654 Paulsen, H., Peters, K., Pincus, R., Pohlmann, H., Pongratz, J., Popp, M., Raddatz, T. J., Rast,

2655 S., Redler, R., Reick, C. H., Rohrschneider, T., Schemann, V., Schmidt, H., Schnur, R.,

2656 Schulzweida, U., Six, K. D., Stein, L., Stemmler, I., Stevens, B., von Storch, J.-S., Tian, F., Voigt,

2657   A., Vrese, P., Wieners, K.-H., Wilkenskjeld, S., Winkler, A., and Roeckner, E.: Developments in

2658   the MPI-M Earth System Model version 1.2 (MPI-ESM1.2) and Its Response to Increasing

2659   CO2, 11, 998–1038, https://doi.org/10.1029/2018MS001400, 2019.

2660   McGrath, M. J., Luyssaert, S., Meyfroidt, P., Kaplan, J. O., Bürgi, M., Chen, Y., Erb, K., Gimmi,

2661   U., McInerney, D., Naudts, K., Otto, J., Pasztor, F., Ryder, J., Schelhaas, M.-J., and Valade, A.:

2662   Reconstructing European forest management from 1600 to 2010, 12, 4291–4316,

2663   https://doi.org/10.5194/bg-12-4291-2015, 2015.

2664   McKinley, G. A., Pilcher, D. J., Fay, A. R., Lindsay, K., Long, M. C., and Lovenduski, N. S.:

2665   Timescales for detection of trends in the ocean carbon sink, Nature, 530, 469–472,

2666   https://doi.org/10.1038/nature16958, 2016.

2667   McKinley, G. A., Fay, A. R., Eddebbar, Y. A., Gloege, L., and Lovenduski, N. S.: External

2668   Forcing Explains Recent Decadal Variability of the Ocean Carbon Sink, AGU Advances, 1,

2669   https://doi.org/10.1029/2019AV000149, 2020.

2670   McNeil, B. I.: Anthropogenic CO2 Uptake by the Ocean Based on the Global

2671   Chlorofluorocarbon Data Set, 299, 235–239, https://doi.org/10.1126/science.1077429,

2672   2003.

2673   Meiyappan, P., Jain, A. K., and House, J. I.: Increased influence of nitrogen limitation on CO 2

2674   emissions from future land use and land use change, Global Biogeochem. Cycles, 29, 1524–

2675   1548, https://doi.org/10.1002/2015GB005086, 2015.

2676   Melton, J. R., Arora, V. K., Wisernig-Cojoc, E., Seiler, C., Fortier, M., Chan, E., and Teckentrup,

2677   L.: CLASSIC v1.0: the open-source community successor to the Canadian Land Surface

2678   Scheme (CLASS) and the Canadian Terrestrial Ecosystem Model (CTEM) – Part 1: Model

2679   framework and site-level performance, Geosci. Model Dev., 13, 2825–2850,

2680   https://doi.org/10.5194/gmd-13-2825-2020, 2020.

2681   Mercado, L. M., Bellouin, N., Sitch, S., Boucher, O., Huntingford, C., Wild, M., and Cox, P. M.:

2682   Impact of changes in diffuse radiation on the global land carbon sink, Nature, 458, 1014–

2683   1017, https://doi.org/10.1038/nature07949, 2009.

2684   Mikaloff Fletcher, S. E., Gruber, N., Jacobson, A. R., Doney, S. C., Dutkiewicz, S., Gerber, M.,

2685   Follows, M., Joos, F., Lindsay, K., Menemenlis, D., Mouchet, A., Müller, S. A., and Sarmiento,

2686   J. L.: Inverse estimates of anthropogenic CO 2 uptake, transport, and storage by the ocean:

2687   air-sea exchange of anthropogenic carbon, Global Biogeochem. Cycles, 20,

2688   https://doi.org/10.1029/2005GB002530, 2006.

2689   Myneni, R. B., Ramakrishna, R., Nemani, R., and Running, S. W.: Estimation of global leaf

2690   area index and absorbed par using radiative transfer models, IEEE Trans. Geosci. Remote

2691   Sensing, 35, 1380–1393, https://doi.org/10.1109/36.649788, 1997.

2692   Naegler, T.: Reconciliation of excess 14C-constrained global CO_2 piston velocity estimates,

2693   61, 372–384, https://doi.org/10.1111/j.1600-0889.2008.00408.x, 2009.

2694   Nakamura, T., Yamazaki, K., Iwamoto, K., Honda, M., Miyoshi, Y., Ogawa, Y., and Ukita, J.: A

2695   negative phase shift of the winter AO/NAO due to the recent Arctic sea-ice reduction in late

2696   autumn, 120, 3209–3227, https://doi.org/10.1002/2014JD022848, 2015.

2697   Narayanan, B., Aguiar, A., and McDougall, R.: Global Trade, Assistance, and Production: The

2698   GTAP 9 Data Base, Cent. Glob. Trade Anal. Purdue Univ., available at: https://

2699   www.gtap.agecon.purdue.edu/databases/v9/default.asp, last access: 11 March 2022, 2015.

2700   NBS: National Bureau of Statistics of China: Statistical Communiqué of the People's Republic

2701   of China on the 2021 National Economic and Social Development, available at:

2702   http://www.stats.gov.cn/english/PressRelease/202202/t20220227_1827963.html, last

2703   access: 11 March 2022, 2022.

2704   NCEP: National Centers for Environmental Prediction. ONI Index. Cold & Warm Episodes by

2705   Season, available at:

2706   https://origin.cpc.ncep.noaa.gov/products/analysis_monitoring/ensostuff/ONI_v5.php, last

2707   access: 11 March 2022, 2021.

2708   Nightingale, P. D., Liss, P. S., and Schlosser, P.: Measurements of air-sea gas transfer during

2709   an open ocean algal bloom, 27, 2117–2120, https://doi.org/10.1029/2000GL011541, 2000.

2710   Niwa, Y., Fujii, Y., Sawa, Y., Iida, Y., Ito, A., Satoh, M., Imasu, R., Tsuboi, K., Matsueda, H., and

2711   Saigusa, N.: A 4D-Var inversion system based on the icosahedral grid model (NICAM-TM 4D-

2712   Var v1.0) – Part 2: Optimization scheme and identical twin experiment of atmospheric CO2

2713   inversion, Geosci. Model Dev., 10, 2201–2219, https://doi.org/10.5194/gmd-10-2201-2017,

2714   2017.

2715   Niwa, Y., Langenfelds, R., Krummel, P., Loh, Zoe, Worthy, Doug, Hatakka, Juha, Aalto, Tuula,

2716   Ramonet, Michel, Delmotte, Marc, Schmidt, Martina, Gheusi, Francois, Mihalopoulos, N.,

2717   Morgui, J.A., Andrews, Arlyn, Dlugokencky, Ed, Lee, John, Sweeney, Colm, Thoning, Kirk,

2718   Tans, Pieter, De Wekker, Stephan, Fischer, Marc L., Jaffe, Dan, McKain, Kathryn, Viner, Brian,

2719   Miller, John B., Karion, Anna, Miller, Charles, Sloop, Christopher D., Saito, Kazuyuki, Aoki,

2720   Shuji, Morimoto, Shinji, Goto, Daisuke, Steinbacher, Martin, Myhre, Cathrine Lund,

2721   Hermanssen, Ove, Stephens, Britton, Keeling, Ralph, Afshar, Sara, Paplawsky, Bill, Cox,

2722   Adam, Walker, Stephen, Schuldt, Kenneth, Mukai, Hitoshi, Machida, Toshinobu, Sasakawa,

2723   Motoki, Nomura, Shohei, Ito, Akihiko, Iida, Yosuke, and Jones, Matthew W.: Long-term

2724   global CO2 fluxes estimated by NICAM-based Inverse Simulation for Monitoring CO2

2725   (NISMON-CO2) (ver.2020.1), https://doi.org/10.17595/20201127.001, 2020.

2726   Obermeier, W. A., Nabel, J. E. M. S., Loughran, T., Hartung, K., Bastos, A., Havermann, F.,

2727   Anthoni, P., Arneth, A., Goll, D. S., Lienert, S., Lombardozzi, D., Luyssaert, S., McGuire, P. C.,

2728   Melton, J. R., Poulter, B., Sitch, S., Sullivan, M. O., Tian, H., Walker, A. P., Wiltshire, A. J.,

2729   Zaehle, S., and Pongratz, J.: Modelled land use and land cover change emissions – a spatio-

2730   temporal comparison of different approaches, 12, 635–670, https://doi.org/10.5194/esd-

2731   12-635-2021, 2021.

2732   O'Rourke, P. R., Smith, S. J., Mott, A., Ahsan, H., McDuffie, E. E., Crippa, M., Klimont, Z.,

2733   McDonald, B., Wang, S., Nicholson, M. B., Feng, L., and Hoesly, R. M.: CEDS v_2021_04_21

2734   Release Emission Data, https://doi.org/10.5281/zenodo.4741285, 2021.

2735   Orr, J. C., Najjar, R. G., Aumont, O., Bopp, L., Bullister, J. L., Danabasoglu, G., Doney, S. C.,

2736   Dunne, J. P., Dutay, J.-C., Graven, H., Griffies, S. M., John, J. G., Joos, F., Levin, I., Lindsay, K.,

2737   Matear, R. J., McKinley, G. A., Mouchet, A., Oschlies, A., Romanou, A., Schlitzer, R.,

2738   Tagliabue, A., Tanhua, T., and Yool, A.: Biogeochemical protocols and diagnostics for the

2739   CMIP6 Ocean Model Intercomparison Project (OMIP), 10, 2169–2199,

2740   https://doi.org/10.5194/gmd-10-2169-2017, 2017.

2741   O'Sullivan, M., Zhang, Y., Bellouin, N., Harris, I., Mercado, L. M., Sitch, S., Ciais, P., and

2742 Friedlingstein, P.: Aerosol–light interactions reduce the carbon budget imbalance, Environ.
2743 Res. Lett., 16, 124072, https://doi.org/10.1088/1748-9326/ac3b77, 2021.

2744 Palmer, P. I., Feng, L., Baker, D., Chevallier, F., Bösch, H., and Somkuti, P.: Net carbon
2745 emissions from African biosphere dominate pan-tropical atmospheric CO2 signal, Nat
2746 Commun, 10, 3344, https://doi.org/10.1038/s41467-019-11097-w, 2019.

2747 Pan, Y., Birdsey, R. A., Fang, J., Houghton, R., Kauppi, P. E., Kurz, W. A., Phillips, O. L.,
2748 Shvidenko, A., Lewis, S. L., Canadell, J. G., Ciais, P., Jackson, R. B., Pacala, S. W., McGuire, A.
2749 D., Piao, S., Rautiainen, A., Sitch, S., and Hayes, D.: A Large and Persistent Carbon Sink in the
2750 World's Forests, Science, 333, 988–993, https://doi.org/10.1126/science.1201609, 2011.

2751 Patra, P. K., Takigawa, M., Watanabe, S., Chandra, N., Ishijima, K., and Yamashita, Y.:
2752 Improved Chemical Tracer Simulation by MIROC4.0-based Atmospheric Chemistry-Transport
2753 Model (MIROC4-ACTM), SOLA, 14, 91–96, https://doi.org/10.2151/sola.2018-016, 2018.

2754 Pendrill, F., Persson, U. M., Godar, J., Kastner, T., Moran, D., Schmidt, S., and Wood, R.:
2755 Agricultural and forestry trade drives large share of tropical deforestation emissions, Global
2756 Environmental Change, 56, 1–10, https://doi.org/10.1016/j.gloenvcha.2019.03.002, 2019.

2757 Peters, G. P., Andrew, R., and Lennox, J.: Constructing an environmentally-extended multi-
2758 regional input–output table using the GTAP database, Economic Systems Research, 23, 131–
2759 152, https://doi.org/10.1080/09535314.2011.563234, 2011a.

2760 Peters, G. P., Minx, J. C., Weber, C. L., and Edenhofer, O.: Growth in emission transfers via
2761 international trade from 1990 to 2008, Proceedings of the National Academy of Sciences,
2762 108, 8903–8908, https://doi.org/10.1073/pnas.1006388108, 2011b.

2763 Peters, G. P., Davis, S. J., and Andrew, R.: A synthesis of carbon in international trade,
2764 Biogeosciences, 9, 3247–3276, https://doi.org/10.5194/bg-9-3247-2012, 2012a.

2765 Peters, G. P., Marland, G., Le Quéré, C., Boden, T., Canadell, J. G., and Raupach, M. R.: Rapid
2766 growth in CO2 emissions after the 2008–2009 global financial crisis, Nature Clim Change, 2,
2767 2–4, https://doi.org/10.1038/nclimate1332, 2012b.

2768 Peters, G. P., Andrew, R. M., Boden, T., Canadell, J. G., Ciais, P., Le Quéré, C., Marland, G.,

2769   Raupach, M. R., and Wilson, C.: The challenge to keep global warming below 2 °C, Nature

2770   Clim Change, 3, 4–6, https://doi.org/10.1038/nclimate1783, 2013.

2771   Peters, G. P., Le Quéré, C., Andrew, R. M., Canadell, J. G., Friedlingstein, P., Ilyina, T.,

2772   Jackson, R. B., Joos, F., Korsbakken, J. I., McKinley, G. A., Sitch, S., and Tans, P.: Towards real-

2773   time verification of CO2 emissions, Nature Clim Change, 7, 848–850,

2774   https://doi.org/10.1038/s41558-017-0013-9, 2017.

2775   Peters, G. P., Andrew, R. M., Canadell, J. G., Friedlingstein, P., Jackson, R. B., Korsbakken, J.

2776   I., Le Quéré, C., and Peregon, A.: Carbon dioxide emissions continue to grow amidst slowly

2777   emerging climate policies, Nat. Clim. Chang., 10, 3–6, https://doi.org/10.1038/s41558-019-

2778   0659-6, 2020.

2779   Petrescu, A. M. R., Peters, G. P., Janssens-Maenhout, G., Ciais, P., Tubiello, F. N., Grassi, G.,

2780   Nabuurs, G.-J., Leip, A., Carmona-Garcia, G., Winiwarter, W., Höglund-Isaksson, L., Günther,

2781   D., Solazzo, E., Kiesow, A., Bastos, A., Pongratz, J., Nabel, J. E. M. S., Conchedda, G., Pilli, R.,

2782   Andrew, R. M., Schelhaas, M.-J., and Dolman, A. J.: European anthropogenic AFOLU

2783   greenhouse gas emissions: a review and benchmark data, Earth Syst. Sci. Data, 12, 961–

2784   1001, https://doi.org/10.5194/essd-12-961-2020, 2020.

2785   Pfeil, B., Olsen, A., Bakker, D. C. E., Hankin, S., Koyuk, H., Kozyr, A., Malczyk, J., Manke, A.,

2786   Metzl, N., Sabine, C. L., Akl, J., Alin, S. R., Bates, N., Bellerby, R. G. J., Borges, A., Boutin, J.,

2787   Brown, P. J., Cai, W.-J., Chavez, F. P., Chen, A., Cosca, C., Fassbender, A. J., Feely, R. A.,

2788   González-Dávila, M., Goyet, C., Hales, B., Hardman-Mountford, N., Heinze, C., Hood, M.,

2789   Hoppema, M., Hunt, C. W., Hydes, D., Ishii, M., Johannessen, T., Jones, S. D., Key, R. M.,

2790   Körtzinger, A., Landschützer, P., Lauvset, S. K., Lefèvre, N., Lenton, A., Lourantou, A.,

2791   Merlivat, L., Midorikawa, T., Mintrop, L., Miyazaki, C., Murata, A., Nakadate, A., Nakano, Y.,

2792   Nakaoka, S., Nojiri, Y., Omar, A. M., Padin, X. A., Park, G.-H., Paterson, K., Perez, F. F.,

2793   Pierrot, D., Poisson, A., Ríos, A. F., Santana-Casiano, J. M., Salisbury, J., Sarma, V. V. S. S.,

2794   Schlitzer, R., Schneider, B., Schuster, U., Sieger, R., Skjelvan, I., Steinhoff, T., Suzuki, T.,

2795   Takahashi, T., Tedesco, K., Telszewski, M., Thomas, H., Tilbrook, B., Tjiputra, J., Vandemark,

2796   D., Veness, T., Wanninkhof, R., Watson, A. J., Weiss, R., Wong, C. S., and Yoshikawa-Inoue,

2797   H.: A uniform, quality controlled Surface Ocean CO2 Atlas (SOCAT), Earth Syst. Sci. Data, 5,

2798   125–143, https://doi.org/10.5194/essd-5-125-2013, 2013.

2799   Piao, S., Ciais, P., Friedlingstein, P., de Noblet-Ducoudré, N., Cadule, P., Viovy, N., and Wang,

2800   T.: Spatiotemporal patterns of terrestrial carbon cycle during the 20th century, 23,

2801   https://doi.org/10.1029/2008GB003339, 2009.

2802   Piao, S., Huang, M., Liu, Z., Wang, X., Ciais, P., Canadell, J. G., Wang, K., Bastos, A.,

2803   Friedlingstein, P., Houghton, R. A., Le Quéré, C., Liu, Y., Myneni, R. B., Peng, S., Pongratz, J.,

2804   Sitch, S., Yan, T., Wang, Y., Zhu, Z., Wu, D., and Wang, T.: Lower land-use emissions

2805   responsible for increased net land carbon sink during the slow warming period, Nature

2806   Geosci, 11, 739–743, https://doi.org/10.1038/s41561-018-0204-7, 2018.

2807   Pongratz, J., Reick, C. H., Houghton, R. A., and House, J. I.: Terminology as a key uncertainty

2808   in net land use and land cover change carbon flux estimates, Earth Syst. Dynam., 5, 177–

2809   195, https://doi.org/10.5194/esd-5-177-2014, 2014.

2810   Potapov, P., Hansen, M. C., Laestadius, L., Turubanova, S., Yaroshenko, A., Thies, C., Smith,

2811   W., Zhuravleva, I., Komarova, A., Minnemeyer, S., and Esipova, E.: The last frontiers of

2812   wilderness: Tracking loss of intact forest landscapes from 2000 to 2013, 3, e1600821,

2813   https://doi.org/10.1126/sciadv.1600821, 2017.

2814   Poulter, B., Frank, D. C., Hodson, E. L., and Zimmermann, N. E.: Impacts of land cover and

2815   climate data selection on understanding terrestrial carbon dynamics and the CO2 airborne

2816   fraction, Biogeosciences, 8, 2027–2036, https://doi.org/10.5194/bg-8-2027-2011, 2011.

2817   Poulter, B., Freeborn, P. H., Jolly, W. M., and Varner, J. M.: COVID-19 lockdowns drive

2818   decline in active fires in southeastern United States, PNAS, 118,

2819   https://doi.org/10.1073/pnas.2105666118, 2021.

2820   Prather, M.: Interactive comment on "Carbon dioxide and climate impulse response

2821   functions for the computation of greenhouse gas metrics: a multi-model analysis" by F. Joos

2822   et al., 6, 2012.

2823   Prentice, I. C., Farquhar, G. D., Fasham, M. J. R., Goulden, M. L., Heimann, M., Jaramillo, V.

2824   J., Kheshgi, H. S., Le Quéré, C., Scholes, R. J., and Wallace, D. W. R.: The Carbon Cycle and

2825   Atmospheric Carbon Dioxide, in Climate Change 2001: The Scientific Basis. Contribution of

2826   Working Group I to the Third Assessment Report of the Intergovernmental Panel on Climate

Change, edited by: Houghton, J. T., Ding, Y., Griggs, D. J., Noguer, M., van der Linden, P. J., Dai, X., Maskell, K., and Johnson, C. A., Cambridge University Press, Cambridge, United Kingdom and New York, NY, USA, 183–237, 2001.

Price, J. T. and Warren, R.: Literature Review of the Potential of "Blue Carbon" Activities to Reduce Emissions, available at: https://avoid-net-uk.cc.ic.ac.uk/wp-content/uploads/delightful-downloads/2016/03/Literature-review-of-the-potential-of-blue-carbon-activities-to-reduce-emissions-AVOID2-WPE2.pdf, last access: 11 March 2022, 2016.

Qin, Y., Xiao, X., Wigneron, J.-P., Ciais, P., Brandt, M., Fan, L., Li, X., Crowell, S., Wu, X., Doughty, R., Zhang, Y., Liu, F., Sitch, S., and Moore, B.: Carbon loss from forest degradation exceeds that from deforestation in the Brazilian Amazon, Nat. Clim. Chang., 11, 442–448, https://doi.org/10.1038/s41558-021-01026-5, 2021.

Qiu, C., Ciais, P., Zhu, D., Guenet, B., Peng, S., Petrescu, A. M. R., Lauerwald, R., Makowski, D., Gallego-Sala, A. V., Charman, D. J., and Brewer, S. C.: Large historical carbon emissions from cultivated northern peatlands, 7, eabf1332, https://doi.org/10.1126/sciadv.abf1332, 2021.

Raupach, M. R., Marland, G., Ciais, P., Le Quere, C., Canadell, J. G., Klepper, G., and Field, C. B.: Global and regional drivers of accelerating CO_2 emissions, Proceedings of the National Academy of Sciences, 104, 10288–10293, https://doi.org/10.1073/pnas.0700609104, 2007.

Regnier, P., Friedlingstein, P., Ciais, P., Mackenzie, F. T., Gruber, N., Janssens, I. A., Laruelle, G. G., Lauerwald, R., Luyssaert, S., Andersson, A. J., Arndt, S., Arnosti, C., Borges, A. V., Dale, A. W., Gallego-Sala, A., Goddéris, Y., Goossens, N., Hartmann, J., Heinze, C., Ilyina, T., Joos, F., LaRowe, D. E., Leifeld, J., Meysman, F. J. R., Munhoven, G., Raymond, P. A., Spahni, R., Suntharalingam, P., and Thullner, M.: Anthropogenic perturbation of the carbon fluxes from land to ocean, Nature Geosci, 6, 597–607, https://doi.org/10.1038/ngeo1830, 2013.

Reick, C. H., Gayler, V., Goll, D., Hagemann, S., Heidkamp, M., Nabel, J. E. M. S., Raddatz, T., Roeckner, E., Schnur, R., and Wilkenskjeld, S.: JSBACH 3 - The land component of the MPI Earth System Model: documentation of version 3.2, https://doi.org/10.17617/2.3279802, 2021.

2855 Remaud, M., Chevallier, F., Cozic, A., Lin, X., and Bousquet, P.: On the impact of recent

2856 developments of the LMDz atmospheric general circulation model on the simulation of CO2

2857 transport, 11, 4489, https://doi.org/10.5194/gmd-11-4489-2018, 2018.

2858 Resplandy, L., Keeling, R. F., Rödenbeck, C., Stephens, B. B., Khatiwala, S., Rodgers, K. B.,

2859 Long, M. C., Bopp, L., and Tans, P. P.: Revision of global carbon fluxes based on a

2860 reassessment of oceanic and riverine carbon transport, Nature Geosci, 11, 504–509,

2861 https://doi.org/10.1038/s41561-018-0151-3, 2018.

2862 Rhein, M., Rintoul, S. R., Aoki, S., Campos, E., Chambers, D., Feely, R. A., Gulev, S., Johnson,

2863 G. C., Josey, S. A., Kostianoy, A., Mauritzen, C., Roemmich, D., and Talley, L. D.:

2864 Observations: Ocean, edited by: Stocker, T. F., Qin, D., Plattner, G.-K., Tignor, M., Allen, S. K.,

2865 Boschung, J., Nauels, A., Xia, Y., Bex, V., and Midgley, P. M., Cambridge University Press,

2866 255–316, 2013.

2867 Rodenbeck, C., Houweling, S., Gloor, M., and Heimann, M.: CO2 flux history 1982–2001

2868 inferred from atmospheric data using a global inversion of atmospheric transport, 46, 2003.

2869 Rödenbeck, C., Keeling, R. F., Bakker, D. C. E., Metzl, N., Olsen, A., Sabine, C., and Heimann,

2870 M.: Global surface-ocean pCO2 and sea–air CO2 flux variability from an observation-driven

2871 ocean mixed-layer scheme, 9, 193–216, https://doi.org/10.5194/os-9-193-2013, 2013.

2872 Rödenbeck, C., Bakker, D. C. E., Metzl, N., Olsen, A., Sabine, C., Cassar, N., Reum, F., Keeling,

2873 R. F., and Heimann, M.: Interannual sea–air CO2 flux variability from an observation-driven

2874 ocean mixed-layer scheme, 11, 4599–4613, https://doi.org/10.5194/bg-11-4599-2014,

2875 2014.

2876 Rödenbeck, C., Bakker, D. C. E., Gruber, N., Iida, Y., Jacobson, A. R., Jones, S., Landschützer,

2877 P., Metzl, N., Nakaoka, S., Olsen, A., Park, G.-H., Peylin, P., Rodgers, K. B., Sasse, T. P.,

2878 Schuster, U., Shutler, J. D., Valsala, V., Wanninkhof, R., and Zeng, J.: Data-based estimates of

2879 the ocean carbon sink variability – first results of the Surface Ocean CO2 Mapping

2880 intercomparison (SOCOM), Biogeosciences, 12, 7251–7278, https://doi.org/10.5194/bg-12-

2881 7251-2015, 2015.

2882 Rödenbeck, C., Zaehle, S., Keeling, R., and Heimann, M.: History of El Niño impacts on the

2883   global carbon cycle 1957–2017: a quantification from atmospheric CO2 data, 373,

2884   20170303, https://doi.org/10.1098/rstb.2017.0303, 2018.

2885   Roobaert, A., Laruelle, G. G., Landschützer, P., and Regnier, P.: Uncertainty in the global

2886   oceanic CO2 uptake induced by wind forcing: quantification and spatial analysis, 15, 1701–

2887   1720, https://doi.org/10.5194/bg-15-1701-2018, 2018.

2888   Rosan, T. M., Klein Goldewijk, K., Ganzenmüller, R., O'Sullivan, M., Pongratz, J., Mercado, L.

2889   M., Aragao, L. E. O. C., Heinrich, V., Randow, C. V., Wiltshire, A., Tubiello, F. N., Bastos, A.,

2890   Friedlingstein, P., and Sitch, S.: A multi-data assessment of land use and land cover

2891   emissions from Brazil during 2000–2019, Environ. Res. Lett., 16, 074004,

2892   https://doi.org/10.1088/1748-9326/ac08c3, 2021.

2893   Rypdal, K., Paciornik, N., Eggleston, S., Goodwin, J., Irving, W., Penman, J., and Woodfield,

2894   M.: Volume 1: Introduction to the 2006 Guidelines in: 2006 IPCC guidelines for national

2895   greenhouse gas inventories., 2006.

2896   Saatchi, S. S., Harris, N. L., Brown, S., Lefsky, M., Mitchard, E. T. A., Salas, W., Zutta, B. R.,

2897   Buermann, W., Lewis, S. L., Hagen, S., Petrova, S., White, L., Silman, M., and Morel, A.:

2898   Benchmark map of forest carbon stocks in tropical regions across three continents,

2899   Proceedings of the National Academy of Sciences, 108, 9899–9904,

2900   https://doi.org/10.1073/pnas.1019576108, 2011.

2901   Sabine, C. L., Feely, R. A., Gruber, N., Key, R. M., Lee, K., Bullister, J. L., Wanninkhof, R.,

2902   Wong, C. S., Wallace, D. W. R., Tilbrook, B., Millero, F. J., Peng, T.-H., Kozyr, A., Ono, T., and

2903   Rios, A. F.: The Oceanic Sink for Anthropogenic CO2, 305, 367–371,

2904   https://doi.org/10.1126/science.1097403, 2004.

2905   Sarmiento, J. L., Orr, J. C., and Siegenthaler, U.: A perturbation simulation of CO2 uptake in

2906   an ocean general circulation model, 97, 3621–3645, https://doi.org/10.1029/91JC02849,

2907   1992.

2908   Sato, M., Hansen, J. E., McCormick, M. P., and Pollack, J. B.: Stratospheric aerosol optical

2909   depths, 1850–1990, 98, 22987–22994, https://doi.org/10.1029/93JD02553, 1993.

2910   Saunois, M., Stavert, A. R., Poulter, B., Bousquet, P., Canadell, J. G., Jackson, R. B., Raymond,

P. A., Dlugokencky, E. J., Houweling, S., Patra, P. K., Ciais, P., Arora, V. K., Bastviken, D., Bergamaschi, P., Blake, D. R., Brailsford, G., Bruhwiler, L., Carlson, K. M., Carrol, M., Castaldi, S., Chandra, N., Crevoisier, C., Crill, P. M., Covey, K., Curry, C. L., Etiope, G., Frankenberg, C., Gedney, N., Hegglin, M. I., Höglund-Isaksson, L., Hugelius, G., Ishizawa, M., Ito, A., Janssens-Maenhout, G., Jensen, K. M., Joos, F., Kleinen, T., Krummel, P. B., Langenfelds, R. L., Laruelle, G. G., Liu, L., Machida, T., Maksyutov, S., McDonald, K. C., McNorton, J., Miller, P. A., Melton, J. R., Morino, I., Müller, J., Murguia-Flores, F., Naik, V., Niwa, Y., Noce, S., O'Doherty, S., Parker, R. J., Peng, C., Peng, S., Peters, G. P., Prigent, C., Prinn, R., Ramonet, M., Regnier, P., Riley, W. J., Rosentreter, J. A., Segers, A., Simpson, I. J., Shi, H., Smith, S. J., Steele, L. P., Thornton, B. F., Tian, H., Tohjima, Y., Tubiello, F. N., Tsuruta, A., Viovy, N., Voulgarakis, A., Weber, T. S., van Weele, M., van der Werf, G. R., Weiss, R. F., Worthy, D., Wunch, D., Yin, Y., Yoshida, Y., Zhang, W., Zhang, Z., Zhao, Y., Zheng, B., Zhu, Q., Zhu, Q., and Zhuang, Q.: The Global Methane Budget 2000–2017, Earth Syst. Sci. Data, 12, 1561–1623, https://doi.org/10.5194/essd-12-1561-2020, 2020.

Schimel, D., Alves, D., Enting, I. G., Heimann, M., Joos, F., Raynaud, D., Wigley, T., Prater, M., Derwent, R., Ehhalt, D., Fraser, P., Sanhueza, E., Zhou, X., Jonas, P., Charlson, R., Rodhe, H., Sadasivan, S., Shine, K. P., Fouquart, Y., Ramaswamy, V., Solomon, S., Srinivasan, J., Albritton, D., Derwent, R., Isaksen, I., Lal, M., and Wuebbles, D.: Radiative Forcing of Climate Change, in: Climate Change 1995 The Science of Climate Change, Contribution of Working Group I to the Second Assessment Report of the Intergovernmental Panel on Climate Change, edited by: Houghton, J. T., Meira Rilho, L. G., Callander, B. A., Harris, N., Kattenberg, A., and Maskell, K., Cambridge University Press, Cambridge, United Kingdom and New York, NY, USA, 1995.

Schimel, D., Stephens, B. B., and Fisher, J. B.: Effect of increasing CO_2 on the terrestrial carbon cycle, Proc Natl Acad Sci USA, 112, 436–441, https://doi.org/10.1073/pnas.1407302112, 2015.

Schourup-Kristensen, V., Sidorenko, D., Wolf-Gladrow, D. A., and Völker, C.: A skill assessment of the biogeochemical model REcoM2 coupled to the Finite Element Sea Ice–Ocean Model (FESOM 1.3), Geosci. Model Dev., 7, 2769–2802, https://doi.org/10.5194/gmd-7-2769-2014, 2014.

2941 Schuh, A. E., Jacobson, A. R., Basu, S., Weir, B., Baker, D., Bowman, K., Chevallier, F., Crowell,

2942 S., Davis, K. J., Deng, F., Denning, S., Feng, L., Jones, D., Liu, J., and Palmer, P. I.: Quantifying

2943 the Impact of Atmospheric Transport Uncertainty on CO 2 Surface Flux Estimates, Global

2944 Biogeochem. Cycles, 33, 484–500, https://doi.org/10.1029/2018GB006086, 2019.

2945 Schwinger, J., Goris, N., Tjiputra, J. F., Kriest, I., Bentsen, M., Bethke, I., Ilicak, M., Assmann,

2946 K. M., and Heinze, C.: Evaluation of NorESM-OC (versions 1 and 1.2), the ocean carbon-cycle

2947 stand-alone configuration of the Norwegian Earth System Model (NorESM1), Geosci. Model

2948 Dev., 9, 2589–2622, https://doi.org/10.5194/gmd-9-2589-2016, 2016.

2949 Séférian, R., Nabat, P., Michou, M., Saint-Martin, D., Voldoire, A., Colin, J., Decharme, B.,

2950 Delire, C., Berthet, S., Chevallier, M., Sénési, S., Franchisteguy, L., Vial, J., Mallet, M.,

2951 Joetzjer, E., Geoffroy, O., Guérémy, J.-F., Moine, M.-P., Msadek, R., Ribes, A., Rocher, M.,

2952 Roehrig, R., Salas-y-Mélia, D., Sanchez, E., Terray, L., Valcke, S., Waldman, R., Aumont, O.,

2953 Bopp, L., Deshayes, J., Éthé, C., and Madec, G.: Evaluation of CNRM Earth System Model,

2954 CNRM-ESM2-1: Role of Earth System Processes in Present-Day and Future Climate, 11,

2955 4182–4227, https://doi.org/10.1029/2019MS001791, 2019.

2956 Sellar, A. A., Jones, C. G., Mulcahy, J. P., Tang, Y., Yool, A., Wiltshire, A., O'Connor, F. M.,

2957 Stringer, M., Hill, R., Palmieri, J., Woodward, S., Mora, L., Kuhlbrodt, T., Rumbold, S. T.,

2958 Kelley, D. I., Ellis, R., Johnson, C. E., Walton, J., Abraham, N. L., Andrews, M. B., Andrews, T.,

2959 Archibald, A. T., Berthou, S., Burke, E., Blockley, E., Carslaw, K., Dalvi, M., Edwards, J.,

2960 Folberth, G. A., Gedney, N., Griffiths, P. T., Harper, A. B., Hendry, M. A., Hewitt, A. J.,

2961 Johnson, B., Jones, A., Jones, C. D., Keeble, J., Liddicoat, S., Morgenstern, O., Parker, R. J.,

2962 Predoi, V., Robertson, E., Siahaan, A., Smith, R. S., Swaminathan, R., Woodhouse, M. T.,

2963 Zeng, G., and Zerroukat, M.: UKESM1: Description and Evaluation of the U.K. Earth System

2964 Model, J. Adv. Model. Earth Syst., 11, 4513–4558, https://doi.org/10.1029/2019MS001739,

2965 2019.

2966 Shu, S., Jain, A. K., Koven, C. D., and Mishra, U.: Estimation of Permafrost SOC Stock and

2967 Turnover Time Using a Land Surface Model With Vertical Heterogeneity of Permafrost Soils,

2968 34, e2020GB006585, https://doi.org/10.1029/2020GB006585, 2020.

2969 Silva Junior, C. H. L., Pessôa, A. C. M., Carvalho, N. S., Reis, J. B. C., Anderson, L. O., and

2970   Aragão, L. E. O. C.: The Brazilian Amazon deforestation rate in 2020 is the greatest of the

2971   decade, Nat Ecol Evol, 5, 144–145, https://doi.org/10.1038/s41559-020-01368-x, 2021.

2972   Sitch, S., Huntingford, C., Gedney, N., Levy, P. E., Lomas, M., Piao, S. L., Betts, R., Ciais, P.,

2973   Cox, P., Friedlingstein, P., Jones, C. D., Prentice, I. C., and Woodward, F. I.: Evaluation of the

2974   terrestrial carbon cycle, future plant geography and climate-carbon cycle feedbacks using

2975   five Dynamic Global Vegetation Models (DGVMs): Uncertainty In Land Carbon Cycle

2976   Feedbacks, 14, 2015–2039, https://doi.org/10.1111/j.1365-2486.2008.01626.x, 2008.

2977   Smith, B., Wårlind, D., Arneth, A., Hickler, T., Leadley, P., Siltberg, J., and Zaehle, S.:

2978   Implications of incorporating N cycling and N limitations on primary production in an

2979   individual-based dynamic vegetation model, Biogeosciences, 11, 2027–2054,

2980   https://doi.org/10.5194/bg-11-2027-2014, 2014.

2981   Stephens, B. B., Gurney, K. R., Tans, P. P., Sweeney, C., Peters, W., Bruhwiler, L., Ciais, P.,

2982   Ramonet, M., Bousquet, P., Nakazawa, T., Aoki, S., Machida, T., Inoue, G., Vinnichenko, N.,

2983   Lloyd, J., Jordan, A., Heimann, M., Shibistova, O., Langenfelds, R. L., Steele, L. P., Francey, R.

2984   J., and Denning, A. S.: Weak Northern and Strong Tropical Land Carbon Uptake from Vertical

2985   Profiles of Atmospheric CO2, Science, 316, 1732–1735,

2986   https://doi.org/10.1126/science.1137004, 2007.

2987   Stocker, T., Qin, D., and Platner, G.-K.: Climate Change 2013: The Physical Science Basis.

2988   Contribution of Working Group I to the Fifth Assessment Report of the Intergovernmental

2989   Panel on Climate Change, edited by: Intergovernmental Panel on Climate Change,

2990   Cambridge University Press, Cambridge, 2013.

2991   Sweeney, C., Gloor, E., Jacobson, A. R., Key, R. M., McKinley, G., Sarmiento, J. L., and

2992   Wanninkhof, R.: Constraining global air-sea gas exchange for CO2 with recent bomb 14C

2993   measurements, 21, https://doi.org/10.1029/2006GB002784, 2007.

2994   Takahashi, T., Sutherland, S. C., Wanninkhof, R., Sweeney, C., Feely, R. A., Chipman, D. W.,

2995   Hales, B., Friederich, G., Chavez, F., Sabine, C., Watson, A., Bakker, D. C. E., Schuster, U.,

2996   Metzl, N., Yoshikawa-Inoue, H., Ishii, M., Midorikawa, T., Nojiri, Y., Körtzinger, A., Steinhoff,

2997   T., Hoppema, M., Olafsson, J., Arnarson, T. S., Tilbrook, B., Johannessen, T., Olsen, A.,

2998   Bellerby, R., Wong, C. S., Delille, B., Bates, N. R., and de Baar, H. J. W.: Climatological mean

2999 and decadal change in surface ocean pCO2, and net sea–air CO2 flux over the global oceans,

3000 Deep Sea Research Part II: Topical Studies in Oceanography, 56, 554–577,

3001 https://doi.org/10.1016/j.dsr2.2008.12.009, 2009.

3002 Thomason, L. W., Ernest, N., Millán, L., Rieger, L., Bourassa, A., Vernier, J.-P., Manney, G.,

3003 Luo, B., Arfeuille, F., and Peter, T.: A global space-based stratospheric aerosol climatology:

3004 1979–2016, 10, 469–492, https://doi.org/10.5194/essd-10-469-2018, 2018.

3005 Tian, H., Xu, X., Lu, C., Liu, M., Ren, W., Chen, G., Melillo, J., and Liu, J.: Net exchanges of

3006 CO2, CH4, and N2O between China's terrestrial ecosystems and the atmosphere and their

3007 contributions to global climate warming, 116, https://doi.org/10.1029/2010JG001393, 2011.

3008 Tian, H., Chen, G., Lu, C., Xu, X., Hayes, D. J., Ren, W., Pan, S., Huntzinger, D. N., and Wofsy,

3009 S. C.: North American terrestrial CO2 uptake largely offset by CH4 and N2O emissions:

3010 toward a full accounting of the greenhouse gas budget, Climatic Change, 129, 413–426,

3011 https://doi.org/10.1007/s10584-014-1072-9, 2015.

3012 Todd-Brown, K. E. O., Randerson, J. T., Post, W. M., Hoffman, F. M., Tarnocai, C., Schuur, E.

3013 A. G., and Allison, S. D.: Causes of variation in soil carbon simulations from CMIP5 Earth

3014 system models and comparison with observations, Biogeosciences, 10, 1717–1736,

3015 https://doi.org/10.5194/bg-10-1717-2013, 2013.

3016 Tohjima, Y., Mukai, H., Machida, T., Hoshina, Y., and Nakaoka, S.-I.: Global carbon budgets

3017 estimated from atmospheric O2∕N2 and CO2 observations in the western Pacific region over

3018 a 15-year period, 19, 9269–9285, https://doi.org/10.5194/acp-19-9269-2019, 2019.

3019 Tubiello, F. N., Conchedda, G., Wanner, N., Federici, S., Rossi, S., and Grassi, G.: Carbon

3020 emissions and removals from forests: new estimates, 1990–2020, 13, 1681–1691,

3021 https://doi.org/10.5194/essd-13-1681-2021, 2021.

3022 UN: United Nations Statistics Division: National Accounts Main Aggregates Database,

3023 available at: http://unstats.un.org/unsd/snaama/Introduction.asp, last access: 11 March

3024 2022, 2021.

3025 UNFCCC: National Inventory Submissions, available at: https://unfccc.int/ghg-inventories-

3026 annex-i-parties/2021, last access: 11 March 2022, 2021a.

3027 UNFCCC: Nationally determined contributions under the Paris Agreement. Synthesis report

3028 by the secretariat, available at: https://unfccc.int/documents/306848, last access: 11 March

3029 2022, 2021b.

3030 Vale, M. M., Berenguer, E., Argollo de Menezes, M., Viveiros de Castro, E. B., Pugliese de

3031 Siqueira, L., and Portela, R. de C. Q.: The COVID-19 pandemic as an opportunity to weaken

3032 environmental protection in Brazil, Biological Conservation, 255, 108994,

3033 https://doi.org/10.1016/j.biocon.2021.108994, 2021.

3034 van der Laan-Luijkx, I. T., van der Velde, I. R., van der Veen, E., Tsuruta, A., Stanislawska, K.,

3035 Babenhauserheide, A., Zhang, H. F., Liu, Y., He, W., Chen, H., Masarie, K. A., Krol, M. C., and

3036 Peters, W.: The CarbonTracker Data Assimilation Shell (CTDAS) v1.0: implementation and

3037 global carbon balance 2001–2015, Geosci. Model Dev., 10, 2785–2800,

3038 https://doi.org/10.5194/gmd-10-2785-2017, 2017.

3039 van der Velde, I. R., Miller, J. B., Schaefer, K., van der Werf, G. R., Krol, M. C., and Peters, W.:

3040 Terrestrial cycling of 13CO2 by photosynthesis, respiration, and biomass burning in SiBCASA,

3041 11, 6553–6571, https://doi.org/10.5194/bg-11-6553-2014, 2014.

3042 van der Velde, I. R., van der Werf, G. R., Houweling, S., Maasakkers, J. D., Borsdorff, T.,

3043 Landgraf, J., Tol, P., van Kempen, T. A., van Hees, R., Hoogeveen, R., Veefkind, J. P., and

3044 Aben, I.: Vast CO2 release from Australian fires in 2019–2020 constrained by satellite, 597,

3045 366–369, https://doi.org/10.1038/s41586-021-03712-y, 2021.

3046 van der Werf, G. R., Randerson, J. T., Giglio, L., Collatz, G. J., Mu, M., Kasibhatla, P. S.,

3047 Morton, D. C., DeFries, R. S., Jin, Y., and van Leeuwen, T. T.: Global fire emissions and the

3048 contribution of deforestation, savanna, forest, agricultural, and peat fires (1997–2009),

3049 Atmos. Chem. Phys., 10, 11707–11735, https://doi.org/10.5194/acp-10-11707-2010, 2010.

3050 van der Werf, G. R., Randerson, J. T., Giglio, L., van Leeuwen, T. T., Chen, Y., Rogers, B. M.,

3051 Mu, M., van Marle, M. J. E., Morton, D. C., Collatz, G. J., Yokelson, R. J., and Kasibhatla, P. S.:

3052 Global fire emissions estimates during 1997–2016, Earth Syst. Sci. Data, 9, 697–720,

3053 https://doi.org/10.5194/essd-9-697-2017, 2017.

3054 Viovy, N.: CRUNCEP data set, available at:

3055   ftp://nacp.ornl.gov/synthesis/2009/frescati/temp/land_use_change/original/readme.htm,

3056   last access: 11 March 2022, 2016.

3057   Vuichard, N., Messina, P., Luyssaert, S., Guenet, B., Zaehle, S., Ghattas, J., Bastrikov, V., and

3058   Peylin, P.: Accounting for carbon and nitrogen interactions in the global terrestrial

3059   ecosystem model ORCHIDEE (trunk version, rev 4999): multi-scale evaluation of gross

3060   primary production, Geosci. Model Dev., 12, 4751–4779, https://doi.org/10.5194/gmd-12-

3061   4751-2019, 2019.

3062   Walker, A. P., Quaife, T., Bodegom, P. M., De Kauwe, M. G., Keenan, T. F., Joiner, J., Lomas,

3063   M. R., MacBean, N., Xu, C., Yang, X., and Woodward, F. I.: The impact of alternative trait-

3064   scaling hypotheses for the maximum photosynthetic carboxylation rate (V_{cmax}) on global

3065   gross primary production, New Phytol, 215, 1370–1386,

3066   https://doi.org/10.1111/nph.14623, 2017.

3067   Walker, A. P., De Kauwe, M. G., Bastos, A., Belmecheri, S., Georgiou, K., Keeling, R. F.,

3068   McMahon, S. M., Medlyn, B. E., Moore, D. J. P., Norby, R. J., Zaehle, S., Anderson-Teixeira, K.

3069   J., Battipaglia, G., Brienen, R. J. W., Cabugao, K. G., Cailleret, M., Campbell, E., Canadell, J. G.,

3070   Ciais, P., Craig, M. E., Ellsworth, D. S., Farquhar, G. D., Fatichi, S., Fisher, J. B., Frank, D. C.,

3071   Graven, H., Gu, L., Haverd, V., Heilman, K., Heimann, M., Hungate, B. A., Iversen, C. M., Joos,

3072   F., Jiang, M., Keenan, T. F., Knauer, J., Körner, C., Leshyk, V. O., Leuzinger, S., Liu, Y.,

3073   MacBean, N., Malhi, Y., McVicar, T. R., Penuelas, J., Pongratz, J., Powell, A. S., Riutta, T.,

3074   Sabot, M. E. B., Schleucher, J., Sitch, S., Smith, W. K., Sulman, B., Taylor, B., Terrer, C., Torn,

3075   M. S., Treseder, K. K., Trugman, A. T., Trumbore, S. E., van Mantgem, P. J., Voelker, S. L.,

3076   Whelan, M. E., and Zuidema, P. A.: Integrating the evidence for a terrestrial carbon sink

3077   caused by increasing atmospheric CO_2, 229, 2413–2445,

3078   https://doi.org/10.1111/nph.16866, 2021.

3079   Wanninkhof, R.: Relationship between wind speed and gas exchange over the ocean, 97,

3080   7373–7382, https://doi.org/10.1029/92JC00188, 1992.

3081   Wanninkhof, R.: Relationship between wind speed and gas exchange over the ocean

3082   revisited, 12, 351–362, https://doi.org/10.4319/lom.2014.12.351, 2014.

3083   Wanninkhof, R., Park, G.-H., Takahashi, T., Sweeney, C., Feely, R., Nojiri, Y., Gruber, N.,

3084 Doney, S. C., McKinley, G. A., Lenton, A., Le Quéré, C., Heinze, C., Schwinger, J., Graven, H.,

3085 and Khatiwala, S.: Global ocean carbon uptake: magnitude, variability and trends,

3086 Biogeosciences, 10, 1983–2000, https://doi.org/10.5194/bg-10-1983-2013, 2013.

3087 Watson, A. J., Schuster, U., Shutler, J. D., Holding, T., Ashton, I. G. C., Landschützer, P.,

3088 Woolf, D. K., and Goddijn-Murphy, L.: Revised estimates of ocean-atmosphere CO2 flux are

3089 consistent with ocean carbon inventory, Nat Commun, 11, 4422,

3090 https://doi.org/10.1038/s41467-020-18203-3, 2020.

3091 Watson, R. T., Rohde, H., Oeschger, H., and Siegenthaler, U.: Greenhouse Gases and

3092 Aerosols, in: Climate Change: The IPCC Scientific Assessment. Intergovernmental Panel on

3093 Climate Change (IPCC), edited by: Houghton, J. T., Jenkins, G. J., and Ephraums, J. J.,

3094 Cambridge University Press, Cambridge, 140, 1990.

3095 Weiss, R. F. and Price, B. A.: Nitrous oxide solubility in water and seawater, Marine

3096 Chemistry, 8, 347–359, https://doi.org/10.1016/0304-4203(80)90024-9, 1980.

3097 Wenzel, S., Cox, P. M., Eyring, V., and Friedlingstein, P.: Projected land photosynthesis

3098 constrained by changes in the seasonal cycle of atmospheric CO2, Nature, 538, 499–501,

3099 https://doi.org/10.1038/nature19772, 2016.

3100 Wilkenskjeld, S., Kloster, S., Pongratz, J., Raddatz, T., and Reick, C. H.: Comparing the

3101 influence of net and gross anthropogenic land-use and land-cover changes on the carbon

3102 cycle in the MPI-ESM, Biogeosciences, 11, 4817–4828, https://doi.org/10.5194/bg-11-4817-

3103 2014, 2014.

3104 Wiltshire, A. J., Burke, E. J., Chadburn, S. E., Jones, C. D., Cox, P. M., Davies-Barnard, T.,

3105 Friedlingstein, P., Harper, A. B., Liddicoat, S., Sitch, S., and Zaehle, S.: JULES-CN: a coupled

3106 terrestrial carbon–nitrogen scheme (JULES vn5.1), 14, 2161–2186,

3107 https://doi.org/10.5194/gmd-14-2161-2021, 2021.

3108 Woodward, F. I. and Lomas, M. R.: Vegetation dynamics – simulating responses to climatic

3109 change, Biol. Rev., 79, 643–670, https://doi.org/10.1017/S1464793103006419, 2004.

3110 Wright, R. M., Le Quéré, C., Buitenhuis, E., Pitois, S., and Gibbons, M. J.: Role of jellyfish in

3111 the plankton ecosystem revealed using a global ocean biogeochemical model, 18, 1291–

1320, https://doi.org/10.5194/bg-18-1291-2021, 2021.

Xi, F., Davis, S. J., Ciais, P., Crawford-Brown, D., Guan, D., Pade, C., Shi, T., Syddall, M., Lv, J., Ji, L., Bing, L., Wang, J., Wei, W., Yang, K.-H., Lagerblad, B., Galan, I., Andrade, C., Zhang, Y., and Liu, Z.: Substantial global carbon uptake by cement carbonation, Nature Geosci, 9, 880–883, https://doi.org/10.1038/ngeo2840, 2016.

Xia, J., Chen, Y., Liang, S., Liu, D., and Yuan, W.: Global simulations of carbon allocation coefficients for deciduous vegetation types, 67, 28016, https://doi.org/10.3402/tellusb.v67.28016, 2015.

Yin, X.: Responses of leaf nitrogen concentration and specific leaf area to atmospheric CO_2 enrichment: a retrospective synthesis across 62 species: Leaf response to atmospheric co_2 enrichment, 8, 631–642, https://doi.org/10.1046/j.1365-2486.2002.00497.x, 2002.

Yuan, W., Liu, D., Dong, W., Liu, S., Zhou, G., Yu, G., Zhao, T., Feng, J., Ma, Z., Chen, J., Chen, Y., Chen, S., Han, S., Huang, J., Li, L., Liu, H., Liu, S., Ma, M., Wang, Y., Xia, J., Xu, W., Zhang, Q., Zhao, X., and Zhao, L.: Multiyear precipitation reduction strongly decreases carbon uptake over northern China, 119, 881–896, https://doi.org/10.1002/2014JG002608, 2014.

Yue, C., Ciais, P., Luyssaert, S., Li, W., McGrath, M. J., Chang, J., and Peng, S.: Representing anthropogenic gross land use change, wood harvest, and forest age dynamics in a global vegetation model ORCHIDEE-MICT v8.4.2, 11, 409–428, https://doi.org/10.5194/gmd-11-409-2018, 2018.

Yue, X. and Unger, N.: The Yale Interactive terrestrial Biosphere model version 1.0: description, evaluation and implementation into NASA GISS ModelE2, Geosci. Model Dev., 8, 2399–2417, https://doi.org/10.5194/gmd-8-2399-2015, 2015.

Zaehle, S. and Friend, A. D.: Carbon and nitrogen cycle dynamics in the O-CN land surface model: 1. Model description, site-scale evaluation, and sensitivity to parameter estimates: Site-scale evaluation of a C-N model, Global Biogeochem. Cycles, 24, https://doi.org/10.1029/2009GB003521, 2010.

Zaehle, S., Ciais, P., Friend, A. D., and Prieur, V.: Carbon benefits of anthropogenic reactive nitrogen offset by nitrous oxide emissions, Nature Geosci, 4, 601–605,

3140   https://doi.org/10.1038/ngeo1207, 2011.

3141   Zeng, J., Nojiri, Y., Landschützer, P., Telszewski, M., and Nakaoka, S.: A Global Surface Ocean

3142   fCO2 Climatology Based on a Feed-Forward Neural Network, 31, 1838–1849,

3143   https://doi.org/10.1175/JTECH-D-13-00137.1, 2014.

3144   Zheng, B., Chevallier, F., Yin, Y., Ciais, P., Fortems-Cheiney, A., Deeter, M. N., Parker, R. J.,

3145   Wang, Y., Worden, H. M., and Zhao, Y.: Global atmospheric carbon monoxide budget 2000–

3146   2017 inferred from multi-species atmospheric inversions, 26, 2019.

3147   Zheng, B., Ciais, P., Chevallier, F., Chuvieco, E., Chen, Y., and Yang, H.: Increasing forest fire

3148   emissions despite the decline in global burned area, 7, eabh2646,

3149   https://doi.org/10.1126/sciadv.abh2646, 2021.

3150   Zscheischler, J., Mahecha, M. D., Avitabile, V., Calle, L., Carvalhais, N., Ciais, P., Gans, F.,

3151   Gruber, N., Hartmann, J., Herold, M., Ichii, K., Jung, M., Landschützer, P., Laruelle, G. G.,

3152   Lauerwald, R., Papale, D., Peylin, P., Poulter, B., Ray, D., Regnier, P., Rödenbeck, C., Roman-

3153   Cuesta, R. M., Schwalm, C., Tramontana, G., Tyukavina, A., Valentini, R., van der Werf, G.,

3154   West, T. O., Wolf, J. E., and Reichstein, M.: Reviews and syntheses: An empirical

3155   spatiotemporal description of the global surface–atmosphere carbon fluxes: opportunities

3156   and data limitations, Biogeosciences, 14, 3685–3703, https://doi.org/10.5194/bg-14-3685-

3157   2017, 2017.

3158

3159

3160

3161

3162

3163

 12 Tables

Table 1. Factors used to convert carbon in various units (by convention, Unit 1 = Unit 2 × conversion).			
Unit 1	Unit 2	Conversion	Source
GtC (gigatonnes of carbon)	ppm (parts per million) (a)	2.124 (b)	Ballantyne et al. (2012)
GtC (gigatonnes of carbon)	PgC (petagrams of carbon)	1	SI unit conversion
GtCO2 (gigatonnes of carbon dioxide)	GtC (gigatonnes of carbon)	3.664	44.01/12.011 in mass equivalent
GtC (gigatonnes of carbon)	MtC (megatonnes of carbon)	1000	SI unit conversion
(a) Measurements of atmospheric CO2 concentration have units of dry-air mole fraction. 'ppm' is an abbreviation for micromole/mol, dry air.			
(b) The use of a factor of 2.124 assumes that all the atmosphere is well mixed within one year. In reality, only the troposphere is well mixed and the growth rate of CO2 concentration in the less well-mixed stratosphere is not measured by sites from the NOAA network. Using a factor of 2.124 makes the approximation that the growth rate of CO2 concentration in the stratosphere equals that of the troposphere on a yearly basis.			

3165

3166

Table 2. How to cite the individual components of the global carbon budget presented here.	
Component	**Primary reference**
Global fossil CO2 emissions (EFOS), total and by fuel type	Andrew and Peters (2021)
National territorial fossil CO2 emissions (EFOS)	Gilfillan and Marland (2021), UNFCCC (2021a)
National consumption-based fossil CO2 emissions (EFOS) by country (consumption)	Peters et al. (2011b) updated as described in this paper
Net land-use change flux (ELUC)	This paper (see Table 4 for individual model references).
Growth rate in atmospheric CO2 concentration (GATM)	Dlugokencky and Tans (2022)
Ocean and land CO2 sinks (SOCEAN and SLAND)	This paper (see Table 4 for individual model references).

3167

Table 3. Main methodological changes in the global carbon budget since 2017. Methodological changes introduced in one year are kept for the following years unless noted. Empty cells mean there were no methodological changes introduced that year. Table A7 lists methodological changes from the first global carbon budget publication up to 2016.

Publication year	Fossil fuel emissions		LUC emissions	Reservoirs			Uncertainty & other changes
	Global	Country (territorial)		Atmosphere	Ocean	Land	
2017 Le Quéré et al. (2018a) GCB2017	Projection includes India-specific data		Average of two bookkeeping models; use of 12 DGVMs		Based on eight models that match the observed sink for the 1990s; no longer normalised	Based on 15 models that meet observation-based criteria (see Sect. 2.5)	Land multi-model average now used in main carbon budget, with the carbon imbalance presented separately; new table of key uncertainties
2018 Le Quéré et al. (2018b) GCB2018	Revision in cement emissions; Projection includes EU-specific data	Aggregation of overseas territories into governing nations for total of 213 countries a	Average of two bookkeeping models; use of 16 DGVMs	Use of four atmospheric inversions	Based on seven models	Based on 16 models; revised atmospheric forcing from CRUNCEP to CRU-JRA-55	Introduction of metrics for evaluation of individual models using observations
2019 Friedlingstein et al. (2019) GCB2019	Global emissions calculated as sum of all countries plus bunkers, rather than taken directly from CDIAC.		Average of two bookkeeping models; use of 15 DGVMs	Use of three atmospheric inversions	Based on nine models	Based on 16 models	
2020 Friedlingstein et al. (2020) GCB2020	Cement carbonation now included in the EFOS estimate, reducing EFOS by about 0.2GtC yr-1 for the last decade	India's emissions from Andrew (2020: India); Corrections to Netherland Antilles and Aruba and Soviet emissions before 1950 as per Andrew (2020: CO2); China's coal emissions in 2019 derived	Average of three bookkeeping models; use of 17 DGVMs. Estimate of gross land use sources and sinks provided	Use of six atmospheric inversions	Based on nine models. River flux revised and partitioned NH, Tropics, SH	Based on 17 models	

		from official statistics, emissions now shown for EU27 instead of EU28.Projection for 2020 based on assessment of four approaches.		6			
2021 Friedlingstein et al. (2021) GCB2021 (This study)	Projections are no longer an assessment of four approaches.	Official data included for a number of additional countries, new estimates for South Korea, added emissions from lime production in China.	ELUC estimate compared to the estimates adopted in national GHG inventories (NGHGI)		Average of means of eight models and means of seven data-products. Current year prediction of SOCEAN using a feed-forward neural network method	Current year prediction of SLAND using a feed-forward neural network method	

Table 4. References for the process models, fCO2-based ocean data products, and atmospheric inversions. All models and products are updated with new data to the end of year 2020, and the atmospheric forcing for the DGVMs has been updated as described in Section C.2.2.

Model/data name	Reference	Change from Global Carbon Budget 2020 (Friedlingstein et al., 2020)
Bookkeeping models for land-use change emissions		
BLUE	Hansis et al. (2015)	No change to model, but simulations performed with updated LUH2 forcing.
updated H&N2017	Houghton and Nassikas (2017)	Adjustment to treatment of harvested wood products. Update to FRA2020 and 2021 FAOSTAT for forest cover and land-use areas. Forest loss in excess of increases in cropland and pastures represented an increase in shifting cultivation. Extratropical peatland drainage emissions added (based on Qiu et al., 2021).
OSCAR	Gasser et al. (2020)	Update to OSCAR3.1.2, which provides finer resolution (96 countries/regions). LUH2-GCB2019 input data replaced by LUH2-GCB2021. FRA2015 (Houghton & Nassikas, 2017) still used as a second driving dataset, with emissions from FRA2015 extended to 2020. Constraining based on this year's budget data.
Dynamic global vegetation models		
CABLE-POP	Haverd et al. (2018)	changes in parameterisation, minor bug fixes
CLASSIC	Melton et al. (2020) (a)	Non-structural carbohydrates are now explicitly simulated.
CLM5.0	Lawrence et al. (2019)	No Change.
DLEM	Tian et al. (2015) (b)	Updated algorithms for land use change processes.
IBIS	Yuan et al. (2014) (c)	Several changes in parameterisation; Dynamic carbon allocation scheme.
ISAM	Meiyappan et al. (2015) (d)	ISAM now accounting for vertically-resolved soil biogeochemistry (carbon and nitrogen) module (Shu et al., 2020)
ISBA-CTRIP	Delire et al. (2020) (e)	Updated spinup protocol + model name updated (SURFEXv8 in GCB2017) + inclusion of crop harvesting module
JSBACH	Reick et al. (2021) (f)	Wood product pools per plant functional type.
JULES-ES	Wiltshire et al. (2021) (g)	Version 1.1 Inclusion of interactive fire Burton et al., (2019)
LPJ-GUESS	Smith et al. (2014) (h)	No code change. Using updated LUH2 and climate forcings.
LPJ	Poulter et al. (2011) (i)	Updated soil data from FAO to HWSD v2.0

LPX-Bern	Lienert and Joos (2018)	No Change.
OCN	Zaehle and Friend (2010) (j)	No change (uses r294).
ORCHIDEEv3	Vuichard et al. (2019) (k)	Updated growth respiration scheme (revision 7267)
SDGVM	Walker et al. (2017) (l)	No changes from version used in Friedlingstein et al. (2019), except for properly switching from grasslands to pasture in the blending of the ESA data with LUH2; this change affects mostly the semi-arid lands.
VISIT	Kato et al. (2013) (m)	Minor bug fix on CH4 emissions of recent few years.
YIBs	Yue and Unger (2015)	Inclusion of nutrient limit with down regulation approach of Arora et al. (2009)
Global ocean biogeochemistry models		
NEMO-PlankTOM12	Wright et al. (2021) (n)	Updated biochemical model to include 12 functional types. Change to spin-up, now using a looped 1990.
MICOM-HAMOCC (NorESM-OCv1.2)	Schwinger et al. (2016)	No change
MPIOM-HAMOCC6	Lacroix et al. (2021)	Added riverine fluxes; cmip6 model version including modifications and bug-fixes in HAMOCC and MPIOM
NEMO3.6-PISCESv2-gas (CNRM)	Berthet et al. (2019) (o)	small bug fixes; updated model-spin-up (new forcings); atm forcing is now JRA55-Do including 2020 year and varying riverine freshwater inputs
FESOM-2.1-REcoM2	Hauck et al. (2020) (p)	Updated physical model version FESOM2.1, and including 2nd zooplankton and 2nd detritus group. Used new atmospheric CO2 time series provided by GCB
MOM6-COBALT (Princeton)	Liao et al. (2020)	Adjustment of the piston velocity prefactor (0.337 cph/m2/s2 to 0.251 cph/m2/s2). MOM6 update from GitHub version b748b1b (2018-10-03) to version 69a096b (2021-02-24). Updated model spin-up and simulation using JRA55-do v1.5. Used new atmospheric CO2 time series provided by GCB.
CESM-ETHZ	Doney et al. (2009)	No change in the model. Used new atmospheric CO2 time series provided by GCB
NEMO-PISCES (IPSL)	Aumont et al. (2015)	No change
ocean fCO2-based data products		
Landschützer (MPI-SOMFFN)	Landschützer et al. (2016)	update to SOCATv2021 measurements and time period 1982-2020; The estimate now covers the full open ocean and coastal domain as well as the Arctic Ocean extension described in Landschützer et al. (2020)
Rödenbeck (Jena-MLS)	Rödenbeck et al. (2014)	update to SOCATv2021 measurements, time period extended to 1957-2020, involvement of a multi-linear regression for extrapolation (combined with an explicitly interannual correction), use of OCIM (deVries, 2014) as decadal prior, carbonate chemistry parameterization now time-dependent, grid resolution increased to 2.5*2 degrees, adjustable degrees

		of freedom now also covering shallow areas and Arctic, some numerical revisions
CMEMS-LSCE-FFNNv2	Chau et al. (2021)	Update to SOCATv2021 measurements and time period 1985-2020. The CMEMS-LSCE-FFNNv2 product now covers both the open ocean and coastal regions (see in Chau et al. 2021 for model description and evaluation).
CSIR-ML6	Gregor et al. (2019)	Updated to SOCATv2021. Reconstruction now spans the period 1985 - 2020 and includes updates using the SeaFlux protocols (Fay et al., 2021b)
Watson et al	Watson et al. (2020)	Updated to SOCAT v2021. A monthly climatology of the skin temperature deviation as calculated for years 2003-2011 is now used in place of a single global average figure. SOM calculation updated to treat the Arctic as a separate biome.
NIES-NN	Zeng et al. (2014)	New this year
JMA-MLR	Iida et al. (2021)	New this year
OS-ETHZ-GRaCER	Gregor and Gruber (2021)	New this year

Atmospheric inversions		
CAMS	Chevallier et al. (2005) (q)	No change.
CarbonTracker Europe (CTE)	van der Laan-Luijkx et al. (2017)	No change.
Jena CarboScope	Rödenbeck et al. (2018) (r)	No change.
UoE in-situ	Feng et al., (2016) (s)	Fossil fuels now from GCP-GridFEDv2021.2
NISMON-CO2	Niwa et al., (2017) (t)	Some inversion parameters were changed.
CMS-Flux	Liu et al., (2021)	New this year

(a) see also Asaadi et al. (2018).

(b) see also Tian et al. (2011)

(c) the dynamic carbon allocation scheme was presented by Xia et al. (2015)

(d) see also Jain et al. (2013). Soil biogeochemistry is updated based on Shu et al. (2020)

(e) see also Decharme et al. (2019) and Seferian et al. (2019)

(f) Mauritsen et al. (2019)

(g) see also Sellar et al. (2019) and Burton et al., (2019). JULES-ES is the Earth System configuration of the Joint UK Land Environment Simulator as used in the UK Earth System Model (UKESM).

(h) to account for the differences between the derivation of shortwave radiation from CRU cloudiness and DSWRF from CRUJRA, the photosynthesis scaling parameter αa was modified (-15%) to yield similar results.

(i) compared to published version, decreased LPJ wood harvest efficiency so that 50 % of biomass was removed off-site compared to 85 % used in the 2012 budget. Residue management of managed grasslands increased so that 100 % of harvested grass enters the litter pool.
(j) see also Zaehle et al. (2011).
(k) see also Zaehle and Friend (2010) and Krinner et al. (2005)
(l) see also Woodward and Lomas (2004)
(m) see also Ito and Inatomi (2012).
(n) see also Buitenhuis et al. (2013)
(o) see also Séférian et al. (2019)
(p) see also Schourup-Kristensen et al (2014)
(q) see also Remaud (2018)
(r) see also Rödenbeck et al. (2003)
(s) see also Feng et al. (2009) and Palmer et al. (2019)
(t) see also Niwa et al. (2020)

Table 5. Comparison of results from the bookkeeping method and budget residuals with results from the DGVMs and inverse estimates for different periods, the last decade, and the last year available. All values are in GtCyr−1. The DGVM uncertainties represent ±1σ of the decadal or annual (for 2020 only) estimates from the individual DGVMs: for the inverse models the range of available results is given. All values are rounded to the nearest 0.1 GtC and therefore columns do not necessarily add to zero.

	Mean (GtC/yr)						
	1960s	1970s	1980s	1990s	2000s	2011-2020	2020
Land-use change emissions (ELUC)							
Bookkeeping methods - net flux (1a)	1.6±0.7	1.3±0.7	1.2±0.7	1.3±0.7	1.2±0.7	1.1±0.7	0.9±0.7
Bookkeeping methods - source	3.4±0.9	3.3±0.8	3.4±0.8	3.6±0.6	3.7±0.6	3.8±0.6	3.6±0.6
Bookkeeping methods - sink	-1.9±0.4	-2±0.4	-2.1±0.3	-2.3±0.4	-2.5±0.4	-2.7±0.4	-2.8±0.4
DGVMs-net flux (1b)	1.6±0.5	1.3±0.4	1.4±0.5	1.4±0.5	1.4±0.5	1.5±0.5	1.4±0.7
Terrestrial sink (SLAND)							
Residual sink from global budget (EFOS+ELUC-GATM-SOCEAN) (2a)	1.8±0.8	1.9±0.8	1.6±0.9	2.5±0.9	2.7±0.9	2.8±0.9	2.1±0.9
DGVMs (2b)	1.2±0.5	2±0.5	1.8±0.5	2.3±0.4	2.6±0.5	3.1±0.6	2.9±1
Total land fluxes (SLAND-ELUC)							
GCB2021 Budget (2b-1a)	-0.4±0.8	0.8±0.8	0.5±0.9	1±0.8	1.4±0.9	1.9±0.9	2±1.2
Budget constraint (2a-1a)	0.2±0.4	0.6±0.5	0.3±0.5	1.2±0.5	1.5±0.6	1.7±0.6	1.3±0.6
DGVMs-net (2b-1b)	-0.4±0.6	0.7±0.4	0.3±0.4	0.9±0.4	1.2±0.4	1.6±0.6	1.5±0.8
Inversions*	---	---	0.5-0.6 (2)	0.9-1.2 (3)	1.3-1.8 (3)	1.3-2 (6)	-0.1-1.3 (6)

- Estimates are adjusted for the pre-industrial influence of river fluxes, for the cement carbonation sink, and adjusted to common EFOS (Sect. 2.6). The ranges given include varying numbers (in parentheses) of inversions in each decade (Table A4)

Table 6. Decadal mean in the five components of the anthropogenic CO2 budget for different periods, and last year available. All values are in GtC yr-1, and uncertainties are reported as ±1σ. Fossil CO$_2$ emissions include cement carbonation. The table also shows the budget imbalance (B$_{IM}$), which provides a measure of the discrepancies among the nearly independent estimates and has an uncertainty exceeding ± 1 GtC yr^{-1}. A positive imbalance means the emissions are overestimated and/or the sinks are too small. All values are rounded to the nearest 0.1 GtC and therefore columns do not necessarily add to zero.

	Mean (GtC/yr)							
	1960s	1970s	1980s	1990s	2000s	2011-2020	2020	2021 (Projection)
Total emissions (EFOS + ELUC)								
Fossil CO2 emissions (EFOS)*	3±0.2	4.7±0.2	5.5±0.3	6.3±0.3	7.7±0.4	9.5±0.5	9.3±0.5	9.9±0.5
Land-use change emissions (ELUC)	1.6±0.7	1.3±0.7	1.2±0.7	1.3±0.7	1.2±0.7	1.1±0.7	0.9±0.7	0.8±0.7
Total emissions	4.6±0.7	5.9±0.7	6.7±0.8	7.7±0.8	9±0.8	10.6±0.8	10.2±0.8	10.7±0.9
Partitioning								
Growth rate in atmos CO2 (GATM)	1.7±0.07	2.8±0.07	3.4±0.02	3.1±0.02	4±0.02	5.1±0.02	5±0.2	5.3±0.1
Ocean sink (SOCEAN)	1.1±0.4	1.3±0.4	1.8±0.4	2±0.4	2.2±0.4	2.8±0.4	3±0.4	2.9±0.4
Terrestrial sink (SLAND)	1.2±0.5	2±0.5	1.8±0.5	2.3±0.4	2.6±0.5	3.1±0.6	2.9±1	3.3±1
Budget Imbalance								
BIM=EFOS+ELUC-(GATM+SOCEAN+SLAND)	0.6	-0.2	-0.2	0.2	0.1	-0.3	-0.8	-0.7

- Fossil emissions excluding the cement carbonation sink amount to 3.1±0.2 GtC/yr, 4.7±0.2 GtC/yr, 5.5±0.3 GtC/yr, 6.4±0.3 GtC/yr, 7.9±0.4 GtC/yr, and 9.7±0.5 GtC/yr for the decades 1960s to 2010s respectively and to 9.5±0.5 GtC/yr for 2020.

Table 7. Comparison of the projection with realised fossil CO2 emissions (EFOS). The 'Actual' values are first the estimate available using actual data, and the 'Projected' values refers to estimates made before the end of the year for each publication. Projections based on a different method from that described here during 2008-2014 are available in Le Quéré et al., (2016). All values are adjusted for leap years.

	World		China		USA		EU28 (h)		India		Rest of World	
	Projected	Actual	Projected	Actual	Projected	Actual	Projected	Actual	Projected	Actual	Projected	Actual
2015 (a)	−0.6% (−1.6 to 0.5)	0.06%	−3.9% (−4.6 to −1.1)	−0.7%	−1.5% (−5.5 to 0.3)	−2.5%	–	–	–	–	1.2% (−0.2 to 2.6)	1.2%
2016 (b)	−0.2% (−1.0 to +1.8)	0.20%	−0.5% (−3.8 to +1.3)	−0.3%	−1.7% (−4.0 to +0.6)	−2.1%	–	–	–	–	1.0% (−0.4 to +2.5)	1.3%
2017 (c)	2.0% (+0.8 to +3.0)	1.6%	3.5% (+0.7 to +5.4)	1.5%	−0.4% (−2.7 to +1.0)	−0.5%	–	–	2.00% (+0.2 to +3.8)	3.9%	1.6% (0.0 to +3.2)	1.9%
2018 (d)	2.7% (+1.8 to +3.7)	2.1%	4.7% (+2.0 to +7.4)	2.3%	2.5% (+0.5 to +4.5)	2.8%	-0.7% (-2.6 to +1.3)	-2.1%	6.3% (+4.3 to +8.3)	8.0%	1.8% (+0.5 to +3.0)	1.7%
2019 (e)	0.5% (-0.3 to +1.4)	0.1%	2.6% (+0.7 to +4.4)	2.2%	-2.4% (-4.7 to -0.1)	-2.6%	-1.7% (-5.1% to +1.8%)	-4.3%	1.8% (-0.7 to +3.7)	1.0%	0.5% (-0.8 to +1.8)	0.5%
2020 (f)	-6.7%	-5.4%	-1.7%	1.4%	-12.2%	-10.6%	-11.3% (EU27)	-10.9%	-9.1%	-7.3%	-7.4%	-7.0%
2021 (g)	4.8% (4.2% to 5.4%)		4.3% (3.0% to 5.4%)		6.8% (6.6% to 7.0%)		6.3% (4.3% to 8.3%)		11.2% (10.7% to 11.7%)		3.2% (2.0% to 4.3%)	

(a) Jackson et al. (2016) and Le Quéré et al. (2015a). (b) Le Quéré et al. (2016). (c) Le Quéré et al. (2018a). (d) Le Quéré et al. (2018b). (e) Friedlingstein et al., (2019), (f) Friedlingstein et al., (2020), (g) This study (median of four reported estimates, Section 3.4.1.2)

(h) EU28 until 2019, EU27 from 2020

Table 8. Cumulative CO₂ for different time periods in gigatonnes of carbon (GtC). All uncertainties are reported as ±1σ. Fossil CO₂ emissions include cement carbonation. The budget imbalance (B$_{IM}$) provides a measure of the discrepancies among the nearly independent estimates. All values are rounded to the nearest 5 GtC and therefore columns do not necessarily add to zero.

	1750-2020	1850-2014	1850-2020	1960-2020	1850-2021
Emissions					
Fossil CO2 emissions (EFOS)	460±25	400±20	455±25	375±20	465±25
Land-use change emissions (ELUC)	235±75	195±60	200±65	80±45	205±65
Total emissions	690±80	595±65	660±65	455±45	670±65
Partitioning					
Growth rate in atmos CO2 (GATM)	290±5	235±5	270±5	205±5	275±5
Ocean sink (SOCEAN)	180±35	150±30	170±35	115±25	170±35
Terrestrial sink (SLAND)	215±50	180±40	195±45	135±25	200±45
Budget imbalance					
BIM=EFOS+ELUC-(GATM+SOCEAN+SLAND)	10	30	25	0	25

Table 9. Major known sources of uncertainties in each component of the Global Carbon Budget, defined as input data or processes that have a demonstrated effect of at least ±0.3 GtC yr-1.

Source of uncertainty	Time scale (years)	Location	Status	Evidence
Fossil CO2 emissions (EFOS; Section 2.1)				
energy statistics	annual to decadal	global, but mainly China & major developing countries	see Sect. 2.1	(Korsbakken et al., 2016, Guan et al., 2012)
carbon content of coal	annual to decadal	global, but mainly China & major developing countries	see Sect. 2.1	(Liu et al., 2015)
system boundary	annual to decadal	all countries	see Sect. 2.1	(Andrew, 2020)
Net land-use change flux (ELUC; section 2.2)				
land-cover and land-use change statistics	continuous	global; in particular tropics	see Sect. 2.2	(Houghton et al., 2012; Gasser et al., 2020)
sub-grid-scale transitions	annual to decadal	global	see Table A1	(Wilkenskjeld et al., 2014)
vegetation biomass	annual to decadal	global; in particular tropics	see Table A1	(Houghton et al., 2012)
forest degradation (fire, selective logging)	annual to decadal	tropics		(Aragão et al., 2018; Qin et al., 2020)
wood and crop harvest	annual to decadal	global; SE Asia	see Table A1	(Arneth et al., 2017, Erb et al., 2018)
peat burning (a)	multi-decadal trend	global	see Table A1	(van der Werf et al., 2010, 2017)
loss of additional sink capacity	multi-decadal trend	global	not included; see Appendix D1.4	(Pongratz et al, 2014, Gasser et al, 2020; Obermeier et al., 2021)
Atmospheric growth rate (GATM; section 2.3) no demonstrated uncertainties larger than ±0.3 GtC yr-1 (b)				
Ocean sink (SOCEAN; section 2.4)				

sparsity in surface fCO2 observations	mean, decadal variability and trend	global, in particular southern hemisphere	see Sect 3.5.2	(Gloege et al., 2021, Denvil-Sommer et al., 2021, Bushinsky et al., 2019)
riverine carbon outgassing and its anthropogenic perturbation	annual to decadal	global, in particular partitioning between Tropics and South	see Sect. 2.4 (anthropogenic perturbations not included)	(Aumont et al., 2001, Resplandy et al., 2018, Lacroix et al., 2020)
interior ocean anthropogenic carbon storage	annual to decadal	global	see Sect 3.5.5	(Gruber et al., 2019)
near-surface temperature and salinity gradients	mean on all time-scales	global	see Sect. 3.8.2	(Watson et al., 2020)
Land sink (SLAND; section 2.5)				
strength of CO2 fertilisation	multi-decadal trend	global	see Sect. 2.5	(Wenzel et al., 2016; Walker et al., 2021)
response to variability in temperature and rainfall	annual to decadal	global; in particular tropics	see Sect. 2.5	(Cox et al., 2013; Jung et al., 2017; Humphrey et al., 2018; 2021)
nutrient limitation and supply				
tree mortality	annual	global in particular tropics	see Sect. 2.5	(Hubau et al., 2021; Brienen et al., 2020)
response to diffuse radiation	annual	global	see Sect. 2.5	(Mercado et al., 2009; O'Sullivan et al., 2021)
a As result of interactions between land-use and climate				
b The uncertainties in GATM have been estimated as ±0.2 GtC yr-1, although the conversion of the growth rate into a global annual flux assuming instantaneous mixing throughout the atmosphere introduces additional errors that have not yet been quantified.				
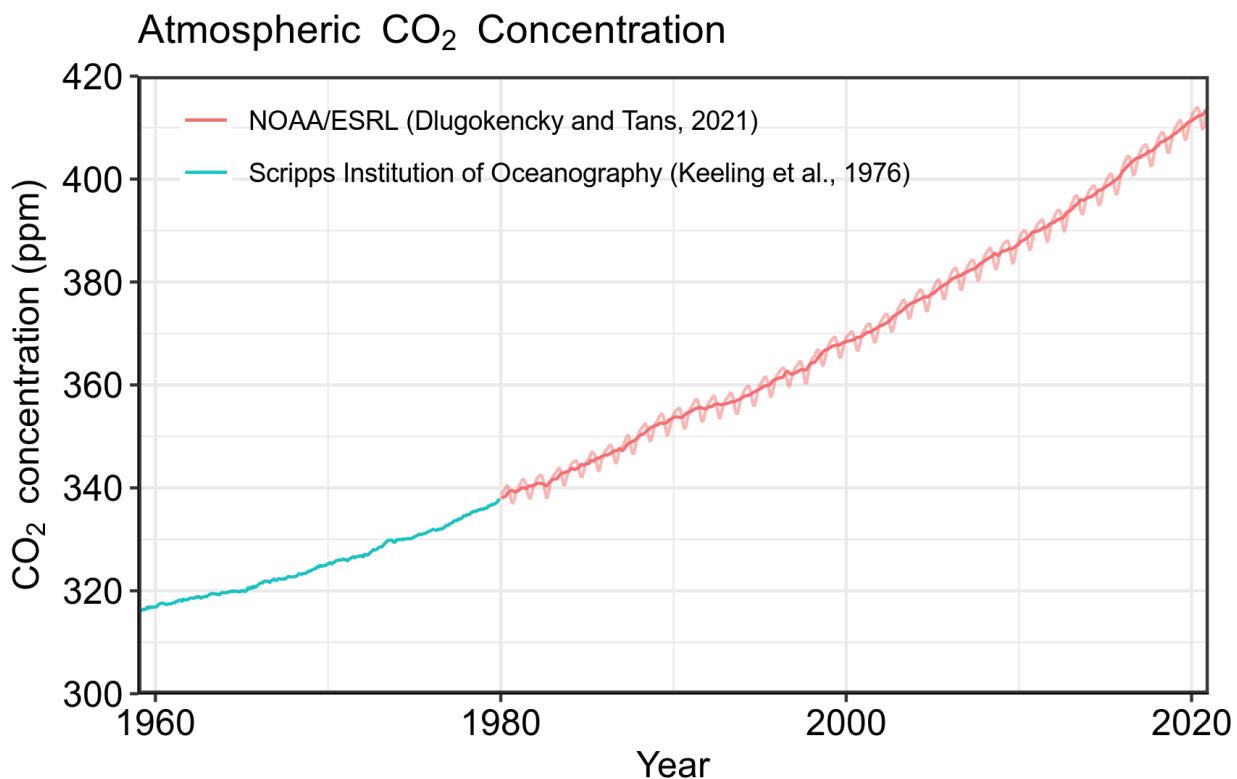
13.1   **Figure 1.** Surface average atmospheric CO_2 concentration (ppm). Since 1980, monthly data

are from NOAA/ESRL (Dlugokencky and Tans, 2022) and are based on an average of direct

atmospheric CO_2 measurements from multiple stations in the marine boundary layer

(Masarie and Tans, 1995). The 1958-1979 monthly data are from the Scripps Institution of

Oceanography, based on an average of direct atmospheric CO_2 measurements from the

Mauna Loa and South Pole stations (Keeling et al., 1976). To account for the difference of

mean CO_2 and seasonality between the NOAA/ESRL and the Scripps station networks used

here, the Scripps surface average (from two stations) was de-seasonalised and adjusted to

match the NOAA/ESRL surface average (from multiple stations) by adding the mean

difference of 0.667 ppm, calculated here from overlapping data during 1980-2012.
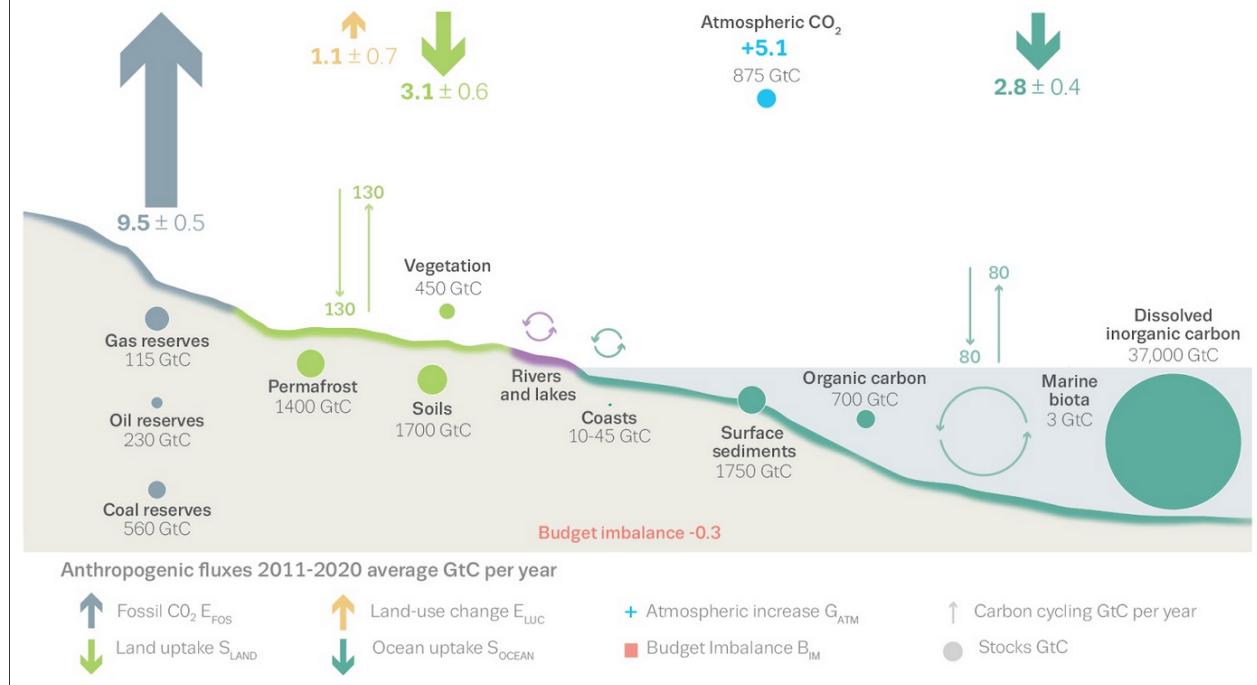
13.2 **Figure 2.** Schematic representation of the overall perturbation of the global carbon cycle caused by anthropogenic activities, averaged globally for the decade 2011-2020. See legends for the corresponding arrows and units. The uncertainty in the atmospheric CO_2 growth rate is very small (±0.02 GtC yr^{-1}) and is neglected for the figure. The anthropogenic perturbation occurs on top of an active carbon cycle, with fluxes and stocks represented in the background and taken from Canadell et al. (2021) for all numbers, except for the carbon stocks in coasts which is from a literature review of coastal marine sediments (Price and Warren, 2016).
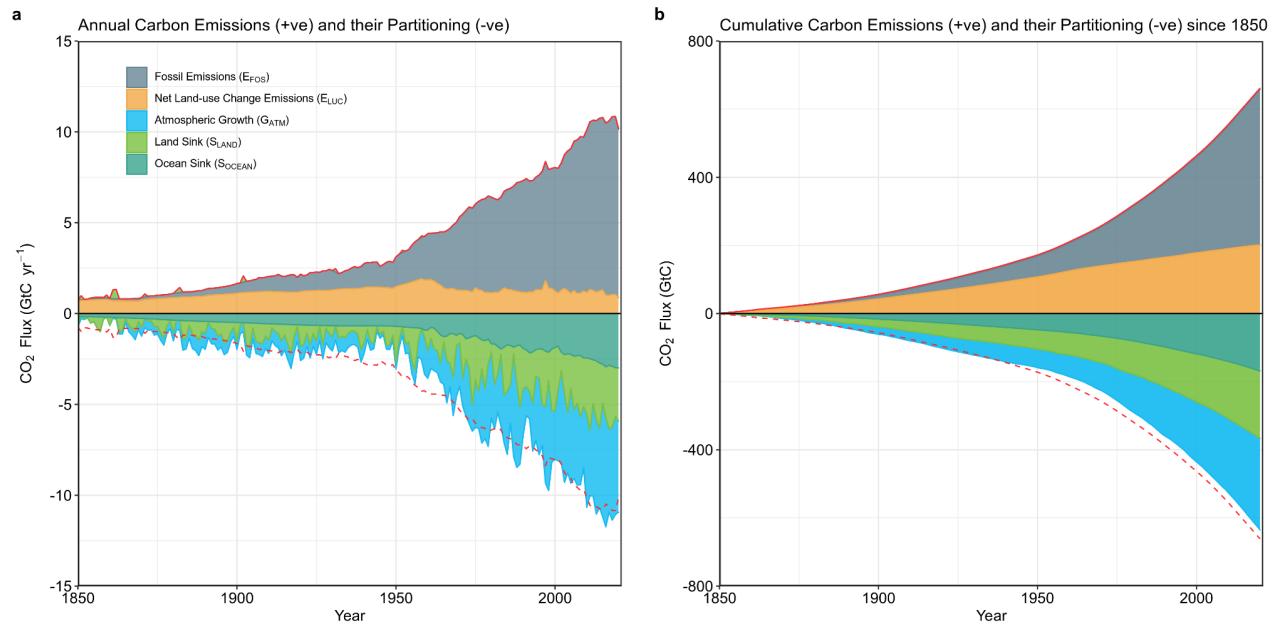
13.3

13.4 **Figure 3.** Combined components of the global carbon budget illustrated in Fig. 2 as a function of time, for fossil CO_2 emissions (E_{FOS}, including a small sink from cement carbonation; grey) and emissions from land-use change (E_{LUC}; brown), as well as their partitioning among the atmosphere (G_{ATM}; cyan), ocean (S_{OCEAN}; blue), and land (S_{LAND}; green). Panel (a) shows annual estimates of each flux and panel (b) the cumulative flux (the sum of all prior annual fluxes) since the year 1850. The partitioning is based on nearly independent estimates from observations (for G_{ATM}) and from process model ensembles constrained by data (for S_{OCEAN} and S_{LAND}) and does not exactly add up to the sum of the emissions, resulting in a budget imbalance (BI_M) which is represented by the difference between the bottom red line (mirroring total emissions) and the sum of carbon fluxes in the ocean, land, and atmosphere reservoirs. All data are in GtC yr^{-1} (panel a) and GtC (panel b). The E_{FOS} estimates are primarily from (Gilfillan and Marland, 2021), with uncertainty of about ±5% (±1σ). The E_{LUC} estimates are from three bookkeeping models (Table 4) with uncertainties of about ±0.7 GtC yr^{-1}. The G_{ATM} estimates prior to 1959 are from Joos and Spahni (2008) with uncertainties equivalent to about ±0.1-0.15 GtC yr^{-1} and from Dlugokencky and Tans (2022) since 1959 with uncertainties of about +-0.07 GtC yr^{-1} during 1959-1979 and ±0.02 GtC yr^{-1} since 1980. The S_{OCEAN} estimate is the average from Khatiwala et al. (2013) and DeVries (2014) with uncertainty of about ±30% prior to 1959, and the average of an ensemble of models and an ensemble of fCO_2 data products (Table 4) with uncertainties of about ±0.4 GtC yr^{-1} since 1959. The S_{LAND} estimate is the average of an ensemble of models (Table 4) with uncertainties of about ±1 GtC yr^{-1}. See the text for more details of each component and their uncertainties.
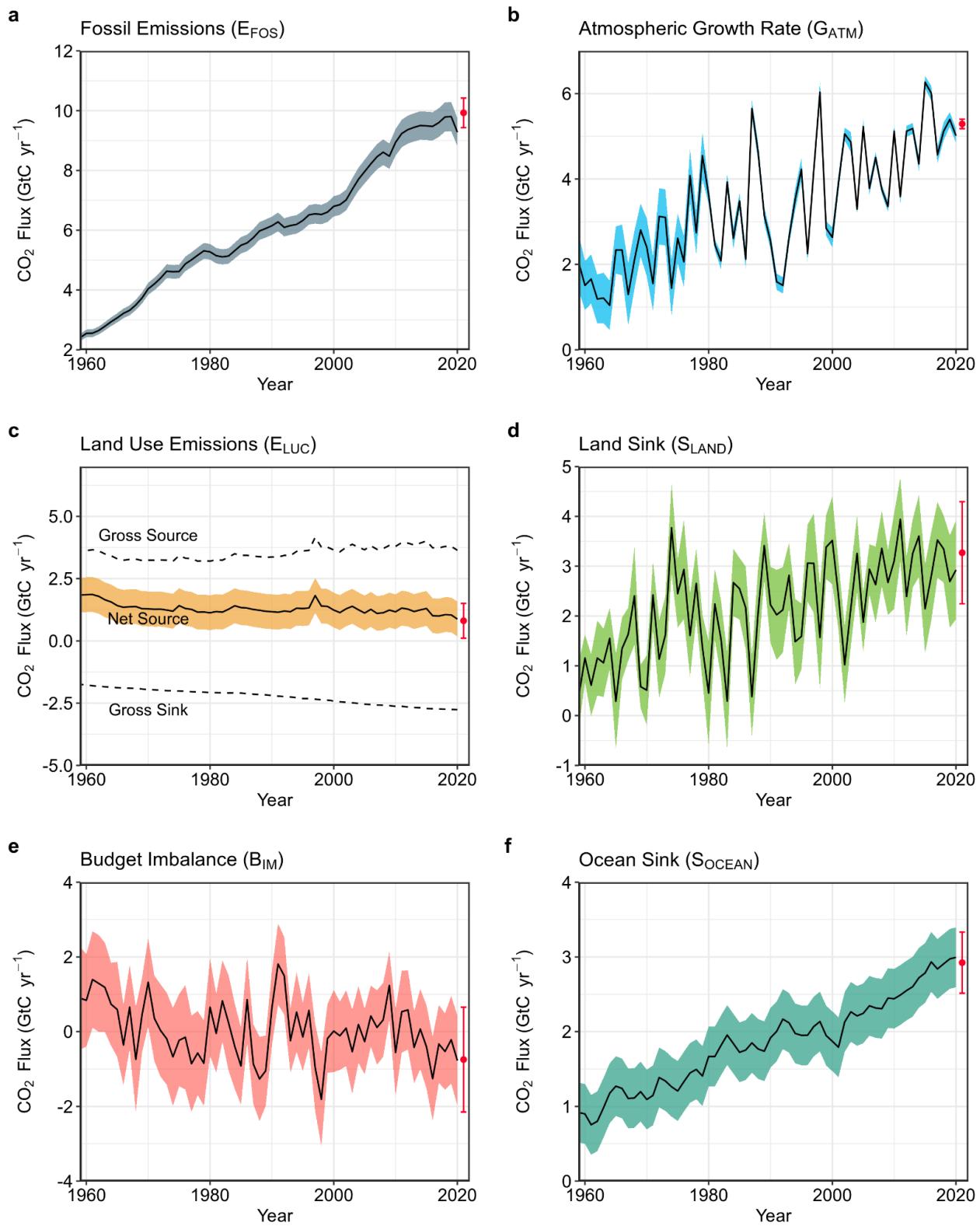
13.5 **Figure 4.** Components of the global carbon budget and their uncertainties as a function of time, presented individually for (a) fossil CO_2 emissions (E_{FOS}), (b) growth rate in atmospheric CO_2 concentration (G_{ATM}), (c) emissions from land-use change (E_{LUC}), (d) the land CO_2 sink (S_{LAND}), (e) the ocean CO_2 sink (S_{OCEAN}), (f) the budget imbalance that is not accounted for by the other terms. Positive values of S_{LAND} and S_{OCEAN} represent a flux from the atmosphere to land or the ocean. All data are in GtC yr^{-1} with the uncertainty bounds representing ±1 standard deviation in shaded colour. Data sources are as in Fig. 3. The red dots indicate our projections for the year 2021 and the red error bars the uncertainty in the projections (see methods).
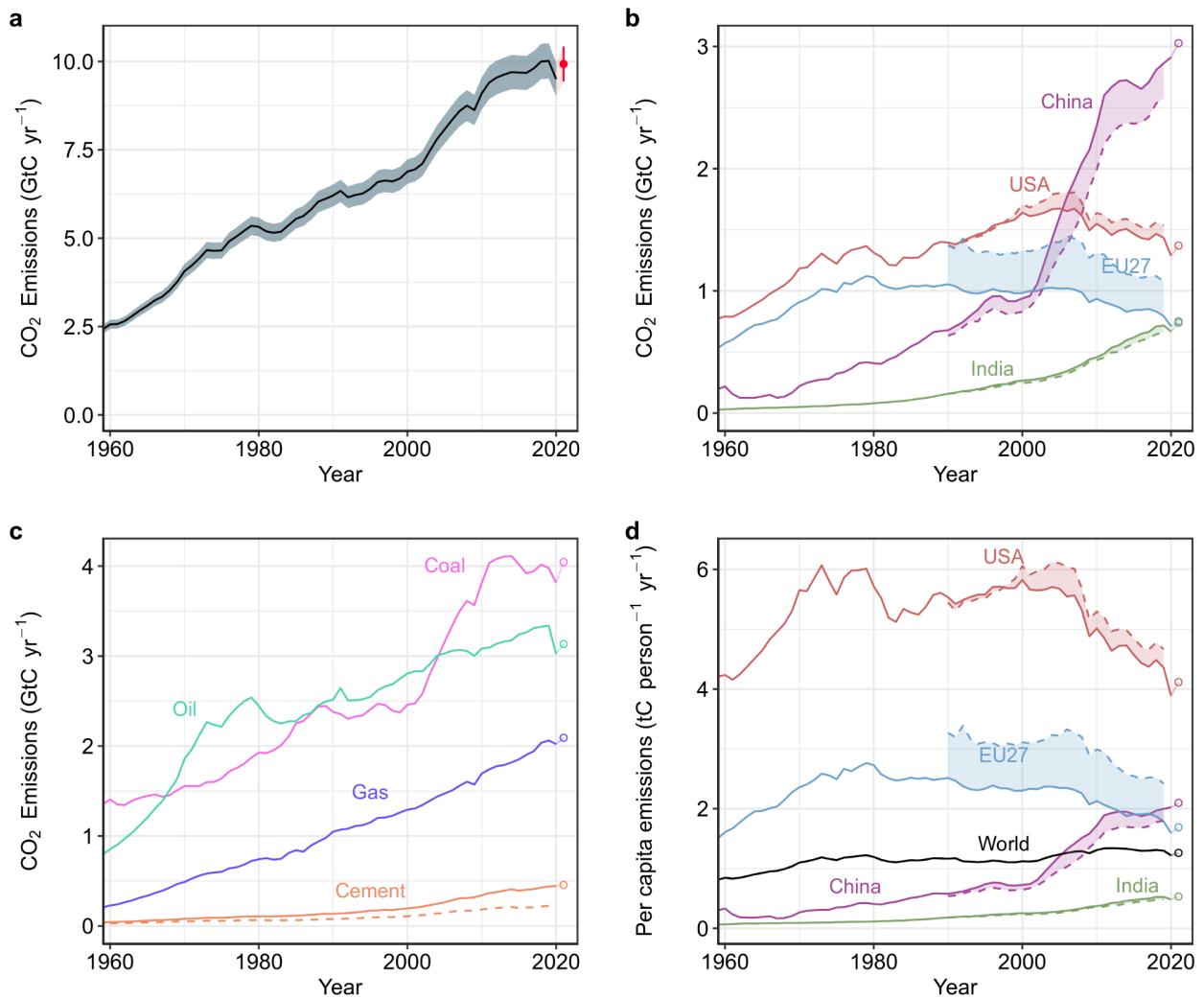
13.6

Figure 5. Fossil CO₂ emissions for (a) the globe, including an uncertainty of ± 5% (grey shading) and a projection through the year 2021 (red dot and uncertainty range), (b) territorial (solid lines) and consumption (dashed lines) emissions for the top three country emitters (USA, China, India) and for the European Union (EU27), (c) global emissions by fuel type, including coal, oil, gas, and cement, and cement minus cement carbonation (dashed), and (d) per-capita emissions the world and for the large emitters as in panel (b). Territorial emissions are primarily from Gilfillan and Marland (2021) except national data for the USA and EU27 for 1990-2018, which are reported by the countries to the UNFCCC as detailed in the text; consumption-based emissions are updated from Peters et al. (2011b). See Section 2.1 and Appendix C.1 for details of the calculations and data sources.
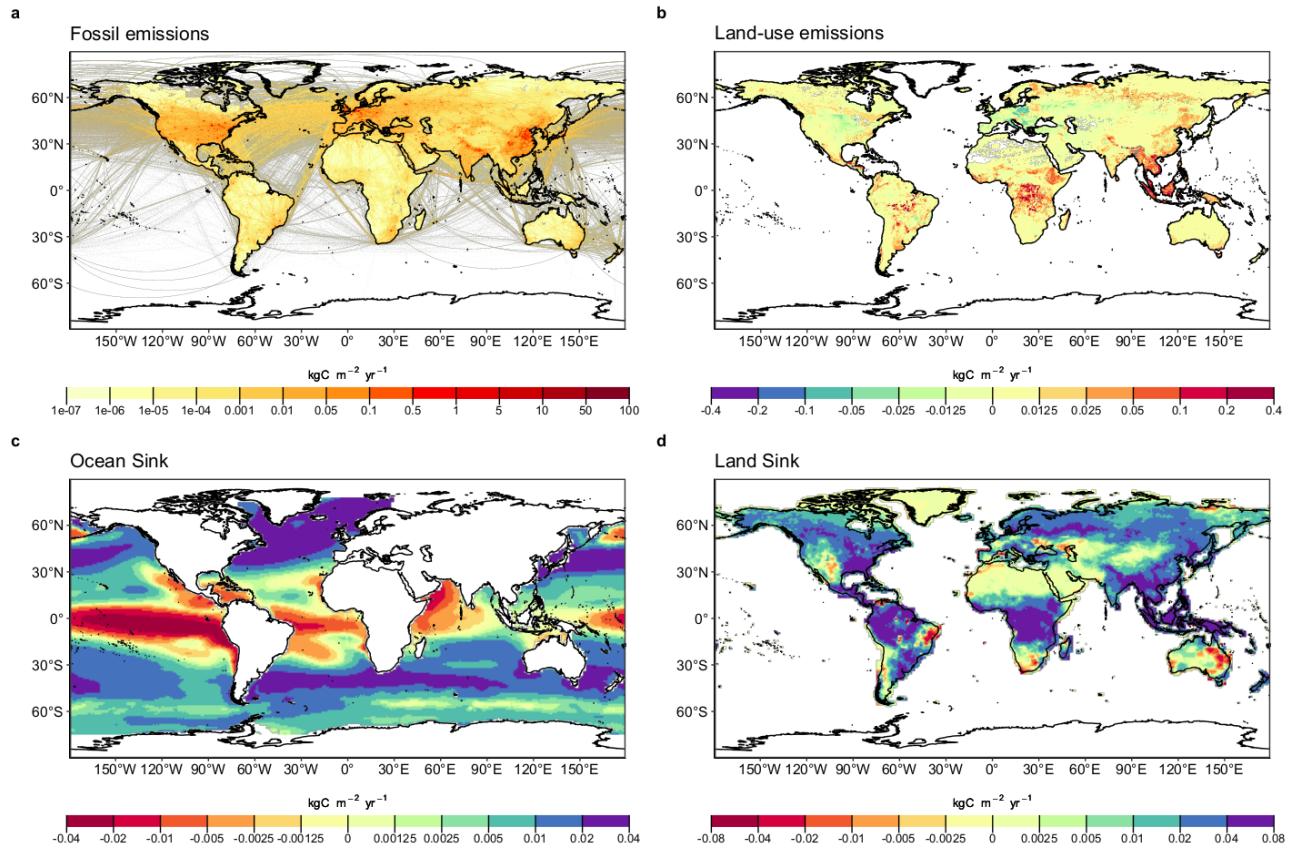
13.7

13.8 Figure 6. The 2011-2020 decadal mean components of the global carbon budget, presented for (a) fossil CO_2 emissions (E_{FOS}), (b) land-use change emissions (E_{LUC}), (c) the ocean CO_2 sink (S_{OCEAN}), and (d) the land CO_2 sink (S_{LAND}). Positive values for E_{FOS} and E_{LUC} represent a flux to the atmosphere, whereas positive values of S_{OCEAN} and S_{LAND} represent a flux from the atmosphere to the ocean or the land. In all panels, yellow/red (green/blue) colours represent a flux from (into) the land/ocean to (from) the atmosphere. All units are in kgC m^{-2} yr^{-1}. Note the different scales in each panel. E_{FOS} data shown is from GCP-GridFEDv2021.2. E_{LUC} data shown is only from BLUE as the updated H&N2017 and OSCAR do not resolve gridded fluxes. S_{OCEAN} data shown is the average of GOBMs and data-products means, using GOBMs simulation A, no adjustment for bias and drift applied to the gridded fields (see Sections 2.4). S_{LAND} data shown is the average of DGVMs for simulation S2 (see Sections 2.5).
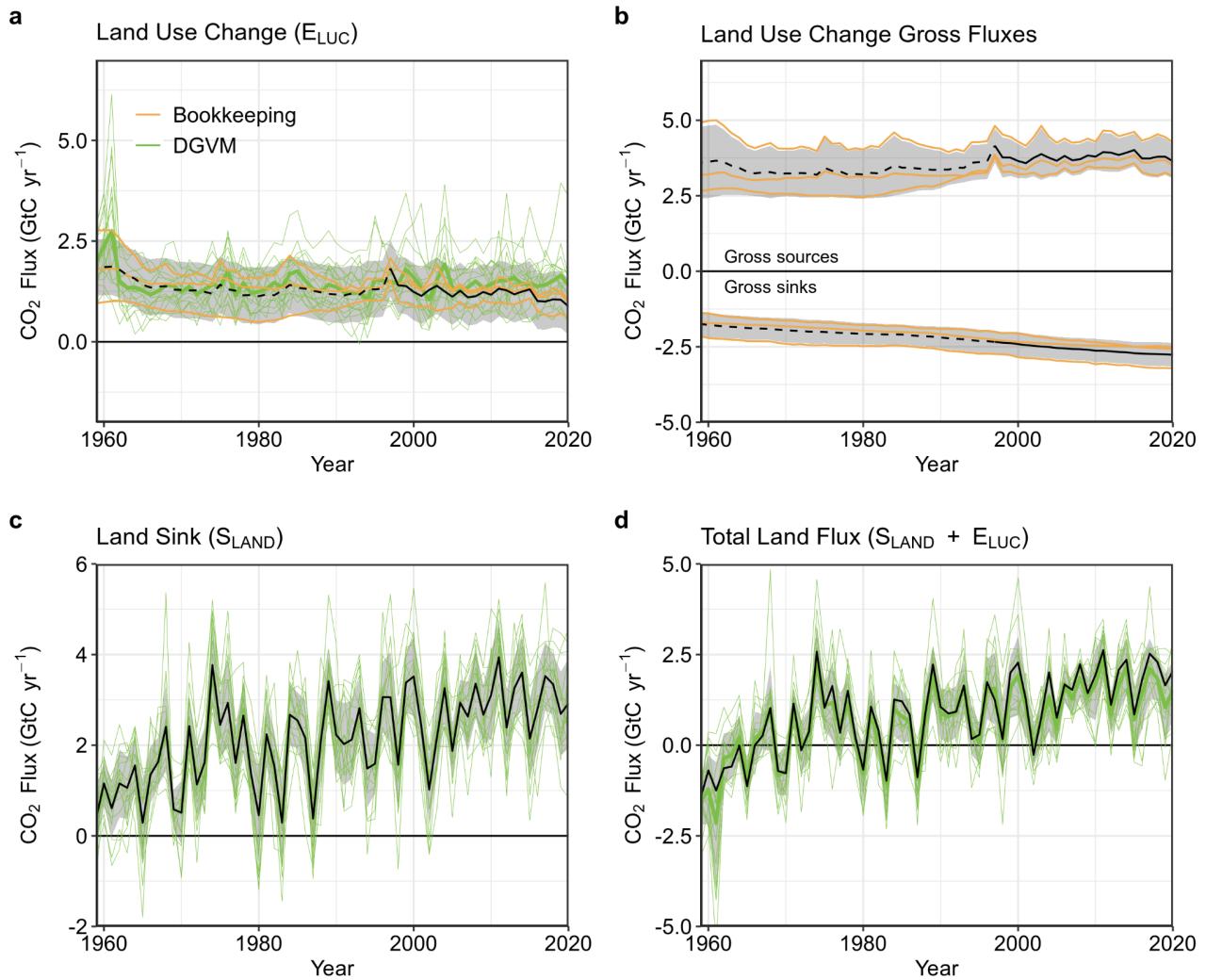
13.9

Figure 7. CO_2 exchanges between the atmosphere and the terrestrial biosphere as used in the global carbon budget (black with ±1σ uncertainty in grey shading in all panels). (a) CO_2 emissions from land-use change (E_{LUC}) with estimates from the three bookkeeping models (yellow lines) and DGVMs models (green) shown individually, with DGVMs ensemble means (dark green). The dashed line identifies the pre-satellite period before the inclusion of peatland burning. (b) CO_2 gross sinks (positive, from regrowth after agricultural abandonment and wood harvesting) and gross sources (negative, from decaying material left dead on site, products after clearing of natural vegetation for agricultural purposes, wood harvesting, and for BLUE, degradation from primary to secondary land through usage of natural vegetation as rangeland, and also from emissions from peat drainage and peat burning) from the three bookkeeping models (yellow lines). The sum of the gross sinks and sources is E_{LUC} shown in panel(a). (c) Land CO_2 sink (S_{LAND}) with individual DGVMs estimates

(green). (d) Total atmosphere-land CO_2 fluxes ($S_{LAND} - E_{LUC}$), with individual DGVMs (green) and their multi-model mean (dark green).

a

Airborne Fraction

b

Land-borne Fraction

c

Ocean-borne Fraction
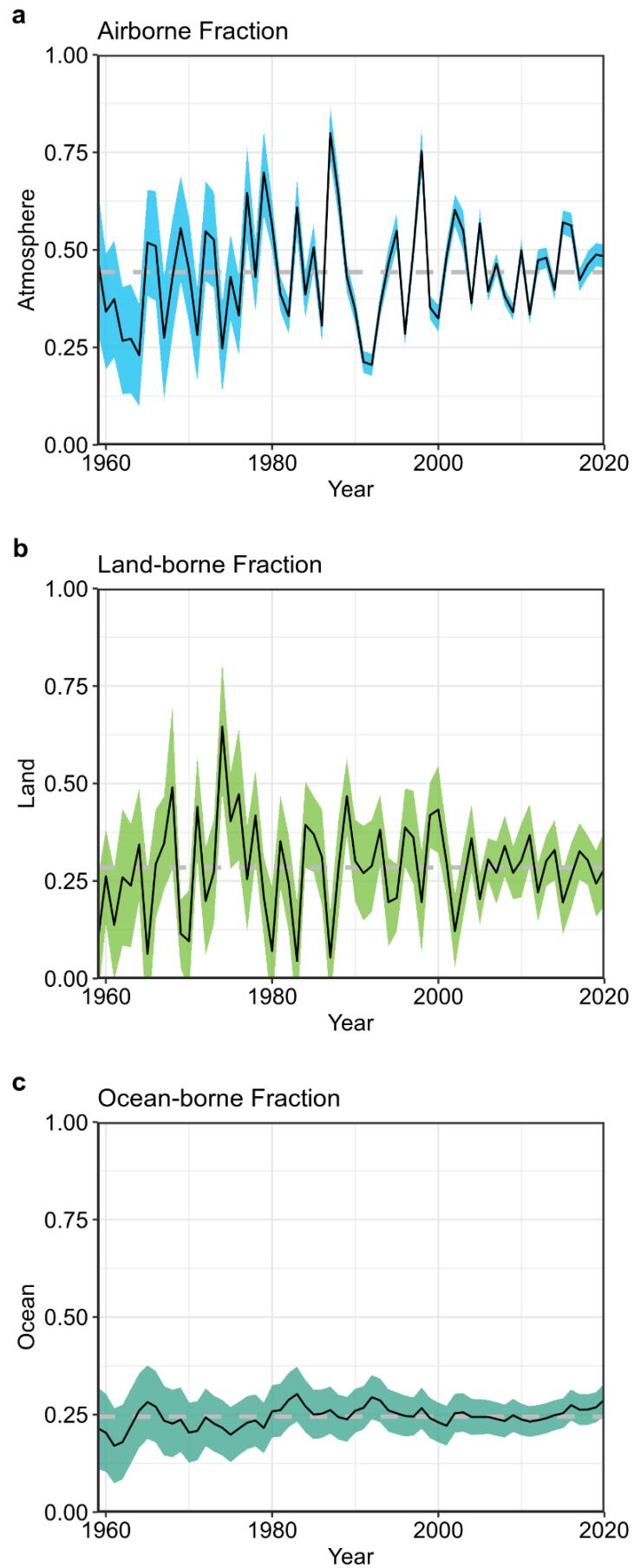
13.10

13.11 **Figure 8.** The partitioning of total anthropogenic CO_2 emissions (E_{FOS} + E_{LUC}) across (a) the atmosphere (airborne fraction), (b) land (land-borne fraction), and (c) ocean (ocean-borne fraction). Black lines represent the central estimate, and the coloured shading represents the uncertainty. The grey dashed lines represent the long-term average of the airborne (44%), land-borne (28%) and ocean-borne (24%) fractions during 1959-2020.

Ocean Sink (S_{OCEAN})
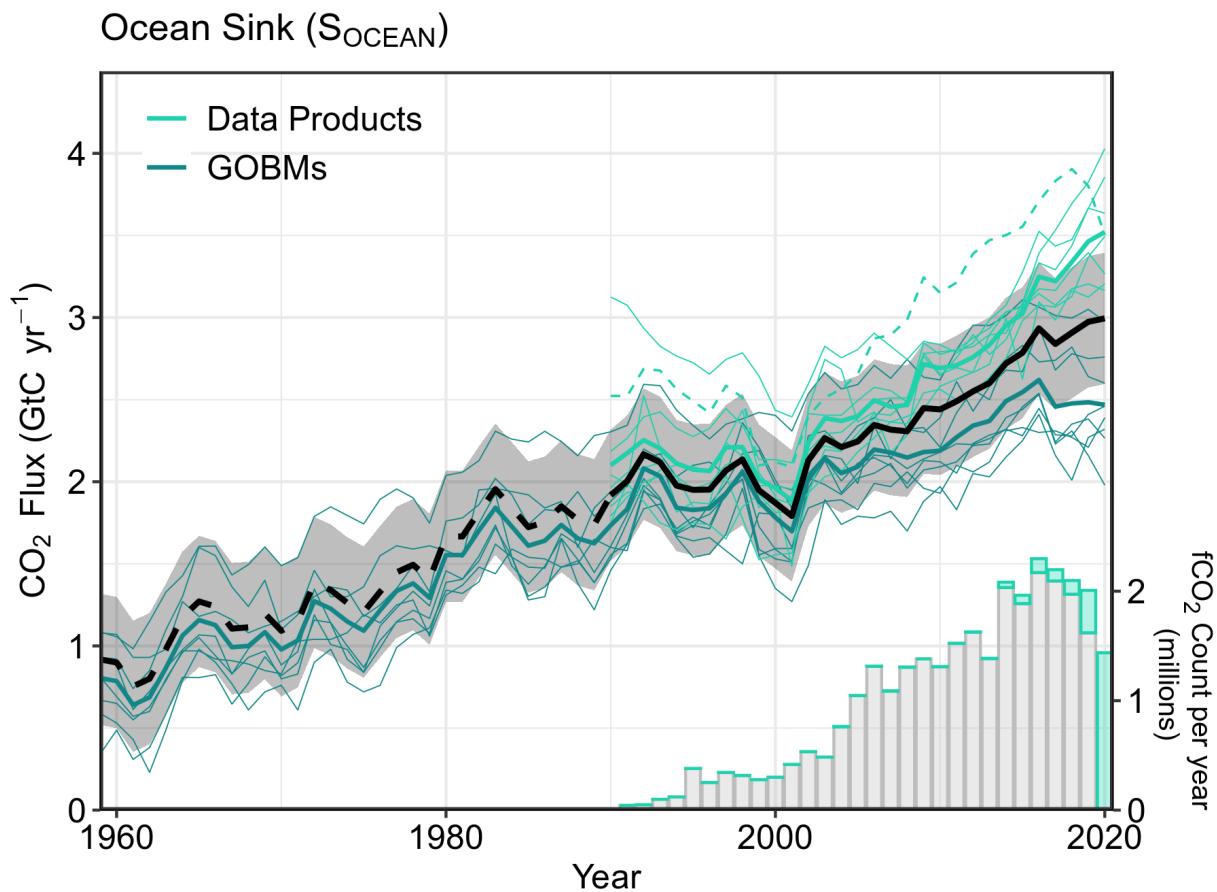
13.12

13.13 **Figure 9.** Comparison of the anthropogenic atmosphere-ocean CO_2 flux showing the budget values of S_{OCEAN} (black; with the uncertainty in grey shading), individual ocean models (teal), and the ocean fCO_2-based data products (cyan; with Watson et al. (2020) in dashed line as not used for ensemble mean). The fCO_2-based data products were adjusted for the pre-industrial ocean source of CO_2 from river input to the ocean, by subtracting a source of 0.61 GtC yr^{-1} to make them comparable to S_{OCEAN} (see Section 2.4). Bar-plot in the lower right illustrates the number of fCO_2 observations in the SOCAT v2021 database (Bakker et al., 2021). Grey bars indicate the number of data points in SOCAT v2020, and coloured bars the newly added observations in v2021.
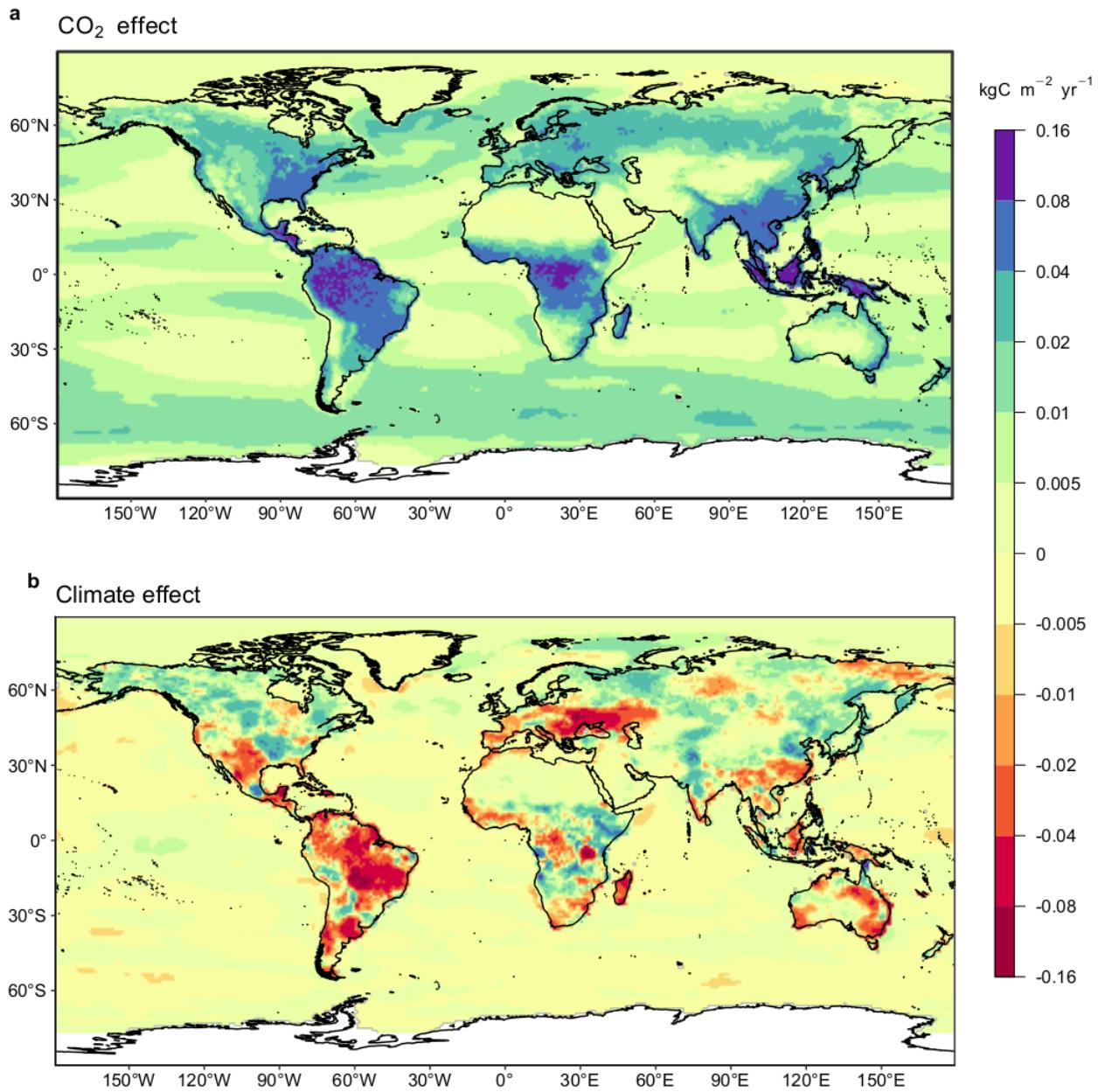
13.14 **Figure 10.** Attribution of the atmosphere-ocean (S_{OCEAN}) and atmosphere-land (S_{LAND}) CO_2 fluxes to (**a**) increasing atmospheric CO_2 concentrations and (**b**) changes in climate, averaged over the previous decade 2011-2020. All data shown is from the processed-based GOBMs and DGVMs. The sum of ocean CO_2 and climate effects will not equal the ocean sink shown in Figure 6 which includes the fCO_2-based data products. See Appendix C.3.2 and C.4.1 for attribution methodology. Units are in kgC m^{-2} yr^{-1} (note the non-linear colour scale).
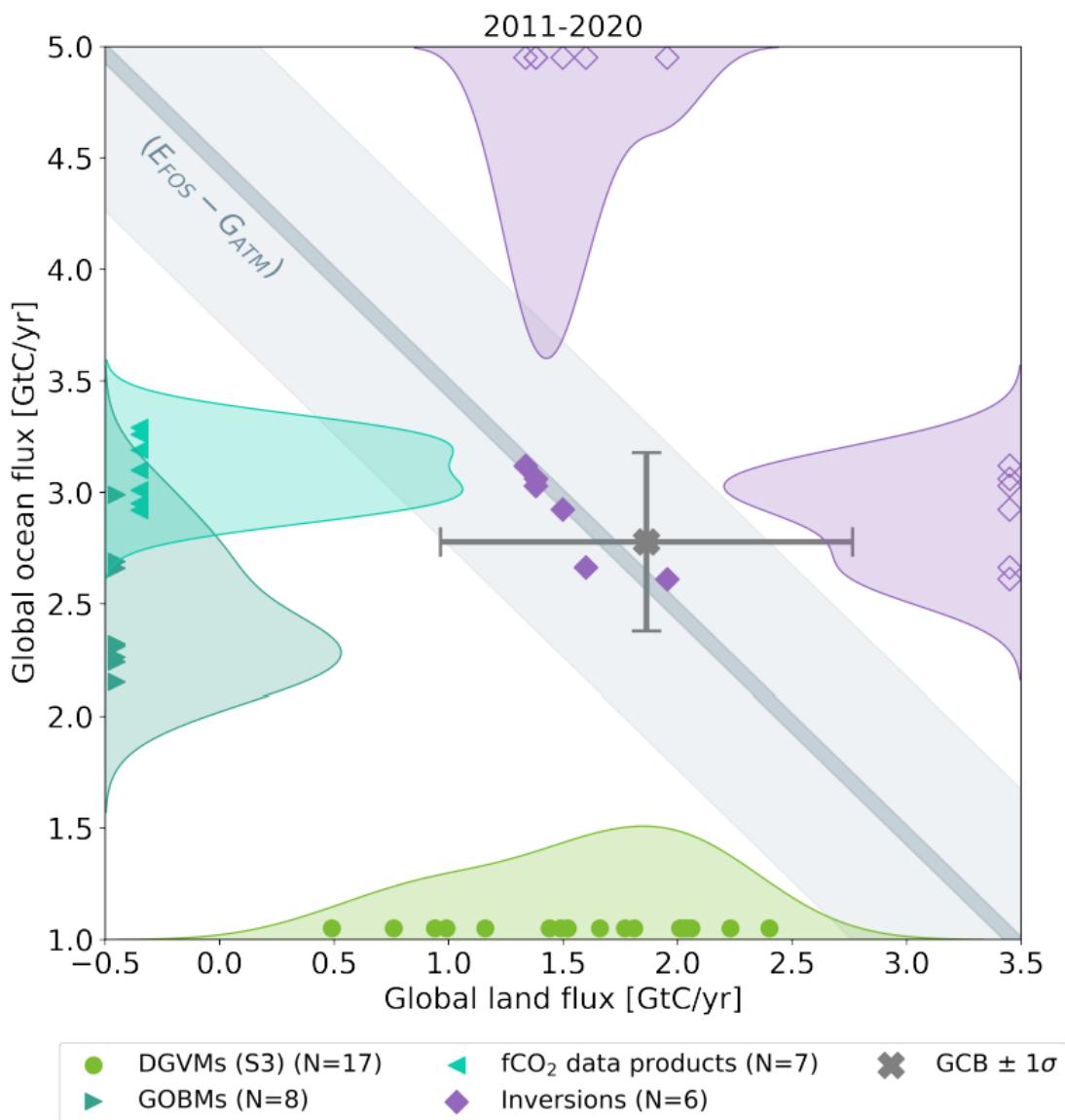
13.15 **Figure 11.** The 2011-2020 decadal mean net atmosphere-ocean and atmosphere-land fluxes derived from the ocean models and fCO_2 products (y-axis, right and left pointing blue triangles respectively), and from the DGVMs (x-axis, green symbols), and the same fluxes estimated from the six inversions (purple symbols on secondary x- and y-axis). The grey central point is the mean (±1σ) of S_{OCEAN} and ($S_{LAND} - E_{LUC}$) as assessed in this budget. The shaded distributions show the density of the ensemble of individual estimates. The grey diagonal band represents the fossil fuel emissions minus the atmospheric growth rate from this budget ($E_{FOS} - G_{ATM}$). Note that positive values are CO_2 sinks.

Annual Carbon Fluxes to (-ve) or from (+ve) the Atmosphere
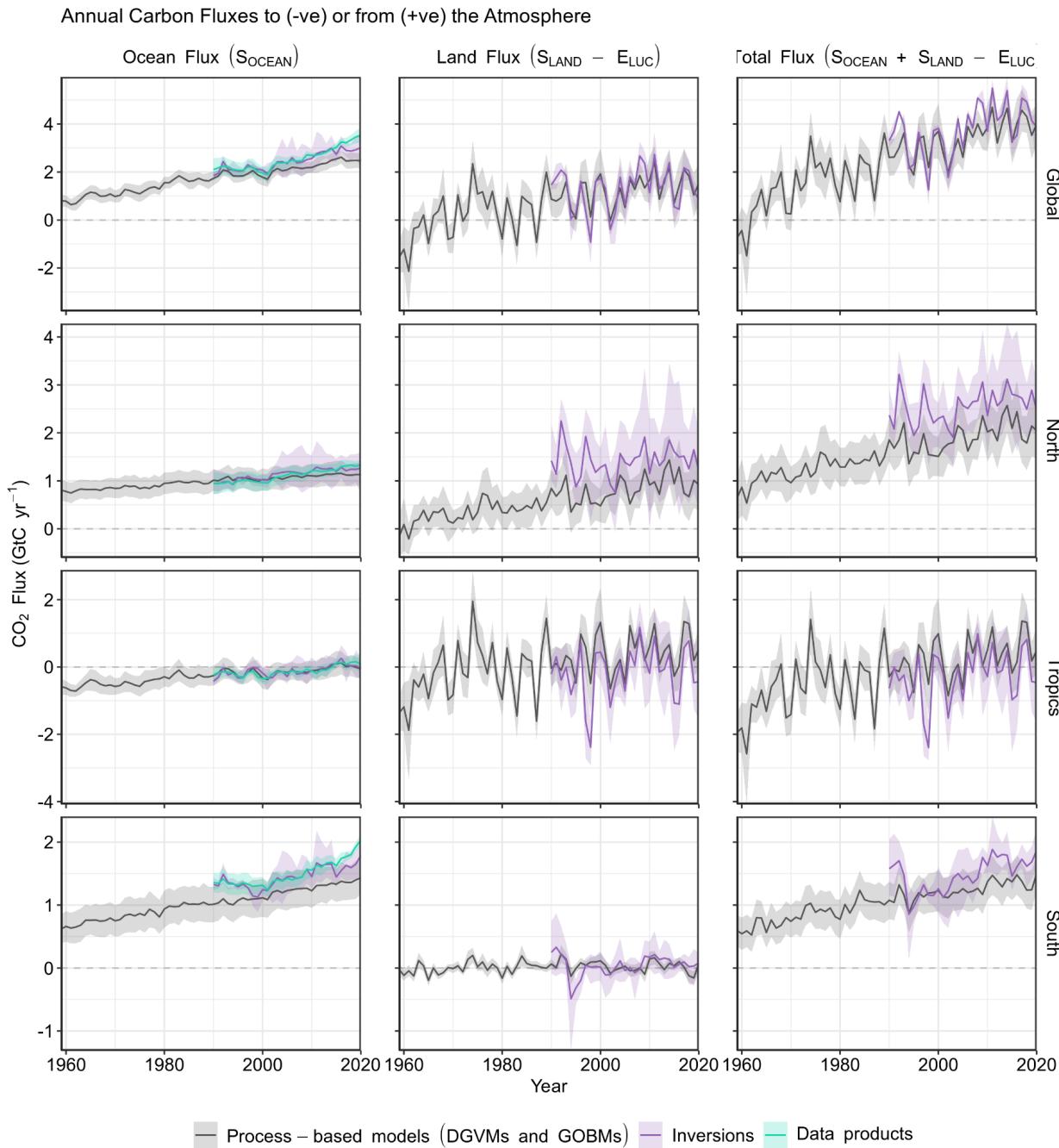
13.16

Figure 12. CO_2 fluxes between the atmosphere and the Earth's surface separated between land and oceans, globally and in three latitude bands. The ocean flux is S_{OCEAN} and the land flux is the net atmosphere-land fluxes from the DGVMs. The latitude bands are (top row) global, (2nd row) north (>30°N), (3rd row) tropics (30°S-30°N), and (bottom row) south (<30°S), and over ocean (left column), land (middle column), and total (right column). Estimates are shown for: process-based models (DGVMs for land, GOBMs for oceans); inversion models (land and ocean); and fCO_2-based data products (ocean only). Positive values indicate a flux from the atmosphere to the land or the ocean. Mean estimates from

the combination of the process models for the land and oceans are shown (black line) with ±1 standard deviation (1σ) of the model ensemble (grey shading). For the total uncertainty in the process-based estimate of the total sink, uncertainties are summed in quadrature. Mean estimates from the atmospheric inversions are shown (purple lines) with their full spread (purple shading). Mean estimates from the fCO_2-based data products are shown for the ocean domain (light blue lines) with their ±1σ spread (light blue shading). The global S_{OCEAN} (upper left) and the sum of S_{OCEAN} in all three regions represents the anthropogenic atmosphere-to-ocean flux based on the assumption that the preindustrial ocean sink was 0 GtC yr^{-1} when riverine fluxes are not considered. This assumption does not hold at the regional level, where preindustrial fluxes can be significantly different from zero. Hence, the regional panels for S_{OCEAN} represent a combination of natural and anthropogenic fluxes. Bias-correction and area-weighting were only applied to global S_{OCEAN}; hence the sum of the regions is slightly different from the global estimate (<0.06 GtC yr^{-1}).

13.17 **Figure 13.** Cumulative changes over the 1850-2020 period (left) and average fluxes over the 2011-2020 period (right) for the anthropogenic perturbation of the global carbon cycle. See the caption of Figure 3 for key information and the methods in text for full details.

13.18 **Figure 14.** Kaya decomposition of the main drivers of fossil CO_2 emissions, considering population, GDP per person, Energy per GDP, and CO_2 emissions per energy, for China (top left), USA (top right), EU27 (middle left), India (middle right), Rest of the World (bottom left), and World (bottom right). Black dots are the annual fossil CO_2 emissions growth rate, coloured bars are the contributions from the different drivers. A general trend is that population and GDP growth put upward pressure on emissions, while energy per GDP and more recently CO_2 emissions per energy put downward pressure on emissions. The changes during 2020 led to a stark contrast to previous years, with different drivers in each region.

14 Appendix A. Supplementary Tables

Table A1. Comparison of the processes included in the bookkeeping method and DGVMs in their estimates of ELUC and SLAND. See Table 4 for model references. All models include deforestation and forest regrowth after abandonment of agriculture (or from afforestation activities on agricultural land). Processes relevant for ELUC are only described for the DGVMs used with land-cover change in this study.

	Bookkeeping Models			DGVMs																
	H&N	BLUE	OSCAR	CABLE-POP	CLASSIC	CLM5.0	DLEM	IBIS	ISAM	ISBA-CTRIP(h)	JSBACH	JULES-ES	LPJ-GUESS	LPJ	LPX-Bern	OCNv2	ORCHIDEEv3	SDGVM	VISIT	YIBs
Processes relevant for ELUC																				
Wood harvest and forest degradation (a)	yes	yes	yes	yes	no	yes	yes	yes	yes	no	yes	no	yes	yes	no (d)	yes	yes	no	yes	no
Shifting cultivation / Subgrid scale transitions	no (b)	yes	yes	yes	no	yes	no	no	no	no	yes	no	yes	yes	no (d)	no	no	no	yes	no
Cropland harvest (removed, R, or added to litter, L)	yes (R) (z)	yes (R) (z)	yes (R)	yes (R)	yes (L)	yes (R)	yes	yes (R)	yes	yes (R+L)	yes (R+L)	yes (R)	yes (R)	yes (L)	yes (R)	yes (R+L)	yes (R)	yes (R)	yse (R)	yes (L)
Peat fires	yes	yes	yes	no	no	yes	no	no	no	no	no	no	no	no	no	no	no	no	no	no
fire as a management tool	yes (z)	yes (z)	yes (j)	no	no	no	no	no	no	no	no	no	no	no	no	no	no	no	no	no
N fertilisation	yes (z)	yes (z)	yes (j)	no	no	yes	yes	no	yes	no	no	yes (k)	yes	no	yes	yes	yes	no	no	no
tillage	yes (z)	yes (z)	yes (j)	no	yes (g)	no	no	no	no	no	no	no	yes	no	no	no	yes (g)	no	no	no
irrigation	yes (z)	yes (z)	yes (j)	no	no	yes	yes	no	yes	no	no	yes	no	no	no	no	no	no	no	no
wetland drainage	yes (z)	yes (z)	yes (j)	no	no	no	no	no	yes	no	no	no	no	no	no	no	no	no	no	no
erosion	yes (z)	yes (z)	yes (j)	no	no	no	yes	no	no	no	no	no	no	no	no	no	no	no	yes	no
peat drainage	yes	yes	yes	no	no	no	no	no	no	no	no	no	no	no	no	no	no	no	no	no
Grazing and mowing Harvest (removed, r, or added to litter, l)	yes (r) (z)	yes (r) (z)	yes (r)	yes (r)	no	no	no	no	yes (l)	no	yes (l)	no	yes (r)	yes (l)	no	yes (r+l)	no	no	no	no
Processes also relevant for SLAND (in addition to CO2 fertilisation and climate)																				
Fire simulation and/or suppression	N.A.	N.A.	N.A.	no	yes	yes	no	yes	no	yes	yes	yes	yes	yes	yes	no	no	yes	yes	no
Carbon-nitrogen interactions, including N deposition	N.A.	N.A.	N.A.	yes	no (f)	yes	yes	no	yes	no (e)	yes	yes	yes	no	yes	yes	yes	yes (c)	no	no (f)

Table A2. Comparison of the processes and model set up for the Global Ocean Biogeochemistry Models for their estimates of SOCEAN. See Table 4 for model references.

	NEMO-PlankTOM12	NEMO-PISCES (IPSL)	MICOM-HAMOCC (NorESM1-OCv1.2)	MPIOM-HAMOCC6	FESOM-2.1-REcoM2	NEMO3.6-PISCESv2-gas (CNRM)	MOM6-COBALT (Princeton)	CESM-ETHZ
SPIN-UP procedure								
Initialisation of carbon chemistry	GLODAPv1 corrected for anthropogenic carbon from Sabine et al. (2004)	GLODAPv2	GLODAP v1 (preindustrial DIC)	initialization from previous model simulations	GLODAPv2 alkalinity and preindustrial DIC	GLODAPv2	GLODAPv2 for Alkalinity and DIC. DIC is corrected to 1959 level for simulation A and C and corrected to pre-industrial level for simulation B using Khatiwala et al. (2009, 2013)	GLODAPv2 preindustrial
Preindustrial spin-up prior to 1850? If yes, how long?	spin-up 1750-1947	spin-up starting in 1836 with 3 loops of JRA55	1000 year spin up	yes, ~2000 years	50 years	long spin-up (> 1000 years)	Other biogeochemical tracers are initialized from a GFDL-ESM2M spin-up (> 1000 years)	spinup 1655-1849
atmospheric forcing for pre-industrial spin-up	looping NCEP year 1990	JRA55	CORE-I (normal year) forcing	spinup with omip climatology to reach steady state with the rivers	JRA55-do v.1.5.0 repeated year 1961	JRA55-do	GFDL-ESM2M internal forcing	COREv2 forcing until 1835, three cycles of conditions from 1949-2009. from 1835-1850: JRA forcing
atmospheric forcing for historical spin-up 1850-1958 for simulation A	1750-1947: looping NCEP year 1990; 1948-2020: NCEP	1836-1958 : looping full JRA55 reanalysis	CORE-I (normal year) forcing; from 1948 onwards NCEP-R1 with CORE-II corrections	NCEP 6 hourly cyclic forcing (10 years starting from 1948) with co2 at 278 ppm and rivers	JRA55-do-v1.5.0 repeated year 1961	JRA55-do cycling year 1958	JRA55-do-v1.5 repeat year 1959 (71 years)	JRA55 version 1.3, repeat cycle between 1958-2018.
atmospheric CO2 for historical spin-up 1850-1958 for simulation A	provided by the GCP; converted to pCO2 temperature formulation (Sarmiento et al., 1992), monthly	xCO2 as provided by the GCB, global mean, annual resolution, converted to pCO2 with sea-level	xCO2 as provided by the GCB, converted to pCO2 with sea level pressure and water vapor correction	provided by the GCB	xCO2 as provided by the GCB, converted to pCO2 with sea-level pressure and water vapour pressure,	xCO2 as provided by the GCB, converted to pCO2 with constant sea-level pressure and water vapour	xCO2 at year 1959 level (315 ppm), converted to pCO2 with sea-level pressure and water vapour pressure,	xCO2 as provided by the GCB (new version 2021), converted to pCO2 with atmospheric pressure,

	resolution	pressure and water vapour pressure			global mean, monthly resolution	pressure, global mean, yearly resolution	global mean, yearly resolution	and locally determined water vapour pressure from SST and SSS (100% saturation)
atmospheric forcing for control spin-up 1850-1958 for simulation B	1750-2020: looping NCEP 1990	1836-1958 : looping full JRA55 reanalysis	CORE-I (normal year) forcing	NCEP 1957 fixed forcing, co2=278 and rivers	JRA55-do-v1.5.0 repeat year 1961	JRA55-do cycling year 1958	JRA55-do-v1.5 repeat year 1959 (71 years)	normal year forcing created from JRA-55 version 1.3, NYF = climatology with anomalies from the year 2001
atmospheric CO2 for control spin-up 1850-1958 for simulation B	constant 278ppm; converted to pCO2 temperature formulation (Sarmiento et al., 1992), monthly resolution	xCO2 of 286.46ppm, converted to pCO2 with constant sea-level pressure and water vapour pressure	xCO2 of 278 ppm, converted to pCO2 with seal level pressure and water vapor correction	278, no conversion, assuming constant standard sea level pressure	xCO2 of 278ppm, converted to pCO2 with sea-level pressure and water vapour pressure	xCO2 of 286.46ppm, converted to pCO2 with constant sea-level pressure and water vapour pressure	xCO2 of 278ppm, converted to pCO2 with sea-level pressure and water vapour pressure	xCO2 as provided by the GCB for 1850, converted to pCO2 with atmospheric pressure, and locally determined water vapour pressure from SST and SSS (100% saturation)
simulation A								
Atmospheric forcing for simulation A	NCEP	JRA55-v1.4 then 1.5 for 2020.	NCEP-R1 with CORE-II corrections	till1948: continue from A_spinup with cyclic NCEP forcing (1948+10) and increasing CO2 => GCBA-1777-1948 -1948-2020 : with transient NCEP forcing and transient monthly CO2	JRA55-do-v1.5.0	JRA55-do	JRA55-do-v1.5.0 1959-2019 and JRA55-do-v1.5.0.1b for 2020	JRA-55 version 1.3
atmospheric CO2 for simulation A	provided by the GCP; converted to pCO2 temperature formulation (Sarmiento et al., 1992), monthly resolution	xCO2 as provided by the GCB, global mean, annual resolution, converted to pCO2 with sea-level pressure and	xCO2 as provided by the GCB, converted to pCO2 with sea level pressure and water vapor correction		xCO2 as provided by the GCB, converted to pCO2 with sea-level pressure and water vapour pressure, global mean,	xCO2 as provided by the GCB, converted to pCO2 with constant sea-level pressure and water vapour pressure,	xCO2 as provided by the GCB, converted to pCO2 with sea-level pressure and water vapour pressure, global mean,	xCO2 as provided by the GCB (new version 2021), converted to pCO2 with atmospheric pressure, and locally

			water vapour pressure			monthly resolution	global mean, yearly resolution	yearly resolution	determined water vapour pressure from SST and SSS (100% saturation)

simulation B

Atmospheric forcing for simulation B	NCEP 1990	N/A	CORE-I (normal year) forcing	1948-2020: continue with B_spinup with fixed NCEP forcing 1957, co2=278 and rivers	JRA55-do-v1.5.0 repeat year 1961	JRA55-do cycling year 1958	JRA55-do-v1.5.0 repeat year 1959	normal year forcing created from JRA-55 version 1.3, NYF = climatology with anomalies from the year 2001
atmospheric CO2 for simulation B	constant 278ppm; converted to pCO2 temperature formulation (Sarmiento et al., 1992), monthly resolution	N/A	xCO2 of 278 ppm, converted to pCO2 with sea level pressure and water vapor correction		xCO2 of 278ppm, converted to pCO2 with sea-level pressure and water vapour pressure	xCO2 of 286.46ppm, converted to pCO2 with constant sea-level pressure and water vapour pressure	xCO2 of 278ppm, converted to pCO2 with sea-level pressure and water vapour pressure	xCO2 as provided by the GCB for 1850, converted to pCO2 with atmospheric pressure, and locally determined water vapour pressure from SST and SSS (100% saturation)

model specifics

Physical ocean model	NEMOv3.6-ORCA2	NEMOv3.6-eORCA1L75	MICOM (NorESM1-OCv1.2)	MPIOM	FESOM-2.1	NEMOv3.6-GELATOv6-eORCA1L75	MOM6-SIS2	CESMv1.3 (ocean model based on POP2)
Biogeochemistry model	PlankTOM12	PISCESv2	HAMOCC (NorESM1-OCv1.2)	HAMOCC6	REcoM-2-M	PISCESv2-gas	COBALTv2	BEC (modified & extended)
Horizontal resolution	2o lon, 0.3 to 1.5o lat	1° lon, 0.3 to 1° lat	1° lon, 0.17 to 0.25 lat (nominally 1°)	1.5°	unstructured multi-resolution mesh. CORE-mesh, with 20-120 km resolution. Highest resolution north of 50N, intermediate in the equatorial belt and Southern Ocean, lowest in the subtropical gyres	1° lon, 0.3 to 1° lat	0.5° lon, 0.25 to 0.5° lat	Lon: 1.125°, Lat varying from 0.53° in the extratropics to 0.27° near the equator

Vertical resolution	31 levels	75 levels, 1m at the surface	51 isopycnic layers + 2 layers representing a bulk mixed layer	40 levels, layer thickness increase with depth	46 levels, 10 m spacing in the top 100 m	75 levels, 1m at surface	75 levels hybrid coordinates, 2 m at surface	60 levels (z-coordinates)
Total ocean area on native grid (km2)	3.6080E+08	3.6270E+08	3.6006E+08	3.6598E+08	3.6475E+08	3.6270E+14	3.6110E+08	3.5926E+08
Ocean area on native grid (km2) - NORTH	6.2646E+07		6.2049E+07	6.4440E+07		6.3971E+13		
Ocean area on native grid (km2) - TROPICS	1.1051E+08		1.9037E+08	1.9248E+08		1.9025E+14		
Ocean area on native grid (km2) - SOUTH	1.8766E+08		1.0765E+08	1.0986E+08		1.0848E+14		
gas-exchange parameterization	Quadratic exchange formulation (function of T + 0.3*U^2)* (Sc/660)^-0.5) ; Wanninkhof (1992, Equation 8); Sweeney et al. (2007)	see Orr et al. (2017): kw parameterized from Wanninkhof (1992), with kw = a* (Sc/660)^-0.5) *u2*(1-f_ice) with a from Wanninkhof (2014)	see Orr et al. (2017): kw parameterized from Wanninkhof (1992), with kw = a* (Sc/660)^-0.5) *u2*(1-f_ice) with a=0.337 following the OCMIP2 protocols	Gas transfer velocity formulation and parameter setup of Wanninkhof (2014), including updated Schmidt number parameterizations for CO2 to comply with OMIP protocol (Orr et al., 2017)	see Orr et al. (2017): kw parameterized from Wanninkhof (1992), with kw = a* (Sc/660)^-0.5) *u2*(1-f_ice) with a from Wanninkhof (2014)	see Orr et al. (2017): kw parameterized from Wanninkhof (1992), with kw = a* (Sc/660)^-0.5) *u2*(1-f_ice) with a from Wanninkhof (2014)	see Orr et al. (2017): kw parameterized from Wanninkhof (1992), with kw = a* (Sc/660)^-0.5) *u2*(1-f_ice) with a from Wanninkhof (2014)	Gas exchange is parameterized using the Wanninkhof (1992) quadratic windspeed dependency formulation, but with the coefficient scaled down to reflect the recent 14C inventories. Concretely, we used a coeffecient a of 0:31 cm hr-1 s2 m-2 to read kw = 0:31 ws^2 (1-fice) (Sc=660)^{-1/2}
time-step	96 mins	45 min	3200 sec	60 mins	45 min	15min	30 min	3757 sec
output frequency	Monthly	monthly	monthly/daily	monthly	monthly	monthly	monthly	monthly
CO2 chemistry routines	Following Broecker et al. (1982)	mocsy	Following Dickson et al. (2007)	as in Ilyina et al. (2013) adapted to comply with OMIP protocol (Orr et al., 2017).	mocsy	mocsy	mocsy	OCMIP2 (Orr et al., 2017)
river carbon input (PgC/yr)	60.24 Tmol/yr; 0.723 PgC/yr	0.61 PgC y-1	0	0.77 PgC/yr	0	~0.611 PgC y-1	~0.15 PgC y-1	0.33 Pg C yr-1
burial/net flux into the sediment (PgC/yr)	0.723 PgC/yr	0.59 GtC y-1	around 0.54	around 0.44 PgC/yr	0	~0.656 GtC y-1	~0.18 PgC y-1	0.21 Pg C yr-1

Table A3: Description of ocean data-products used for assessment of SOCEAN. See Table 4 for references.

	Jena-MLS	MPI-SOMFFN	CMEMS-LSCE-FFNN	CSIR-ML6	Watson et al	NIES-NN	JMA-MLR	OS-ETHZ-GRaCER
Method	Spatio-temporal interpolation (update of Rödenbeck et al., 2013, version oc_v2021). Specifically, the sea-air CO_2 fluxes and the pCO_2 field are numerically linked to each other and to the spatio-temporal field of ocean-internal carbon sources/sinks through process parametrizations, and the ocean-internal sources/sink field is then fit to the SOCATv2021 pCO_2 data (Bakker et al., 2021). The fit includes a multi-linear regression against environmental drivers to bridge data gaps, and interannually explicit corrections to represent the data signals more completely.	2-step neural network method where in a first step the global ocean is clustered into 16 biogeochemical provinces (one stand alone province for the Arctic Ocean - see Landschützer et al 2020) using a self-organizing map (SOM). In a second step, the non-linear relationship between available pCO_2 measurements from the SOCAT database (Bakker et al 2016) and environmental predictor data (SST, SSS, MLD, CHL-a, atmospheric CO_2 - references see Landschützer et al 2016) are established using a feed-forward neural network (FFN) for each province separately. The established relationship is then used to fill the existing data gaps (see Landschützer et al. 2013, 2016).	An ensemble of neural network models trained on 100 subsampled datasets from the Surface Ocean CO_2 Atlas v2021 (SOCATv2021, Bakker et al. 2021) . Like the original data, subsamples are distributed after interpolation on 1x1 grid cells along ship tracks. Sea surface salinity, temperature, sea surface height, mixed layer depth, atmospheric CO_2 mole fraction, chlorophyll-a, pCO_2 climatology, latitude and longitude are used as predictors. The models are used to reconstruct sea surface pCO_2 and convert to air-sea CO_2 fluxes (see the proposed ensemble-based approach and analysis in Chau et al. 2020, 2021).	An ensemble average of six machine learning estimates of surface ocean pCO_2 using the approach described in Gregor et al. (2019) with the updated product using SOCAT v2021 (Bakker et al., 2016). All ensemble members use a cluster-regression approach. Two different cluster configurations are used: (1) based on K-means clustering; (2) Fay and McKinley (2014) 's CO_2 biomes. Three regression algorithms are used: (1) gradient boosted decision trees; (2) feed-forward neural network; (3) support vector regression. The product of the cluster configurations and the regression algorithms results in an ensemble with six members., hence the CSIR-ML6.	Derived from the SOCAT(v2021) pCO_2 database, but corrected to the subskin temperature of the ocean as measured by satellite, using the methodology described by Goddijn-Murphy et al. (2015). A correction to the flux calculation is also applied for the cool and salty surface skin. In other respects the product uses interpolation of the data using the two step neural network based on MPI-SOMFFN :in the first step the ocean is divided into a monthly climatology of 16 biogeochemical provinces using a SOM, In the second step a feed-forward neural network establishes non-linear relationships between pCO_2 and SST, SSS, mixed layer depth(MLD) and atmospheric xCO2 in each	A feed forward neural network model was used to reconstruct monthly global surface ocean CO_2 concentrations 1x1 degree meshes and estimate air-sea CO_2 fluxes. The target variable is the per cruise weighted fCO2 mean of SOCAT 2021. Feature variables include sea surface temperature (SST), salinity, chlorophyll-a, mixed layer depth, and the monthly nomaly of SST. See Zeng et al. (2014)	Fields of total alkalinity (TA) were estimated by using a multiple linear regressions (MLR) method based on GLODAPv2.2021 and satellite observation data. TA = f(SSDH, SSS) SOCATv2021 fCO2 data were converted to total dissolved inorganic carbon (DIC) concentrations in combination with the TA, and then fields of DIC were estimated by using a MLR method based on the DIC and satellite observation data. DIC = f(SSDH, SST, SSS, log(Chl), log(MLD), time)	OceanSODA-ETHZ's Geospatial Random Cluster Ensemble Regression is a two-step cluster-regression approach, where multiple clustering instances with slight variations are run to create an ensemble of estimates (n_membersd= 16). We use K-means clustering (n_clusters=21) for the clustering step and a combination of Gradient boosted trees (n_members=8) and Feed-forward neural-networks (n_members=8) to estimate SOCAT v2021 fCO2. Clustering is performed on the following variables: SOCOM_pCO2_climatology, SST_clim, MLD_clim, CHL_clim. Regression is performed on the following variables: xCO2atm, SST, SST_anomaly, SSS, CHL, MLD, u10_wind, v10_wind, sea-

					of the 16 provinces. Further description in Watson et al. (2020).			ice changes, SSH (note that the latter two variables are an update from Gregor and Gruber, 2021).
Gas-exchange parameterization	Quadratic exchange formulation $(k*U^2*(Sc/660)^{-0.5})$ (Wanninkhof, 1992) with the transfer coefficient k scaled to match a global mean transfer rate of 16.5 cm/hr by Naegler (2009)	Quadratic exchange formulation $(k*U^2*(Sc/660)^{-0.5})$ (Wanninkhof, 1992) with the transfer coefficient k scaled to match a global mean transfer rate of 16.5 cm/hr (calculated myself over the full period 1982-2020)	Quadratic exchange formulation $(k*U^2*(Sc/660)^{-0.5})$ (Wanninkhof., 2014) with the transfer coefficient k scaled to match a global mean transfer rate of 16.5 cm/hr (Naegler, 2009).	Quadratic formulation $kw = a *U10^2 * (Sc/660)^{0.5}()$. We use scaled kw for ERA5 reanalysis wind data, which is scaled globally to 16.5 cm/hr (after Naegler 2009) like in Fay and Gregor et al. (2021) https://doi.org/10.5194/essd-2021-16	Nightingale et al. (2000) formulation : $K=((Sc/600)^{-0.5})*(0.333*U+0.222*U^2)$	$Kw=0.251*Wnd*Wnd/sqrt(Sc/660.0)$ (Wanninkhof, 2014)	Quadratic exchange formulation $(k*U^2*(Sc/660)^{-0.5})$ (Wanninkhof., 2014) with the transfer coefficient k scaled to match a global mean transfer rate of 16.5 cm/hr (Naegler, 2009) under fitted to the JRA55 wind field.	Quadratic formulation of bulk air-sea CO_2 flux: $kw = a * U10^2 * (Sc/660)^{0.5}$ We use individually scaled kw's for JRA55, ERA5, and NCEP-R1, which are all scaled globally to 16.5 cm/hr (after Naegler, 2009). See Fay and Gregor et al. (2021)
Wind product	JMA55-do reanalysis	ERA 5	ERA5	ERA5	CCMP wind product, 0.25 x 0.25 degrees x 6-hourly, from which we calculate mean and mean square winds over 1 x 1 degree and 1 month intervals. CCMP product does not cover years 1985-1987, for which we use a monthly climatology calculated as the means of 1988-1991.	ERA5	JRA55	JRA55, ERA5, NCEP1
Spatial resolution	2.5 degrees longitude * 2 degrees latitude	1x1 degree	1x1 degree	1 x 1	1 x 1 degree	1x1 degree	1x1 degree	1x1 degree

Temporal resolution	daily	monthly	monthly	monthly	monthly	monthly	monthly	monthly
Atmospheric CO2	Spatially and temporally varying field based on atmospheric CO2 data from 169 stations (Jena CarboScope atmospheric inversion sEXTALL_v2021)	atmospheric pCO2_wet calculated from the NOAA ESRL marine boundary layer xCO2 and the NCEP sea level pressure with the moisture correction by Dickson et al 2007 (details and references can be obtained from Appendix A3 in Landschützer et al 2013)	Spatially and monthly varying fields of atmospheric pCO2 computed from CO2 mole fraction (Chevallier, 2013; CO2 atmospheric inversion from the Copernicus Atmosphere Monitoring Service), and atmospheric dry-air pressure which is derived from monthly surface pressure (ERA5) and water vapour pressure fitted by Weiss and Price (1980)	The NOAA's marine boundary layer product for the mole fraction of carbon dioxide (xCO2) is linearly interpolated onto a 1°x1° grid and resampled from weekly to monthly. Basically, xCO2 is multiplied by ERA5 mean sea level pressure (MSLP), and a water vapour pressure correction is applied to MSLP using the equation from Dickson et al. (2007). This results in monthly 1°x 1° atmospheric pCO2.	Atmospheric pCO2 (wet) calculated from NOAA marine boundary layer XCO2 and NCEP sea level pressure, with pH2O calculated from Cooper et al. (1998). (2019 XCO2 marine boundary values were not available at submission so we used preliminary values, estimated from 2018 values and increase at Mauna Loa.)	NOAA Greenhouse Gas Marine Boundary Layer Reference. https://gml.noaa.gov/ccgg/mbl/mbl.html	Atmospheric xCO2 fields of JMA-GSAM inversion model (Maki et al. 2010; Nakamura et al. 2015) were used. They were converted to pCO2 by using JRA55 sea level pressure. xCO2 fields in 2020 were not available at this stage, and we use observation data of obspack_co2_1_NRT_v6.1.1_2021-05-17 (Di Sarra et al. 2021) to estimate the increase from 2019 to 2020.	NOAA's marine boundary layer product for xCO2 is linearly interpolated onto a 1x1 degree grid and resampled from weekly to monthly. xCO2 is multiplied by ERA5 mean sea level pressure, where the latter corrected for water vapour pressure using Dickson et al. (2007). This results in monthly 1x1 degree pCO2atm.
Total ocean area on native grid (km2)	3.63E+08	3.63E+08	3.46E+08	3.48E+08	3.51E+08	3.28E+08 (3.23E+08 to 3.35E+08, depending on ice cover)	3.05E+08 (2.98E+08 to 3.15E+08, depending on ice cover)	3.55E+08
method to extend product to full global ocean coverage		Arctic and marginal seas added following Landschützer et al. (2020). previously applied coastal cut (1degree off coast) was dropped					We used the same method as Fay et al. (2021a)	Method has near full coverage
Ocean area on native grid (km2) - NORTH			5.4545E+07	5.0528E+07	5.0700E+07		3.90E+07 (3.75E+07 to 4.09E+07, depending on ice cover)	5.9771E+07
Ocean area on native grid (km2) - TROPICS			1.8875E+08	1.8933E+08	1.9230E+08		1.74E+08	1.8779E+08

			1.0241E+08	1.0767E+08	1.0868E+08		9.20E+07 (8.47E+07 to 1.02E+08, depending on ice cover)	1.0705E+08
Ocean area on native grid (km2) - SOUTH								

Table A4. Comparison of the inversion set up and input fields for the atmospheric inversions. Atmospheric inversions see the full CO2 fluxes, including the anthropogenic and pre-industrial fluxes. Hence they need to be adjusted for the pre-industrial flux of CO2 from the land to the ocean that is part of the natural carbon cycle before they can be compared with SOCEAN and SLAND from process models. See Table 4 for references.

	CarbonTracker Europe (CTE)	Jena CarboScope	Copernicus Atmosphere Monitoring Service (CAMS)	UoE	CMS-Flux	NISMON-CO2
Version number	CTE2021	sEXTocNEET_v2021	v20r2	in-situ		v2021.1
Observations						
Atmospheric observations	Hourly resolution (well-mixed conditions) obspack GLOBALVIEWplus v6.1 and NRT_v6.1.1 (a)	Flasks and hourly from various institutions (outliers removed by 2-sigma criterion)	Hourly resolution (well-mixed conditions) obspack GLOBALVIEWplus v6.1 and NRT_v6.1.1 (a), WDCGG, RAMCES and ICOS ATC	Hourly resolution (well-mixed conditions) obspack GLOBALVIEWplus v6.1 and NRT_v6.1.1 (a)	ACOS-GOSAT v9 (6) retrievals between July 2009 and Dec 2014 and OCO-2 b10 (7) retrievals between Jan 2015 to Dec 2015. In addition, surface flask observations from remote sites were also assimilated from GLOBALVIEWplus v6.1 and NRT_v6.1.1 .	Hourly resolution (well-mixed conditions) obspack GLOBALVIEWplus v6.1 and NRT_v6.1.1 (a)
Period covered	2001-2020	1957-2020	1979-2021	2001-2020	2010-2020	1990-2020
Prior fluxes						
Biosphere and fires	SIBCASA biosphere (b) with 2019-2020 climatological, GFAS fires	No prior	ORCHIDEE (climatological), GFEDv4.1s	CASA v1.0, climatology after 2016 & GFED4.0	yearly repeating CARDAMOM biosphere+fires	VISIT & GFEDv4.1s
Ocean	oc_v2020 (Rodenbeck et al., 2014), with updates, For 2020: climatology based on years 2015-2019	oc_v2021 (Rödenbeck et al., 2014) with updates	CMEMS Copernicus ocean fluxes (Denvil-Sommer et al., 2019), with updates	Takahashi climatology	MOM6	JMA global ocean mapping (Iida et al., 2015)
Fossil fuels	GCP-GridFEDv2021.1 (Jones et al., 2021) for 2000-2018, GCP-GridFEDv2021.2 for 2019+2020 (c)	GCP-GridFEDv2021.2 (Jones et al., 2021b) (c)	GCP-GridFEDv2021.2 (Jones et al., 2021b) (c)	GCP-GridFEDv2021.2 (Jones et al., 2021b) (c)	GCP-GridFEDv2021.2 (Jones et al., 2021b) (c)	GCP-GridFEDv2021.2 (Jones et al., 2021b) (c)
Transport and optimization						
Transport model	TM5	TM3	LMDZ v6	GEOS-CHEM	GEOS-CHEM	NICAM-TM
Weather forcing	ECMWF	NCEP	ECMWF	MERRA2	MERRA-2	JRA55

Horizontal Resolution	Global: 3° x 2°, Europe: 1° x 1°, North America: 1° x 1°	Global: 4° x 5°	Global: 3.75° x 1.875°	Global: 4° x 5°	Global: 4° x 5°	isocahedral grid: ~225km
Optimization	Ensemble Kalman filter	Conjugate gradient (re-ortho-normalization) (d)	Variational	Ensemble Kalman filter	Variational	Variational

(a) (Cox et al., 2021; Di Sarra et al., 2021)

(b) (van der Velde et al., 2014)

(c) GCP-GridFEDv2021.2 (Jones et al., 2021b) is an update through the year 2020 of the GCP-GridFED dataset presented by Jones et al. (2021a).

(d) ocean prior not optimised

Table A5 Attribution of fCO2 measurements for the year 2020 included in SOCATv2021 (Bakker et al., 2016, 2021) to inform ocean fCO2-based data products.

Platform name	Regions	No. of measurements	Principal Investigators	No. of data sets	Platform type
1 degree	North Atlantic, Coastal	8,652	Gutekunst, S.	2	Ship
Allure of the Seas	North Atlantic, Tropical Atlantic, Coastal	19,321	Wanninkhof, R.; Pierrot, D.	8	Ship
Atlantic Explorer	North Atlantic	15,665	Bates, N.	11	Ship
Atlantic Sail	North Atlantic, Coastal	25,082	Steinhoff, T.; Körtzinger, A.	6	Ship
Aurora Australis	Southern Ocean	14,316	Tilbrook, B.	1	Ship
Bjarni Saemundsson	Coastal	3,269	Benoit-Cattin A.; Ólafsdóttir, S. R.	1	Ship
BlueFin	North Pacific, Tropical Pacific, Coastal	76,505	Alin, S. R.; Feely, R. A.	12	Ship
Cap San Lorenzo	Tropical Atlantic, Coastal	12,417	Lefèvre, N.	2	Ship
Celtic Explorer	North Atlantic, Coastal	18,617	Cronin, M.	6	Ship
Colibri	North Atlantic, Tropical Atlantic, Coastal	13,402	Lefèvre, N.	2	Ship
Equinox	North Atlantic, Coastal	25,052	Wanninkhof, R.; Pierrot, D.	11	Ship
F. G. Walton Smith	Coastal	10,460	Rodriguez, C.; Millero, F. J.; Pierrot, D.; Wanninkhof, R.	6	Ship
Finnmaid	Coastal	253,894	Rehder, G.; Glockzin, M.	11	Ship
Flora	Tropical Pacific	4,099	Wanninkhof, R.; Pierrot, D.	2	Ship
G.O. Sars	Arctic, North Atlantic, Coastal	75,833	Skjelvan, I.	7	Ship
GAKOA_149W_60N	Coastal	68	Cross, J. N.; Monacci, N. M.	3	Mooring
Gulf Challenger	Coastal	2,717	Salisbury, J.; Vandemark, D.; Hunt, C.	3	Ship
Healy	Arctic, North Pacific, Coastal	16,943	Sweeney, C.; Newberger, T.; Sutherland, S. C.; Munro, D. R.	4	Ship
Henry B. Bigelow	North Atlantic, Coastal	14,436	Wanninkhof, R.; Pierrot, D.	4	Ship
Heron Island	Coastal	768	Tilbrook B.	1	Mooring
James Clark Ross	Southern Ocean	2,000	Kitidis, V.	1	Ship
James Cook	North Atlantic, Tropical Atlantic, Coastal	46,710	Theetaert, H.	1	Ship
KC_BUOY	Coastal	1,983	Evans, W.	1	Mooring
Laurence M. Gould	Southern Ocean	25,414	Sweeney, C.; Newberger, T.; Sutherland, S. C.; Munro, D. R.	4	Ship
Maria. S. Merian	Tropical Atlantic, Coastal	35,806	Ritschel, M.	1	Ship
Marion Dufresne	Southern Ocean, Indian	4,709	Lo Monaco, C.; Metzl, N.	1	Ship
Nathaniel B. Palmer	Southern Ocean, Tropical Pacific	34,357	Sweeney, C.; Newberger, T.; Sutherland, S. C.; Munro, D. R.	3	Ship
New Century 2	North Pacific, Tropical Pacific, Tropical Atlantic, North Atlantic, Coastal	27,793	Nakaoka, S.-I.	14	Ship
Nuka Arctica	North Atlantic, Coastal	26,576	Becker, M.; Olsen, A.	6	Ship
Oscar Dyson	Arctic, North Pacific, Coastal	28,196	Alin, S. R.; Feely, R. A.	6	Ship
Quadra Island Field Station	Coastal	78,098	Evans, W.	1	Mooring
Ronald H. Brown	Southern Ocean, Tropical Atlantic, North Atlantic, Coastal	51,611	Wanninkhof, R.; Pierrot, D.	6	Ship

Saildrone1030	North Atlantic, Tropical Atlantic, Coastal	4,080	Skjelvan, I.; Fiedler, B.; Pfeil, B.; Jones, S. D.	1	Saildrone
Sea Explorer	Southern Ocean, Tropical Atlantic, North Atlantic, Coastal	89,896	Landschützer, P.; Tanhua, T.	6	Ship
Sikuliaq	Arctic, North Pacific, Coastal	36,278	Sweeney, C.; Newberger, T.; Sutherland, S. C.; Munro, D. R.	10	Ship
Simon Stevin	Coastal	16,448	Gkritzalis, T.	4	Ship
Soyo Maru	Coastal	46,280	Ono, T.	2	Ship
Tangaroa	Southern Ocean, Tropical Pacific	121,135	Currie, K. I.	13	Ship
TAO110W_0N	Tropical Pacific	1,518	Sutton, A. J.	3	Mooring
Tavastland	Coastal	4,214	Willstrand Wranne, A., Steinhoff, T.	5	Ship
Thomas G. Thompson	Southern Ocean, Tropical Atlantic	1,317	Alin, S. R.; Feely, R. A.	1	Ship
Trans Carrier	Coastal	24,135	Omar, A. M.	13	Ship
Trans Future 5	Southern Ocean, Coastal	16,404	Nakaoka, S.-I.; Nojiri, Y.	15	Ship
Wakataka Maru	North Pacific, Coastal	101,327	Tadokoro, K.; Ono, T.	7	Ship

Table A6. Aircraft measurement programs archived by Cooperative Global Atmospheric Data Integration Project (CGADIP; Cox et al., 2021) that contribute to the evaluation of the atmospheric inversions (Figure B4).				
Site code	Measurement program name in Obspack	Specific doi	Data providers	used in 2021
AAO	Airborne Aerosol Observatory, Bondville, Illinois		Sweeney, C.; Dlugokencky, E.J.	yes
ACG	Alaska Coast Guard		Sweeney, C.; McKain, K.; Karion, A.; Dlugokencky, E.J.	yes
ACT	Atmospheric Carbon and Transport - America		Sweeney, C.; Dlugokencky, E.J.; Baier, B; Montzka, S.; Davis, K.	yes
ALF	Alta Floresta		Gatti, L.V.; Gloor, E.; Miller, J.B.;	yes
AOA	Aircraft Observation of Atmospheric trace gases by JMA		ghg_obs@met.kishou.go.jp	yes
BGI	Bradgate, Iowa		Sweeney, C.; Dlugokencky, E.J.	yes
BNE	Beaver Crossing, Nebraska		Sweeney, C.; Dlugokencky, E.J.	yes
BRZ	Berezorechka, Russia		Sasakama, N.; Machida, T.	yes
CAR	Briggsdale, Colorado		Sweeney, C.; Dlugokencky, E.J.	yes
CMA	Cape May, New Jersey		Sweeney, C.; Dlugokencky, E.J.	yes
CON	CONTRAIL (Comprehensive Observation Network for TRace gases by AIrLiner)	http://dx.doi.org/10.17595/20180208.001	Machida, T.; Matsueda, H.; Sawa, Y. Niwa, Y.	yes
CRV	Carbon in Arctic Reservoirs Vulnerability Experiment (CARVE)		Sweeney, C.; Karion, A.; Miller, J.B.; Miller, C.E.; Dlugokencky, E.J.	yes
DND	Dahlen, North Dakota		Sweeney, C.; Dlugokencky, E.J.	yes
ESP	Estevan Point, British Columbia		Sweeney, C.; Dlugokencky, E.J.	yes
ETL	East Trout Lake, Saskatchewan		Sweeney, C.; Dlugokencky, E.J.	yes
FWI	Fairchild, Wisconsin		Sweeney, C.; Dlugokencky, E.J.	yes
GSFC	NASA Goddard Space Flight Center Aircraft Campaign		Kawa, S.R.; Abshire, J.B.; Riris, H.	yes
HAA	Molokai Island, Hawaii		Sweeney, C.; Dlugokencky, E.J.	yes
HFM	Harvard University Aircraft Campaign		Wofsy, S.C.	yes
HIL	Homer, Illinois		Sweeney, C.; Dlugokencky, E.J.	yes
HIP	HIPPO (HIAPER Pole-to-Pole Observations)	https://doi.org/10.3334/CDIAC/HIPPO_010	Wofsy, S.C.; Stephens, B.B.; Elkins, J.W.; Hintsa, E.J.; Moore, F.	yes
IAGOS-CARIBIC	In-service Aircraft for a Global Observing System		Obersteiner, F.; Boenisch., H; Gehrlein, T.; Zahn, A.; Schuck, T.	yes
INX	INFLUX (Indianapolis Flux Experiment)		Sweeney, C.; Dlugokencky, E.J.; Shepson, P.B.; Turnbull, J.	yes
LEF	Park Falls, Wisconsin		Sweeney, C.; Dlugokencky, E.J.	yes
NHA	Offshore Portsmouth, New Hampshire (Isles		Sweeney, C.; Dlugokencky, E.J.	yes

			Sweeney, C.; Dlugokencky, E.J.	
	of Shoals)			
OIL	Oglesby, Illinois		Sweeney, C.; Dlugokencky, E.J.	yes
PFA	Poker Flat, Alaska		Sweeney, C.; Dlugokencky, E.J.	yes
RBA-B	Rio Branco		Gatti, L.V.; Gloor, E.; Miller, J.B.	yes
RTA	Rarotonga		Sweeney, C.; Dlugokencky, E.J.	yes
SCA	Charleston, South Carolina		Sweeney, C.; Dlugokencky, E.J.	yes
SGP	Southern Great Plains, Oklahoma		Sweeney, C.; Dlugokencky, E.J.; Biraud, S.	yes
TAB	Tabatinga		Gatti, L.V.; Gloor, E.; Miller, J.B.	yes
TGC	Offshore Corpus Christi, Texas		Sweeney, C.; Dlugokencky, E.J.	yes
THD	Trinidad Head, California		Sweeney, C.; Dlugokencky, E.J.	yes
WBI	West Branch, Iowa		Sweeney, C.; Dlugokencky, E.J.	yes

Table A7. Main methodological changes in the global carbon budget since first publication. Methodological changes introduced in one year are kept for the following years unless noted. Empty cells mean there were no methodological changes introduced that year.

Publication year	Fossil fuel emissions			LUC emissions	Reservoirs			Uncertainty & other changes
	Global	Country (territorial)	Country (consumption)		Atmosphere	Ocean	Land	
2006 (a)		Split in regions						
2007 (b)				ELUC based on FAO-FRA 2005; constant ELUC for 2006	1959-1979 data from Mauna Loa; data after 1980 from global average	Based on one ocean model tuned to reproduced observed 1990s sink		±1σ provided for all components
2008 (c)				Constant ELUC for 2007				
2009 (d)		Split between Annex B and non-Annex B	Results from an independent study discussed	Fire-based emission anomalies used for 2006-2008		Based on four ocean models normalised to observations with constant delta	First use of five DGVMs to compare with budget residual	
2010 (e)	Projection for current year based on GDP	Emissions for top emitters		ELUC updated with FAO-FRA 2010				
2011 (f)			Split between Annex B and non-Annex B					
2012 (g)		129 countries from 1959	129 countries and regions from 1990-2010 based on GTAP8.0	ELUC for 1997-2011 includes interannual anomalies from fire-based emissions	All years from global average	Based on 5 ocean models normalised to observations with ratio	Ten DGVMs available for SLAND; First use of four models to compare with ELUC	
2013 (h)		250 countriesb	134 countries and regions 1990-2011 based on GTAP8.1, with detailed estimates for years 1997, 2001, 2004, and 2007	ELUC for 2012 estimated from 2001-2010 average		Based on six models compared with two data-products to year 2011	Coordinated DGVM experiments for SLAND and ELUC	Confidence levels; cumulative emissions; budget from 1750
2014 (i)	Three years of BP data	Three years of BP data	Extended to 2012 with updated GDP data	ELUC for 1997-2013 includes interannual anomalies from fire-based emissions		Based on seven models	Based on ten models	Inclusion of breakdown of the sinks in three latitude bands and comparison with three atmospheric inversions

2015 (j)	Projection for current year based Jan-Aug data	National emissions from UNFCCC extended to 2014 also provided	Detailed estimates introduced for 2011 based on GTAP9			Based on eight models	Based on ten models with assessment of minimum realism	The decadal uncertainty for the DGVM ensemble mean now uses $\pm 1\sigma$ of the decadal spread across models
2016 (k)	Two years of BP data	Added three small countries; China's emissions from 1990 from BP data (this release only)		Preliminary ELUC using FRA-2015 shown for comparison; use of five DGVMs		Based on seven models	Based on fourteen models	Discussion of projection for full budget for current year

a Raupach et al. (2007)
b Canadell et al. (2007)
c GCP (2008)
d Le Quéré et al. (2009)
e Friedlingstein et al. (2010)
f Peters et al. (2012b)
g Le Quéré et al. (2013), Peters et al. (2013)
h Le Quéré et al. (2014)
i Le Quéré et al. (2015a)
j Le Quéré et al. (2015b)
k Le Quéré et al. (2016)

			2001-2010	2011-2020
Table A8: Mapping of global carbon cycle models' land flux definitions to the definition of the LULUCF net flux used in national reporting to UNFCCC. Non-intact lands are used here as proxy for "managed lands" in the country reporting				
ELUC from bookkeeping estimates (from Tab. 5)			1.21	1.13
SLAND	Total (from Tab. 5)	from DGVMs	-2.54	-3.06
	on non-forest lands	from DGVMs	-0.90	-1.14
	on non-intact forest	from DGVMs	-1.27	-1.50
	on intact land (intact forest only for DGVMs)	from DGVMs	-0.37	-0.42
		from ORCHIDEE-MICT	-1.29	-1.47
SLAND on non-intact lands plus ELUC		from DGVMs and bookkeeping ELUC	-0.06	-0.37
		from ORCHIDEE-MICT	1.00	0.61
National greenhouse gas inventories (LULUCF)			-0.43	-0.57
FAOSTAT (LULUCF)			0.39	0.20

Table A9. Funding supporting the production of the various components of the global carbon budget in addition to the authors' supporting institutions (see also acknowledgements).

Funder and grant number (where relevant)	Author Initials
Australia, Integrated Marine Observing System (IMOS)	BT
Australian National Environment Science Program (NESP)	JGC
Belgium, FWO (Flanders Research Foundation, contract IRI I001019N)	TG
BNP Paribas Foundation through Climate & Biodiversity initiative, philanthropic grant for developments of the Global Carbon Atlas	PC
Canada, Tula Foundation	WE
China, National Natural Science Foundation (grant no. 41975155)	XY
Commonwealth Scientific and Industrial Organization (CSIRO) - Climate Science Centre	JGC, JK
EC Copernicus Atmosphere Monitoring Service implemented by ECMWF on behalf of the European Commission	FC
EC Copernicus Marine Environment Monitoring Service implemented by Mercator Ocean	TTTC
EC H2020 (4C; grant no 821003)	PF, RMA, SS, GPP, PC, JIK, TI, LB, PL, LG, SL, NG
EC H2020 (CHE; grant no 776186)	MWJ
EC H2020 (CoCO2: grant no. 958927)	RMA, GPP
EC H2020 (COMFORT: grant no. 820989)	DCEB, LG
EC H2020 (CONSTRAIN: grant no 820829)	RS, PMF, TG
EC H2020 (CRESCENDO: grant no. 641816)	RS, EJ AJPS, TI
EC H2020 (ESM2025 – Earth System Models for the Future; grant agreement No 101003536).	RS, TG, TI, LB, BD
EC H2020 (EuroSea: grant no. 862626)	SDJ
EC H2020 (JERICO-S3: grant no. 871153)	GR
EC H2020 (QUINCY; grant no 647204)	SZ
EC H2020 (RINGO: grant no. 730944)	DCEB
EC H2020 (VERIFY: grant no. 776810)	MWJ, RMA, GPP, PC, JIK, NV, GG
Efg International	TT
EFG International	TT
European Space Agency Climate Change Initiative ESA-CCI RECCAP2 project 655 (ESRIN/4000123002/18/I-NB)	PF, SS, PC
European Space Agency OceanSODA project (grant no. 4000112091/14/I-LG)	LG
France, ICOS (Integrated Carbon Observation System) France	NL
France, Institut de Recherche pour le Développement (IRD)	NL
Germany, Blue Ocean and Federal Ministry of Education (BONUS INTEGRAL; Grant No. 03F0773A)	GR
Germany, Deutsche Forschungsgemeinschaft (DFG) under Germany's Excellence Strategy – EXC 2037 'Climate, Climatic Change, and Society' – Project Number: 390683824	TI
Germany, Federal Ministry for Education and Research (BMBF)	GR
Germany, GEOMAR Helmholtz Centre for Ocean Research	SKL
Germany, German Federal Ministry of Education and Research under project "DArgo2025" (03F0857C)	AK
Germany, Helmholtz Association ATMO programme	PA
Germany, Helmholtz Young Investigator Group Marine Carbon and Ecosystem Feedbacks in the Earth System (MarESys), grant number VH-NG-1301	JH, OG
Germany, ICOS (Integrated Carbon Observation System) Germany	GR, NL
Hapag-Lloyd	TT

Ireland, Marine Institute	MC
Japan, Environment Research and Technology Development Fund of the Ministry of the Environment (JPMEERF21S20810)	YN
Japan, Global Environmental Research Coordination System, Ministry of the Environment (grant number E1751)	SN, TO, CW
Kuehne + Nagel International AG	TT
Mediterranean Shipping Company (MSc)	TT
Monaco, Fondation Prince Albert II de Monaco	TT
Monaco, Yacht Club de Monaco	TT
NASA Interdisciplinary Research in Earth Science Program.	BP
Netherlands Organization for Scientific Research (NWO; grant no. SH-312, 17616)	WP
New Zealand, NIWA MBIE Core funding	KIC
Norway, Norwegian Research Council (grant no. 270061)	JS
Norway, Research Council of Norway, ICOS (Integrated Carbon Observation System) Norway and OTC (Ocean Thematic Centre) (grant no. 245927)	SKL, MB, SDJ
PEAK6 Investments	SKL
Saildrone Inc.	SKL
South Africa, Department of Science and Innovation	LD
South Africa, National Science Foundation	LD
Swiss National Science Foundation (grant no. 200020_172476)	SL
UK Royal Society (grant no. RP\R1\191063)	CLQ
UK, CLASS ERC funding	TG
UK, National Centre for Atmospheric Science (NCAS)	PCM
UK, Natural Environment Research Council (SONATA: grant no. NE/P021417/1)	DW
UK, Natural Environmental Research Council (NE/R016518/1)	LF
UK, Newton Fund, Met Office Climate Science for Service Partnership Brazil (CSSP Brazil)	AJWi
UK, Royal Society: The European Space Agency OCEANFLUX projects	AJWa
UK, University of Reading Research Endowment Trust Fund	PCM
USA, Department of Commerce, Office of Oceanic and Atmospheric Research (OAR)'s / National Oceanic and Atmospheric Administration (NOAA)'s Global Ocean Monitoring and Observation Program (GOMO)	DRM, CS, DP, RW, SRA, RAF, AJS, NRB
USA, Department of Commerce, Office of Oceanic and Atmospheric Research (OAR)'s / National Oceanic and Atmospheric Administration (NOAA)'s Ocean Acidification Program	DP, RW, SRA, RAF, AJS
USA, Department of Energy, Office of Science and BER prg. (grant no. DE-SC000 0016323)	AKJ
USA, Department of Energy, SciDac (DESC0012972)	GCH, LPC
USA, NASA Carbon Monitoring System probram and OCO Science team program (80NM0018F0583) .	JL
USA, NASA Interdisciplinary Research in Earth Science (IDS) (80NSSC17K0348)	GCH, LPC
USA, National Science Foundation (grant number 1903722)	HT
USA, National Science Foundation (grant number PLR 1543457)	DRM, CS
USA, Princeton University Environmental Institute and the NASA OCO2 science team, grant number 80NSSC18K0893.	LR
Computing resources	
bwHPC, High Performance Computing Network of the State of Baden-Württemberg, Germany	PA
Cheyenne supercomputer, Computational and Information Systems Laboratory (CISL) at National Center for Atmospheric Research (NCAR)	DK
Deutsches Klimarechenzentrum (allocation bm0891)	JEMSN, JP
HPC cluster Aether at the University of Bremen, financed by DFG within the scope of the Excellence Initiative	ITL, WP

MRI (FUJITSU Server PRIMERGY CX2550M5)	YN
NIES (SX-Aurora)	YN
NIES supercomputer system	EK
supercomputer 'Gadi' of the National Computational Infrastructure (NCI), Australia	JK
Supercomputing time was provided by the Météo-France/DSI supercomputing center.	RS, BD
TGCC under allocation 2019-A0070102201 made by GENCI	FC
UEA High Performance Computing Cluster, UK	MWJ, CLQ, DRW
UNINETT Sigma2, National Infrastructure for High Performance Computing and Data Storage in Norway (NN2980K/NS2980K)	JS

15 Appendix B. Supplementary Figures
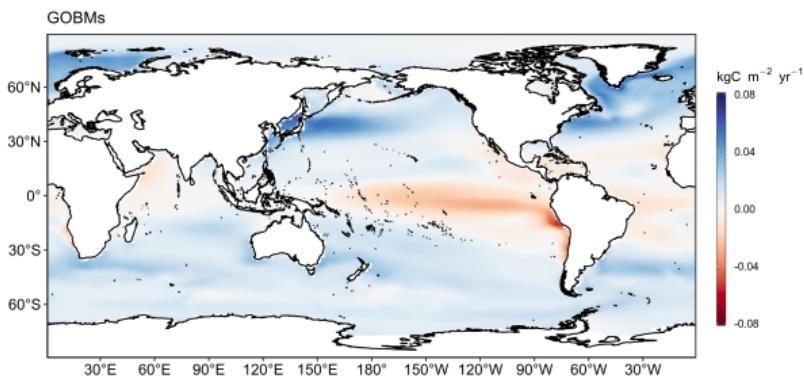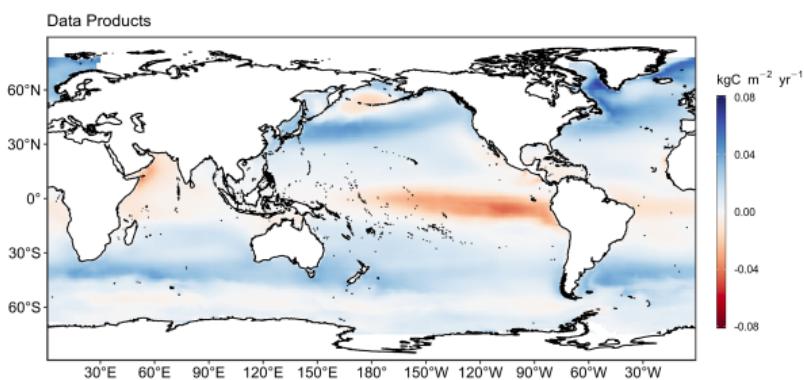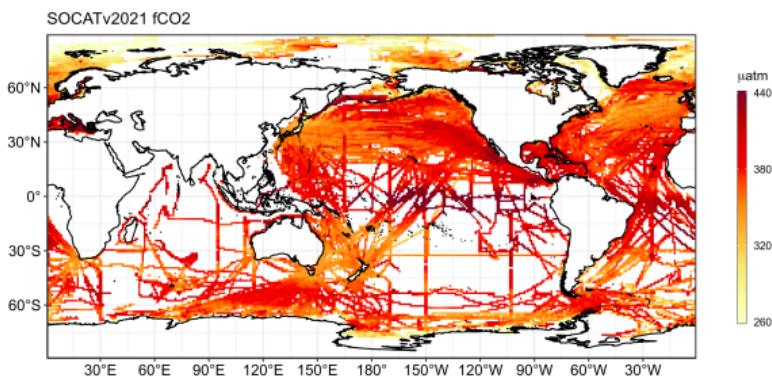
Figure B1. Ensemble mean air-sea CO_2 flux from a) global ocean biogeochemistry models and b) fCO_2 based data products, averaged over 2011-2020 period (kgC m^{-2} yr^{-1}). Positive numbers indicate a flux into the ocean. c) gridded SOCAT v2021 fCO_2 measurements, averaged over the 2011-2020 period (µatm). In (a) model simulation A is shown. The data-products represent the contemporary flux, i.e. including outgassing of riverine carbon, which is estimated to amount to 0.615 GtC yr^{-1} globally.
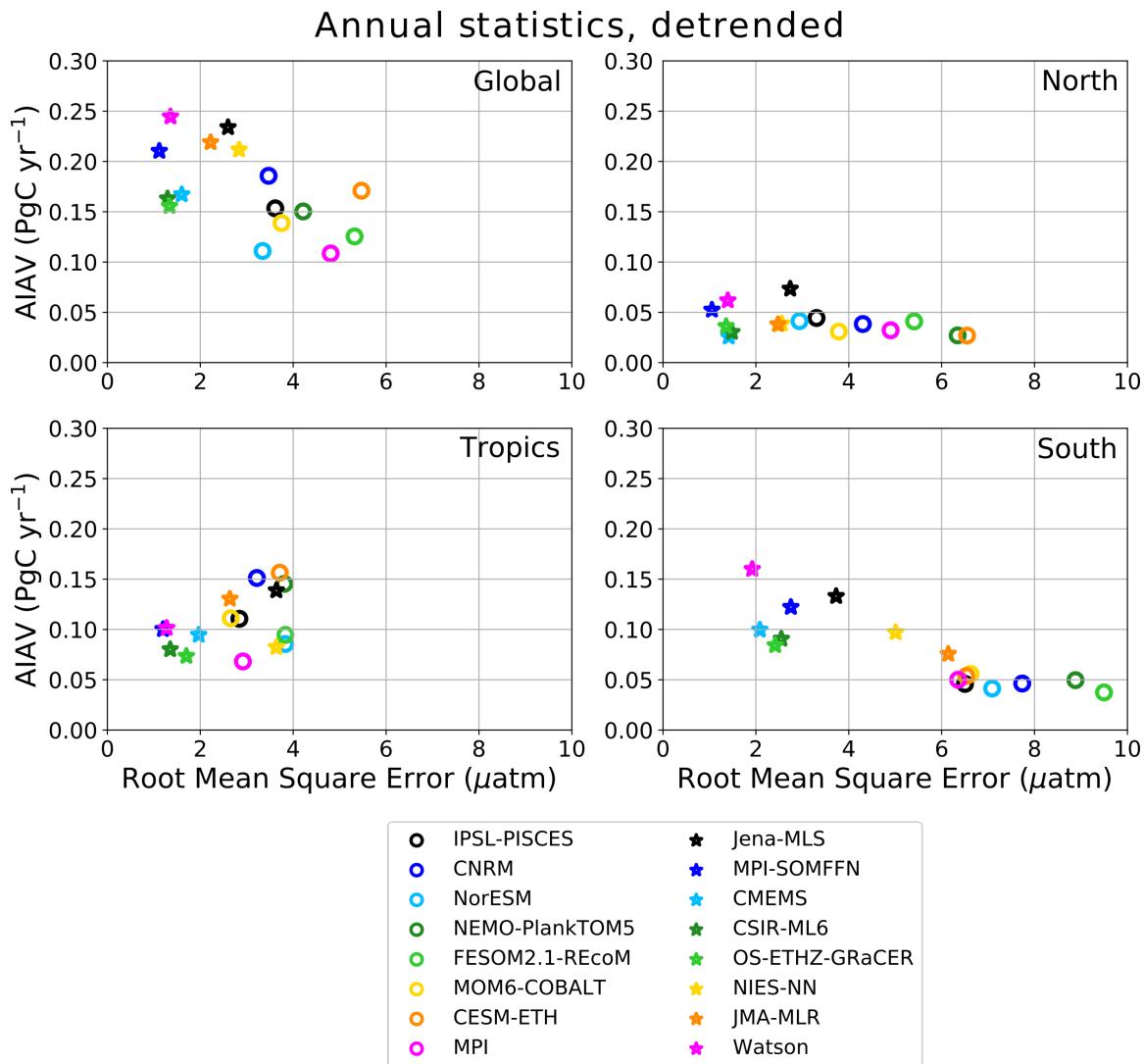
Figure B2. Evaluation of the GOBMs and data products using the root mean squared error (RMSE) for the period 1990 to 2020, between the individual surface ocean fCO_2 mapping schemes and the SOCAT v2021 database. The y-axis shows the amplitude of the interannual variability (A-IAV, taken as the standard deviation of a detrended time series calculated as a 12-months running mean over the monthly flux time series, Rödenbeck et al., 2015). Results are presented for the globe, north (>30°N), tropics (30°S-30°N), and south (<30°S) for the GOBMs (see legend circles) and for the fCO_2-based data products (star symbols). The fCO_2-based data products use the SOCAT database and therefore are not independent from the data (see section 2.4.1).
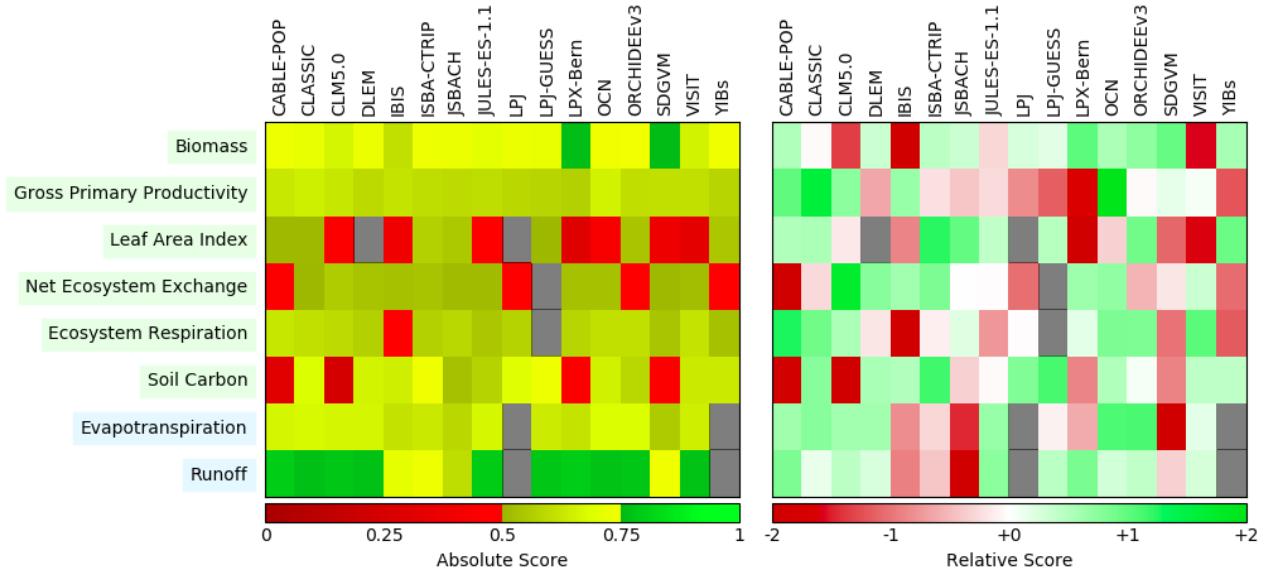
Figure B3. Evaluation of the DGVMs using the International Land Model Benchmarking system (ILAMB; Collier et al., 2018) (left) absolute skill scores and (right) skill scores relative to other models. The benchmarking is done with observations for vegetation biomass (Saatchi et al., 2011; and GlobalCarbon unpublished data; Avitabile et al., 2016), GPP (Jung et al., 2010; Lasslop et al., 2010), leaf area index (De Kauwe et al., 2011; Myneni et al., 1997), net ecosystem exchange (Jung et al., 2010;Lasslop et al., 2010), ecosystem respiration (Jung et al., 2010;Lasslop et al., 2010), soil carbon (Hugelius et al., 2013;Todd-Brown et al., 2013), evapotranspiration (De Kauwe et al., 2011), and runoff (Dai and Trenberth, 2002). For each model-observation comparison a series of error metrics are calculated, scores are then calculated as an exponential function of each error metric, finally for each variable the multiple scores from different metrics and observational data sets are combined to give the overall variable scores shown in the left panel. Overall variable scores increase from 0 to 1 with improvements in model performance. The set of error metrics vary with data set and can include metrics based on the period mean, bias, root mean squared error, spatial distribution, interannual variability and seasonal cycle. The relative skill score shown in the right panel is a Z-score, which indicates in units of standard deviation the model scores relative to the multi-model mean score for a given variable. Grey boxes represent missing model data.
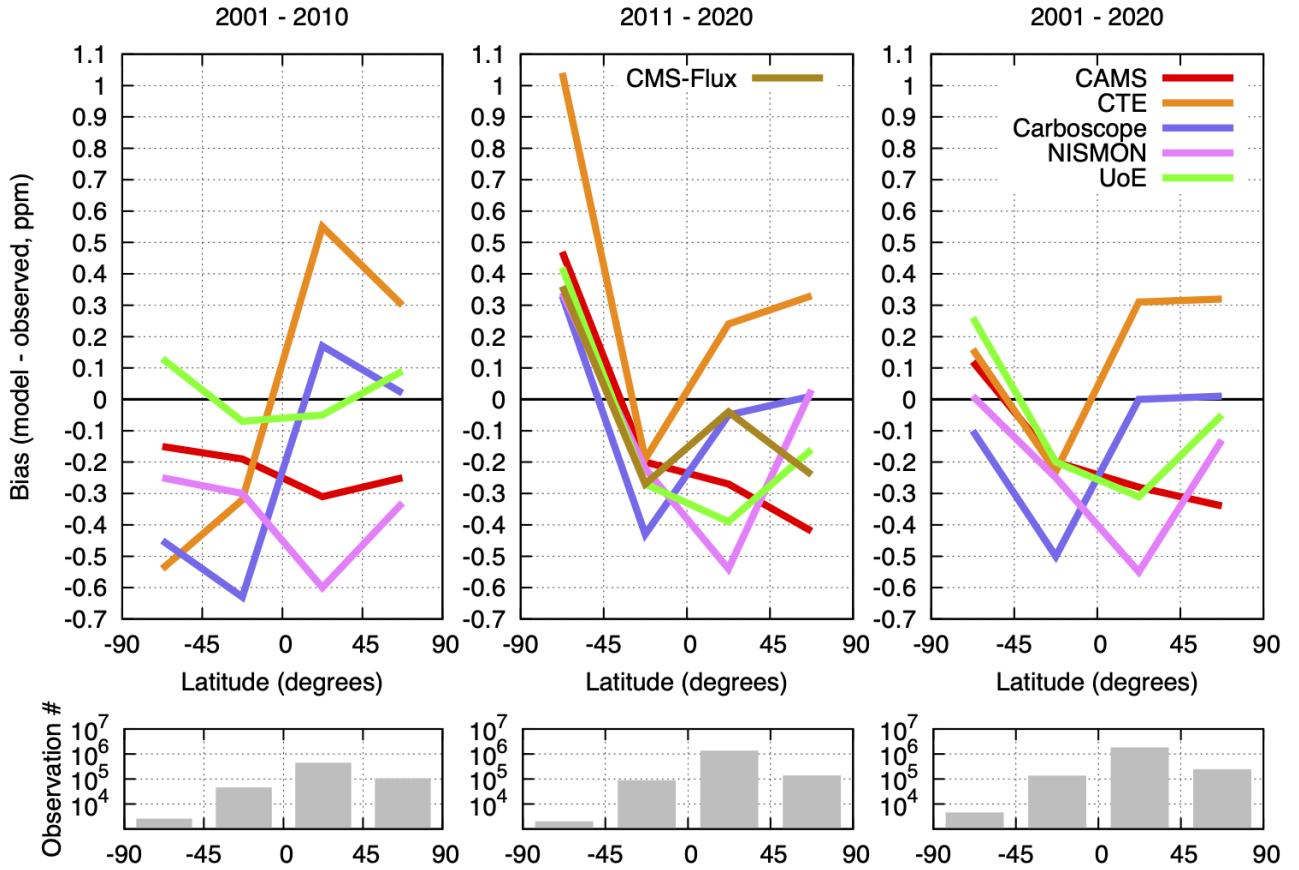
Figure B4. Evaluation of the atmospheric inversion products. The mean of the model minus observations is shown for four latitude bands in three periods: (left) 2001-2010, (centre) 2011-2020, (right) 2001-2020. The six models are compared to independent CO_2 measurements made onboard aircraft over many places of the world between 2 and 7 km above sea level. Aircraft measurements archived in the Cooperative Global Atmospheric Data Integration Project (CGADIP; Cox et al., 2021) from sites, campaigns or programs that cover at least 9 months between 2001 and 2020 and that have not been assimilated, have been used to compute the biases of the differences in four 45° latitude bins. Land and ocean data are used without distinction, and observation density varies strongly with latitude and time as seen on the lower panels.
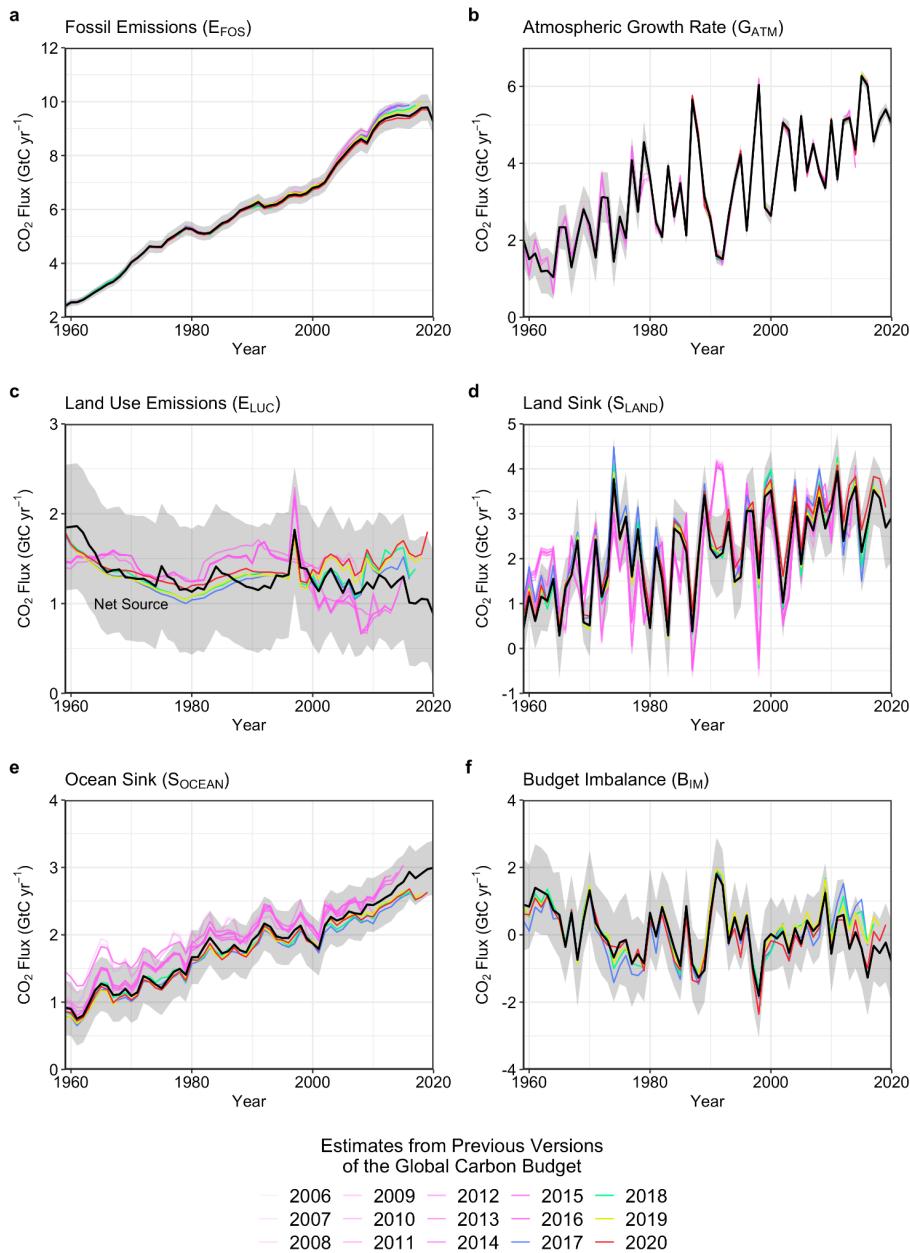
Figure B5. Comparison of the estimates of each component of the global carbon budget in this study (black line) with the estimates released annually by the GCP since 2006. Grey shading shows the uncertainty bounds representing ±1 standard deviation of the current global carbon budget, based on the uncertainty assessments described in Appendix C. CO_2 emissions from (a) fossil CO_2 emissions (E_{FOS}), and (b) land-use change (E_{LUC}), as well as their partitioning among (c) the atmosphere (G_{ATM}), (d) the land (S_{LAND}), and (e) the ocean (S_{OCEAN}). See legend for the corresponding years, and Tables 3 and A7 for references. The budget year corresponds to the year when the budget was first released. All values are in GtC yr^{-1}.
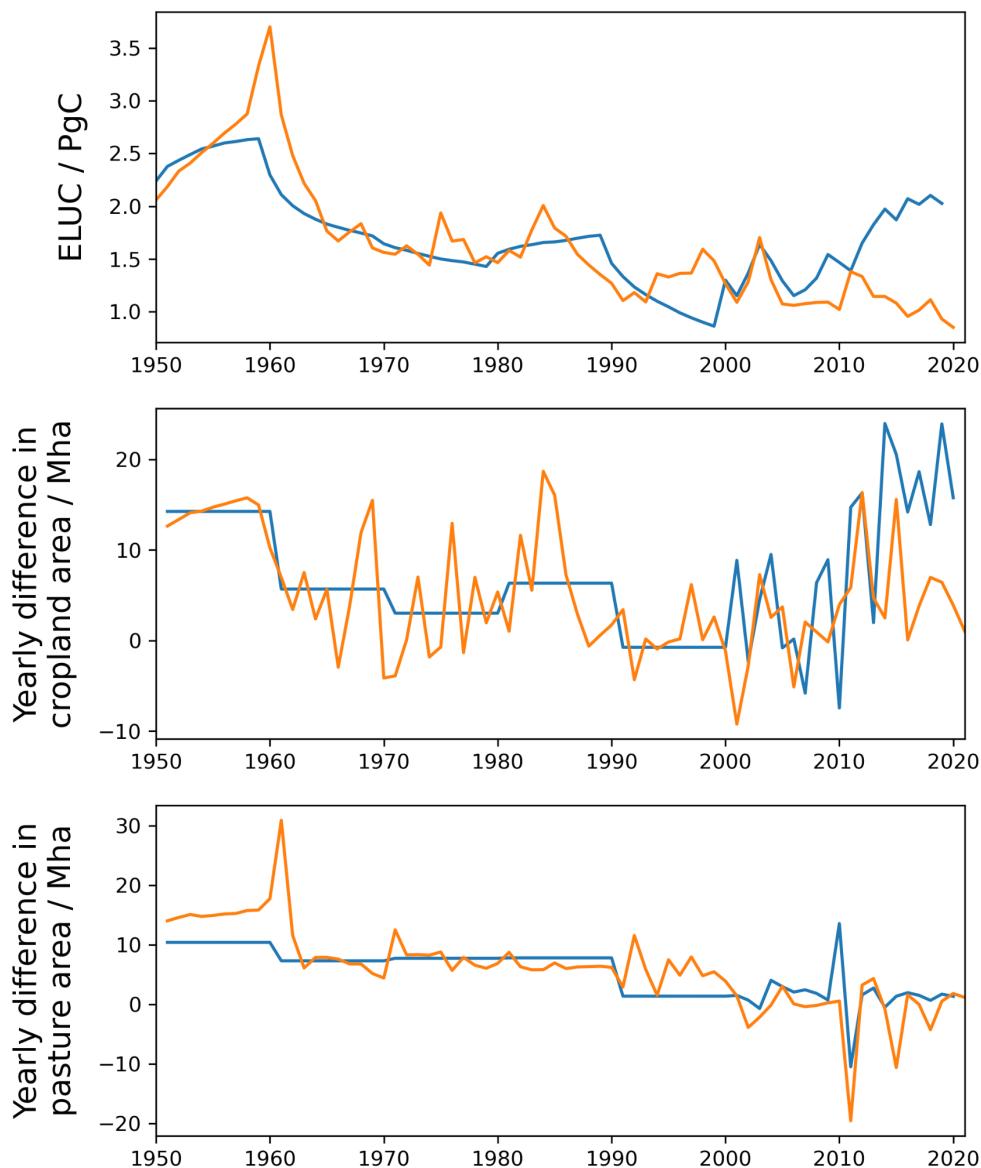
Figure B6. Changes in the HYDE/LUH2 land-use forcing from last year's global carbon budget (Friedlingstein et al., 2020, in blue) to this year (orange). Shown are year-to-year changes in cropland area (middle panel) and pasture area (bottom panel). To illustrate the relevance of the update in the land-use forcing to the recent trends in E_{LUC}, the top panel shows the land-use emission estimate from the bookkeeping model BLUE (original model output, i.e. excluding peat fire and drainage emissions).

17 Appendix C. Extended Methodology

17.1 Appendix C.1 Methodology Fossil Fuel CO_2 emissions (E_{FOS})

17.1.1 C.1.1 Cement carbonation

From the moment it is created, cement begins to absorb CO_2 from the atmosphere, a process known as 'cement carbonation'. We estimate this CO_2 sink, as the average of two studies in the literature (Cao et al., 2020; Guo et al., 2021). Both studies use the same model, developed by Xi et al. (2016), with different parameterisations and input data, with the estimate of Guo and colleagues being a revision of Xi et al (2016). The trends of the two studies are very similar. Modelling cement carbonation requires estimation of a large number of parameters, including the different types of cement material in different countries, the lifetime of the structures before demolition, of cement waste after demolition, and the volumetric properties of structures, among others (Xi et al., 2016). Lifetime is an important parameter because demolition results in the exposure of new surfaces to the carbonation process. The main reasons for differences between the two studies appear to be the assumed lifetimes of cement structures and the geographic resolution, but the uncertainty bounds of the two studies overlap. In the present budget, we include the cement carbonation carbon sink in the fossil CO_2 emission component (E_{FOS}).

17.1.2 C.1.2 Emissions embodied in goods and services

CDIAC, UNFCCC, and BP national emission statistics 'include greenhouse gas emissions and removals taking place within national territory and offshore areas over which the country has jurisdiction' (Rypdal et al., 2006), and are called territorial emission inventories. Consumption-based emission inventories allocate emissions to products that are consumed within a country, and are conceptually calculated as the territorial emissions minus the 'embodied' territorial emissions to produce exported products plus the emissions in other countries to produce imported products (Consumption = Territorial – Exports + Imports). Consumption-based emission attribution results (e.g. Davis and Caldeira, 2010) provide additional information to territorial-based emissions that can be used to understand emission drivers (Hertwich and Peters, 2009) and quantify emission transfers by the trade of products between countries (Peters et al., 2011b). The consumption-based emissions have the same global total, but reflect the trade-driven movement of emissions across the Earth's surface in response to human activities. We estimate consumption-

based emissions from 1990-2018 by enumerating the global supply chain using a global model of the economic relationships between economic sectors within and between every country (Andrew and Peters, 2013; Peters et al., 2011a). Our analysis is based on the economic and trade data from the Global Trade and Analysis Project (GTAP; Narayanan et al., 2015), and we make detailed estimates for the years 1997 (GTAP version 5), 2001 (GTAP6), and 2004, 2007, and 2011 (GTAP9.2), covering 57 sectors and 141 countries and regions. The detailed results are then extended into an annual time series from 1990 to the latest year of the Gross Domestic Product (GDP) data (2018 in this budget), using GDP data by expenditure in current exchange rate of US dollars (USD; from the UN National Accounts main Aggregrates database; UN, 2021) and time series of trade data from GTAP (based on the methodology in Peters et al., 2011a). We estimate the sector-level CO_2 emissions using the GTAP data and methodology, include the flaring and cement emissions from CDIAC, and then scale the national totals (excluding bunker fuels) to match the emission estimates from the carbon budget. We do not provide a separate uncertainty estimate for the consumption-based emissions, but based on model comparisons and sensitivity analysis, they are unlikely to be significantly different than for the territorial emission estimates (Peters et al., 2012a).

17.1.3 C.1.3 Uncertainty assessment for E_{FOS}

We estimate the uncertainty of the global fossil CO2 emissions at ±5% (scaled down from the published ±10 % at ±2σ to the use of ±1σ bounds reported here; Andres et al., 2012). This is consistent with a more detailed analysis of uncertainty of ±8.4% at ±2σ (Andres et al., 2014) and at the high-end of the range of ±5-10% at ±2σ reported by (Ballantyne et al., 2015). This includes an assessment of uncertainties in the amounts of fuel consumed, the carbon and heat contents of fuels, and the combustion efficiency. While we consider a fixed uncertainty of ±5% for all years, the uncertainty as a percentage of emissions is growing with time because of the larger share of global emissions from emerging economies and developing countries (Marland et al., 2009). Generally, emissions from mature economies with good statistical processes have an uncertainty of only a few per cent (Marland, 2008), while emissions from strongly developing economies such as China have uncertainties of around ±10% (for ±1σ; Gregg et al., 2008; Andres et al., 2014). Uncertainties of emissions are likely to be mainly systematic errors related to underlying biases of energy statistics and to the accounting method used by each country.

17.1.4 C.1.4 Growth rate in emissions

We report the annual growth rate in emissions for adjacent years (in percent per year) by calculating the difference between the two years and then normalising to the emissions in the first year: (EFOS(t0+1)-EFOS(t0))/EFOS(t0)×100%. We apply a leap-year adjustment where relevant to ensure valid interpretations of annual growth rates. This affects the growth rate by about 0.3% yr-1 (1/366) and causes calculated growth rates to go up approximately 0.3% if the first year is a leap year and down 0.3% if the second year is a leap year.

The relative growth rate of E_{FOS} over time periods of greater than one year can be rewritten using its logarithm equivalent as follows:

$$\frac{1}{E_{FOS}} \frac{dE_{FOS}}{dt} = \frac{d(lnE_{FOS})}{dt} \tag{2}$$

Here we calculate relative growth rates in emissions for multi-year periods (e.g. a decade) by fitting a linear trend to $ln(E_{FOS})$ in Eq. (2), reported in percent per year.

17.1.5 C.1.5 Emissions projection for 2021

To gain insight on emission trends for 2021, we provide an assessment of global fossil CO_2 emissions, E_{FOS}, by combining individual assessments of emissions for China, USA, the EU, and India (the four countries/regions with the largest emissions), and the rest of the world. We provide full year estimates for two datasets: IEA (2021b) and our own analysis. This approach differs from last year where we used four independent estimates including our own, because of the unique circumstances related to the COVID-19 pandemic. This year's analysis is more in line with earlier budgets.

Previous editions of the Global Carbon Budget (GCB) have estimated year to date (YTD) emissions, and performed projections, using sub-annual energy consumption data from a variety of sources depending on the country or region. The YTD estimates have then been projected to the full year using specific methods for each country or region. The methods described in detail below.

China: We use the growth in total fossil CO_2 emissions in 2021 reported by the National Bureau of Statistics (NBS) in their 2022 Statistical Communique (NBS, 2022). This report includes growth rates of energy consumption for coal, oil, and natural gas as well as the growth in cement production, which are used to determine the changes in emissions from these four categories.

USA: We use emissions estimated by the U.S. Energy Information Administration (EIA) in their Short-Term Energy Outlook (STEO) for emissions from fossil fuels to get both YTD and a full year projection (EIA, 2022). The STEO also includes a near-term forecast based on an energy forecasting model which is updated monthly (last update with preliminary data through September 2021), and takes into account expected temperatures, household expenditures by fuel type, energy markets, policies, and other effects. We combine this with our estimate of emissions from cement production using the monthly U.S. cement clinker production data from USGS for January-June 2021, assuming changes in cement production over the first part of the year apply throughout the year.

India: We use monthly emissions estimates for India updated from Andrew (2020b) through August 2021. These estimates are derived from many official monthly energy and other activity data sources to produce direct estimates of national CO_2 emissions, without the use of proxies. Emissions from coal are then extended to September using a regression relationship based on power generated from coal, coal dispatches by Coal India Ltd., the composite PMI, time, and days per month. For the last 3-4 months of the year, each series is extrapolated assuming typical trends.

EU: We use a refinement to the methods presented by Andrew (2021), deriving emissions from monthly energy data reported by Eurostat. Some data gaps are filled using data from the Joint Organisations Data Initiative (JODI, 2022). Sub-annual cement production data are limited, but data for Germany and Poland, the two largest producers, suggest a small decline. For fossil fuels this provides estimates through July. We extend coal emissions through September using a regression model built from generation of power from hard coal, power from brown coal, total power generation, and the number of working days in Germany and Poland, the two biggest coal consumers in the EU. These are then extended through the end of the year assuming typical trends. We extend oil emissions by building a regression model between our monthly CO2 estimates and oil consumption reported by the EIA for Europe in its Short-Term Energy Outlook (October edition), and then using this model with EIA's monthly forecasts. For natural gas, the strong seasonal signal allows the use of the bias-adjusted Holt-Winters exponential smoothing method (Chatfield, 1978).

Rest of the world: We use the close relationship between the growth in GDP and the growth in emissions (Raupach et al., 2007) to project emissions for the current year. This is based on a

simplified Kaya Identity, whereby E_{FOS} (GtC yr^{-1}) is decomposed by the product of GDP (USD yr^{-1}) and the fossil fuel carbon intensity of the economy (I_{FOS}; GtC USD^{-1}) as follows:

$$E_{FOS} = GDP \times I_{FOS} \qquad (3)$$

Taking a time derivative of Equation (3) and rearranging gives:

$$\frac{1}{E_{FOS}}\frac{dE_{FOS}}{dt} = \frac{1}{GDP}\frac{dGDP}{dt} + \frac{1}{I_{FOS}}\frac{dI_{FOS}}{dt} \qquad (4)$$

where the left-hand term is the relative growth rate of E_{FOS}, and the right-hand terms are the relative growth rates of GDP and I_{FOS}, respectively, which can simply be added linearly to give the overall growth rate.

The I_{FOS} is based on GDP in constant PPP (Purchasing Power Parity) from the International Energy Agency (IEA) up to 2017 (IEA/OECD, 2019) and extended using the International Monetary Fund (IMF) growth rates through 2020 (IMF, 2022). Interannual variability in I_{FOS} is the largest source of uncertainty in the GDP-based emissions projections. We thus use the standard deviation of the annual I_{FOS} for the period 2009-2019 as a measure of uncertainty, reflecting a ±1σ as in the rest of the carbon budget.

World: The global total is the sum of each of the countries and regions.

17.2 Appendix C.2 Methodology CO$_2$ emissions from land-use, land-use change and forestry (E_{LUC})

The net CO_2 flux from land-use, land-use change and forestry (E_{LUC}, called land-use change emissions in the rest of the text) includes CO_2 fluxes from deforestation, afforestation, logging and forest degradation (including harvest activity), shifting cultivation (cycle of cutting forest for agriculture, then abandoning), and regrowth of forests following wood harvest or abandonment of agriculture. Emissions from peat burning and drainage are added from external datasets (see section C.2.1 below). Only some land-management activities are included in our land-use change emissions estimates (Table A1). Some of these activities lead to emissions of CO_2 to the atmosphere, while others lead to CO_2 sinks. E_{LUC} is the net sum of emissions and removals due to all anthropogenic activities considered. Our annual estimate for 1960-2020 is provided as the average of results from three bookkeeping approaches (Section C.2.1 below): an estimate using the Bookkeeping of Land Use Emissions model (Hansis et al., 2015; hereafter BLUE) and one using

the compact Earth system model OSCAR (Gasser et al., 2020), both BLUE and OSCAR being updated here to new land-use forcing covering the time period until 2020, and an updated version of the estimate published by Houghton and Nassikas (2017) (hereafter updated H&N2017). All three data sets are then extrapolated to provide a projection for 2021 (Section C.2.5 below). In addition, we use results from Dynamic Global Vegetation Models (DGVMs; see Section 2.5 and Table 4) to help quantify the uncertainty in E_{LUC} (Section C.2.4), and thus better characterise our understanding. Note that in this budget, we use the scientific E_{LUC} definition, which counts fluxes due to environmental changes on managed land towards S_{LAND}, as opposed to the national greenhouse gas inventories under the UNFCCC, which include them in E_{LUC} and thus often report smaller land-use emissions (Grassi et al., 2018; Petrescu et al., 2020). However, we provide a methodology of mapping of the two approaches to each other further below (Section C.2.3).

17.2.1 C.2.1 Bookkeeping models

Land-use change CO_2 emissions and uptake fluxes are calculated by three bookkeeping models. These are based on the original bookkeeping approach of Houghton (2003) that keeps track of the carbon stored in vegetation and soils before and after a land-use change (transitions between various natural vegetation types, croplands, and pastures). Literature-based response curves describe decay of vegetation and soil carbon, including transfer to product pools of different lifetimes, as well as carbon uptake due to regrowth. In addition, the bookkeeping models represent long-term degradation of primary forest as lowered standing vegetation and soil carbon stocks in secondary forests, and include forest management practices such as wood harvests.

BLUE and the updated H&N2017 exclude land ecosystems' transient response to changes in climate, atmospheric CO_2 and other environmental factors, and base the carbon densities on contemporary data from literature and inventory data. Since carbon densities thus remain fixed over time, the additional sink capacity that ecosystems provide in response to CO_2-fertilisation and some other environmental changes is not captured by these models (Pongratz et al., 2014). On the contrary, OSCAR includes this transient response, and it follows a theoretical framework (Gasser and Ciais, 2013) that allows separating bookkeeping land-use emissions and the loss of additional sink capacity. Only the former is included here, while the latter is discussed in Appendix D4. The bookkeeping models differ in (1) computational units (spatially explicit treatment of land-use change for BLUE, regional-/ mostly country-level for the updated H&N2017 and OSCAR), (2) processes represented (see Table A1), and (3) carbon densities assigned to vegetation and soil of

each vegetation type (literature-based for the updated H&N2017 and BLUE, calibrated to DGVMs for OSCAR). A notable difference between models exists with respect to the treatment of shifting cultivation. The update of H&N2017 changed the approach over the earlier H&N2017 version: H&N2017 had assumed the "excess loss" of tropical forests (i.e., when FRA indicated a forest loss larger than the increase in agricultural areas from FAO) resulted from converting forests to croplands at the same time older croplands were abandoned. Those abandoned croplands began to recover to forests after 15 years. The updated H&N2017 now assumes that forest loss in excess of increases in cropland and pastures represented an increase in shifting cultivation. When the excess loss of forests was negative, it was assumed that shifting cultivation was returned to forest. Historical areas in shifting cultivation were extrapolated taking into account country-based estimates of areas in fallow in 1980 (FAO/UNEP, 1981) and expert opinion (from Heinimann et al., 2017). In contrast, the BLUE and OSCAR models include sub-grid-scale transitions between all vegetation types. Furthermore, the updated H&N2017 assume conversion of natural grasslands to pasture, while BLUE and OSCAR allocate pasture proportionally on all natural vegetation that exists in a grid-cell. This is one reason for generally higher emissions in BLUE and OSCAR. Bookkeeping models do not directly capture carbon emissions from peat fires, which can create large emissions and interannual variability due to synergies of land-use and climate variability in Southeast Asia, particularly during El-Niño events, nor emissions from the organic layers of drained peat soils. To correct for this, the updated H&N2017 includes carbon emissions from burning and draining of peatlands in Indonesia, Malaysia, and Papua New Guinea (based on the Global Fire Emission Database (GFED4s; van der Werf et al., 2017) for fire and Hooijer et al. for drainage. Further, estimates of carbon losses from peatlands in extra-tropical regions are added from Qiu et al. (2021). We add GFED4s peat fire emissions to BLUE and OSCAR output as well as the global FAO peat drainage emissions 1990-2018 from croplands and grasslands (Conchedda and Tubiello, 2020), keeping post-2018 emissions constant. We linearly increase tropical drainage emissions from 0 in 1980, consistent with H&N2017's assumption, and keep emissions from the often old drained areas of the extra-tropics constant pre-1990. This adds 9.0 GtC for FAO compared to 5.6 GtC for Hooijer et al. (2010). Peat fires add another 2.0 GtC over the same period.

The three bookkeeping estimates used in this study differ with respect to the land-use change data used to drive the models. The updated H&N2017 base their estimates directly on the Forest

Resource Assessment of the FAO which provides statistics on forest-area change and management at intervals of five years currently updated until 2020 (FAO, 2020). The data is based on country reporting to FAO and may include remote-sensing information in more recent assessments. Changes in land-use other than forests are based on annual, national changes in cropland and pasture areas reported by FAO (FAOSTAT, 2021). On the other hand, BLUE uses the harmonised land-use change data LUH2-GCB2021 covering the entire 850-2020 period (an update to the previously released LUH2 v2h dataset; Hurtt et al., 2017; Hurtt et al., 2020), which was also used as input to the DGVMs (Section C.2.2). It describes land-use change, also based on the FAO data as described in Section C.2.2 as well as the HYDE3.3 dataset (Klein Goldewijk et al., 2017a, 2017b), but provided at a quarter-degree spatial resolution, considering sub-grid-scale transitions between primary forest, secondary forest, primary non-forest, secondary non-forest, cropland, pasture, rangeland, and urban land (Hurtt et al., 2020; Chini et al., 2021). LUH2-GCB2021 provides a distinction between rangelands and pasture, based on inputs from HYDE. To constrain the models' interpretation on whether rangeland implies the original natural vegetation to be transformed to grassland or not (e.g., browsing on shrubland), a forest mask was provided with LUH2-GCB2021; forest is assumed to be transformed to grasslands, while other natural vegetation remains (in case of secondary vegetation) or is degraded from primary to secondary vegetation (Ma et al., 2020). This is implemented in BLUE. OSCAR was run with both LUH2-GCB2021 and FAO/FRA (as used by Houghton and Nassikas, 2017), where emissions from the latter were extended beyond 2015 with constant 2011–2015 average values. The best-guess OSCAR estimate used in our study is a combination of results for LUH2-GCB2021 and FAO/FRA land-use data and a large number of perturbed parameter simulations weighted against an observational constraint. All three bookkeeping estimates were extended from 2020 to provide a projection for 2021 by adding the annual change in emissions from tropical deforestation and degradation and peat burning and drainage to the respective model's estimate for 2020 (van der Werf et al., 2017, Conchedda & Tubiello, 2020).

For E_{LUC} from 1850 onwards we average the estimates from BLUE, the updated H&N2017 and OSCAR. For the cumulative numbers starting 1750 an average of four earlier publications is added (30 ± 20 PgC 1750-1850, rounded to nearest 5; Le Quéré et al., 2016).

We provide estimates of the gross land use change fluxes from which the reported net land-use change flux, E_{LUC}, is derived as a sum. Gross fluxes are derived internally by the three bookkeeping

models: Gross emissions stem from decaying material left dead on site and from products after clearing of natural vegetation for agricultural purposes, wood harvesting, emissions from peat drainage and peat burning, and, for BLUE, additionally from degradation from primary to secondary land through usage of natural vegetation as rangeland. Gross removals stem from regrowth after agricultural abandonment and wood harvesting. Gross fluxes for the updated H&N2017 2016-2020 and for the 2021 projection of all three models were based on a regression of gross sources (including peat emissions) to net emissions for recent years.

Due to an artefact in the HYDE3.3 dataset expressed as an abrupt shift in the pattern of pastures/rangelands in 1960, the year 1960 exhibits much larger gross transitions between natural vegetation and pastures/rangelands than prior and subsequent years. Although these gross transitions cancel in terms of net area changes causing large abrupt transitions, an unrealistic peak in emissions occurs around 1960 in BLUE and OSCAR. To correct for this, we replace the estimates for 1959-1961 by the average of 1958 and 1962 in each BLUE and OSCAR. Abrupt transitions will immediately influence gross emissions, which have a larger instantaneous component. Processes with longer timescales, such as slow legacy emissions and regrowth, are inseparable from the carbon dynamics due to subsequent land-use change events. We therefore do not adjust gross removals, but only gross emissions to match the corrected net flux. Since DGVMs estimates are only used for an uncertainty range of E_{LUC}, which is independent of land-use changes, no correction is applied to the DGVMs data.

17.2.2 C.2.2 Dynamic Global Vegetation Models (DGVMs)

Land-use change CO_2 emissions have also been estimated using an ensemble of 17 DGVMs simulations. The DGVMs account for deforestation and regrowth, the most important components of E_{LUC}, but they do not represent all processes resulting directly from human activities on land (Table A1). All DGVMs represent processes of vegetation growth and mortality, as well as decomposition of dead organic matter associated with natural cycles, and include the vegetation and soil carbon response to increasing atmospheric CO_2 concentration and to climate variability and change. Most models explicitly simulate the coupling of carbon and nitrogen cycles and account for atmospheric N deposition and N fertilisers (Table A1). The DGVMs are independent from the other budget terms except for their use of atmospheric CO_2 concentration to calculate the fertilisation effect of CO_2 on plant photosynthesis.

DGVMs that do not simulate subgrid scale transitions (i.e., net land-use emissions; see Table A1) used the HYDE land-use change data set (Klein Goldewijk et al., 2017a, 2017b), which provides annual (1700-2019), half-degree, fractional data on cropland and pasture. The data are based on the available annual FAO statistics of change in agricultural land area available until 2015. The new HYDE3.3 cropland/grazing land dataset which now in addition to FAO country-level statistics is constrained spatially based on multi-year satellite land cover maps from ESA CCI LC. Data from HYDE3.3 is based on a FAO which includes yearly data from 1961 up to and including the year 2017. After the year 2017 HYDE extrapolates the cropland, pasture, and urban data linearly based on the trend over the previous 5 years, to generate data until the year 2020. HYDE also uses satellite imagery from ESA-CCI from 1992 – 2018 for more detailed yearly allocation of cropland and grazing land, with the ESA area data scaled to match the FAO annual totals at country-level. The 2018 map is also used for the 2019-2020 period. The original 300 metre resolution data from ESA was aggregated to a 5 arc minute resolution according to the classification scheme as described in Klein Goldewijk et al (2017a). DGVMs that simulate subgrid scale transitions (i.e., gross land-use emissions; see Table A1) also use the LUH2-GCB2021 data set, an update of the more comprehensive harmonised land-use data set (Hurtt et al., 2020), that further includes fractional data on primary and secondary forest vegetation, as well as all underlying transitions between land-use states (850-2020; Hurtt et al., 2011, 2017, 2020; Chini et al., 2021; Table A1). This new data set is of quarter degree fractional areas of land-use states and all transitions between those states, including a new wood harvest reconstruction, new representation of shifting cultivation, crop rotations, management information including irrigation and fertiliser application. The land-use states include five different crop types in addition to the pasture-rangeland split discussed before. Wood harvest patterns are constrained with Landsat-based tree cover loss data (Hansen et al. 2013). Updates of LUH2-GCB2021 over last year's version (LUH2-GCB2020) are using the most recent HYDE/FAO release (covering the time period up to 2021 included). We also use the most recent FAO wood harvest data for all years from 1961 to 2019. After the year 2019 we extrapolated the wood harvest data until the year 2020. The HYDE3.3 population data is also used to extend the wood harvest time series back in time. Other wood harvest inputs (for years prior to 1961) remain the same in LUH2. With the switch from HYDE3.2 to HYDE3.3 changes in the land-use forcing compared to the version used in the GCB2020 (Friedlingstein et al., 2020) are pronounced. They are thus compared in Fig. 6B and their relevance for land-use emissions discussed in Section 3.4.2. DGVMs implement land-use change differently

(e.g., an increased cropland fraction in a grid cell can either be at the expense of grassland or shrubs, or forest, the latter resulting in deforestation; land cover fractions of the non-agricultural land differ between models). Similarly, model-specific assumptions are applied to convert deforested biomass or deforested area, and other forest product pools into carbon, and different choices are made regarding the allocation of rangelands as natural vegetation or pastures.

The difference between two DGVMs simulations (See Section C4.1 below), one forced with historical changes in land-use and a second with time-invariant pre-industrial land cover and pre-industrial wood harvest rates, allows quantification of the dynamic evolution of vegetation biomass and soil carbon pools in response to land-use change in each model (E_{LUC}). Using the difference between these two DGVMs simulations to diagnose E_{LUC} means the DGVMs account for the loss of additional sink capacity (around 0.4 ± 0.3 GtC yr-1; see Section 2.7.4, Appendix D4), while the bookkeeping models do not.

As a criterion for inclusion in this carbon budget, we only retain models that simulate a positive E_{LUC} during the 1990s, as assessed in the IPCC AR4 (Denman et al., 2007) and AR5 (Ciais et al., 2013). All DGVMs met this criterion, although one model was not included in the E_{LUC} estimate from DGVMs as it exhibited a spurious response to the transient land cover change forcing after its initial spin-up.

17.2.3 C.2.3 Mapping of national GHG inventory data to E_{LUC}

An approach was implemented to reconcile the large gap between ELUC from bookkeeping models and land use, land-use change and forestry (LULUCF) from national GHG Inventories (NGHGI) (see Tab. A8). This gap is due to different approaches to calculating "anthropogenic" CO_2 fluxes related to land-use change and land management (Grassi et al. 2018). In particular, the land sinks due to environmental change on managed lands are treated as non-anthropogenic in the global carbon budget, while they are generally considered as anthropogenic in NGHGIs ("indirect anthropogenic fluxes"; Eggleston et al., 2006). Building on previous studies (Grassi et al. 2021), the approach implemented here adds the DGVMs estimates of CO_2 fluxes due to environmental change from countries' managed forest area (part of the S_{LAND}) to the original E_{LUC} flux. This sum is expected to be conceptually more comparable to LULUCF than simply E_{LUC}.

ELUC data are taken from bookkeeping models, in line with the global carbon budget approach. To determine S_{LAND} on managed forest, the following steps were taken: Spatially gridded data of

"natural" forest NBP (S_{LAND} i.e., due to environmental change and excluding land use change fluxes) were obtained with S2 runs from DGVMs up to 2019 from the TRENDY v9 dataset. Results were first masked with the Hansen forest map (Hansen et al. 2013), with a 20% tree cover and following the FAO definition of forest (isolated pixels with maximum connectivity less than 0.5 ha are excluded), and then further masked with the "intact" forest map for the year 2013, i.e. forest areas characterised by no remotely detected signs of human activity (Potapov et al. 2017). This way, we obtained the S_{LAND} in "intact" and "non-intact" forest area, which previous studies (Grassi et al. 2021) indicated to be a good proxy, respectively, for "unmanaged" and "managed" forest area in the NGHGI. Note that only 4 models (CABLE-POP, CLASSIC, YIBs and ORCHIDEE-CNP) had forest NBP at grid cell level. Two models (OCN and ISBA-CTRIP) provided forest NEP and simulated disturbances at pixel level that were used as basis, in addition to forest cover fraction, to estimate forest NBP. For the other DGVMs, when a grid cell had forest, all the NBP was allocated to forest.

LULUCF data from NGHGIs are from Grassi et al. (2021) until 2017, updated until 2019 for UNFCCC Annex I countries. For non-Annex I countries, the years 2018 and 2019 were assumed to be equal to the average 2013-2017. This data includes all CO2 fluxes from land considered managed, which in principle encompasses all land uses (forest land, cropland, grassland, wetlands, settlements, and other land), changes among them, emissions from organic soils and from fires. In practice, although almost all Annex I countries report all land uses, many non-Annex I countries report only on deforestation and forest land, and only few countries report on other land uses. In most cases, NGHGI include most of the natural response to recent environmental change, because they use direct observations (e.g., national forest inventories) that do not allow separating direct and indirect anthropogenic effects (Eggleston et al., 2006).

To provide additional, largely independent assessments of fluxes on unmanaged vs managed lands, we include a DGVM that allows diagnosing fluxes from unmanaged vs managed lands by tracking vegetation cohorts of different ages separately. This model, ORCHIDEE-MICT (Yue et al., 2018), was run using the same LUH2 forcing as the DGVMs used in this budget (Section 2.5) and the bookkeeping models BLUE and OSCAR (Section 2.2). Old-aged forest was classified as primary forest after a certain threshold of carbon density was reached again, and the model-internal distinction between primary and secondary forest used as proxies for unmanaged vs managed forests; agricultural lands are added to the latter to arrive at total managed land.

Tab. A8 shows the resulting mapping of global carbon cycle models' land flux definitions to that of the NGHGI (discussed in Section 3.2.2). ORCHIDEE-MICT estimates for SLAND on intact forests are expected to be higher than based on DGVMs in combination with the NGHGI managed/unmanaged forest data because the unmanaged forest area, with about 27 mio km2, is estimated to be substantially larger by ORCHIDEE-MICT than, with less than 10 mio km2, by the NGHGI, while managed forest area is estimated to be smaller (22 compared to 32 mio km2). Related to this, S_{LAND} on non-intact lands plus E_{LUC} is a larger source estimated by ORCHIDEE-MICT compared to NGHGI. We also show as comparison FAOSTAT emissions totals (FAO, 2021), which include emissions from net forest conversion and fluxes on forest land (Tubiello et al., 2021) as well as CO_2 emissions from peat drainage and peat fires.

17.2.4 C.2.4 Uncertainty assessment for E_{LUC}

Differences between the bookkeeping models and DGVMs models originate from three main sources: the different methodologies, which among others lead to inclusion of the loss of additional sink capacity in DGVMs (see Appendix D1.4), the underlying land-use/land cover data set, and the different processes represented (Table A1). We examine the results from the DGVMs models and of the bookkeeping method and use the resulting variations as a way to characterise the uncertainty in E_{LUC}.

Despite these differences, the E_{LUC} estimate from the DGVMs multi-model mean is consistent with the average of the emissions from the bookkeeping models (Table 5). However there are large differences among individual DGVMs (standard deviation at around 0.5 GtC yr^{-1}; Table 5), between the bookkeeping estimates (average difference 1850-2020 BLUE-updated H&N2017 of 0.8 GtC yr^{-1}, BLUE-OSCAR of 0.4 GtC yr^{-1}, OSCAR-updated H&N2017 of 0.3 GtC yr^{-1}), and between the updated estimate of H&N2017 and its previous model version (Houghton et al., 2012). A factorial analysis of differences between BLUE and H&N2017 attributed them particularly to differences in carbon densities between natural and managed vegetation or primary and secondary vegetation (Bastos et al., 2021). Earlier studies additionally showed the relevance of the different land-use forcing as applied (in updated versions) also in the current study (Gasser et al., 2020).

The uncertainty in E_{LUC} of ±0.7 GtC yr^{-1} reflects our best value judgement that there is at least 68% chance (±1σ) that the true land-use change emission lies within the given range, for the range of processes considered here. Prior to the year 1959, the uncertainty in E_{LUC} was taken from the

standard deviation of the DGVMs. We assign low confidence to the annual estimates of E_{LUC} because of the inconsistencies among estimates and of the difficulties to quantify some of the processes in DGVMs.

17.2.5 C.2.5 Emissions projections for E_{LUC}

We project the 2021 land-use emissions for BLUE, the updated H&N2017 and OSCAR, starting from their estimates for 2020 assuming unaltered peat drainage, which has low interannual variability, and the highly variable emissions from peat fires, tropical deforestation and degradation as estimated using active fire data (MCD14ML; Giglio et al., 2016). Those latter scale almost linearly with GFED over large areas (van der Werf et al., 2017), and thus allows for tracking fire emissions in deforestation and tropical peat zones in near-real time.

17.3 Appendix C.3 Methodology Ocean CO_2 sink

17.3.1 C.3.1 Observation-based estimates

We primarily use the observational constraints assessed by IPCC of a mean ocean CO_2 sink of 2.2 ± 0.7 GtC yr^{-1} for the 1990s (90% confidence interval; Ciais et al., 2013) to verify that the GOBMs provide a realistic assessment of S_{OCEAN}. This is based on indirect observations with seven different methodologies and their uncertainties, using the methods that are deemed most reliable for the assessment of this quantity (Denman et al., 2007; Ciais et al., 2013). The observation-based estimates use the ocean/land CO_2 sink partitioning from observed atmospheric CO_2 and O_2/N_2 concentration trends (Manning and Keeling, 2006; Keeling and Manning, 2014), an oceanic inversion method constrained by ocean biogeochemistry data (Mikaloff Fletcher et al., 2006), and a method based on penetration time scale for chlorofluorocarbons (McNeil et al., 2003). The IPCC estimate of 2.2 GtC yr^{-1} for the 1990s is consistent with a range of methods (Wanninkhof et al., 2013). We refrain from using the IPCC estimates for the 2000s (2.3 ± 0.7 GtC yr^{-1}), and the period 2002-2011 (2.4 ± 0.7 GtC yr^{-1}, Ciais et al., 2013) as these are based on trends derived mainly from models and one data-product (Ciais et al., 2013). Additional constraints summarised in AR6 (Canadell et al., 2021) are the interior ocean anthropogenic carbon change (Gruber et al., 2019) and ocean sink estimate from atmospheric CO_2 and O_2/N_2 (Tohjima et al., 2019) which are used for model evaluation and discussion, respectively.

We also use eight estimates of the ocean CO_2 sink and its variability based on surface ocean fCO_2 maps obtained by the interpolation of surface ocean fCO_2 measurements from 1990 onwards due

to severe restriction in data availability prior to 1990 (Figure 9). These estimates differ in many respects: they use different maps of surface fCO_2, different atmospheric CO_2 concentrations, wind products and different gas-exchange formulations as specified in Table A3. We refer to them as fCO_2-based flux estimates. The measurements underlying the surface fCO_2 maps are from the Surface Ocean CO_2 Atlas version 2021 (SOCATv2021; Bakker et al., 2021), which is an update of version 3 (Bakker et al., 2016) and contains quality-controlled data through 2020 (see data attribution Table A5). Each of the estimates uses a different method to then map the SOCAT v2021 data to the global ocean. The methods include a data-driven diagnostic method (Rödenbeck et al., 2013; referred to here as Jena-MLS), three neural network models (Landschützer et al., 2014; referred to as MPI-SOMFFN; Chau et al., 2021; Copernicus Marine Environment Monitoring Service, referred to here as CMEMS-LSCE-FFNN; and Zeng et al., 2014; referred to as NIES-FNN), two cluster regression approaches (Gregor et al., 2019; referred to here as CSIR-ML6; and Gregor and Gruber, 2021, referred to as OS-ETHZ-GRaCER), and a multi-linear regression method (Iida et al., 2021; referred to as JMA-MLR). The ensemble mean of the fCO_2-based flux estimates is calculated from these seven mapping methods. Further, we show the flux estimate of Watson et al. (2020) who also use the MPI-SOMFFN method to map the adjusted fCO_2 data to the globe, but resulting in a substantially larger ocean sink estimate, owing to a number of adjustments they applied to the surface ocean fCO_2 data and the gas-exchange parameterization. Concretely, these authors adjusted the SOCAT fCO_2 downward to account for differences in temperature between the depth of the ship intake and the relevant depth right near the surface, and included a further adjustment to account for the cool surface skin temperature effect. The Watson et al. flux estimate hence differs from the others by their choice of adjusting the flux to a cool, salty ocean surface skin. Watson et al. (2020) showed that this temperature adjustment leads to an upward correction of the ocean carbon sink, up to 0.9 GtC yr^{-1}, that, if correct, should be applied to all fCO_2-based flux estimates. So far, this adjustment is based on a single line of evidence and hence associated with low confidence until further evidence is available. The Watson et al flux estimate presented here is therefore not included in the ensemble mean of the fCO_2-based flux estimates. This choice will be re-evaluated in upcoming budgets based on further lines of evidence.

The CO_2 flux from each fCO_2-based product is either already at or above 98% areal coverage (Jena-MLS, OS-ETHZ-GRaCER), filled by the data-provider (using Fay et al., 2021a, method for JMA-MLR; and Landschützer et al., 2020, methodology for MPI-SOMFFN) or scaled for the remaining

products by the ratio of the total ocean area covered by the respective product to the total ocean area ($361.9e6$ km^2) from ETOPO1 (Amante and Eakins, 2009; Eakins and Sharman, 2010). In products where the covered area varies with time (e.g., CMEMS-LSCE-FFNN) we use the maximum area coverage. The lowest coverage is 93% (NIES-NN), resulting in a maximum adjustment factor of 1.08 (Table A3, Hauck et al., 2020).

We further use results from two diagnostic ocean models, Khatiwala et al. (2013) and DeVries (2014), to estimate the anthropogenic carbon accumulated in the ocean prior to 1959. The two approaches assume constant ocean circulation and biological fluxes, with S_{OCEAN} estimated as a response in the change in atmospheric CO_2 concentration calibrated to observations. The uncertainty in cumulative uptake of ±20 GtC (converted to ±1σ) is taken directly from the IPCC's review of the literature (Rhein et al., 2013), or about ±30% for the annual values (Khatiwala et al., 2009).

17.3.2 C.3.2 Global Ocean Biogeochemistry Models (GOBMs)

The ocean CO_2 sink for 1959-2019 is estimated using eight GOBMs (Table A2). The GOBMs represent the physical, chemical, and biological processes that influence the surface ocean concentration of CO_2 and thus the air-sea CO_2 flux. The GOBMs are forced by meteorological reanalysis and atmospheric CO_2 concentration data available for the entire time period. They mostly differ in the source of the atmospheric forcing data (meteorological reanalysis), spin up strategies, and in their horizontal and vertical resolutions (Table A2). All GOBMs except one (CESM-ETHZ) do not include the effects of anthropogenic changes in nutrient supply (Duce et al., 2008). They also do not include the perturbation associated with changes in riverine organic carbon (see Section 2.7.3).

Three sets of simulations were performed with each of the GOBMs. Simulation A applied historical changes in climate and atmospheric CO_2 concentration. Simulation B is a control simulation with constant atmospheric forcing (normal year or repeated year forcing) and constant pre-industrial atmospheric CO_2 concentration. Simulation C is forced with historical changes in atmospheric CO_2 concentration, but repeated year or normal year atmospheric climate forcing. To derive S_{OCEAN} from the model simulations, we subtracted the annual time series of the control simulation B from the annual time series of simulation A. Assuming that drift and bias are the same in simulations A and B, we thereby correct for any model drift. Further, this difference also removes the natural

steady state flux (assumed to be 0 GtC yr^{-1} globally without rivers) which is often a major source of biases. Simulation B of IPSL had to be treated differently as it was forced with constant atmospheric CO_2 but observed historical changes in climate. For IPSL, we fitted a linear trend to the simulation B and subtracted this linear trend from simulation A. This approach assures that the interannual variability is not removed from IPSL simulation A.

The absolute correction for bias and drift per model in the 1990s varied between <0.01 GtC yr^{-1} and 0.26 GtC yr^{-1}, with six models having positive biases, and one model having essentially no bias (NorESM). The remaining model (MPI) uses riverine input and therefore simulates outgassing in simulation B, i.e., a seemingly negative bias. By subtracting simulation B, also the ocean carbon sink of the MPI model follows the definition of S_{OCEAN}. This correction reduces the model mean ocean carbon sink by 0.03 GtC yr^{-1} in the 1990s. The ocean models cover 99% to 101% of the total ocean area, so that area-scaling is not necessary.

17.3.3 C.3.3 GOBM evaluation and uncertainty assessment for S_{OCEAN}

The ocean CO_2 sink for all GOBMs and the ensemble mean falls within 90% confidence of the observed range, or 1.5 to 2.9 GtC yr^{-1} for the 1990s (Ciais et al., 2013) after applying adjustments. An exception is the MPI model, which simulates a low ocean carbon sink of 1.38 GtC yr^{-1} for the 1990s in simulation A owing to the inclusion of riverine carbon flux. After adjusting to the GCB's definition of S_{OCEAN} by subtracting simulation B, the MPI model falls into the observed range with an estimated sink of 1.69 GtC yr^{-1}.

The GOBMs and data products have been further evaluated using the fugacity of sea surface CO_2 (fCO_2) from the SOCAT v2021 database (Bakker et al., 2016, 2021). We focused this evaluation on the root mean squared error (RMSE) between observed and modelled fCO_2 and on a measure of the amplitude of the interannual variability of the flux (modified after Rödenbeck et al., 2015). The RMSE is calculated from detrended, annually and regionally averaged time series calculated from GOBMs and data-product fCO_2 subsampled to open ocean (water depth > 400 m) SOCAT sampling points to measure the misfit between large-scale signals (Hauck et al., 2020) The amplitude of the S_{OCEAN} interannual variability (A-IAV) is calculated as the temporal standard deviation of the detrended CO_2 flux time series (Rödenbeck et al., 2015, Hauck et al., 2020). These metrics are chosen because RMSE is the most direct measure of data-model mismatch and the A-

IAV is a direct measure of the variability of S_{OCEAN} on interannual timescales. We apply these metrics globally and by latitude bands. Results are shown in Fig. B2 and discussed in Section 3.5.5.

We quantify the 1-σ uncertainty around the mean ocean sink of anthropogenic CO_2 by assessing random and systematic uncertainties for the GOBMs and data-products. The random uncertainties are taken from the ensemble standard deviation (0.3 GtC yr^{-1} for GOBMs, 0.3 GtC yr^{-1} for data-products). We derive the GOBMs systematic uncertainty by the deviation of the DIC inventory change 1994-2007 from the Gruber et al (2019) estimate (0.5 GtC yr^{-1}) and suggest these are related to physical transport (mixing, advection) into the ocean interior. For the data-products, we consider systematic uncertainties stemming from uncertainty in fCO_2 observations (0.2 GtC yr^{-1}, Takahashi et al., 2009; Wanninkhof et al., 2013), gas-transfer velocity (0.2 GtC yr^{-1}, Ho et al., 2011; Wanninkhof et al., 2013; Roobaert et al., 2018), wind product (0.1 GtC yr^{-1}, Fay et al., 2021a), river flux adjustment (0.2 GtC yr^{-1}, Jacobson et al., 2007; Resplandy et al., 2018), and fCO_2 mapping (0.2 GtC yr^{-1}, Landschützer et al., 2014). Combining these uncertainties as their squared sums, we assign an uncertainty of ± 0.6 GtC yr^{-1} to the GOBMs ensemble mean and an uncertainty of ± 0.5 GtC yr^{-1} to the data-product ensemble mean. These uncertainties are propagated as $\sigma(S_{OCEAN}) = (1/2^2 * 0.6^2 + 1/2^2 * 0.5^2)^{1/2}$ GtC yr^{-1} and result in an ± 0.4 GtC yr^{-1} uncertainty around the best estimate of S_{OCEAN}.

We examine the consistency between the variability of the model-based and the fCO_2-based data products to assess confidence in S_{OCEAN}. The interannual variability of the ocean fluxes (quantified as A-IAV, the standard deviation after detrending, Figure B2) of the seven fCO_2-based data products plus the Watson et al. (2020) product for 1990-2020, ranges from 0.16 to 0.26 GtC yr^{-1} with the lower estimates by the three ensemble methods (CSIR-ML6, CMEMS-LSCE-FFNN, OS-ETHZ-GRaCER). The inter-annual variability in the GOBMs ranges between 0.10 and 0.19 GtC yr^{-1}, hence there is overlap with the lower A-IAV estimates of three data-products.

Individual estimates (both GOBMs and data products) generally produce a higher ocean CO_2 sink during strong El Niño events. There is emerging agreement between GOBMs and data-products on the patterns of decadal variability of S_{OCEAN} with a global stagnation in the 1990s and an extra-tropical strengthening in the 2000s (McKinley et al., 2020, Hauck et al., 2020). The central estimates of the annual flux from the GOBMs and the fCO_2-based data products have a correlation *r* of 0.94 (1990-2020). The agreement between the models and the data products reflects some

consistency in their representation of underlying variability since there is little overlap in their methodology or use of observations.

17.4 Appendix C.4 Methodology Land CO_2 sink

17.4.1 C.4.1 DGVM simulations

The DGVMs model runs were forced by either the merged monthly Climate Research Unit (CRU) and 6 hourly Japanese 55-year Reanalysis (JRA-55) data set or by the monthly CRU data set, both providing observation-based temperature, precipitation, and incoming surface radiation on a 0.5°x0.5° grid and updated to 2020 (Harris et al., 2014, 2020). The combination of CRU monthly data with 6 hourly forcing from JRA-55 (Kobayashi et al., 2015) is performed with methodology used in previous years (Viovy, 2016) adapted to the specifics of the JRA-55 data.

New to this budget is the revision of incoming short-wave radiation fields to take into account aerosol impacts and the division of total radiation into direct and diffuse components as summarised below.

The diffuse fraction dataset offers 6-hourly distributions of the diffuse fraction of surface shortwave fluxes over the period 1901-2020. Radiative transfer calculations are based on monthly-averaged distributions of tropospheric and stratospheric aerosol optical depth, and 6-hourly distributions of cloud fraction. Methods follow those described in the Methods section of Mercado et al. (2009), but with updated input datasets.

The time series of speciated tropospheric aerosol optical depth is taken from the historical and RCP8.5 simulations by the HadGEM2-ES climate model (Bellouin et al., 2011). To correct for biases in HadGEM2-ES, tropospheric aerosol optical depths are scaled over the whole period to match the global and monthly averages obtained over the period 2003-2020 by the CAMS Reanalysis of atmospheric composition (Inness et al., 2019), which assimilates satellite retrievals of aerosol optical depth.

The time series of stratospheric aerosol optical depth is taken from the by Sato et al. (1993) climatology, which has been updated to 2012. Years 2013-2020 are assumed to be background years so replicate the background year 2010. That assumption is supported by the Global Space-based Stratospheric Aerosol Climatology time series (1979-2016; Thomason et al., 2018). The time series of cloud fraction is obtained by scaling the 6-hourly distributions simulated in the Japanese

Reanalysis (Kobayashi et al., 2015) to match the monthly-averaged cloud cover in the CRU TS v4.03 dataset (Harris et al., 2021). Surface radiative fluxes account for aerosol-radiation interactions from both tropospheric and stratospheric aerosols, and for aerosol-cloud interactions from tropospheric aerosols, except mineral dust. Tropospheric aerosols are also assumed to exert interactions with clouds.

The radiative effects of those aerosol-cloud interactions are assumed to scale with the radiative effects of aerosol-radiation interactions of tropospheric aerosols, using regional scaling factors derived from HadGEM2-ES. Diffuse fraction is assumed to be 1 in cloudy sky. Atmospheric constituents other than aerosols and clouds are set to a constant standard mid-latitude summer atmosphere, but their variations do not affect the diffuse fraction of surface shortwave fluxes.

In summary, the DGVMs forcing data include time dependent gridded climate forcing, global atmospheric CO_2 (Dlugokencky and Tans, 2022), gridded land cover changes (see Appendix C.2.2), and gridded nitrogen deposition and fertilisers (see Table A1 for specific models details).

Four simulations were performed with each of the DGVMs. Simulation 0 (S0) is a control simulation which uses fixed pre-industrial (year 1700) atmospheric CO2 concentrations, cycles early 20th century (1901-1920) climate and applies a time-invariant pre-industrial land cover distribution and pre-industrial wood harvest rates. Simulation 1 (S1) differs from S0 by applying historical changes in atmospheric CO2 concentration and N inputs. Simulation 2 (S2) applies historical changes in atmospheric CO_2 concentration, N inputs, and climate, while applying time-invariant pre-industrial land cover distribution and pre-industrial wood harvest rates. Simulation 3 (S3) applies historical changes in atmospheric CO2 concentration, N inputs, climate, and land cover distribution and wood harvest rates.

S2 is used to estimate the land sink component of the global carbon budget (S_{LAND}). S3 is used to estimate the total land flux but is not used in the global carbon budget. We further separate S_{LAND} into contributions from CO_2 (=S1-S0) and climate (=S2-S1-S0).

17.4.2 C.4.2 DGVM evaluation and uncertainty assessment for S_{LAND}

We apply three criteria for minimum DGVMs realism by including only those DGVMs with (1) steady state after spin up, (2) global net land flux ($S_{LAND} - E_{LUC}$) that is an atmosphere-to-land carbon flux over the 1990s ranging between -0.3 and 2.3 GtC yr^{-1}, within 90% confidence of constraints by global atmospheric and oceanic observations (Keeling and Manning, 2014;

Wanninkhof et al., 2013), and (3) global E_{LUC} that is a carbon source to the atmosphere over the 1990s, as already mentioned in section C.2.2. All 17 DGVMs meet these three criteria.

In addition, the DGVMs results are also evaluated using the International Land Model Benchmarking system (ILAMB; Collier et al., 2018). This evaluation is provided here to document, encourage and support model improvements through time. ILAMB variables cover key processes that are relevant for the quantification of S_{LAND} and resulting aggregated outcomes. The selected variables are vegetation biomass, gross primary productivity, leaf area index, net ecosystem exchange, ecosystem respiration, evapotranspiration, soil carbon, and runoff (see Fig. B3 for the results and for the list of observed databases). Results are shown in Fig. B3 and discussed in Section 3.6.5.

For the uncertainty for S_{LAND}, we use the standard deviation of the annual CO_2 sink across the DGVMs, averaging to about $\pm$ 0.6 GtC yr^{-1} for the period 1959 to 2019. We attach a medium confidence level to the annual land CO_2 sink and its uncertainty because the estimates from the residual budget and averaged DGVMs match well within their respective uncertainties (Table 5).

17.5 Appendix C.5 Methodology Atmospheric Inversions

Six atmospheric inversions (details of each in Table A4) were used to infer the spatio-temporal distribution of the CO_2 flux exchanged between the atmosphere and the land or oceans. These inversions are based on Bayesian inversion principles with prior information on fluxes and their uncertainties. They use very similar sets of surface measurements of CO_2 time series (or subsets thereof) from various flask and in situ networks. One inversion system also used satellite xCO_2 retrievals from GOSAT and OCO-2.

Each inversion system uses different methodologies and input data but is rooted in Bayesian inversion principles. These differences mainly concern the selection of atmospheric CO_2 data and prior fluxes, as well as the spatial resolution, assumed correlation structures, and mathematical approach of the models. Each system uses a different transport model, which was demonstrated to be a driving factor behind differences in atmospheric inversion-based flux estimates, and specifically their distribution across latitudinal bands (Gaubert et al., 2019; Schuh et al., 2019). The inversion systems prescribe same global fossil fuel emissions for E_{FOS}; specifically, the GCP's Gridded Fossil Emissions Dataset version 2021 (GCP-GridFEDv2021.2; Jones et al., 2021b), which is an update through 2020 of the first version of GCP-GridFED presented by Jones et al. (2021a).

GCP-GridFEDv2021.2 scales gridded estimates of CO_2 emissions from EDGARv4.3.2 (Janssens-Maenhout et al., 2019) within national territories to match national emissions estimates provided by the GCP for the years 1959-2020, which were compiled following the methodology described in Appendix C.1 based on all information available on 31st July 2021 (R. Andrew, *pers. comm.*). Typically, the GCP-GridFED adopts the seasonal variation in emissions (the monthly distribution of annual emissions) from EDGAR and applies small corrections based on heating or cooling degree days to account for the effects of inter-annual climate variability on the seasonality emissions (Jones et al., 2021a). However, strategies taken to deal with the COVID-19 pandemic during 2020 mean that the seasonality of emissions diverged substantially in 2020 from a typical year. To account for this change, GCP-GridFEDv2021.2 adopts the national seasonality in emissions from Carbon Monitor (Liu et al., 2020a,b) during the years 2019-2020 (Jones et al. 2021b).

The consistent use of GCP-GridFEDv2021.2 for E_{FOS} ensures a close alignment with the estimate of E_{FOS} used in this budget assessment, enhancing the comparability of the inversion-based estimate with the flux estimates deriving from DGVMs, GOBMs and fCO_2-based methods. To account for small differences in regridding, and the use of a slightly earlier file version (GCP-GridFEDv2021.1) for 2000-2018 in CarbonTracker Europe, small fossil fuel corrections were applied to all inverse models to make the estimated uptake of atmospheric CO2 fully consistent. Finally, we note that GCP-GridFEDv2021.2 includes emissions from cement production, but it does not include the cement carbonation CO_2 sink (Xi et al., 2016; Cao et al., 2020; Guo et al. 2021) that is applied to the GCB estimate of E_{FOS} in Table 6.

The land and ocean CO_2 fluxes from atmospheric inversions contain anthropogenic perturbation and natural pre-industrial CO_2 fluxes. On annual time scales, natural pre-industrial fluxes are primarily land CO_2 sinks and ocean CO_2 sources corresponding to carbon taken up on land, transported by rivers from land to ocean, and outgassed by the ocean. These pre-industrial land CO_2 sinks are thus compensated over the globe by ocean CO_2 sources corresponding to the outgassing of riverine carbon inputs to the ocean, using the exact same numbers and distribution as described for the oceans in Section 2.4. To facilitate the comparison, we adjusted the inverse estimates of the land and ocean fluxes per latitude band with these numbers to produce historical perturbation CO_2 fluxes from inversions. Finally, for the presentation of the comparison in Figure 11 we modified the FF-corrected and riverine-adjusted land sinks from the inversions further, by removing a 0.2 GtCyr^{-1} CO_2 sink that is ascribed to cement carbonation in the GCB, rather than to

terrestrial ecosystems. The latter is not applied in the inversion products released through GCB or the original data portals of these products.

All participating atmospheric inversions are checked for consistency with the annual global growth rate, as both are derived from the global surface network of atmospheric CO2 observations. In this exercise, we use the conversion factor of 2.086 GtC/ppm to convert the inverted carbon fluxes to mole fractions, as suggested by Prather (2012). This number is specifically suited for the comparison to surface observations that do not respond uniformly, nor immediately, to each year's summed sources and sinks. This factor is therefore slightly smaller than the GCB conversion factor in Table 1 (2.142 GtC/ppm, Ballantyne et al., 2012). Overall, the inversions agree with the growth rate with biases between 0.03-0.08 ppm (0.06-0.17 GtCyr^{-1}) on the decadal average.

The atmospheric inversions are also evaluated using vertical profiles of atmospheric CO_2 concentrations (Fig. B4). More than 30 aircraft programs over the globe, either regular programs or repeated surveys over at least 9 months, have been used in order to draw a robust picture of the model performance (with space-time data coverage irregular and denser in the 0-45°N latitude band; Table A6). The six models are compared to the independent aircraft CO_2 measurements between 2 and 7 km above sea level between 2001 and 2020. Results are shown in Fig. B4, where the inversions generally match the atmospheric mole fractions to within 0.6 ppm at all latitudes, except for CT Europe in 2010-2020 over the more sparsely sampled southern hemisphere.

18   Appendix D Processes not included in the global carbon budget

18.1   Appendix D.1 Contribution of anthropogenic CO and CH$_4$ to the global carbon budget

Equation (1) includes only partly the net input of CO_2 to the atmosphere from the chemical oxidation of reactive carbon-containing gases from sources other than the combustion of fossil fuels, such as: (1) cement process emissions, since these do not come from combustion of fossil fuels, (2) the oxidation of fossil fuels, (3) the assumption of immediate oxidation of vented methane in oil production. However, it omits any other anthropogenic carbon-containing gases that are eventually oxidised in the atmosphere, such as anthropogenic emissions of CO and CH$_4$. An attempt is made in this section to estimate their magnitude and identify the sources of uncertainty. Anthropogenic CO emissions are from incomplete fossil fuel and biofuel burning and deforestation fires. The main anthropogenic emissions of fossil CH$_4$ that matter for the global

(anthropogenic) carbon budget are the fugitive emissions of coal, oil and gas sectors (see below). These emissions of CO and CH_4 contribute a net addition of fossil carbon to the atmosphere.

In our estimate of E_{FOS} we assumed (Section 2.1.1) that all the fuel burned is emitted as CO_2, thus CO anthropogenic emissions associated with incomplete fossil fuel combustion and its atmospheric oxidation into CO_2 within a few months are already counted implicitly in E_{FOS} and should not be counted twice (same for E_{LUC} and anthropogenic CO emissions by deforestation fires). Anthropogenic emissions of fossil CH_4 are however not included in E_{FOS}, because these fugitive emissions are not included in the fuel inventories. Yet they contribute to the annual CO_2 growth rate after CH_4 gets oxidized into CO_2. Emissions of fossil CH_4 represent 30% of total anthropogenic CH_4 emissions (Saunois et al. 2020; their top-down estimate is used because it is consistent with the observed CH_4 growth rate), that is 0.083 GtC yr^{-1} for the decade 2008-2017. Assuming steady state, an amount equal to this fossil CH_4 emission is all converted to CO_2 by OH oxidation, and thus explain 0.083 GtC yr^{-1} of the global CO_2 growth rate with an uncertainty range of 0.061 to 0.098 GtC yr^{-1} taken from the min-max of top-down estimates in Saunois et al. (2020). If this min-max range is assumed to be 2 σ because Saunois et al. (2020) did not account for the internal uncertainty of their min and max top-down estimates, it translates into a 1-σ uncertainty of 0.019 GtC yr^{-1}.

Other anthropogenic changes in the sources of CO and CH_4 from wildfires, vegetation biomass, wetlands, ruminants, or permafrost changes are similarly assumed to have a small effect on the CO_2 growth rate. The CH_4 and CO emissions and sinks are published and analysed separately in the Global Methane Budget and Global Carbon Monoxide Budget publications, which follow a similar approach to that presented here (Saunois et al., 2020; Zheng et al., 2019).

18.2 Appendix D.2 Contribution of other carbonates to CO_2 emissions

Although we do account for cement carbonation (a carbon sink), the contribution of emissions of fossil carbonates (carbon sources) other than cement production is not systematically included in estimates of $E_{FOS,}$ except at the national level where they are accounted for in the UNFCCC national inventories. The missing processes include CO_2 emissions associated with the calcination of lime and limestone outside cement production. Carbonates are also used in various industries, including in iron and steel manufacture and in agriculture. They are found naturally in some coals. CO_2 emissions from fossil carbonates other than cement are estimated to amount to about 1% of

E_{FOS} (Crippa et al., 2019), though some of these carbonate emissions are included in our estimates (e.g., via UNFCCC inventories).

18.3 Appendix D.3 Anthropogenic carbon fluxes in the land-to-ocean aquatic continuum

The approach used to determine the global carbon budget refers to the mean, variations, and trends in the perturbation of CO_2 in the atmosphere, referenced to the pre-industrial era. Carbon is continuously displaced from the land to the ocean through the land-ocean aquatic continuum (LOAC) comprising freshwaters, estuaries, and coastal areas (Bauer et al., 2013; Regnier et al., 2013). A substantial fraction of this lateral carbon flux is entirely 'natural' and is thus a steady state component of the pre-industrial carbon cycle. We account for this pre-industrial flux where appropriate in our study (see Appendix C.3). However, changes in environmental conditions and land-use change have caused an increase in the lateral transport of carbon into the LOAC – a perturbation that is relevant for the global carbon budget presented here.

The results of the analysis of Regnier et al. (2013) can be summarised in two points of relevance for the anthropogenic CO_2 budget. First, the anthropogenic perturbation of the LOAC has increased the organic carbon export from terrestrial ecosystems to the hydrosphere by as much as 1.0 ± 0.5 GtC yr^{-1} since pre-industrial times, mainly owing to enhanced carbon export from soils. Second, this exported anthropogenic carbon is partly respired through the LOAC, partly sequestered in sediments along the LOAC and to a lesser extent, transferred to the open ocean where it may accumulate or be outgassed. The increase in storage of land-derived organic carbon in the LOAC carbon reservoirs (burial) and in the open ocean combined is estimated by Regnier et al. (2013) at 0.65 ± 0.35 GtC yr^{-1}. The inclusion of LOAC related anthropogenic CO_2 fluxes should affect estimates of S_{LAND} and S_{OCEAN} in Eq. (1) but does not affect the other terms. Representation of the anthropogenic perturbation of LOAC CO_2 fluxes is however not included in the GOBMs and DGVMs used in our global carbon budget analysis presented here.

18.4 Appendix D.4 Loss of additional land sink capacity

Historical land-cover change was dominated by transitions from vegetation types that can provide a large carbon sink per area unit (typically, forests) to others less efficient in removing CO_2 from the atmosphere (typically, croplands). The resultant decrease in land sink, called the 'loss of additional sink capacity', can be calculated as the difference between the actual land sink under changing land-cover and the counterfactual land sink under pre-industrial land-cover. This term is

not accounted for in our global carbon budget estimate. Here, we provide a quantitative estimate of this term to be used in the discussion. Seven of the DGVMs used in Friedlingstein et al. (2019) performed additional simulations with and without land-use change under cycled pre-industrial environmental conditions. The resulting loss of additional sink capacity amounts to 0.9 ± 0.3 GtC yr^{-1} on average over 2009-2018 and 42 ± 16 GtC accumulated between 1850 and 2018 (Obermeier et al., 2021). OSCAR, emulating the behaviour of 11 DGVMs finds values of the loss of additional sink capacity of 0.7 ± 0.6 GtC yr^{-1} and 31 ± 23 GtC for the same time period (Gasser et al., 2020). Since the DGVM-based ELUC estimates are only used to quantify the uncertainty around the bookkeeping models' ELUC, we do not add the loss of additional sink capacity to the bookkeeping estimate.